Measurements of Prompt Photon Photoproduction at HERA

Sung Won Lee

Department of Physics and Astronomy

University of Glasgow

Glasgow, Scotland, UK

Thesis submitted for the degree of
Doctor of Philosophy

November 2000

Abstract

Measurements of inclusive prompt photon and prompt photons, together with an accompanying jet, in photoproduction at HERA have been made with the ZEUS detector, using an integrated luminosity of 38.4 pb^{-1}. We have performed two analyses in the study of prompt photon production.

First inclusive cross section measurements for prompt photon production have been presented as a function of the pseudorapidity and the transverse energy (η^γ, E_T^γ) of the photon, for $E_T^\gamma > 5$ GeV in the γp centre-of-mass energy range 134–285 GeV. Comparisons are made with predictions from Monte Carlo models having leading–logarithm parton showers, and with next–to–leading order QCD calculations, using currently available parameterisations of the photon structure. For positive η^γ (proton direction) there is good agreement, but for negative η^γ all predictions fall below the data. None of the available variations of the model parameters was found to be capable of removing the discrepancy with the data. The results indicated a need to review the present theoretical modelling of the parton structure of the photon at high x_γ regions.

A study of the intrinsic parton transverse momentum, k_T , of the quarks in the proton, as modelled within the framework of the PYTHIA Monte Carlo, has been performed using the kinematical properties of events with a measured jet as well as a prompt photon. A fit to the data gives a value of $<k_T>= 1.39 \pm 0.36\ ^{+0.12}_{-0.23}$ GeV. This result is compared with earlier high–energy proton–scattering measurements. A rising trend of $<k_T>$ with interaction energy is confirmed.

To My Parents

&

The late Professor Björn H Wiik

Outline

Two analyses of prompt photon photoproduction at HERA using 1996 and 1997 ZEUS data are presented in this thesis. Chapter 1 gives a brief resumé of the current understanding of QCD leading on to more detail about photoproduction processes. Chapter 2 then describes theoretical aspects and earlier experimental results in prompt photon production. Chapter 3 briefly describes the HERA machine and ZEUS detector with more detail given to specific components relevant to these analyses. Chapter 4 concerns work done by author on the ZEUS Barrel presampler detector. In Chapter 5 the Monte Carlo programs and samples used are discussed and in Chapter 6 we present the details of reconstruction and event selection procedure for the analyses presented in this thesis. Chapter 7 describes the separation procedure of photon signal from background to obtain a clean sample of prompt photon events. In Chapter 8, a first analysis, namely cross section measurements of inclusive prompt photons is discussed. A second analysis, a study of parton intrinsic transverse momentum in the proton using prompt photon photoproduction, is discussed in Chapter 9. Chapters 8 and 9 also discusses the physics implications of the results. The conclusions drawn from the two analyses are summarised in Chapter 10.

Earlier study of inclusive prompt photon procuction and the final results have been presented by author on behalf of the ZEUS collaboration at the *"Photon99"* and at the *"DIS 2000"* conference, respectively. My contribution to the proceedings constitutes appendix A and B. The main results of the inclusive prompt photon study have been published by ZEUS collaboration in Phys. Letters B (`Phys.Lett.B472`). The contribution to the ZEUS publication is included as appendix C.

Acknowledgements

First of all I am deeply grateful to my supervisor, Dr. Peter Bussey, for his continual support, encouragement and guidance and for providing physics advice on prompt photon analysis. I very much thank Prof. David Saxon for giving me the opportunity to join the Glasgow University PPE group and ZEUS Collaboration as a Ph.D student and his continous support.

The generous award of the British Chevening fellowship from the British Foreign and Commomwealth Office as well as financial support in the form of a Björn Wiik scholarship from the ICSC–Worldlab gave me the opportunity to concentrate on my research and these are most gratefully acknowledged. Special thanks go to Dr. M Cherrett, Prof. G. Wolf, Dr. L. Böhr and Prof. A. Zichichi.

I am extremely grateful to K. Umemori for his collaboration and for many useful discussions. I am also grateful to L. Gordon, M. Krawczyk and A. Zembrzuski for helpful conversations, and for making available to us calculations of the NLO prompt photon cross section. The main results of this analysis have been accepted by ZEUS collaboration for publication. I would like to thank the coordinators, L. Sinclair, J. Terrón and J. Repond of the physics analysis group for their help and encouragement. I am also grateful to M. Derrick, B. Foster, R. Yoshida, S. Schlenstedt and W. Smith for their encouraging support. Thanks must go to J. Hart and N. McCubbin for answering all my dumb questions when doing a CTD DQM shift. Also thanks to S. Chekanov and S. Magil for their help with the Barrel Presampler detector, and to L. Apanasevich, M. Begel, N. Brook, J. Butterworth, C. Foudas, M. Kimber, M. Klasen, B. Oh, M. Seymour, J. Womersley, Y. Yamazaki and M. Zielinski for many useful physics discussions.

The UK contingent at DESY have been a family away from home – so many good friends, too many to mention all of them here, but special thanks to those in the Glasgow office there – Anna, Claudia, Gavin, Laurel, Neil, Nick, Mairi and Rob, and also back in Glasgow – Esther, Jane, Tony, Peter, David and Ian, who have made the three years a lot more interesting than I hoped for. I gratefully acknowledge the help and support from DESY Koreans, Drs. J. Lee (his wife J. Moon), S. Nam, C. Kim and Miss H. Lim, and ZEUS–UK members. I am very grateful to Profs. D. Son, D. Kim, Il. Park, S. Hong, S. Choi, D. S. Kim, K. Sohn, J. Bae, E. Lee and Dr. Oh for the invaluable advice and encouragement.

Last but emphatically not least, my thanks goes out to Catherine McIntyre and Susan Ketels for their ever friendly help; despite many pressures they were always there for us.

Finally, I would like to thank Mum, Dad, Sung–Ho, Sung–Chang, for their love, support and encouragement throughout all of my education. Especially many thank–yous to Yoon–Hee for encouraging and believing in me with your love and support. I dedicate this thesis to them.

Contents

List of Figures

List of Tables

Chapter 1

Introduction

1.1 Preamble

Quantum ChromoDynamics (QCD) is a highly successful field theory in describing the interactions between the fundamental constituent of hadrons–quark and gluons. It is in good agreement with previous and current experimental data collected both at fixed target and collider experiments. The analysis of such large amounts of data has led us to a deeper understanding of the properties of the fundamental interactions, and also reveals the substructure of the hadrons. In particular, the electron–proton collider at HERA offers an excellent testing–ground for many aspects of QCD. However the use of perturbative QCD (pQCD), and its description of the hadronic structure with the parton model, still need further investigation. The role played by gluons, propagators of the strong force, was originally inferred indirectly via higher–order processes [1].

In this chapter Deep Inelastic Scattering in electron–proton collisions is used to define the relevant kinematics and the concept of a structure function. A discussion of photoproduction at HERA is also introduced.

1.2 Deep Inelastic Scattering

The scattering of high energy leptons off protons generally results in an inelastic reaction, ie. the proton disintegrates, and a large number of particles with a high total invariant mass can be produced in the final state. This process is called "deep–inelastic scattering" (DIS). Measuring the final state of the deep–inelastic *ep* scattering events allows us to determine the structure of proton. Within the picture of the Quark Parton model, the proton consists of quarks and gluons.

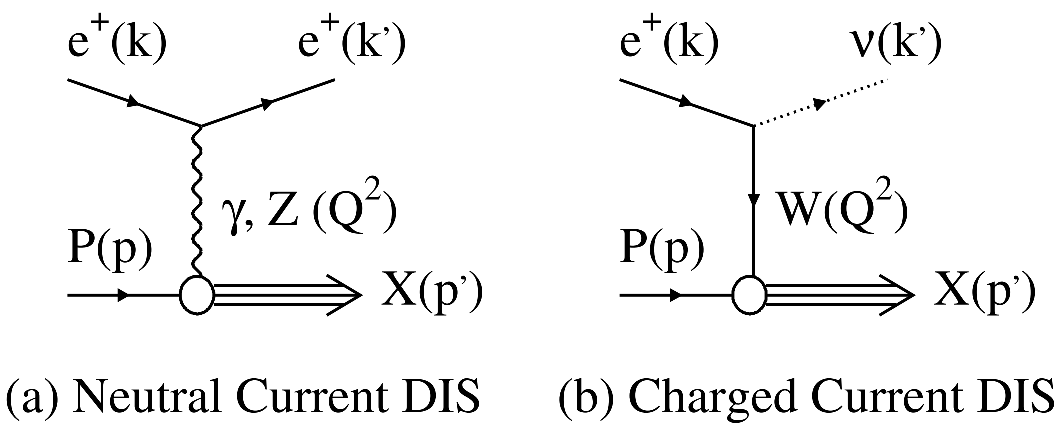

Figure 1.1: Lowest–order Feyman diagrams of (a) neutral current and (b) charged current deep–inelastic scattering reactions.

The highly–energetic incoming electron then probes the structure of the proton by coupling through the electroweak current to one of the partons inside the proton.

1.2.1 HERA Kinematics

There are two fundamental classes of DIS events and figure 1.1 shows a schematic diagrams of the reactions.

$$e^{\pm}p \rightarrow e^{\pm} + \mathrm{X} \qquad \text{and} \qquad e^{\pm}p \rightarrow \nu_e + \mathrm{X}$$

where X represents the spray of particles produced by the break–up of the proton (the hadronic final state). In the first process; (a) the charge of the lepton is conserved and the intermediate vector boson is neutral; γ, Z^0. This process is referred to as neutral current (NC) DIS. In the second process; (b) the lepton converts to an anti–neutrino via the exchange of a charged vector boson; $\mathrm{W}^{\pm}$. Therefore this process is called charged current (CC) DIS.

At a given centre of mass energy $\sqrt{s}$ the kinematics of electron–proton scattering are completely described by two of the following three Lorentz–invariant variables. The first, Q^2, is defined by the negative square of momentum transfer and specifies the virtuality of exchanged boson.

$$Q^2 = -q^2 = -(k - k')^2 \tag{1.1}$$

where k and k' denote the 4–momentum of the incoming and scattered lepton, respectively. The quantity $q = (k - k')$ denotes the 4–momentum transfer from the electron. The two dimensionless variables, x and y, are defined as:

$$x = \frac{-q^2}{2p \cdot q} \tag{1.2}$$

$$y = \frac{q \cdot p}{k \cdot p} \tag{1.3}$$

where p is the 4–momentum of the proton. In the parton model, x can be interpreted as the proton momentum fraction carried by struck quark and is referred to as the Bjorken scaling variable. In the proton rest frame, y corresponds to the fraction of the energy transferred from the lepton to the proton: $\frac{E-E'}{E} = \frac{E_\gamma}{E}$.

These three variables are related to each other and the square of the centre of mass energy, $s = (p+k)^2 = m_p^2 + 2p \cdot k$, by

$$Q^2 = s \cdot x \cdot y \tag{1.4}$$

hence only two of these variables are independent.

The square of the invariant mass W^2 of the hadronic final state X is related to x and Q^2 by the momentum conservation at the hadronic vertex;

$$W^2 = (p)^2 = (p+q)^2 = m_p^2 - Q^2 + 2p \cdot q \sim ys - Q^2 \tag{1.5}$$

The proton mass m_p is neglected in the approximation of the equations 1.4 and 1.5. Throughout the rest of this thesis, the natural system of units is used, where $\hbar = c = 1$.

1.2.2 The DIS cross section and structure function

The deep–inelastic ep scattering cross section can be factorised into a leptonic tensor, $L_{\mu\nu}$, and a hadronic tensor, $W^{\mu\nu}$.

$$d\sigma^{ep} \sim L_{\mu\nu} W^{\mu\nu} \tag{1.6}$$

At low Q^2 ($Q^2 \ll M^2_{Z^0,W^\pm}$), the contribution of weak neutral bosons to the cross section is small, since the Q^2–dependence of the photon cross section is $1/Q^4$, while that of the weak boson is $1/(M^2_{Z^0,W^\pm} + Q^2)^2$. Therefore the contribution of the weak boson is negligible in the low Q^2 region and it is possible to regard the electron–proton scattering via photon exchange. In this case, the general expression of the $W^{\mu\nu}$ can be parametrized by two functions W_1 and W_2. It depends on two independent Lorentz–invariant scalar variables, ν and Q^2, and have been renamed;

$$F_1(x, Q^2) \equiv m_p W_1(\nu, Q^2)$$
$$F_2(x, Q^2) \equiv \nu W_2(\nu, Q^2)$$

where the F_1 and F_2 are called proton structure functions, and $\nu = p \cdot q/m_p$ is the photon energy in the proton rest frame. The deep–inelastic $ep \to eX$ scattering cross section can then be written as;

$$\frac{d^2\sigma^{ep}}{dxdQ^2} = \frac{4\pi\alpha^2}{xQ^4}\left[\frac{y^2}{2}2xF_1(x, Q^2) + (1-y)\, F_2(x, Q^2)\right] \tag{1.7}$$

or with the definition of $F_L = F_2 - 2xF_1$

$$\frac{d^2\sigma^{ep}}{dxdQ^2} = \frac{2\pi\alpha^2}{xQ^4}\left[\left(1 + (1-y)^2\right) F_2 + 2\,(1-y)\, F_L\right] \tag{1.8}$$

where $F_L = \frac{Q^2}{4\pi^2\alpha}\sigma_L$ and is referred to as the Longitudinal structure function.

1.3 The Quark Parton Model

The naive quark parton model (QPM) relates the cross section formula to the quark distribution inside the proton, considering that the charged partons are the quarks [2]. It is assumed that each quark carries only the longitudinal momentum fraction ξ of the proton and does not carry the transverse momentum. In the QPM, the electron–proton scattering is regarded as a scattering between an electron and a quark. No interaction among partons inside the proton is assumed to occur during the electron–quark scattering. In this case the Bjorken scaling variable x is the same as the momentum fraction ξ.

In 1968 Bjorken predicted that the structure functions would depend only on one dimensionless scaling variable, x, in the limit $Q^2 \to \infty$ and $\nu \to \infty$, and it was confirmed by SLAC experiment [3]. In the QPM, the structure function F_2 corresponds to the sum of the partons momentum distribution $xf_i(x)$ weighted with the square of their electric charge e_i.

$$F_2(x, Q^2) = F_2(x) = \sum_i e_i^2 x f_i(x) \tag{1.9}$$

$$F_1(x, Q^2) = F_1(x) = \frac{1}{2x}F_2(x) \tag{1.10}$$

This equation 1.10 is a consequence of the partons having spin–$\frac{1}{2}$ and implies that the cross section for longitudinally polarised photons is zero [4]. The predicted fractional charge of the quarks was confirmed using neutrino–nucleon scattering experiment and the postulated number of 3 valence quarks in the proton (uud) and neutron (ddu) was experimentally confirmed using the Gross–Llewellyn-Smith sum rule [5].

1.3.1 The QCD Improved Parton Model

Although the QPM was a successful theory in explaining some of earlier experimental data, some problems of the model became apparent. If the proton consisted only of charged quarks, their momentum would be expected to add up to the proton momentum;

$$\sum_i \int_0^1 dx f_i(x) x = 1.$$

However, experimentally, this value was found to be ≈ 0.5 [6], implying that about half of the proton's momentum is carried by neutral partons. Direct evidence for the existence of these partons, called gluons, was found in 1979 via the observation of 3–jet events in e^+e^- annihilation at DESY [7].

This problem was solved by the formulation of a gauge theory of the strong interaction, Quantum ChromoDynamics (QCD), which is based on a SU(3) colour gauge symmetry group. The gluons are the gauge bosons of the strong force and QCD is the theory describing the colour interaction between quarks and gluons. Therefore the naive QPM was modified by QCD as quarks interact through gluons, and can radiate gluons in a QCD Compton process. Radiated gluons can split into quark pairs or gluons. The radiated gluons result in the quarks having a component of transverse momentum. Coupling to longitudinally polarised photons is then possible, thereby violating the equation 1.10. The value of the longitudinal structure function, F_L, is therefore no longer zero, but lies in the range $0 < F_L < F_2$.

Another consequence of the gluon radiation is scaling violations of the structure functions, which exhibit a logarithmic dependence on Q^2 at fixed x. The exchanged photon at low Q^2 is then interpreted as resolving the valence quark substructure. At high Q^2 a quark may have radiated a gluon and consequently has a fraction of momentum, x, less than its original value, or alternatively, it may have arisen from gluon splitting. At large x, where the valence quarks dominate, the quark density and hence F_2 falls with Q^2 as a result of the gluon radiation, while at small x the number of "sea" quarks and gluons is larger, so F_2 increases with Q^2. These scaling violations with a strong dependence of F_2 at small x for fixed Q^2 have been found at HERA [8].

1.3.2 The Evolution of Parton Distributions

Although the parton densities in a hadron cannot be calculated perturbatively when probed at low Q^2 values, the evolution of the quark ($q_i(x)$) and the gluon ($g(x)$) momentum distribution with Q^2 is quantitatively described in perturbative QCD by the Dokshitzer–Gribov–Lipatov–Altarelli–Parisi (DGLAP) equations [9], if the density at a certain initial $Q^2 = Q_0^2$ value is given. The DGLAP evolution of the quark and gluon densities is given by;

$$\frac{dq_i(x,Q^2)}{d\ln Q^2} = \frac{\alpha_s(Q^2)}{2\pi}\int_x^1 \frac{dy}{y}\left[q_i(y,Q^2)P_{qq}\left(\frac{x}{y}\right) + g(y,Q^2)P_{qg}\left(\frac{x}{y}\right)\right] \quad (1.11)$$

$$\frac{dg(x,Q^2)}{d\ln Q^2} = \frac{\alpha_s(Q^2)}{2\pi}\int_x^1 \frac{dy}{y}\left[\sum_i q_i(y,Q^2)P_{gq}\left(\frac{x}{y}\right) + g(y,Q^2)P_{gg}\left(\frac{x}{y}\right)\right] \quad (1.12)$$

where $q_i(x,Q^2) = \sum_i [q_i(x,Q^2) + \overline{q}_i(x,Q^2)]$ is the singlet quark and anti–quark density function summed over all quark flavours i, and $g(x,Q^2)$ is the gluon density function. The splitting function P_{jk} represents the probability of finding parton j splitting to the parton k with momentum fraction z of the parent parton.

1.4 Hard Photoproduction

The e^+p collisions provided by the HERA offer an excellent testing ground for QCD. In particular, the large flux of quasi–real photons at the virtuality scale $Q^2 \sim 0$ GeV^2, *i.e.* almost on–shell state, emitted from the positron beam have made HERA an outstanding laboratory in which to study photon physics via the photon–proton γp interaction.

As we can now think of electron–proton scattering at low Q^2 as photon–proton scattering due to the exchange of the quasi–real photon between the electron and proton, the total cross section of ep scattering, $\sigma^{ep\to eX}$, can be factorized into contributions from the total γp cross section, $\sigma_{\rm tot}^{\gamma p}$, and photon flux $f_{\gamma/e}(y)$. For

$Q^2 > 0$, photons may have both transverse and longitudinal polarisation so that $\sigma_{\rm tot}^{\gamma p} = \sigma_{\rm T} + \sigma_{\rm L}$ and

$$d\sigma^{ep\to eX} = \int dy \left[f_{\gamma_{\rm L}/e}(y) d\sigma_{\rm L}^{\gamma_{\rm L}p} + f_{\gamma_{\rm T}/e}(y) d\sigma_{\rm T}^{\gamma_{\rm T}p} \right]$$

In the limit of low $Q^2 \sim 0$, i.e. photoproduction region, the photons can only be transversely polarised so $\sigma_{\rm L}$ can be ignored. The ep cross section of photoproduction processes of interest can then be written as;

$$\frac{d^2\sigma^{ep}}{dydQ^2} = f_{\gamma/e}(y, Q^2)\sigma_{\rm tot}^{\gamma p}(y, Q^2) \tag{1.13}$$

where $\sigma_{\rm tot}^{\gamma p}$ is the total cross section of the process at a given centre of mass energy of the γp system and the photon flux, $f_{\gamma/e}(y, Q^2)$, is given by;

$$f_{\gamma/e}(y, Q^2) = \frac{\alpha}{2\pi}\frac{1}{Q^2}\left[\frac{1 + (1-y)^2}{y} - 2\frac{(1-y)}{y}\frac{Q^2_{\rm min}}{Q^2}\right] \tag{1.14}$$

where $Q^2_{\rm min} = m_e^2 y^2/(1-y)$ is the kinematic lower bound. This is known as the "equivalent photon approximation" (EPA). Neglecting the Q^2 dependence of the γp cross section, $f_{\gamma/e}(y)$ can be calculated by the Weizsäcker-Williams approximation (WWA) [10].

$$f_{\gamma/e}^{\rm WWA}(y) = \frac{\alpha}{2\pi}\left[\frac{1 + (1-y)^2}{y}\ln\frac{Q^2_{\rm max}}{Q^2_{\rm min}} - 2\frac{(1-y)}{y}\left(1 - \frac{Q^2_{\rm min}}{Q^2_{\rm max}}\right)\right] \tag{1.15}$$

where $Q^2_{\rm max}$ corresponds to the maximum scattering angle of the electron considered.

One of the primary tasks of photoproduction measurements at HERA is the investigation of the hadronic behaviour of photon. In describing the hard interaction of photons of low virtuality with protons, two major classes of diagram are important. In one of these the photon couples in a pointlike way to a $q\bar{q}$ pair, while in the other the photon interacts via an intermediate hadronic state, which provides quarks and gluons which then take part in the hard QCD subprocesses.

1.4.1 Direct Photoproduction

An example of the first class, direct photoproduction, is shown in figure 1.2. Here the whole photon participates directly in the interaction, acting as a point–like particle. As all the photon's energy couples to the parton, the final state

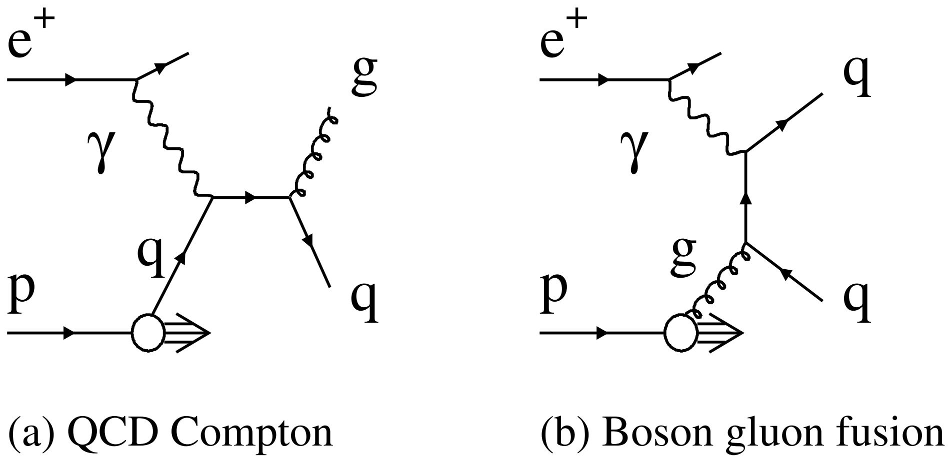

Figure 1.2: Leading order direct processes; (a) QCD Compton and (b) Boson gluon fusion.

of the process can be of higher transverse momentum than for hadronic type interactions in which only part of the photon's energy participates. At these low photon virtualities, the hard scatter may also be sensitive to the structure of photon.

The two leading–order (LO) direct photoproduction diagrams can be seen in figure 1.2. The QCD Compton process (a) shows the photon coupling to a quark within the proton which then radiates a gluon before hadronisation. In figure (b), the photon couples to a quark coming from a "split" gluon in the proton which produced a quark–antiquark pair. This is termed boson–gluon fusion. Both have final states consisting of two high transverse energy jets where in the case of the QCD Compton process one is a quark and the other a gluon jet and in boson–gluon fusion both are quark jets.

1.4.2 Resolved Photoproduction

Instead of interacting directly with a parton from the proton the photon may be first fluctuate into a hadronic state. One of the hadronic constituents, carrying a fraction of the momentum of the photon, takes part in the hard scatter. This is known as resolved photoproduction and two example diagrams at LO can be seen in figure 1.3.

In figure (a), a gluon from the photon interacts with a gluon from the proton in what is termed gluon–gluon fusion. However, in figure (b) it is a quark from the photon which interacts with the gluon from the proton. Again these two

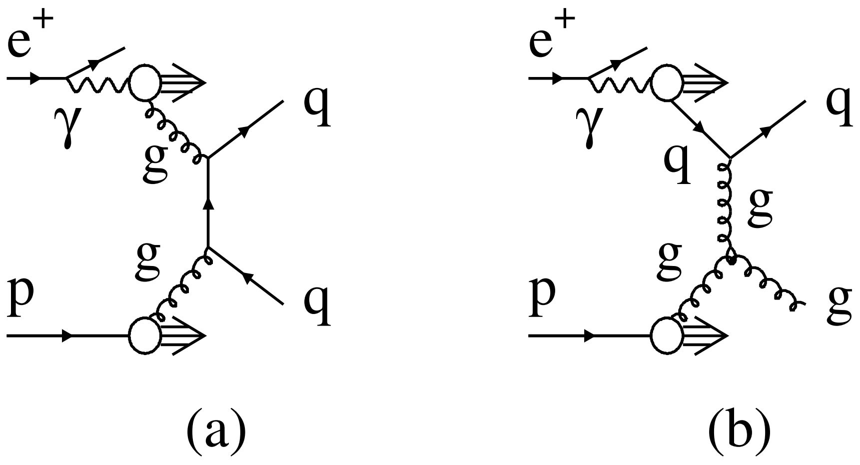

Figure 1.3: Examples of leading order resolved processes.

processes differ in that the final state consists of two quark jets in the case of figure (a) and one quark and one gluon jet in the case of figure (b).

The final state in both direct and resolved processes contains the positron, only very slightly scattered and not detected in the detector, two high transverse energy jets from the hard scatter and proton remnant. In addition, a photon remnant, analogous to the proton remnant, is present in resolved photoproduction. At higher–orders the distinction between these classes of events is no longer uniquely defined due to radiative processes. Inclusive jet (one or more jets), dijet (two or more jets) and prompt photons (we will discuss it in detail in chapter.2) studied in hard photoproduction at HERA have been used to investigate various aspects of QCD and the structure of the photon. Studies of events with three or more jets provide a means to test QCD at higher–orders.

1.5 The Structure of Photon

The first experimental data on photon structure function, F_2^γ, came from the electron–positron colliders [11]. A photon from each lepton interacts, producing photon–photon collisions. One photon is quasi–real, and the other is virtual, and probes the quark content of the real photon. By detecting one of the scattered leptons, these measurements ensure that a highly virtual photon probes an almost real target photon. The F_2^γ data from PETRA and PEP as well as from TRISTAN and LEP experiments have been used to parametrise photon parton densities in the resolved photon process.

Analogous to the ep scattering, a cross section for the process $e\gamma \to eX$ can be defined in terms of F_2^γ, and is given by

$$\frac{d^2\sigma_{e\gamma\to eX}}{dxdy} = \frac{2\pi\alpha}{xQ^4}\left\{\left[1+(1-y)^2\right]F_2^\gamma(x,Q^2) - y^2F_L^\gamma(x,Q^2)\right\} \tag{1.16}$$

where $x \equiv Q^2/(2\gamma\cdot q)$, $y \equiv Q^2/(sx)$ with $\sqrt{s}$ being the total centre of mass energy and γ is the 4–momentum of the incoming photon. The F_2^γ and F_L^γ are the photon structure functions which describe the internal structure of the photon.

In a similar way to proton structure function F_2, the structure function of the photon, F_2^γ can also be written in terms of the quark densities in the photon, $q_i^\gamma(x,Q^2)$, in LO diagram.

$$F_2^\gamma(x,Q^2) = 2x\sum_i e_{q_i}^2 q_i^\gamma(x,Q^2) \tag{1.17}$$

where the sum runs over all quark flavours, i, of quark charge e_{q_i} and the factor of two accounts for quarks and antiquarks. Therefore the deep inelastic $e\gamma$ scattering cross section at electron–positron collision is sensitive to the quark distribution in a photon.

The x and Q^2 dependence of the photon parton density is expressed by the modified DGLAP evolution equations similar to that for the proton, as described in section 1.3.2, and the DGLAP equations then has the following form;

$$\frac{dq_i(x,Q^2)}{d\log Q^2} = a(x) + \frac{\alpha_s(Q^2)}{2\pi}\int_x^1\frac{dy}{y}\left[P_{qq}\left(\frac{x}{y}\right)q_i(y,Q^2) + P_{qg}\left(\frac{x}{y}\right)g(y,Q^2)\right] \tag{1.18}$$

$$\frac{dg(x,Q^2)}{d\log Q^2} = \frac{\alpha_s(Q^2)}{2\pi}\int_x^1\frac{dy}{y}\left[P_{gq}\left(\frac{x}{y}\right)2\sum_i^f q_i(y,Q^2) + P_{gg}\left(\frac{x}{y}\right)g(y,Q^2)\right] \tag{1.19}$$

where,

$$a(x) = 3e_i^2\frac{\alpha}{2\pi}\left[x^2+(1-x)^2\right]$$

and it represents the initial $\gamma \to q\overline{q}$ splitting. The P_{jk} are the splitting functions as mentioned in section 1.3.2. In particular, the photon has an additional term due to the possibility of a photon splitting into a quark–antiquark pair. This so–called box term introduces an inhomogeneity into the photon parton density functions which is not present in the case of proton. The solution of the inhomogeneous equation is identified with the so–called "anomalous" photon component while the homogeneous equations are related to the hadron–like or Vector Meson Dominance (VDM) model [12] component which originates in the vacuum polarization of the photon to quark–antiquark pair.

At large values of x, the production of quarks comes predominantly via the $\gamma \to q\overline{q}$ splitting. As this coupling is electromagnetic, the number of u quarks produced is four times that of the d quarks due to their relative electronic charge. At low values of x however, the quarks are produced from the gluon splitting process and here there are an equal number of u and d quarks as the strong force does not differentiate between charge.

1.5.1 Model of the photon structure

Many parton parametrizations for the real photon have been proposed so far and were grouped into two classes; one is given for fixed number of massless flavours and the other is for the number of flavours dependent on the scale Q^2. Here two photon parton density functions, GS and GRV, are briefly reviewed.

- Gordon and Storrow (GS)

Gordon and Storrow, were the first to produce NLO parameterisations for the photon parton densities [13], producing fits including both the available F_2^γ data and jet data from TRISTAN [14, 15]. The input structure function at the scale $Q_0^2 = 5.3$ GeV^2 and $Q_0^2 = 3.0$ GeV^2 is chosen in the LO analysis as a sum of a hadronic part from the VMD model and of a pointlike part based on the Parton Model;

$$q^{\gamma}_{q,g}(x, Q_0^2) = \kappa \frac{4\pi\alpha}{f_\rho^2} q^{\pi}_{q,g}(x, Q_0^2) + q^{PL}_{q,g}(x, Q_0^2). \tag{1.20}$$

Free parameters (e.g. k) and light quark masses are fitted to the data with $Q^2 \geq Q_0^2$. The input gluon distribution in LO is assumed in two different forms (set GS1 and GS2). The NLO distribution in the $\overline{\mathrm{MS}}$ scheme is obtained by matching the F_2^γ in the LO and the NLO approaches at the Q_0^2 scale. $N_f = 3$, 4 and 5 are used and the number of flavours equal to $N_f = 3$ for $Q_0^2 \leq Q^2 \leq 50$ GeV^2 and $N_f = 4$ for 50 GeV$^2 \leq Q^2$ was used.

- Glück, Reya and Vogt (GRV) [16]

The LO and NLO parametrizations of the parton distributions generated dynamically with the boundary conditions at Q_0^2 given by a VMD input. The physical photon is then assumed to be a coherent superposition of vector mesons, whose parton distributions are further assumed to be similar to those of a pion. Non–perturbative input is used at the starting scale taken to be of the form

$$q^{\gamma}_{q,g}(x, Q_0^2) = \kappa \frac{4\pi\alpha}{f_\rho^2} q^{\pi}_{q,g}(x, Q_0^2)$$

where $q^i_{q,g}$ are the quark and gluon densities within particle i respectively. The low initial scale $Q_0^2(\mathrm{LO}) = 0.25$, $Q_0^2(\mathrm{NLO}) = 0.3$ GeV^2 is universal for structure functions of p, π, γ etc. The one free parameter, k, which is the VMD input normalization constant relative to π, is fixed by the data.

Chapter 2

Prompt Photon Production

2.1 Introduction

One of the primary tasks of photoproduction measurements at high energy is the investigation of the hadronic behaviour of photon. Here we are concerned with interactions that involve a hard transverse energy E_T. In describing the hard interaction of photons of low virtuality with protons, two major classes of process can be defined in lowest–order QCD, depending on how the photon interacts with a parton in the proton: (1) those in which the photon couples in a pointlike way to a high–E_T $q\bar{q}$ pair, and (2) those in which the photon provides quarks and gluons which then take part in the hard QCD subprocesses. At leading–order (LO) in QCD, these two types of diagram are distinct and are commonly referred to as direct and resolved processes, respectively.

These subprocesses most commonly give two outgoing quarks or gluons, which at high E_T can give rise to two observed jets. However final states containing a high E_T jet together with a high E_T photon are also possible, as seen in figure 2.1. Such photons are known as "prompt photons" to distinguish them from those produced via particle decays [18]. In the kinematic region accessible with ZEUS, the direct channel in prompt photon processes is expected to be dominated by the so–called "direct Compton" process $\gamma q \to \gamma q$, i.e. by the elastic scattering of a photon by a quark in the proton, while the main contribution to the resolved channel are the processes $qg \to q\gamma$ and $q\bar{q} \to g\gamma$ [17].

A further source of prompt photons is dijet events in which an outgoing quark radiates a high-E_T photon. In measuring prompt photon processes, these radiative contributions are largely suppressed by restricting the measurement to prompt photons that are isolated from other particles in the event. Such a condition is also needed in order to reduce experimental backgrounds from neutral mesons in jets.

More recently, photoproduced final states containing an isolated high transverse energy photon have been measured by ZEUS at HERA [18], providing a further means to study the photoproduction mechanism. This could be hoped to yield information about the quark and gluon content of the photon, together with the gluon structure of the proton [19]. The particular virtue of prompt photon processes is that the observed final–state photon emerges directly from a QCD diagram without the subsequent hadronisation which complicates the study of high E_T quarks and gluons. The cross section of the direct Compton process depends only on the quark charge, together with the quark density in the proton. The above considerations, together with the availability of next-to-leading order (NLO) calculations [19, 20, 21], make prompt photon processes an attractive and relatively clean means for studying QCD, despite the low cross sections.

In this chapter the theoretical aspect of prompt photon production at HERA will be briefly discussed. The previous experimental results and the current issues in prompt photon production will then be reviewed.

2.2 Prompt Photon Production at HERA

As with all photoproduction processes at HERA, two major classes of process can be defined in lowest order QCD, direct and resolved processes. In the case of prompt photon production there are two further subclasses in each process; the non–fragmentation and the fragmentation processes. In the non–fragmentation process a prompt photon is produced directly in the hard scattering, while in the fragmentation process it is produced via fragmentation of the final state parton.

2.2.1 Prompt photon processes

- Direct/Resolved non–fragmentation processes

  In the kinematic region available at HERA, the direct non–fragmentation process in prompt photon production is dominated by the LO "QCD Compton" process (Figure 2.1 (a)) ;

$$\gamma q^p \to \gamma q$$

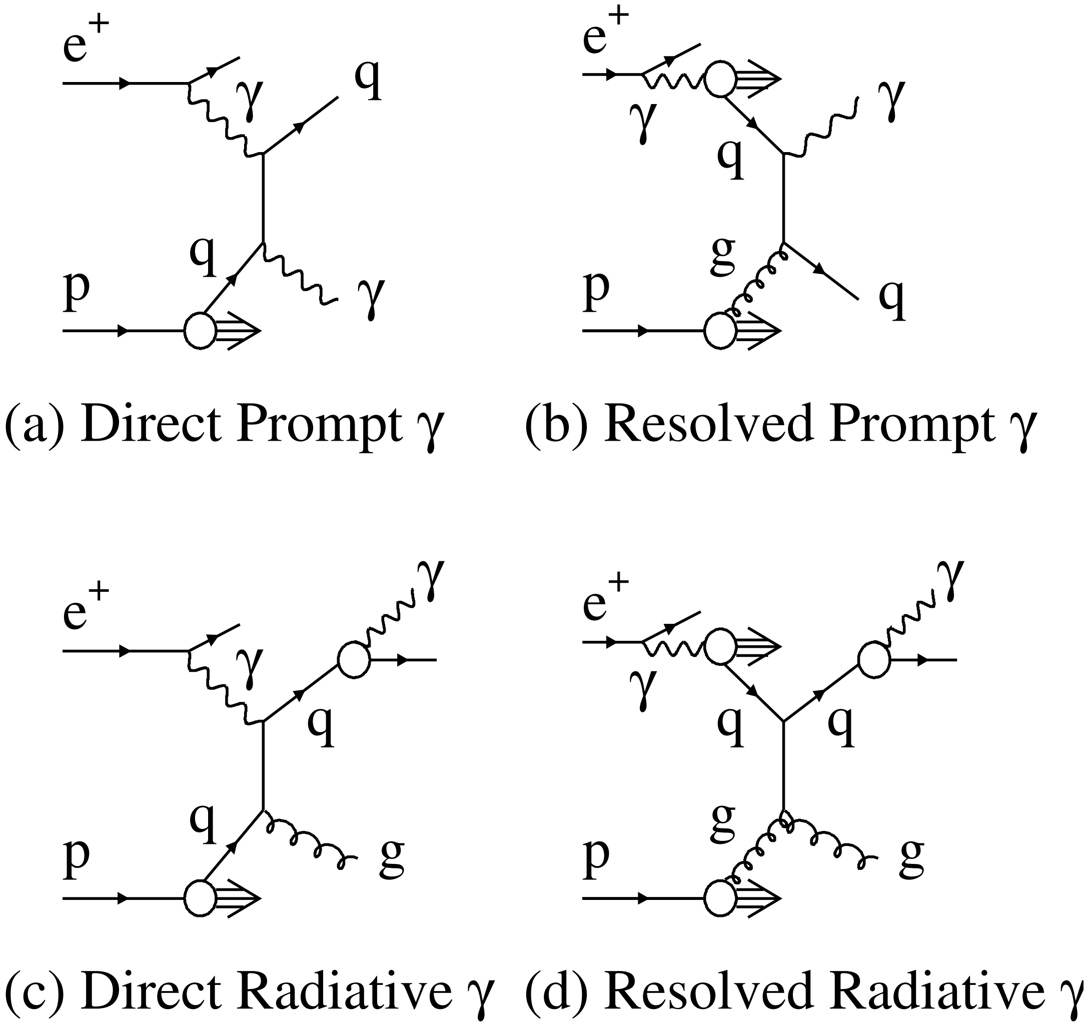

Figure 2.1: Main LO diagrams for (a) direct non–fragmentation, (b) resolved non–fragmentation, (c) direct fragmentation (radiative) and (d) resolved fragmentation (radiative) processes in hard photoproduction producing an outgoing prompt photon. Two of the corresponding dijet diagrams may be obtained by replacing the final–state photon here by a gluon in (a) and (b). Broad arrows represent photon or proton remnants.

where q^p denotes the quark contents of a proton. An incoming photon interacts with a quark in a proton. There are a high P_T photon and a high P_T jet in the observed final state. This process contributes to the cross section with the order of $O(\alpha_{em}^2)$, where α_{em} is an electromagnetic coupling constant.

In the resolved non–fragmentation process, there are three processes (Figure 2.1 (b)) ;

$$q^\gamma g^p \to \gamma q$$
$$q^\gamma q^p \to \gamma g$$
$$g^\gamma q^p \to \gamma q$$

In principle the resolved prompt photon processes have an ability to extract not only quark but also gluon distributions in a photon. However the kinematic coverage available in this analysis has less sensitivity to the gluon distributions from the photon. The magnitude of the hard scattering is the order of $O(\alpha_{em}\alpha_s)$, where α_s is a strong coupling constant. However, after taking into account a factor of $O(\alpha_{em}/\alpha_s)$ for the photon structure, the cross section is the order of $O(\alpha_{em}^2)$, the same as that of the direct.

- Direct/Resolved fragmentation processes

A prompt photon can also come from the fragmentation of a jet. Thus the diagrams that contribute to the cross section are the same as with the dijet process. The direct and resolved fragmentation processes;

$$\gamma q^p \to qg$$
$$q^\gamma g^p \to qg$$

are shown in figure 2.1 (c) and (d) respectively. A further factor for the fragmentation into a photon is given as $O(\alpha_{em}/\alpha_s)$. After taking into account the factor for the fragmentation and photon structure, the cross section is $O(\alpha_{em}^2)$ for both direct and resolved fragmentation processes. Since the cross section from the fragmentation processes depends on the fragmentation functions, its contribution reduces the measured sensitivity to the photon parton density. If such a photon takes nearly all the energy of the initial quark, the event may experimentally resemble one coming from the non–fragmentation processes. Events of this kind will be referred to as radiative prompt photon events in the thesis. An isolation requirement reduces their contribution to the measured cross section. (See figure 2.2 (a))

2.2.2 Prompt photon cross section

The inclusive prompt photon cross section for $\gamma p \to \gamma X$ can be schematically written with a convolution of the parton distributions in the incoming particles and the cross section of the hard scattering between the partons. Assuming a and b as a parton in a photon and proton and c and d as outgoing partons, the LO cross section is written by the following general formula ;

$$\begin{aligned} E_\gamma \frac{d^3\sigma^{\gamma p\to\gamma X}}{d^3P_\gamma} &= \sum \int \frac{dz}{z^2} \int dx_\gamma \int dx_p f_a^\gamma(x_\gamma, M^2) f_b^p(x_p, M^2) \\ &\quad \cdot D_\gamma^c(z, M_F^2) E_\gamma \frac{d^3\sigma^{ab\to cd}}{d^3P_\gamma} \end{aligned} \quad (2.1)$$

where the f_a^γ and f_b^p denote the parton distributions of a photon and that of a proton, respectively. The quantity D_γ^c is the fragmentation function at scale M_F^2 for the fragmentation of parton c into a photon. The parameters x_γ and x_p respectively denote the fraction of a photon and proton momentum carried by the interacting parton. The parameter z denotes a fraction of parton momentum carried by the final photon. For the direct process f_a^γ is replaced by $\delta(x_\gamma - 1)$ and for the non-fragmentation process D_γ^c is replaced by $\delta(z-1)$. The M^2 and M_F^2 are scales for the factorisation and fragmentation, respectively.

The γp cross section can be related to the ep cross section by the equivalent photon approximation (EPA) ;

$$\sigma^{ep\to\gamma X} = \int f_{\gamma/e}(y)\sigma^{\gamma p\to\gamma X} dy \quad (2.2)$$

The Weizsäcker–Williams (WW) approximation is used to estimate the flux, $f_{\gamma/e}(y)$, of quasi–real photons radiated from the positron beam. Thus the electron structure function, $f_e(x_e, Q^2)$, is given by a convolution of the photon structure function, $f^\gamma(x^\gamma, Q^2)$, and the WW function;

$$\begin{aligned} f_{\gamma/e}(y) &= \frac{\alpha_{em}}{2\pi}\left[\left\{\frac{1+(1-y)^2}{y}\right\} \ln \frac{Q^2_{max}(1-y)}{m_e^2 y^2}\right. \\ &\quad - \left. 2m_e^2 y^2 \left\{\frac{(1-y)}{m_e^2 y^2} - \frac{1}{Q^2_{max}}\right\}\right] \end{aligned} \quad (2.3)$$

where m_e is the electron mass, and

$$f_e(x_e, Q^2) = \int_{x_e}^1 \frac{dy}{y} f_{\gamma/e}(y) f^\gamma\left(\frac{x_e}{y}, Q^2\right) \quad (2.4)$$

2.2.3 Theoretical prediction

Over the past few years many theoretical studies of prompt photon production at HERA have been performed with continuous improvements in the theoretical precision [19, 22]. More recently L. Gordon and W. Vogelsang have studied the expectations for prompt photon production rates at HERA in a fully consistent NLO QCD analysis, taking into account the effects of experimental isolation requirements [19]. In particular they examined the sensitivity of the isolated cross section to the photon's gluon content using both GS and GRV photon parton density functions.

Figure 2.2 shows the theoretical predictions from L. Gordon and W. Vogelsang's NLO QCD calculation. Figure (a) represents the full inclusive prompt photon cross section (solid line) containing both direct and resolved, fragmentation and non–fragmentation contributions as a function of photon pseudorapidity in the lab frame at $p_T^\gamma = 5$ GeV. After an isolation cut in the NLO calculation, there is approximately a 15 % reduction in the full cross section (dashed curve). This also shows the strong effects of isolation on the fragmentation processes. The dash–dotted and dotted lines show the result after and before the isolation cut respectively.

Figure (c) shows the sensitivity of the cross section to the proton and photon parton densities. There is a significant difference between the predictions given by the GRV and GS photon parton densities at negative photon pseudorapidity. This is understood as a result of the different modelling of the quark contents in a photon. Simultaneously the sensitivity to the proton parton density is also tested, in which GRV, MRS(A') and CTEQ3M were used. It becomes clear that the prompt photon cross section at HERA does not depend significantly on the proton parton density. Figure (d) shows the decomposition into the contributions of the subprocesses ;

$$p\gamma^{dir} \to \gamma X$$

$$pq^\gamma \to \gamma X, \quad pg^\gamma \to \gamma X$$

where γ^{dir} stands for the direct photon process. The prompt photon cross section at $|\eta| < 1$ is dominated by $p\gamma^{dir} \to \gamma X$ and $pq^\gamma \to \gamma X$ processes. On the other hand, the processes involving g^γ dominate the cross section at large positive photon pseudorapidity, which seems to give no chance of measuring the gluon content of the photon at HERA via prompt photon production.

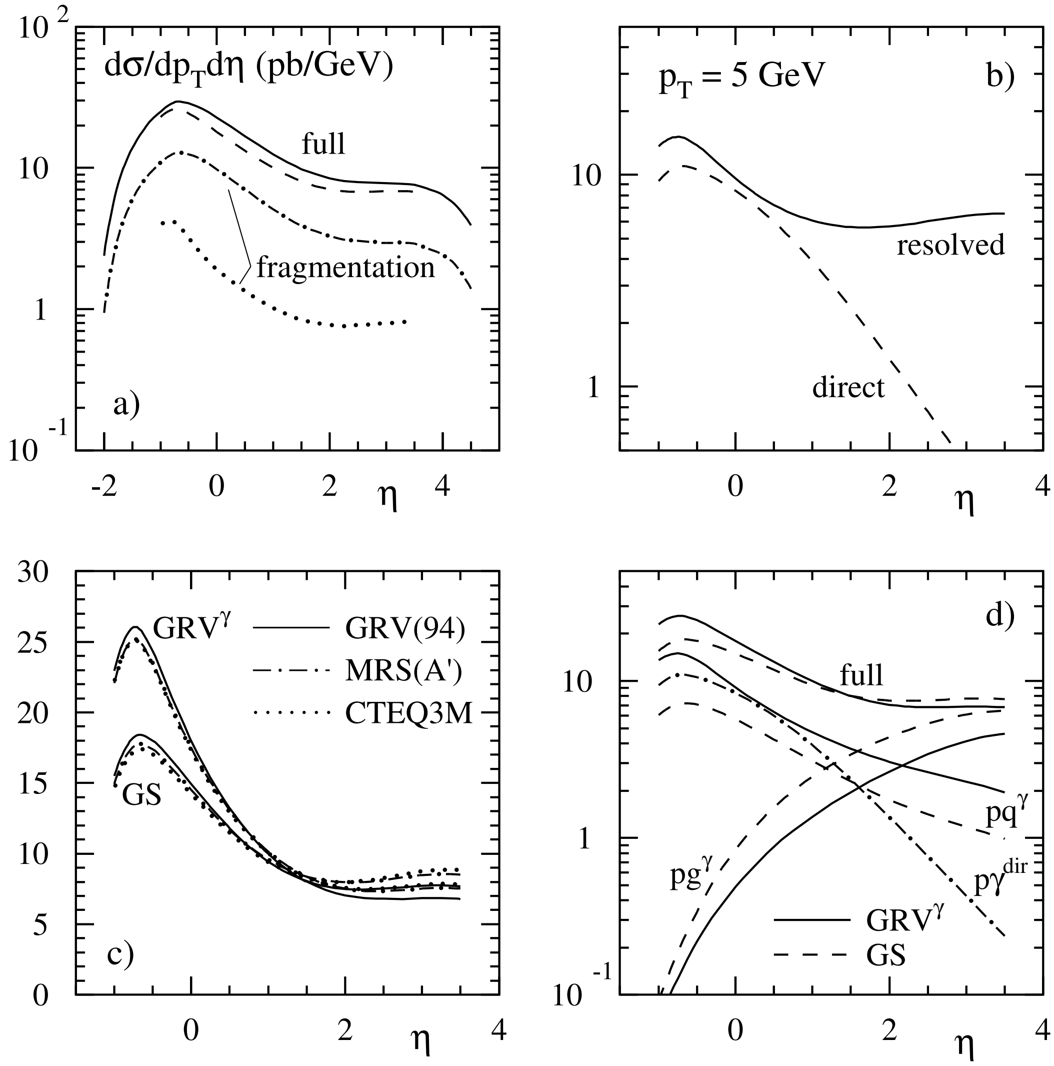

Figure 2.2: The prompt photon cross section, $d\sigma/dP_T d\eta$, calculated by L. Gordon and W. Vogelsang [19]. (a) Comparison of fully inclusive and isolated results for the full cross section and its fragmentation part. (b) Resolved and direct contributions to the isolated cross section. The direct contribution is strongly peaked at negative rapidities, corresponding to the probing of the proton at small x_p by an energetic photon. The resolved contribution remains sizeable and dominant also at positive η. (c) Full isolated cross section for various sets of parton distributions of the proton and the photon. There is a significant difference between the predictions given by the GRV and GS photon parton distributions at negative η, where the uncertainties coming from the proton structure functions are rather small. (d) Full isolated cross section and its decomposition into the contributions of subprocesses; direct and resolved processes, for GRV and GS photon parton distributions.

2.2.4 Background processes

The main backgrounds that resemble the prompt photon events come from high p_T–neutral mesons, such as π^0 and η mesons which decay into two photons, produced through the fragmentation of a jet.

In order to suppress the fraction of such backgrounds in the data sample an isolation cone was imposed around photon candidates within a cone of unit radius in (η, ϕ). Details of the energy isolation requirement is described in section 6. Even after the isolation requirement, some fraction of the backgrounds still remain as prompt photon candidates in the prompt photon candidate sample. Due to the large cross section for jet production, the size of neutral meson background is roughly the same as the prompt photon signal. These events are statistically subtracted as described in section 7.

2.3 Previous Experimental Results

A strong motivation for the early prompt photon measurements was the extraction of the gluon density in nucleons. Due to large statistical and systematic uncertainties in the experiments and large uncertainties in the theoretical predictions, the first generation of prompt photon experiments failed to distinguish between hard gluon and soft gluon distributions, because changing an input gluon structure function could be compensated for by a change in the Λ_{QCD} parameter. Later, new phenomenological modelling was introduced to interpret the experimental results in this era. It included the definition of the scale of the interaction, and unknown amounts of intrinsic transverse momentum of the initial state partons, called the intrinsic k_T effect, and a lack of a complete calculation of higher–order contributions for prompt photon production. The new phenomenology will be discussed in section 2.4.

In this section the previous prompt photon experiments are reviewed, along with relevant parameters for the experiments and the results.

2.3.1 Prompt photons at HERA

The ZEUS experiment published the first observation at HERA of prompt photons, accompanied by balancing jets, at high transverse momentum in photoproduction reactions [18], based on an integrated luminosity of 6.4 pb^{-1}.

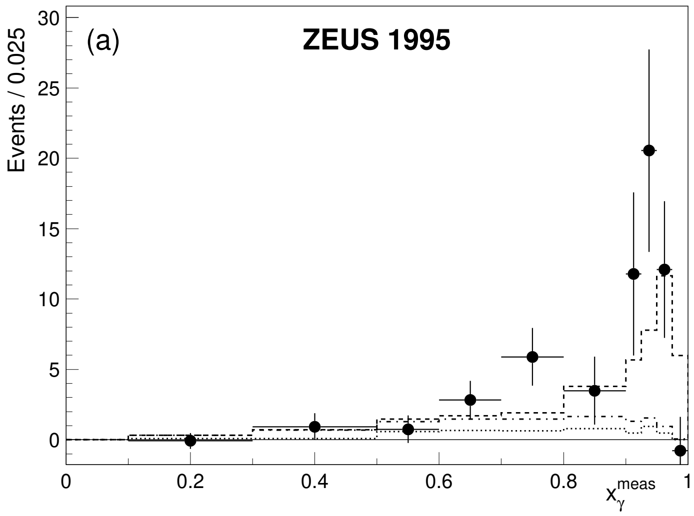

Figure 2.3: Distribution in x_γ of prompt photon events after background subtraction. Points = data; dotted histogram = MC radiative contribution; dash–dotted = radiative + resolved; dashed = radiative + resolved + direct. Plotted values represent numbers of events per 0.025 interval of x_γ. Errors are statistical only and no corrections have been applied to the data.

The fraction of the incoming photon energy participating in the production of the prompt photon and the jet, x_γ, is in good agreement with LO QCD Monte Carlo predictions as calculated using PYTHIA. In particular, a pronounced peak at high x_γ is observed (See figure 2.3), indicating the presence of a direct process.

The ZEUS experiment has also measured the cross section for prompt photon production in ep collisions satisfying the conditions of having (i) an isolated final–state photon with $5 \leq E_T^\gamma < 10$ GeV, accompanied by a jet with $E_T^{jet} \geq 5$ GeV, (ii) the photon and jet lying within the respective laboratory pseudorapidity ranges $-0.7 < \eta^\gamma < 0.8$ and $-1.5 < \eta^{jet} < 1.8$, (iii) $x_\gamma^{\text{OBS}} \geq 0.8$, (iv) $0.16 < y^{true} < 0.8$, (v) $Q^2 < 1$ GeV^2. The value obtained was 15.3±3.8±1.8 pb, in good agreement with a NLO calculation by Gordon [22] at the parton level; 14.05 pb using the GS photon parton density and 17.93 pb using that of GRV at a QCD scale $\mu = 0.25(E_T^\gamma)^2$. It indicates the feasibility of distinguishing between different models of the photon structure.

The H1 experiment has also observed a signal of prompt photons with high transverse energy in photoproduction. The cross section for the prompt photon photoproduction with $E_T^\gamma > 5$ GeV and $-1.2 < \eta^\gamma < 1.6$ was measured to be 104.8±5.9±15.7 pb, in agreement with QCD prediction; 84 pb [23].

2.3.2 Prompt photons at fixed target experiments

Prompt photon production has been extensively studied in a number of fixed target experiments at centre–of–mass energies of 20–40 GeV. Initially the E629 experiment at FNAL observed a clean signal for the inclusive prompt photon production in the 200 GeV collisions of proton and π^+ mesons on a carbon target for $p_T > 2.5$ GeV [24].

The NA14 experiment then showed the first measurement of inclusive prompt photon in photoproduction at transverse momenta above 2.5 GeV [25]. The experiment was performed in a high intensity photon beam with energy between 50 and 150 GeV at the CERN SPS using an open spectrometer. The cross section as a function of p_T^γ agreed with a theoretical calculation (QEDC Born term + additional contributions from pQCD) within the statistical uncertainties. The data disfavoured the gauge–integer–charge–quark models proposed at that time.

The NA3 experiment at CERN measured the cross sections for prompt photon production from incoming π^-, π^+ and proton beams on an isoscalar carbon target at $\sqrt{s} = 19.4$ GeV [26]. The cross section was consistent with an available NLO QCD calculation, within the experimental uncertainties.

The WA70 experiment at the CERN SPS also measured the prompt photon production cross sections in $\pi^- p$ and $\pi^+ p$ collisions at 280 GeV [27]. The transverse momentum and Feynman X_T ranges were $4 < p_T < 7$ GeV and -0.45 $< X_T$ $(= 2p_T/\sqrt{s}\ ) < 0.55$ respectively. In addition, similar experimental results on inclusive prompt photon were measured by the NA24 experiment with a beam momentum of 300 GeV [28]. They found that the increase of the cross section ratio $\sigma(\pi^- p \to \gamma + X)/\ \sigma(\pi^+ p \to \gamma + X)$ with p_T indicates the occurrence of valence–quark–antiquark annihilation. Both results were described by NLO QCD calculations.

The UA6 experiment measured prompt photon production in both $\bar{p}p$ and pp interactions at $\sqrt{s} = 24.3$ GeV [29]. The first measurement of the experiment was done in 1985/1986 for $\bar{p}p$, performed again in 1988 for pp and 1989/1990 for $\bar{p}p$ reactions. All data samples covered ranges in $0.1 < y < 0.9$ and in $4.1 < p_T <$ 7.7 GeV, which corresponds to $0.34 < X_T < 0.63$. They measured the inclusive prompt photon cross sections in both pp and $\bar{p}p$ interactions at the given centre–of–mass energy and the cross section difference $\sigma(\bar{p}p) - \sigma(pp)$ as a function of the p_T of photon, and compared the results with NLO QCD predictions.

The fixed target experiments for prompt photon production at CERN (*e.g.* NA24 and WA70) commonly used an invariant mass distribution method for π^0

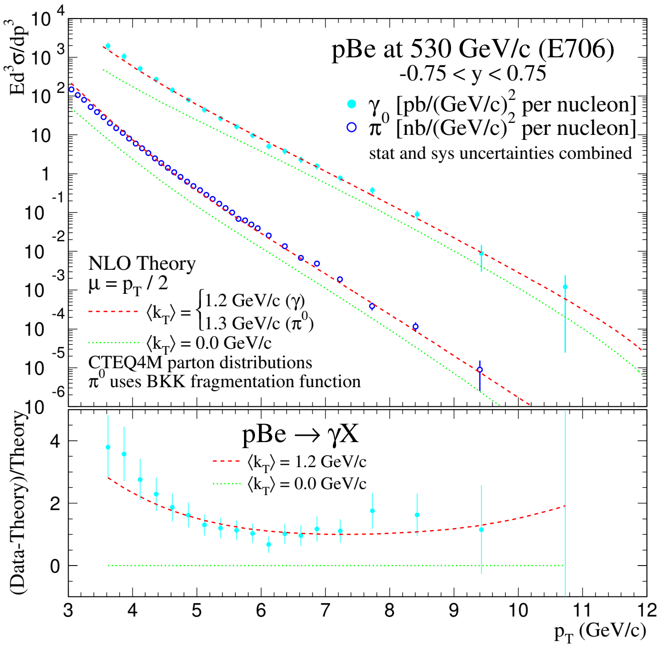

Figure 2.4: E706 prompt photon and π^0 inclusive cross sections as function of p_T for 530 GeV/c proton–nucleon interactions compared to NLO theory without $<k_T>$ (dashed) and with $<k_T>$ enhancement for $\langle k_T \rangle = 1.2$ GeV/c for the photon and $\langle k_T \rangle = 1.3$ GeV/c for the π^0 (dotted). Bottom: The quantity (Data–Theory)/Theory, overlaid with the expected effect from k_T enhancement for $\langle k_T \rangle = 1.2$ GeV/c.

and η–meson subtraction to select pure prompt photon signals from huge backgrounds. In addition, the UA6 experiment used an extra topological shower shape method in the longitudinal shower development to reject showers not consistent with a single photon event.

More recently the Fermilab E706 experiment [30], designed to measure large p_T production of high statistics prompt photons, neutral mesons and associated particles, has measured the inclusive π^0 and prompt photon cross sections in the kinematic range, $3.5 < p_T < 12$ GeV with central rapidities for 530 and 800 GeV proton beams and 515 GeV π^- beams incident on Be targets. They reported that current NLO pQCD calculations fail to account for the measured cross sections using conventional choices of scales. Significant parton $<k_T>$ effects (~ 1.2 GeV at $\sqrt{s}$ =31.6 GeV; and ~ 1.3 GeV at $\sqrt{s}$ =38.8 GeV; see figure 2.4) were observed in the kinematic distributions of high–mass π^0 pairs, as well as high–mass $\gamma\pi^0$ pairs. They found that a simple implementation of supplemental parton $<k_T>$ in pQCD calculations provides a reasonable description of the inclusive cross sections. More details of the parton $<k_T>$ issues in prompt photon production will be discussed in section 2.4 and chapter 9.

2.3.3 Prompt photons in hadron collider experiments

During the past 25 years, the physics of prompt photon production has undergone very successfully experimental developments. A number of precise data from hadron colliders have been published covering a large domain of centre of mass energy from 40 GeV to 1.8 TeV as well as a wide range of transverse momenta of the prompt photons.

The first published measurement of high p_T prompt photons at a hadron collider was made in 1976 by the R412 experiment in proton–proton collisions at $\sqrt{s} = 45$ GeV and 53 GeV at the CERN ISR (Intersecting Storage Rings) [31]. The large systematic uncertainties due mainly to the detector energy response and antineutron contamination were not understood well enough to make a strong claim of evidence for prompt photon production.

In 1978 the R107 experiment reported the results of a search for prompt photons produced at 90° in pp collisions at the ISR for $\sqrt{s} = 53.2$ GeV and $p_T > 2.3$ GeV [32]. They established an upper limit of 6% at 95% C.L. for the γ/π^0 ratio in the p_T region 2.3–3.7 GeV, but did not give any indication of prompt photon production due to large experimental uncertainties. This was true also of the R412 experiment.

The first convincing evidence for the existence of prompt photon events in pp collisions at ISR was demonstrated by the R806 experiment in 1982 at $\sqrt{s} =$ 31, 45, 53 and 63 GeV [33]. The transverse momentum range extended up to 12 GeV. The distinguishing feature of the experiment was the use of detectors with relatively high granularity and good energy resolution. Calculations based on the lowest–order QCD diagrams agreed qualitatively with the experimental results.

In the higher centre–of–mass energy regime, both the UA1 [34] and UA2 [35] experiments opened new windows for the measurement of prompt photon production with very high transverse momentum from $\bar{p}p$ collisions at the $Sp\bar{p}S$ collider at CERN. In particular the UA2 apparatus was equipped with preshower detector in front of the calorimeters. These detectors allowed a precise determination of the conversion point for photons that start showering in a converter.

The inclusive cross section was measured for production of high p_T prompt photons in $\bar{p}p$ collisions at $\sqrt{s} = 546$ GeV and $\sqrt{s} = 630$ GeV [34, 35]. The UA1 and UA2 results supported predictions from QCD calculations. Both experiments also studied the structure of events containing a high p_T photon, and they found that in most of the events the photon p_T is balanced by that of a single jet. In addition, they measured a differential cross section for double prompt photon

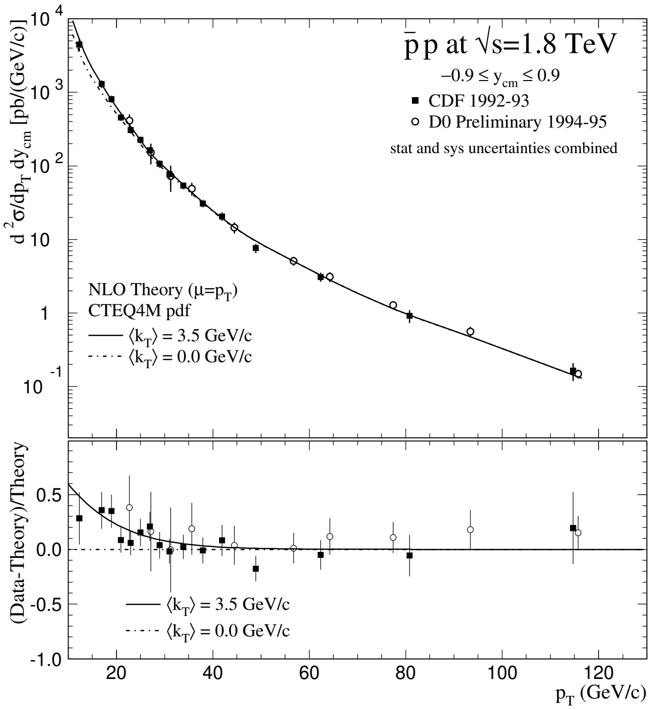

Figure 2.5: The CDF and DØ prompt photon cross sections, compared to NLO theory without $<k_T>$ (dashed) and with $<k_T>$ enhancement for $\langle k_T \rangle = 3.5$ GeV$/c$ (solid), as a function of p_T. Bottom: The quantity (Data–Theory)/Theory, overlaid with the expected effect from k_T enhancement for $\langle k_T \rangle = 3.5$ GeV$/c$. The error bars have experimental statistical and systematic uncertainties added in quadrature.

production as a function of the p_T of photon [34, 36]. Furthermore, from the study of prompt photon + jet production, the UA2 experiment measured the gluon structure function, $\mathrm{G}(x, Q^2)$, in a direct way in the range $0.049 < X_T < 0.207$ for Q^2 values between 280 GeV^2 and 3670 GeV^2 [37]. The result was found to be in good agreement with the parametrizations of the deep inelastic lepton–nucleon scattering data.

The CDF and DØ experiments at the TeVatron collider at Fermilab have performed pure QCD tests with photons in a number of different ways [38, 39, 40]: the cross section measurement of inclusive prompt photon production at $\sqrt{s} =$ 1.8 TeV and $\sqrt{s} = 630$ GeV; photon + one or two jet angular distributions; photon + charm production and diphoton production, in order to provide some constraint on the gluon distributions, $\mathrm{G}(x)$, through the LO Compton scattering process ($gq \rightarrow \gamma q$); and a direct measurement of the parton intrinsic transverse momentum, $<k_T>$, and to test the charm content of the proton. The kinematic range of previous prompt photon measurements at both fixed target and hadron collider experiments was greatly extended by the TeVatron's $\sqrt{s} = 1.8$ TeV and the measurement of photon transverse momentum of up to 120 GeV.

The CDF and DØ photon measurements are consistent and complementary. For the inclusive photon cross section measurements, both experiments agree with NLO QCD predictions for the high E_T^γ region (> 25 GeV), while both lie above theory at lower E_T^γ (see figure 2.5). This discrepancy may originate from additional soft gluon radiation beyond that included in the QCD calculation, or it may reflect inadequacies in the parton distribution and fragmentation contributions. Further details are given in section 2.4.

The CDF and DØ measurements of prompt photon production employ different analysis tools to sort out the background level. For the CDF measurement the fraction of photon candidate events that have an observed conversion in the material just in front of the calorimeter is used, along with the transverse shower shape measured in a proportional chamber at shower maximum in the calorimeter itself. In the end one of the two methods is used to evaluate point–by–point the fraction of photons in the data sample. For the DØ measurement the fraction of energy observed in the first two radiation lengths of the calorimeter is used. The fraction is then fitted to a smooth function as a function of transverse energy of the photon and this smooth curve is used to evaluate the purity.

2.3.4 Prompt photons at lepton collider experiments

The production of isolated prompt photons was studied in great detail by all four LEP experiments [41], ALEPH, DELPHI, L3 and OPAL. At LEP the first measurement of prompt photon production in hadronic Z^0 decays was made by the OPAL experiment for photons isolated from other particles in the event [42].

The physics motivation of prompt photon measurements at LEP differ considerably from that of the experiments discussed above. The main thrust of this work has been to compare the data with QCD calculations at the parton level and to test the detailed predictions of the parton shower models and thus gain some insight into the parton evolution mechanism. For example the ALEPH experiment extracted the quark–to–photon fragmentation function from the study of non–isolated photons in jets containing a photon carrying more than 70 % of the jet energy [43]. The OPAL experiment has also measured the inclusive production of prompt photons with energy above 10 GeV in hadronic Z^0 decays. Good agreements were found with current QCD predictions for the quark–to–photon fragmentation function [44].

The observation of prompt photon production in $\gamma\gamma$ collisions was also reported by the TOPAZ experiment at the e^+e^- centre–of–mass energy $\sqrt{s} = 58$

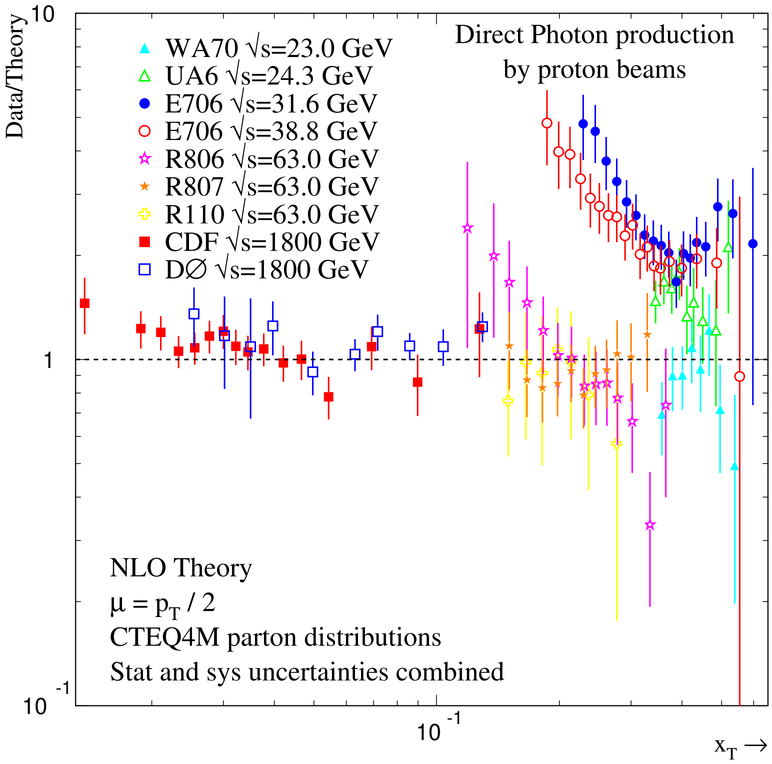

Figure 2.6: Comparison of photon $X_T(= 2E_T^{\gamma}/\sqrt{s})$ for different prompt photon experiments. Differing various experiments have reported excesses at lower values of x_T compared to NLO predictions.

GeV [45]. The prompt photon cross section for $E_T^{\gamma} > 2$ GeV and -1 $< \eta^{\gamma} <$ 1 was measured to be $\sigma(e^+e^- \rightarrow \gamma + X) = 1.72 \pm 0.67$ *pb*. The result was a little bit larger than LO parton–shower MC predictions, but agreed within 2 σ since the statistical uncertainty is large.

2.4 Current issues in photon production

As described in the previous section the prompt photon production in both hadronic and leptonic collisions in the high p_T regime has long been viewed as a clean test of pQCD, and large amounts of data exist now from fixed target, $\bar{p}p$ and γp interactions, as well as from LEP. However there are several problems associated with the interpretation of these data. In particular, it is difficult to fit all the data to NLO QCD calculations.

As seen in figure 2.6, a pattern of deviations has been observed between measured prompt photon cross sections and QCD calculations [21]. Much larger

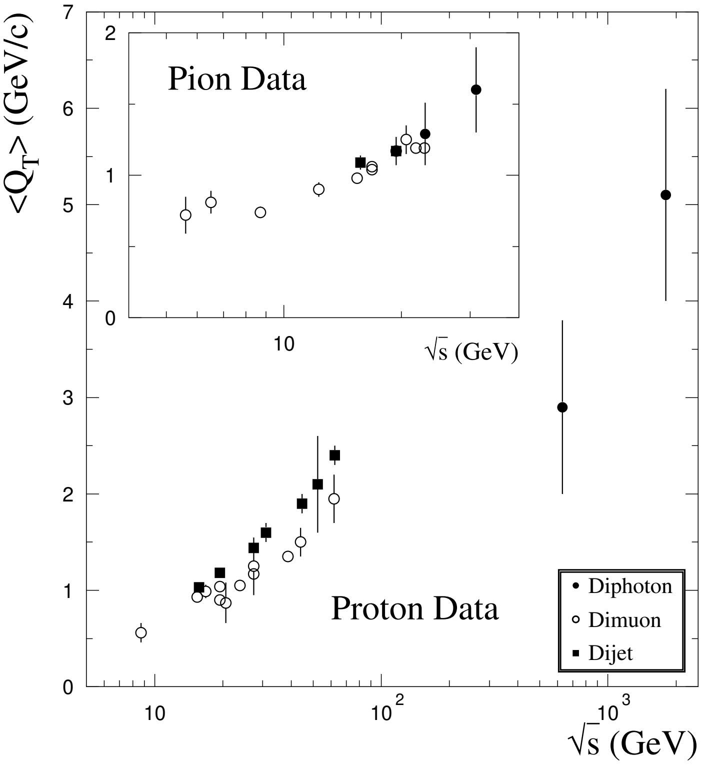

Figure 2.7: $< Q_T >$ of pairs of muons, photons, and jets produced in hadronic collisions versus $\sqrt{s}$. The ZEUS data point will be included on this kind of plot in chapter 9.

deviations from QCD are observed in the higher–statistics photon data from the E706 experiment [30] (see figure 2.4). The final prompt photon results from UA6 also exhibit evidence for similar discrepancies. Recent results from CDF and DØ also have a steeper slope above theory at low E_T region [46].

One offered explanation is that the partons in the proton may effectively have a considerably higher mean intrinsic transverse momentum, $<k_T>$, than expected from non–perturbative proton size effects, traditionally of the order of 0.3–0.5 GeV. The CTEQ collaboration also reported that one way to understand the discrepancy between data and theory models is the introduction of two phenomenological quantities into theory models for both LO MC and NLO pQCD calculations. A discrepancy of this kind could arise from the transverse momentum of the initial–state partons, which is affected by the multiple initial soft gluon radiation and the intrinsic transverse momentum k_T, of the partons in the incoming hadrons, or from multiple initial–state soft gluon radiation as the parton interacts.

Evidence for significant $<k_T>$ effects has been found in several measurements of dimuon, diphoton, and dijet pairs. Figure 2.7 shows the summary of $< Q_T >$,

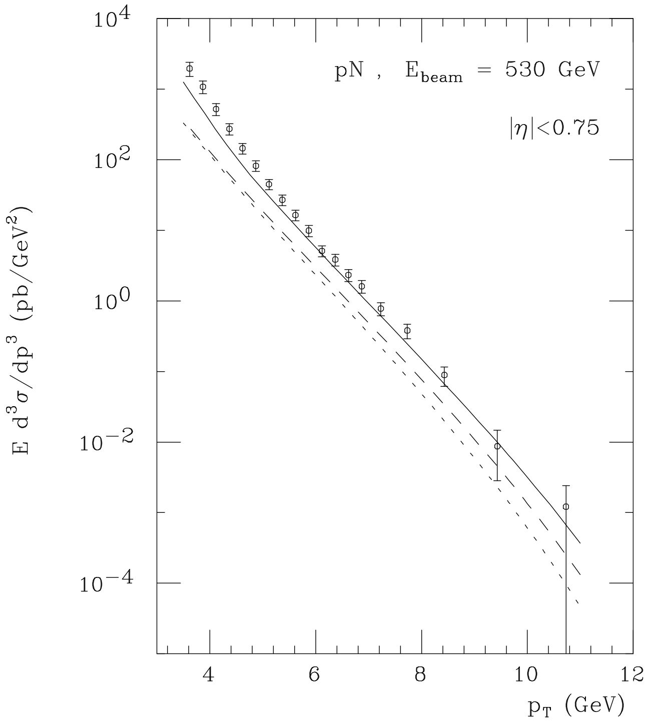

Figure 2.8: One of recent resummed pQCD calculations for the E706 prompt photon production. The dotted line represents the NLO calculation, while the dashed and solid lines respectively incorporate pure threshold resummation and joint threshold and recoil resummation, within the formalism of collinear factorization.

average total momentum imbalance of the pairs, for a wide range of $\sqrt{s}$. Further discussion of the physics interpretation of these data will be given in chapter 9.

The latest prompt photon results from the TeVatron collider have confirmed that k_T smearing effects implemented in simple Gaussian smearing models in MC work well in their recent data [46]. High cross sections are observed below photon transverse momenta of 36 GeV. Measurements by CDF [38] are consistent with a $<k_T>$ value of 3.5 GeV applied to a NLO QCD calculation. Recently published results from D0 [39] are consistent with those of CDF (see figure 2.5). From a more basic point of view, the presence of additional initial–state gluon radiation beyond NLO in QCD can increase the effective k_T values of hard–scattering partons, and may help to generate the effects observed [47, 48, 49, 50].

In the recent theoretical work the resummed pQCD calculations for inclusive prompt photon production are currently under development in order to interpret the k_T issues in photon physics [51, 52, 53, 54, 55, 56]. Two recent independent threshold–resummed pQCD calculations for prompt photons [51, 52] do not include $<k_T>$ effects, but exhibit less dependence on QCD scales than the NLO theory. These calculations agree with the NLO prediction for the scale $\mu \approx p_T/2$ at low p_T, and show an enhancement in cross section at high p_T.

A method for simultaneous treatment of recoil and threshold corrections in inclusive photon cross sections has been developed [56] within the formalism of collinear factorization. At moderate p_T, substantial enhancements from higher–order perturbative and power–law non–perturbative corrections have been found at fixed–target energies, as illustrated in figure 2.8 in a comparison with the E706 prompt photon measurement at $\sqrt{s} = 31.6$ GeV. Although the present numerical results are only exploratory estimates of the size of expected effects, it is clear that the phenomenological consequences are potentially significant.

2.5 Summary

In this chapter, we have considered the knowledge of prompt photon production mechanisms at HERA, the status of experimental results so far and finally current issues in this area, in both experimental and theoretical aspects. The aim of this thesis is to present measurements of prompt photon production to lead us to a deeper understanding of some fundamental questions of QCD and the partonic nature of matter.

Chapter 3

HERA and the ZEUS Detector

3.1 The HERA Accelerator

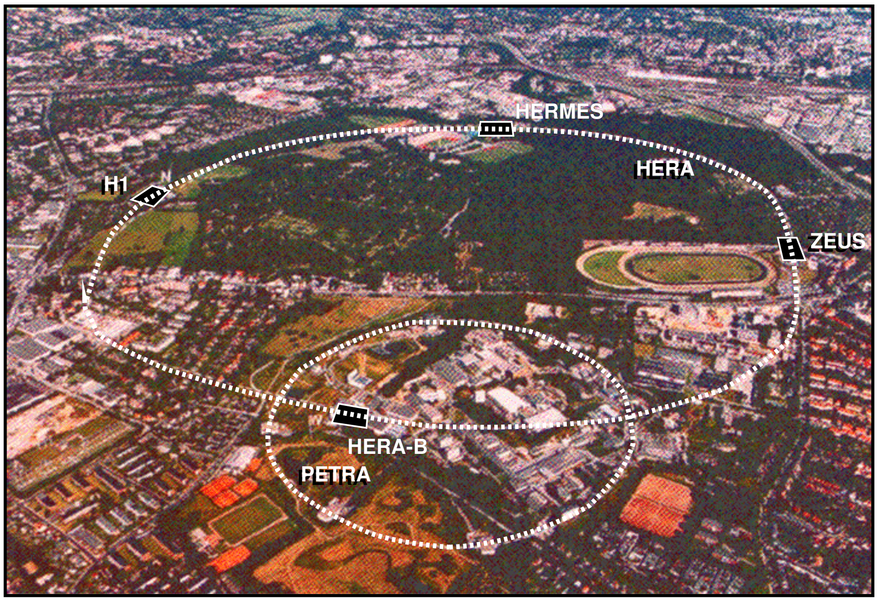

Figure 3.1: The HERA collider enclosing the Volkspark in Hamburg, Germany shown with the pre-accelerator, PETRA and the four experiments.

The HERA (Hadron Electron Ring Anlage) is the world's first lepton–proton collider and is situated at DESY (Deutsches Elektronen Synchrotron) in Hamburg, Germany (see figure 3.1). HERA was designed to accelerate electrons or positrons to 30 GeV and protons to 820 GeV energy, yielding a centre of mass energy $\sqrt{s} = 314$ GeV, in two independent rings. Figure 3.2 shows a schematic layout of the HERA accelerator complex. The electron (positron) and proton

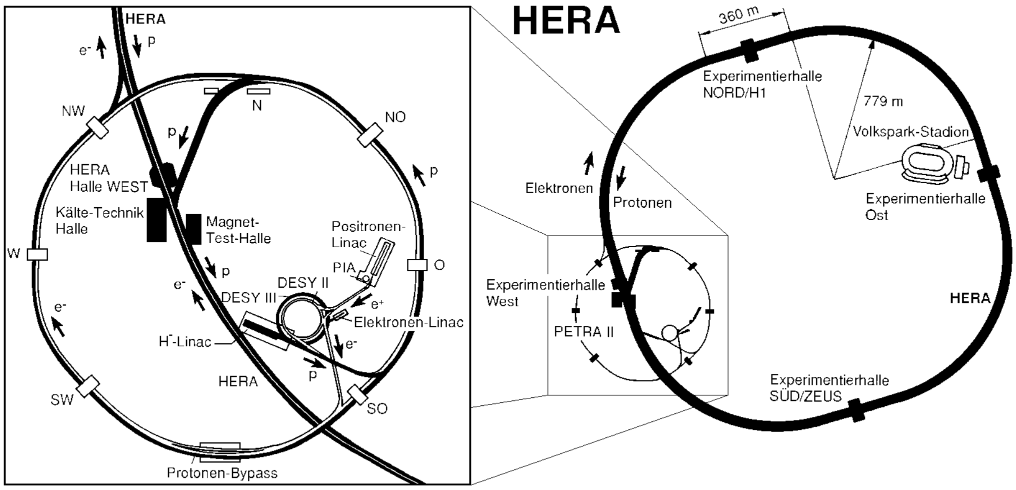

Figure 3.2: A schematic diagram showing the layout of the HERA accelerator complex; four experimental halls and the pre-accelerator ring with the injection system enlarged.

rings use conventional and superconducting magnets respectively. For 1996–97 running, the lepton ring operated at an energy of 27.52 GeV yielding a centre of mass energy $\sqrt{s} = 300$ GeV. The electron ring was first commissioned in 1989, while the proton ring was first operated in March 1991. First electron–proton interactions were achieved and recorded in October 1991.

The HERA ring is approximately circular and is 6.34 km in circumference. Experimental halls are situated at four equidistant points along the circumference of the ring as shown in figure 3.1 and 3.2. The two *ep* collider experiments H1 and ZEUS are located in the north and south halls respectively. There are also two fixed–target experiments HERMES and HERA–B which are situated in the east and west halls respectively. HERMES is designed to study the spin structure of the nucleon using the scattering of longitudinally polarized electrons off polarized gas jet targets. HERA–B is designed to investigate CP violation in the B hadron sector, using wire targets in the proton beam.

In the proton injection system, H^- ions are accelerated to 50 MeV using a linear accelerator. Before injection into the DESY III storage ring, the electrons are stripped off the hydrogen ions, yielding protons. This is filled with 11 bunches having a 96 ns bunch spacing, the same as in HERA, and accelerated up to 7.5 GeV. The proton bunches are then transferred to the PETRA ring, where they are accelerated to 70 bunches of 40 GeV and injected into the HERA proton machine. This process is repeated until HERA is filled with up to 210 bunches, which are then accelerated to 820 GeV with a lifetime of a few days.

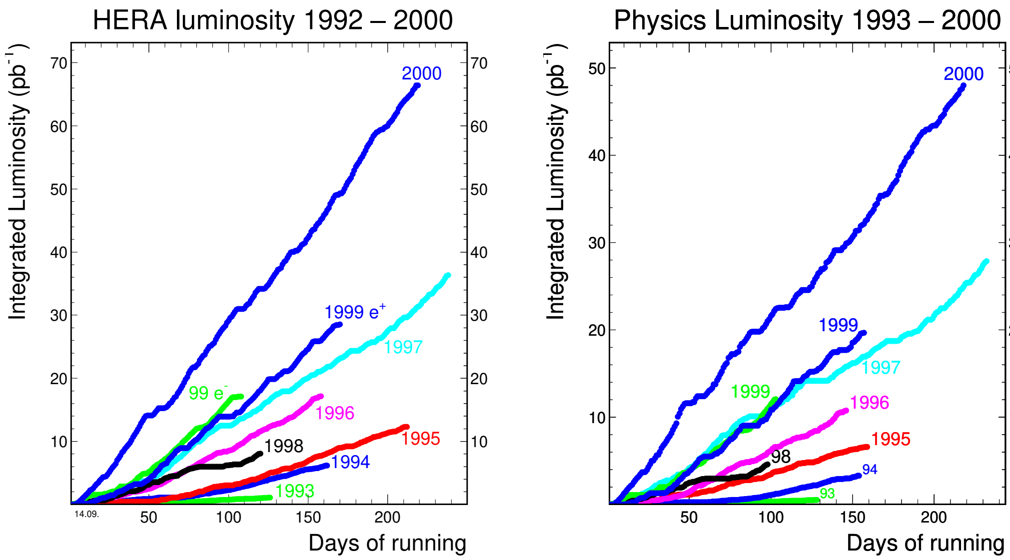

Figure 3.3: The left plot shows the integrated luminosity delivered by HERA versus the date for the years since the start of HERA operation. The luminosity which was taken by the ZEUS detector and which is useful for physics analysis is shown in the right plot. Since 1998 the proton energy was raised to 920 GeV.

The electron injection begins with the LINAC's I and II which accelerate the electrons to 220 and 450 MeV respectively, and fill the positron accumulator (PIA) with a single bunch of up to 60 mA. These are then transferred to the DESY II storage ring and accelerated to 7.5 GeV. The transfer to the PETRA II storage ring is performed such that 70 bunches of 96 ns spacing are obtained. After accelerating the electrons to 14 GeV, the electron bunches are transferred to HERA until this is filled with up to 210 bunches and the electrons are accelerated to 27.52 GeV with a life time of about 8 (2–3) hours for positron (electron) beam.

Since HERA started operating in 1992, the integrated luminosity delivered by HERA has been continuously increased. The left plot in figure 3.3 shows the HERA luminosity for the different years versus the days of running. The right plot shows the luminosity which was taken by the ZEUS detector. During 1996 and 1997 running period 38 pb^{-1} of data were taken by ZEUS detector. The analysis presented in the thesis is based on this data set. Since 1998 the proton energy was raised to 920 GeV and the HERA luminosity upgrade is planned during the shutdown in the year 2000, with the aim to increase the luminosity by a factor five.

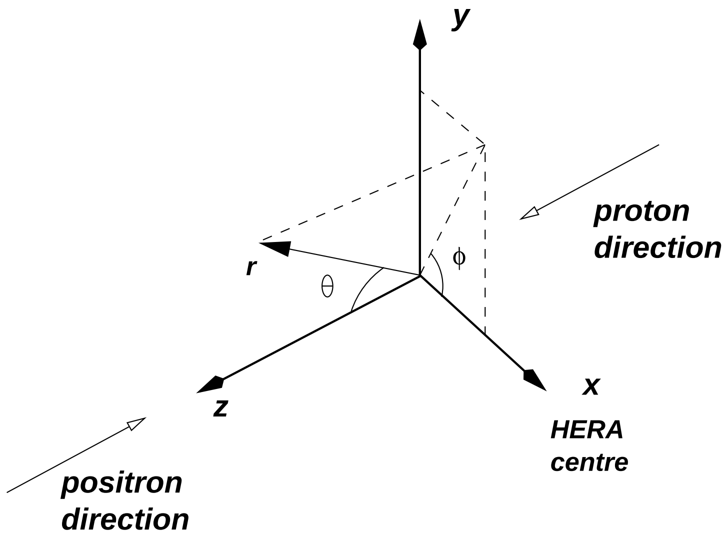

Figure 3.4: The ZEUS coordinate system.

3.2 The ZEUS Detector

The ZEUS detector is a large multipurpose detector, designed to study lepton–hadron scattering, and has near 4π coverage in solid angle, except for small regions around the forward and rear beampipes. The ZEUS coordinate system is shown in figure 3.4. The z axis follows the line of the beam direction. The x and y axes point to the centre of the HERA ring and directly upwards, respectively. The polar angle, θ, is measured with respect to the proton beam direction. The azimuthal angle, ϕ, is measured with respect to the x axis in the x–y plane.

Figure 3.5 and 3.6 show a cross sectional view of the layout of the ZEUS detector in the longitudinal (z–y) and transverse (x–y) planes with respect to the beam direction, respectively. A brief outline of the detector components is given in the following. The parts of the detector essential for the present analysis are described in more detail in the following sections. A full description of the ZEUS detector is given in [57].

The innermost component is the central tracking detector (CTD) which is a cylindrical drift chamber consisting of 9 superlayers with 8 planes of sense wires each. These chambers are surrounded by a thin superconducting solenoidal coil with a thickness of one radiation length (X_0), producing an axial field of 1.8 Tesla for determining the momenta of charged particles from their curvature in the magnetic field. At both ends of the CTD there are forward (FTD) and rear tracking detectors (RTD) which provide additional tracking and particle identification informations. The final tracking detector is the Small angle Rear Tracking

Detector (SRTD) which improves the angular resolution on the scattered positron, in the rear direction. All tracking components provide an angular acceptance of 7.5°–170°.

The uranium scintillator sampling calorimeter (UCAL) totally encloses these tracking devices and the solenoid coil, and measures with high precision the energies and directions of particles and jets. The presamplers were installed on the front surface of the UCAL (see chapter 4 for details). Inside the F/RCAL, the Hadron–Electron Seperator (HES) of 3 cm $\times$ 3 cm silicon diodes was installed in order to improve the hadron electron separation and the spatial resolution. In the rear direction there is a small–angle rear tracking detector (SRTD) in front of the RCAL near the beam pipe to study the energy degradation due to inactive materials placed between RCAL and the interaction point. The energy leakage out of the UCAL can be detected by the backing calorimeter (BAC) which is constructed from a sandwich of 7.3 cm thick iron plates and aluminium proportional tubes with a total depth of 6 to 4 λ (interaction length; the mean free path of a particle before undergoing an interaction) The iron plates serve as a return path for the magnetic flux of the solenoid coil. In addition, since 1994 the Beam Pipe Calorimeter (BPC) sits around the beampipe within the RCAL and provides position and energy measurements on DIS electrons at very small scattering angles. It extends the Q^2 coverage to events with a Q^2 of 0.1–0.6 GeV^2.

The outermost components are the muon detecting systems: the forward muon detector (FMUON) consists of 5 planes of limited streamer tubes, 4 planes of drift chambers, 1 time–of–flight counter, and 2 magnetized iron toroids. The barrel and rear muon detectors (BMUON, RMUON) both consist of 2 pairs of the inner and outer components, each of 2 layers of limited streamer tubes. An iron wall covered with 2 planes of large area scintillation counters (Veto Wall) behind the rear calorimeter, 7 m from the interaction point, protects the detector from particles from the beam halo accompanying the proton bunches. The C5 counter is situated 3.2 m from the interaction point upstream of the proton beam and is used to measures the timing of the positron and proton bunches and detects proton beam interactions upstream of the interaction point.

There are other additional detector components which are not shown in figure 3.5 and 3.6. A silicon–strip leading proton spectrometer (LPS) consists of several elements between 20 and 100 m downstream in the proton direction. It is used for detecting proton remnant jets and scattered protons. Similarly a forward neutron calorimeter (FNC) provides information on the hadronic final state at small angles in the proton direction. A luminosity measurement is provided by small–angle electron and photon calorimeters (LUMI) in the HERA tunnel which are located 35 and 105 m from the interaction point in the electron direction, respectively.

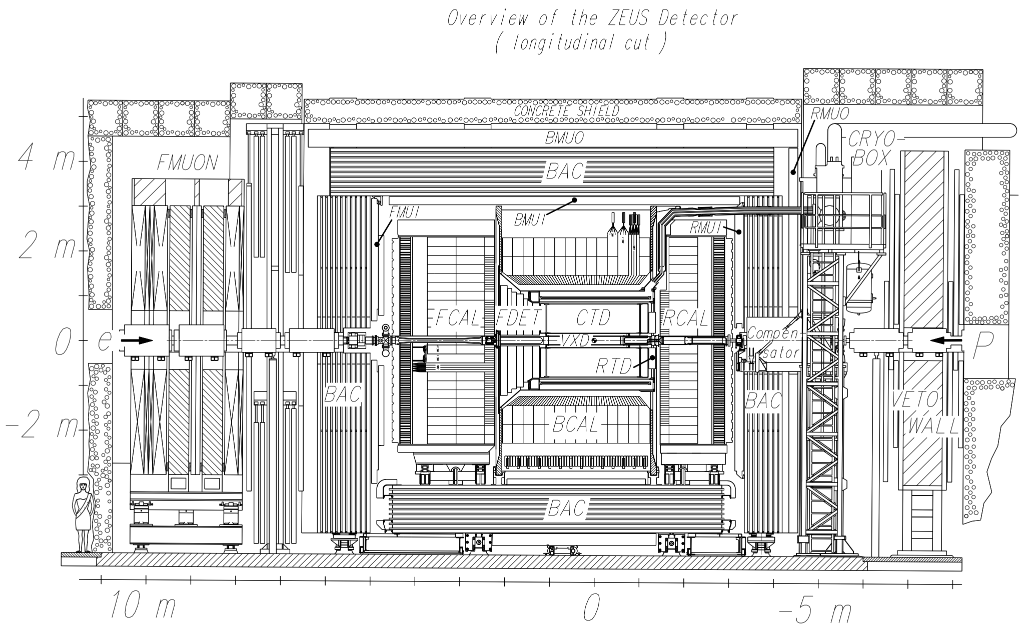

Figure 3.5: A schematic diagram showing a longitudinal section through the components which make up the ZEUS Detector.

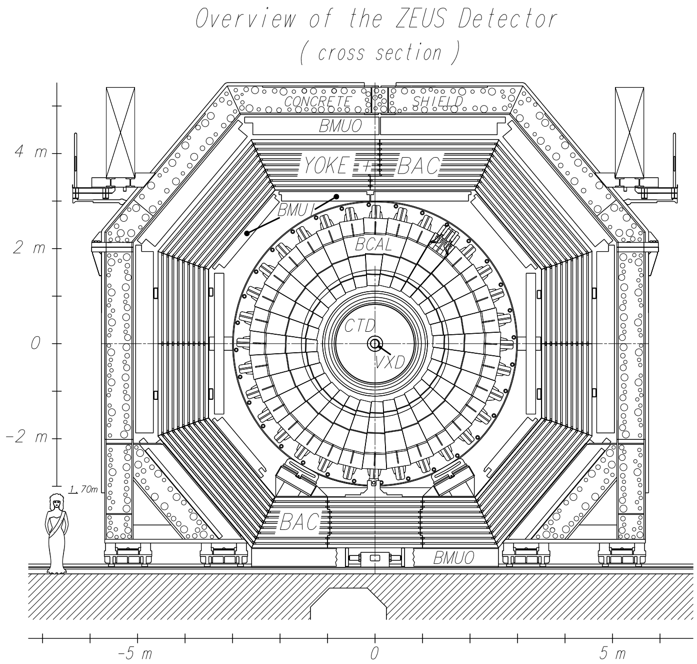

Figure 3.6: A schematic diagram of the ZEUS detector in the xy plane.

3.2.1 The Uranium Calorimeter

The main part of the ZEUS detector is the uranium scintillator calorimeter (UCAL) [58] which measures with high precision energies and directions of particles and jets. It has a layered structure and is built from depleted uranium (DU; 98.1% ^{238}U, 0.2% ^{235}U, 1.7% Nb) plates interleaved with plastic scintillator (SCSN–38) plates. Readout of the light from the scintillator is achieved by means of plastic wavelength shifters (WLS) with associated photo–multipliers.

The layout of the calorimeter is shown in figure 3.5 and 3.6. It consists mechanically of three independent components: Forward Calorimeter (FCAL), Barrel Calorimeter (BCAL) and Rear Calorimeter (RCAL), covering the polar angle ranges 2°–40° ($4.3 \leq \eta < 1.1$), 37°–129° ($1.1 \leq \eta < -0.75$) and 128°–177° ($-0.75 \leq \eta < -3.8$), respectively. It provides a solid angle coverage of 99.8% in the forward hemisphere and 99.5% in the backward hemisphere. The front face of FCAL (RCAL) is 2.2 m (1.5 m) distant from the nominal electron–proton interaction point. In units of interaction lengths FCAL has a maximum depth of 7.2 λ, BCAL of 5.3 λ and RCAL of 4 λ. The depth of the calorimeter was optimized by requiring that 95 % of the shower energy is contained for 90 % of the jets of maximum possible energy from the HERA kinematics which falls from 800 GeV at the forward proton direction ($\theta = 0°$) to about 300 GeV at $\theta = 30°$, 100 GeV at $\theta = 60°$ and less than 50 GeV for $\theta \geq 90°$.

The UCAL has a modular structure. Each FCAL/RCAL module has a width of 20 cm, an active depth up to 1.53 m and a height for the active part varying from 2.2 to 4.6 m, depending on its position with respect to the beam. The modular structure of BCAL constructed from 32 identical modules each covering an angle wedge of 11.25° in ϕ with a length of 3.3 m in the beam direction. The inner/outer radius of the BCAL is 1.22/2.29 m from the beam axis. All modules are tilted by 2.5° to avoid particles from the interaction point travelling through module boundaries. Each calorimeter component is segmented longitudinally into two sections, an electromagnetic (EMC) with a depth of 1 interaction length (λ), or equivalently 25 radiation lengths (X_0), and hadronic sections (HAC). The HAC sections of FCAL and BCAL are further segmented longitudinally into two sections with a depth of $2 \times 3.1\lambda$ in the FCAL, $2 \times 2.1\lambda$ in the BCAL, while RCAL has a single HAC section 3.1 λ deep.

The FCAL/RCAL modules have a non–projective tower structure. The cell readout in the transverse direction is made in terms of towers of 20×20 cm^2 for HAC sections of both FCAL and RCAL. The EMC sections are further segmented into 5×20 cm^2 and 10×20 cm^2 sections for FCAL and RCAL respectively. Each

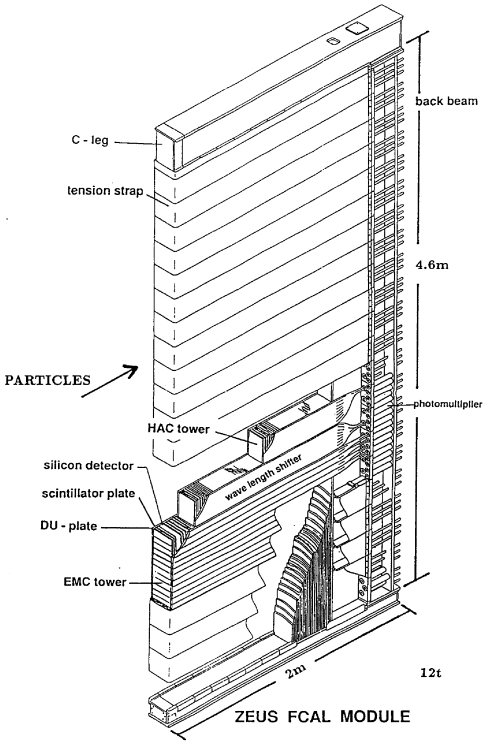

Figure 3.7: Internal structure of a FCAL module. The 20×20 cm^2 towers with their longitudinal division into EMC and HAC section are shown.

module of the BCAL consists of 53 EMC towers. Throughout most of the BCAL four EMC towers are backed by one HAC tower which measures 20×28 cm^2 at the inner radius. Both the EMC and the HAC towers of the BCAL are projective in azimuthal angle (ϕ) but only the EMC of BCAL is projective in θ.

As an example of the construction geometry of the calorimeter, Figure 3.7 illustrates the internal structure of an FCAL module. It is made up of layers of 3.3 mm thick DU plates yielding 1 X_0 of sampling thickness for both EMC and HAC and 2.6 mm thick SCSN–38 scintillator plates. The thickness of the uranium and scintillator plates was optimized to achieve an equal response of the calorimeter to electrons and hadrons (compensation; $e/h = 1$).

The UCAL is compensating with an electromagnetic energy resolution of $18\%/\sqrt{E} \oplus 1\%$ (GeV) and an hadronic energy resolution of $35\%\sqrt{E} \oplus 2\%$ (GeV). The calorimeter response to electrons is linear within $\pm 2\%$ up to 110 GeV/c. The angular resolution for the scattered electron is better than 10 mrad. In addition the UCAL provides excellent timing, better than 1.5 ns compared to the HERA bunch crossing time of 96 ns, which has played a crucial role in the fast rejection of beam gas background from the physics samples.

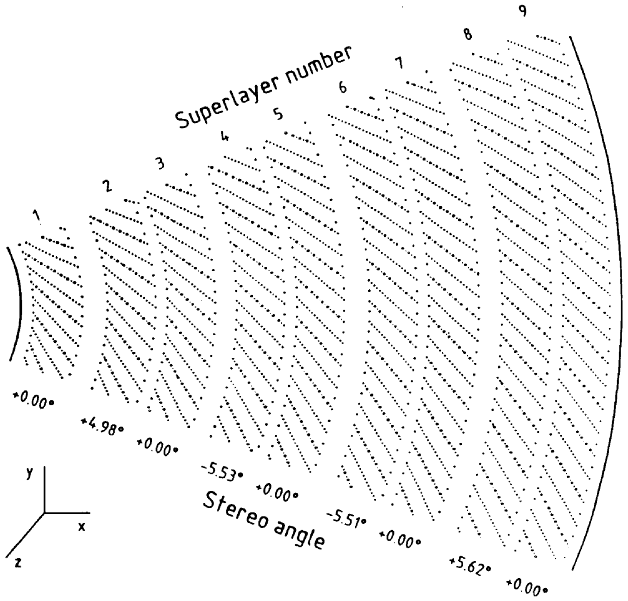

Figure 3.8: A schematic diagram of one octant of the CTD.

3.2.2 The Central Tracking Detector

The central tracking detector (CTD) [59] measures the direction and momentum of charged particles with high precision and estimates the energy loss dE/dx used for particle identification. The CTD is a cylindrical drift chamber with an inner radius of 18.2 cm, outer radius 79.4 cm and length of 205 cm, filled with a gas mixture of 90% argon, 8% CO_2 and 2% ethane. It covers a polar angle of 15° to 164° and consists of 72 radial layers, organised into 9 superlayers.

Figure 3.8 shows the wire layout in a single octant of the CTD. Alternating layers of sense and field wires are indicate by the dots. The larger dots are the sense wires. The odd superlayers are axial layers which have sense wires parallel to the beam axis, while the even superlayers are stereo layers, inclined at angle $\sim \pm 5°$ with respect to the beam axis, which allows the determination of the z–position of the hits. For trigger purpose, the inner three axial layers are additionally equipped with a z–by–timing system ($\sigma_z \sim 4$ cm) which determines z–position of a hit from the difference in arrival times of a pulse at both ends of the chamber. With the 1996 calibration of the chamber, the nominal resolution of the CTD was per hit around 180 μm–190 μm in r–ϕ, resulting in a transverse momentum resolution of 0.005 $p_T \pm 0.0016$ for long tracks (> 3 superlayers). The z–vertex resolution for medium and high multiplicity events, taken from many track measurements, is < 1.5 mm.

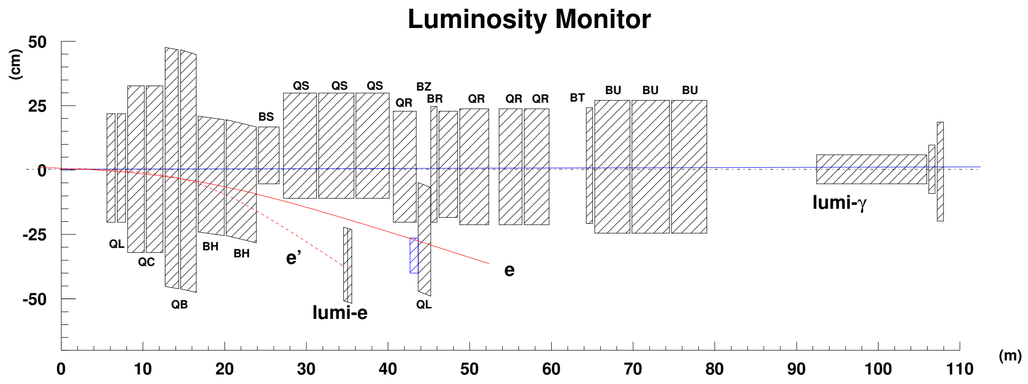

Figure 3.9: The luminosity monitor.

3.2.3 The Luminosity Monitor

The luminosity at HERA is measured via the rate of the bremsstrahlung process $ep \rightarrow ep\gamma$. The luminosity monitor (LUMI) consists of two separate detectors; one of which measures the scattered electron and the other the photon [60].

A lead–scintillator sampling electron calorimeter, situated 35 m from the interaction point in the electron direction, measures the energy of electrons scattered at small angle to the beam direction. It detects electrons with $\theta_e^{'} < 6$ mrad with an efficiency greater than 70% for $0.35E_e < E_e^{'} < 0.65E_e$. A sample of photoproduction events can be isolated where the electron has been scattered with $\theta_e^{'} < 6$ mrad and is detected in the LUMI. An upper limit of $Q^2 < 0.002$ GeV^2 is set on the virtuality of the photon for these events from the maximum angle an electron can have while still escaping along the beam pipe, i.e., 6 mrad. The LUMI tagged photoproduction events provide a well characterised sample which can be used to find ways of reducing background in photoproduction events where the electron is not detected.

A photon detector is located close to the proton beam 107 m downstream of the interaction point in the direction of the electron beam. A carbon filter is used to absorb synchrotron radiation, a Cerenkov counter vetos charged particles and finally a lead–scintillator sampling calorimeter measures the energy of the photon. The geometrical acceptance is 98% for the process $ep \rightarrow ep\gamma$ and is independent of the energy of the photon. The luminosity measurement is obtained from the rate of photon events measured in this calorimeter corrected as follows :

$$R_{ep} = R_{tot} - R_{unp}\frac{I_{tot}}{I_{unp}} \tag{3.1}$$

where R_{tot} is the total rate, R_{unp} is the rate in unpaired electron bunches, I_{tot} is the total current and I_{unp} is the current in unpaired electron bunches. This corrects for beam gas backgrounds. The value of the integrated luminosity in 1995 and 1996 was measured to an accuracy of $\pm$ 1.5%.

3.3 The ZEUS Trigger System

The short bunch crossing time at HERA of 96 ns, equivalent to a nominal rate of $\sim$ 10 MHz, is a technical challenge which puts stringent requirements upon both the ZEUS Trigger and the Data Acquisition (DAQ) system. The total interaction rate, which is dominated by background from upstream interactions of the proton beam with residual gas in the beam pipe, is of the order 10–100 kHz while the rate of *ep* physics events in the ZEUS detector is of the order of a few Hz. Other background sources are electron beam gas collisions, beam halo and cosmic ray events.

ZEUS employed a sophisticated three–level trigger system in order to select *ep* physics events efficiently while reducing the rate to a few Hz. A schematic overview of the ZEUS trigger system is shown in figure 3.10 [61].

The First Level Trigger (FLT) is a hardware trigger, designed to reduce the input rate below 1 kHz. Each detector component has its own FLT, which stores the data in a pipeline, and makes a trigger decision within 2 μs after the bunch crossing. The decision from the local FLTs are passed to the Global First Level Trigger (GFLT), which decides whether to accept or reject the event, and returns this decision to the component readout within 4.4 μs.

If the event is accepted, the data are transfered to the Second Level Trigger (SLT), which is software–based and runs on a network of Transputers. It is designed to reduce the rate below 100 Hz. Each component can also have its own SLT, which passes a trigger decision to the Global Second Level Trigger (GSLT). The GSLT decides then on accepting or rejecting the event.

If the event is accepted by the GSLT, all detector components send their data to the Event Builder, which produces an event structure on which the Third Level Trigger (TLT) code runs. The TLT is software based and runs part of the offline reconstruction code on a farm of Silicon Graphics CPUs. It is designed to reduce the rate to a few Hz. Events accepted by the TLT are written to tape via a fibre–link (FLINK) connection. The size of an event is typically $\sim$ 100 kBytes. From here on events are available for full offline reconstruction and data analysis.

The trigger logic used for the online selection of photoproduction events, on which the present analyses are based, is described in section 6.3.

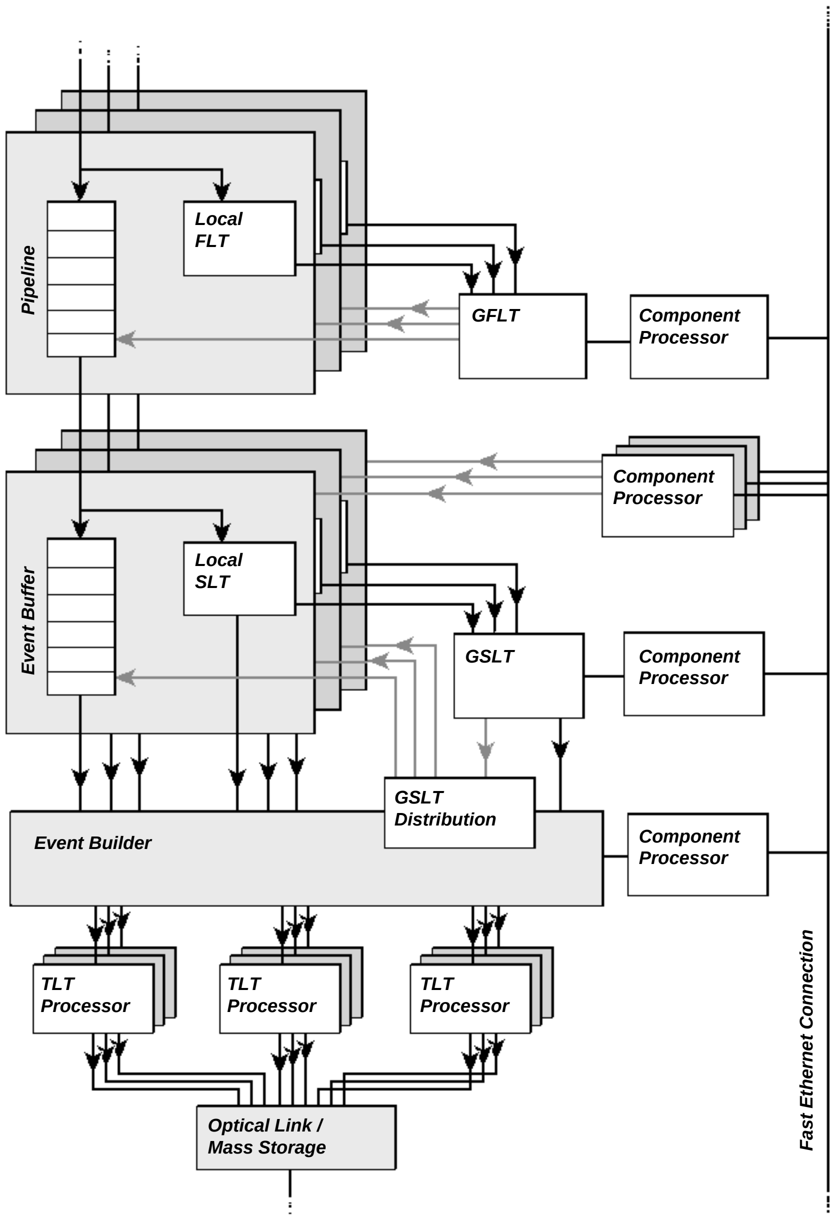

Figure 3.10: A schematic diagram of the processes which make up the ZEUS three-level trigger system [61].

Chapter 4

The ZEUS Barrel Presampler

This chapter concerns work done by author on the ZEUS Barrel PREsampler detector (BPRE). A brief description of the presampler detector and the ZEUS BPRE are presented in section 4.1 and section 4.2 respectively. The initial performance of the BPRE is given in section 4.3 with results from the charge injection study, and the development of the BPRE geometry setup for the ZEUS detector simulation package is presented in section 4.4, which also gives some perspective for future analysis.

4.1 Introduction

A Presampler detector provides a link between tracking devices and calorimeters. It is placed just in front of the calorimeter and consists of some conversion material interspersed with or followed by an active element. It must be, by definition, thick enough to start an EM shower, yet thin enough to allow the shower maximum to occur well inside the calorimeter. This early sampling of the EM shower gives the presampler detector an advantage over devices at which have a shower maximum in the area of electron/hadron discrimination. In addition, their better position resolution is directly correlated with how well they can distinguish between real electrons and fake signals produced by the overlap of π^0's or γ's and a charged track. The advantages of using a preshower detector can be summarized as :

- the precise determination of the starting position of an EM shower ;
- reduction of accidental π^0/charged–track overlaps which fake an electron ;
- γ/π^0 separation on an event–by–event basis ;

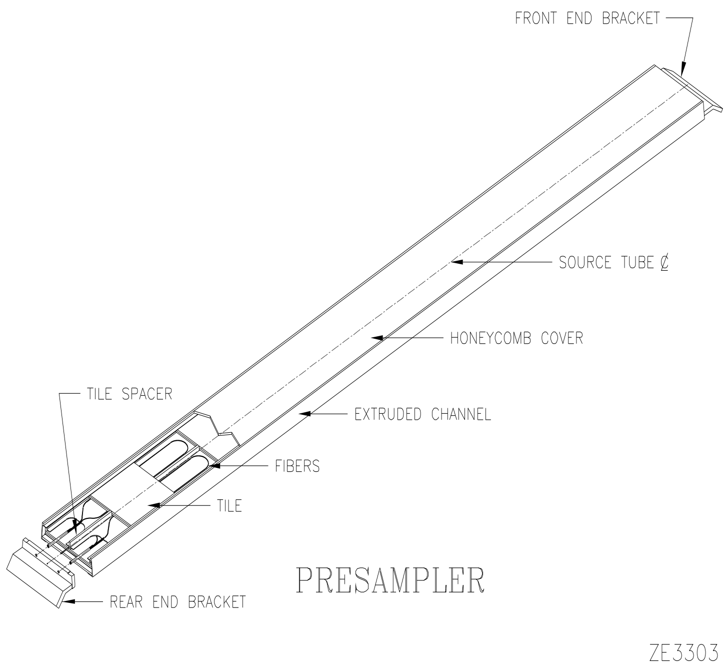

Figure 4.1: Exploded view of a BCAL presampler module cassette.

- improved electron/hadron discrimination in isolated events and electron identification.

4.2 The ZEUS Barrel Presampler

The BPRE is a detector component placed just in front of the BCAL that is separately read out. The signal in the presampler, which counts the number of charged particles impinging on it, is then proportional to the energy loss of the incident particle, since the predominant energy loss mechanisms result in electromagnetic showers for photons, electrons and low energy pions (through charge exchange), and other charged particles for higher energy ($\geq$ several GeV) pions.

A presampler is needed in the ZEUS detector to correct energies measured in the calorimeter for the energy losses due to the dead material between the interaction point and the face of the calorimeter. It can be also used to improve the e/π discrimination ability of the calorimeter as well as providing some γ/π^0

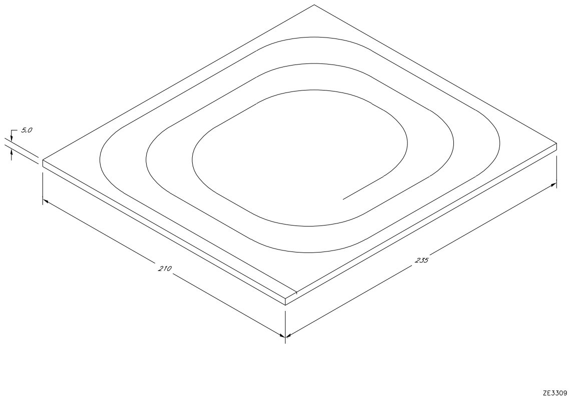

Figure 4.2: Configuration of WLS fibres inside a BCAL presampler scintillator tile.

separation. It has a particular importance in prompt photon physics since it enables us to evaluate the photon signal independently of the energy of the photon. More details will be discussed in section 4.4.

Initially the forward and rear calorimeters of ZEUS detector were equipped with a complete presampler consisting of a single layer of 5 mm thick SCSN38 plastic scintillator that is read out by wave–length–shifting (WLS) fibres. In 1996 an additional presampler detector was proposed for the barrel region, covering the BCAL face and providing overlap coverage with the FCAL and RCAL presamplers [62].

The BPRE detector consists of 32 individual cassettes each containing 13 scintillator tiles oriented along the Z direction, installed directly in front of each of the 32 BCAL modules. The BPRE module cassettes are made from two sheets of aluminium hex–cell honeycomb glued at the side to an aluminium extrusion, as shown in the exploded view of figures 4.1.

The scintillator tiles consists of 2 pieces of SCSN–38 plastic scintillator, each approximately 20 cm × 18 cm and 5 mm thick, read out by 2 fibres embedded in each tile in a spiral pattern as shown in figure 4.2. To maximise the light yield, the groove length over tile area should be maximised. The chosen design satisfies this requirement and also gives a reasonable uniformity of response. The spiral groove is 2 mm deep in the 5 mm thick scintillator, and two 0.83 mm diameter Y11 multi–clad fibres are held in the groove. The length of each WLS fibres is 175 cm. They are spliced to 5 m long, clear multi–clad plastic fibres. The attenuation length of the clear fibre is about 7 m, compared to the distance from the tile to the PMT of 5 m. The scintillator tiles were wrapped in white Tyvek paper and the end of each WLS fibres in the scintillator is aluminised.

The 4 clear fibres from a scintillator tower transport the light signal to a PMT whose HV is set and controlled individually by Cockroft–Walton (CW) bases. HV control is supplied by a PC interfaced to CAMAC via GPIB. The HV set values are routed to DACs in the CAMAC crate which then send a voltage level to the CW bases on the detector. The HV monitoring signal is sent back to a multiplexed ADC in the same CAMAC crate to analyze the HV set and read–back voltage.

4.3 Initial Performance of the BPRE

The ZEUS BPRE was commissioned in the fall of 1998 and has taken useful data since January 1999.

Several plots of the inclusive BPRE data from the 1999 HERA run are shown in figure 4.3. The data sample analyzed is the 1999 luminosity runs (run numbers; 31784–31943). The total luminosity of this sample on tape is about 11.87 pb^{-1}. Figure (a) and (b) show the correlation between hits in the BPRE compared to hits in the BCAL EMC. The BPRE/BCAL Contour plot; (a) shows the clear correlation between hits in the BPRE and BCAL channels for inclusive data. The following requirements are required;

- BCAL EMC energy $>$ 1.0 GeV
- BPRE signal $>$ 1.5 pC

The BPRE/BCAL scatter plot (b) shows the correlation between BPRE signal in pC and electron energy in BCAL EMC in GeV. Figure (c) show that the mapping between 32 BPRE modules and 13 BPRE tiles for a given channel. BPRE energy distribution for the events is shown in figure (d).

To check the performance of BPRE analog card readout system, the test for the charge injection (Q_{inj}) was done using the calorimeter data acquisition software (CALDAQ). Figure 4.4 shows the charge injection results of all BPRE channels; (a) before and (b) after energy correction. There is one bad channel between channel 260 and 270, indicating the non–operation of one BPRE channel. After energy correction, all gain are same at 15000 pC (see figure 4.4 (b)). In the figure 4.4 (b) there are 4 dips due to 16 unused channels of four crates in the front–end electronics.

The CALDAQ does not do any energy correction per sample. The DSP code running on the digital cards, which receives the buffer–multiplexer information

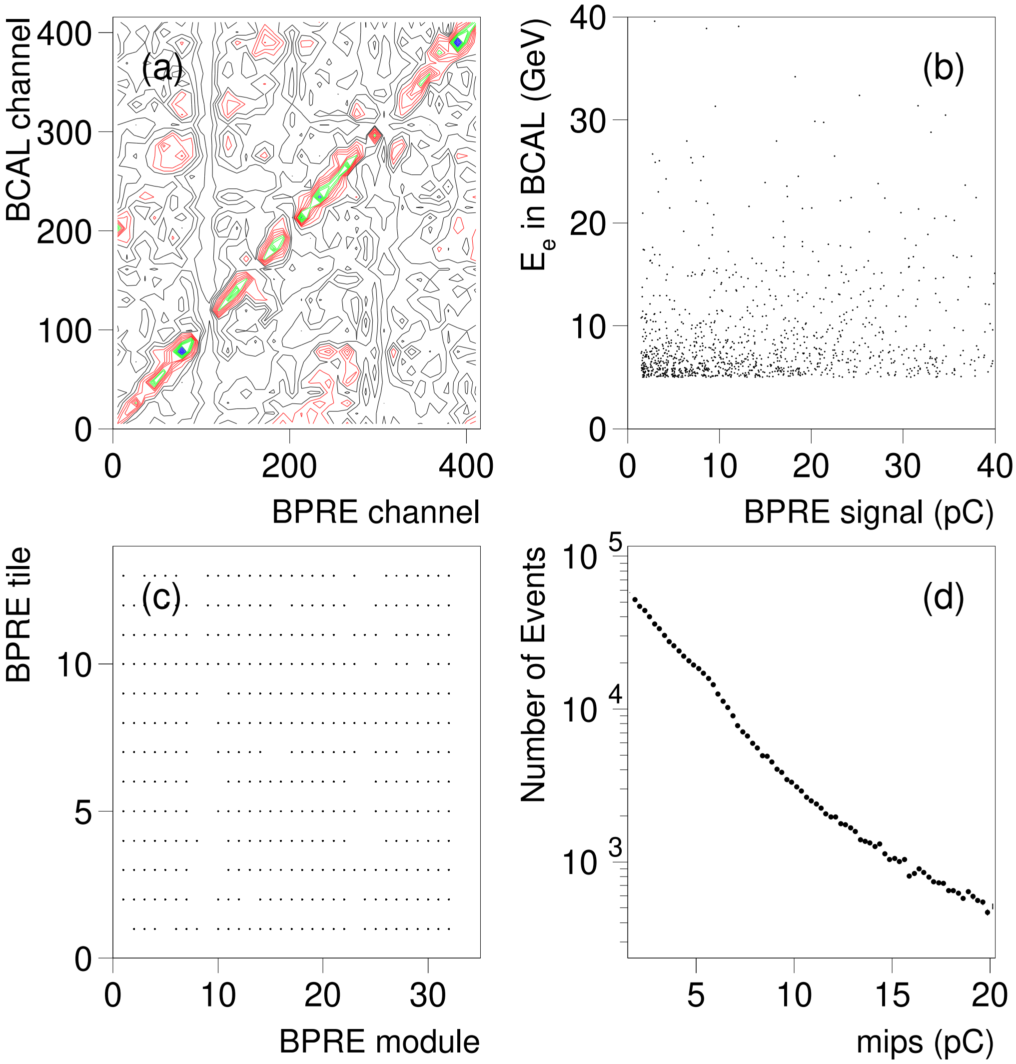

Figure 4.3: (a) Correlation between hits in the BPRE and BCAL channels, (b) correlation between BPRE signal in pC and electron energy in BCAL EMC in GeV, (c) mapping between 32 BPRE module and 13 BPRE tile for a given channel and (d) BPRE energy distribution in pC.

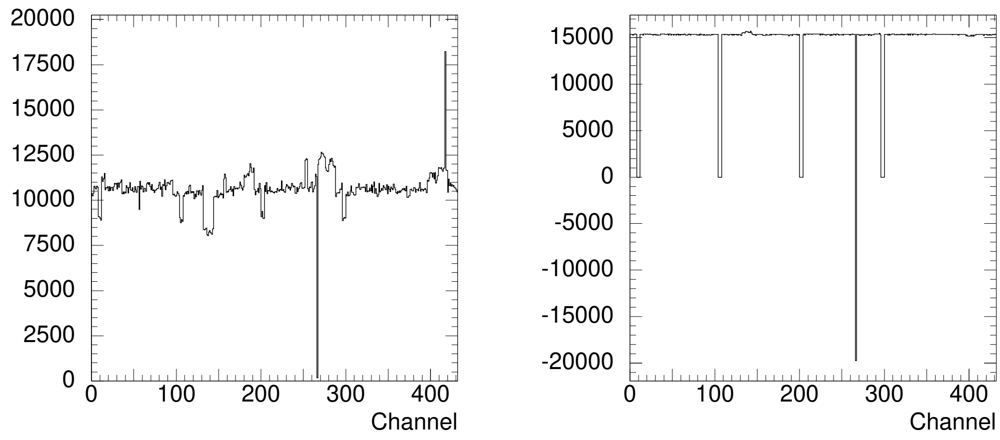

Figure 4.4: Charge injection results (a) before and (b) after energy correction for the BPRE using Calorimeter DAQ, Unit is MeV.

from the front–end cards, corrects the Q_{inj} samples for pedestals and gains in the pipeline–buffer chain. These pedestals and gains are calculated during a front–end calibration for all components in the CALDAQ. These corrected samples are then used to calculate **H** and **T** values in unit of ADC count,[1] where **H** is weighted sum of the two samples, **h1** and **h2**, used to reconstruct energy;

$$\mathbf{H} = \mathbf{h1} + 1.8 \cdot \mathbf{h2}$$

where 1.8 is the calibration constant obtained from a beam–test. The **H** value is eventually converted to a charge Q (in pC) using shaper constants calculated during the calibration.

Finally it is converted to MeV by a simple scale factor. In figure 4.4 (b) the Q_{inj} spectrum looks reasonably flat because front–end card differences have been taken into account, and all channels are injected with the same charge. If we take a run with dummy constants all pedestals are set to 0, all gains to 1, and all shaper constants to some default values. Therefore the samples are not corrected properly, nor is Q_{inj} calculated with the proper shaper constants, so the Q_{inj} spectrum reflects channel–to–channel (and card–to–card) hardware differences.

On–line data quality monitoring (DQM) for the BPRE runs on the TLT processor. Every 30 minutes during data–taking, the DQM program analyses the basic quantities, generating a status report containing the average signal from inclusive data for each of BPRE channels. To avoid large statistical fluctuations

[1] $0 \sim 4095$ per sample, therefore **H** has a maximum of $4095 \cdot 2.8$

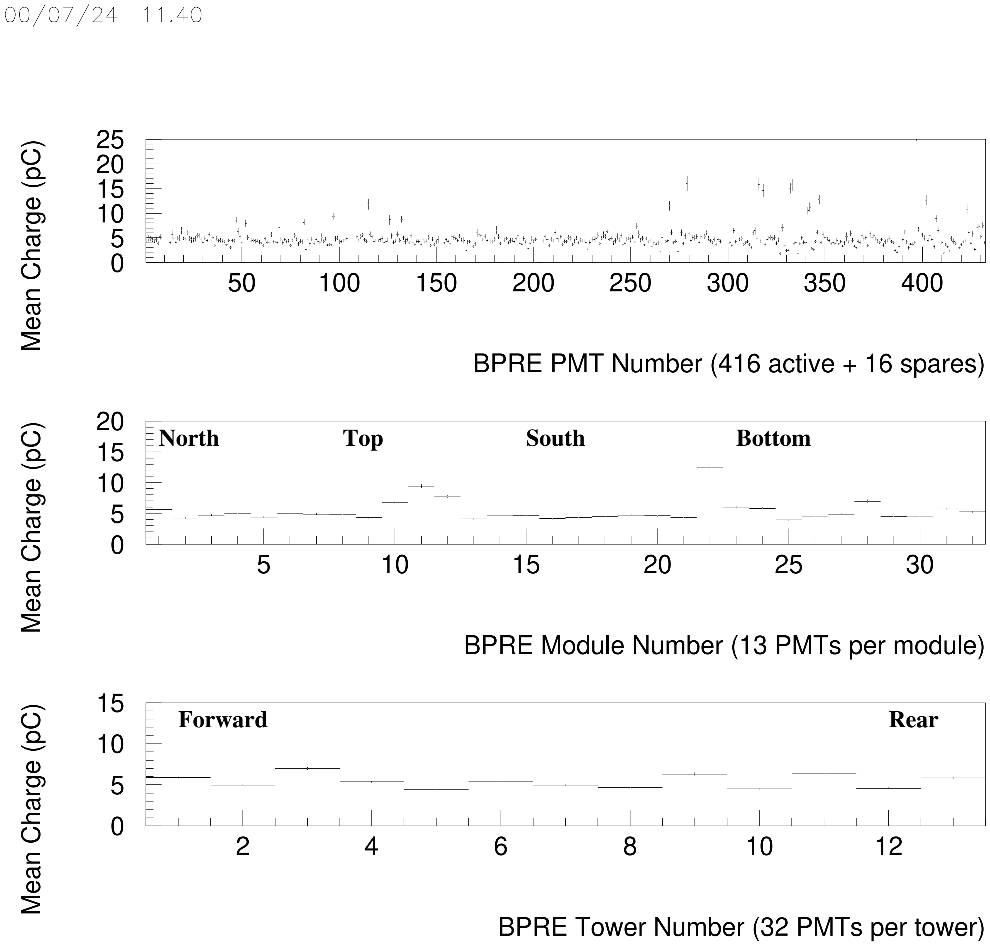

Figure 4.5: Example of BPRE Off–line DQM Histograms. The average signals (mean charge in pC) per (top:) PMT number (416 channels are active), (middle:) module number (13 PMTs per module) and (bottom:) tower number (32 PMTs per tower)

and subsequent misinterpretation of the average signals, the program preselects events with energy greater than 1.0 GeV found in BCAL. A status flag, (1) Normal, (2) Warning and (3) Alarm, transported to the general ZEUS DQM, is displayed in the Slow Control system. If fewer than 70 channels are dead, the status of BPRE is regards as Normal.

Off–line DQM for the BPRE is performed once every few days, running on ZEUS–Offline cluster. The program analyses the average signals for each channel using approximate 6000 inclusive events and checks the timing and the mean charge of the signals for each channel;

There are two sets of Off–line DQM histograms available. Figure 4.5 shows one of the Off–line DQM histograms for the data taken on July 24, 2000. It shows that the average signals (mean charge in pC) per PMT number (top plot: 416 channels are active), module number (middle plot: 13 PMTs per module) and tower number (bottom plot: 32 PMTs per tower). In the figure, the average signals (mean charge in pC) per channel are about 5 pC. This is consistent with the other calibration programs for which the 5 pC charge is a reference signal.

4.4 Geometry Setup using GEANT

There was originally an incorrect geometry description for the BPRE in the latest version of ZEUS detector simulation package, MOZART. According to the incorrect geometry setup, the BPRE tiles number 1 and 14 had a different size in transverse dimension. Here the tiles 1 and 14 are the first and the last scintillator tile in the Z direction. In the real experimental configuration for the BPRE geometry, however, there are 13 tiles, each having same transverse size, 20 cm, in one module. Therefore a correct geometry setup and material definition of the BPRE in the MOZART was written by the author, using the GEANT software [63].

As described in section 4.1, the full BPRE consists of 32 cassettes, one for each BCAL module. Each module contains 13 SCSN–38 scintillator tiles with 5 mm thick and about 20×18 cm^2 cross section.

In the GEANT description, the mother volume containing the whole setup is named 'BPRE', that is the first level volume. In the second level, a virtual volume 'SCI3' is made to insert a individual SCSN–38 scintillator tiles. The 'SCI3' is then placed in the realistic (x, y, z) position of the BPRE tiles for a given module and tile. Figure 4.6 shows the new BPRE geometry generated by GEANT.

4.5 γ/π^0 Separation

Figure 4.7 shows the differences of shower development between photons (a) and π^0 mesons (b) in the ZEUS detector. Even narrowing the class of events to those with a well isolated photon candidate leaves a substantial number of events with mesons that "fake" a real photon. To measure the prompt photon events effectively further methods are needed.

There are two statistical methods available in the ZEUS experiment. Both methods depend on the fact that the showers from meson decays come from more than one photon. One method, the shower profile method used in the present analysis, uses measurements of the transverse shower shape of the EM shower

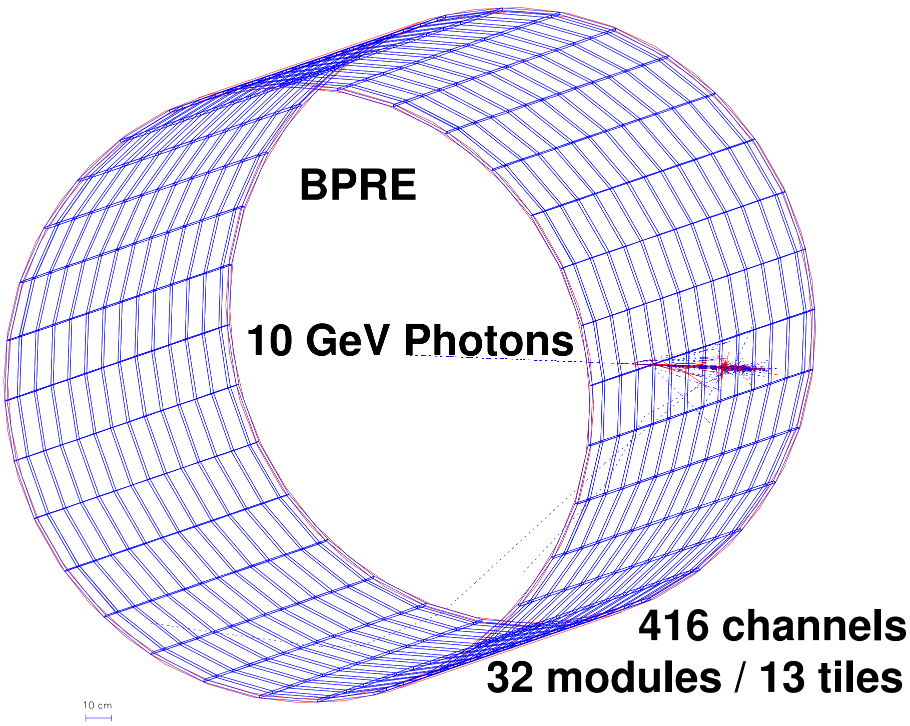

Figure 4.6: BPRE geometry generated by GEANT 3.16. The BPRE detector consists of 32 individual module containing 13 SCSN–38 plastic scintillator tiles oriented along the Z direction, installed directly in front of each of the 32 BCAL modules. The total BPRE channel is 416. As an example a 10 GeV photon generated at the interaction point and propagated to the BPRE module is shown.

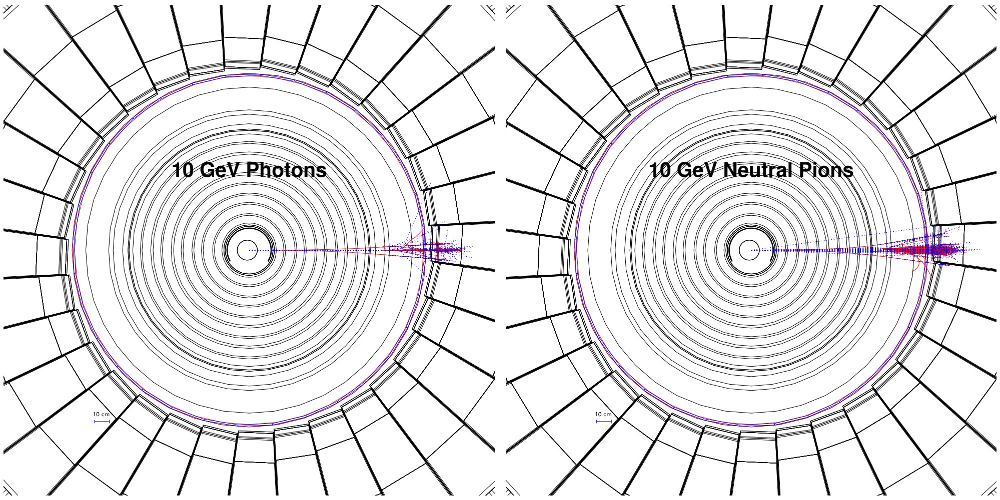

Figure 4.7: GEANT pictures of 10 GeV photons (left) and neutral pions (right) generated at the interaction point and propagated through the ZEUS detector to the BPRE/BCAL for a certain module. The BPRE cassette is seen in front of each BCAL module.

in the calorimeter to quantify the fraction of events with single photon showers. The second method, the conversion probability method, depends on the fact that multiple photons are more likely than single photons to produce an e^+e^- pair in the presampler.

In the BPRE proposal [62], use of the BPRE to identify photon conversions was postulated as a means of separating signals of prompt photons from π^0 backgrounds. This method relies on the ability of the BPRE to distinguish between zero, one, and two photon conversions in order to help classify candidates. Along with the shower shape analysis presently in use, it was seen as a largely complimentary approach that could enhance the selection of prompt photon candidates, especially at higher energies since the BPRE signal is not degraded by the spatial separation of the photon conversion products.

As a first look at the future analysis capabilities of the BPRE, a comparison of BPRE signals with the BCAL shower shape–dependent quantities used in the present analysis (see chapter 7 for details) has been made [64]. These are (1) the mean width $<\delta Z>$ of the BEMC cluster in Z and (2) the fraction f_{max} of the total cluster energy found in the most energetic cell in the cluster. These quantities are described in detail in chapter 7.2.

The data used here were obtained from e^-p running in 1999 at HERA, with $E_e = 27.5$ GeV, $E_p = 920$ GeV. The integrated luminosity is 11.87 pb^{-1}. The

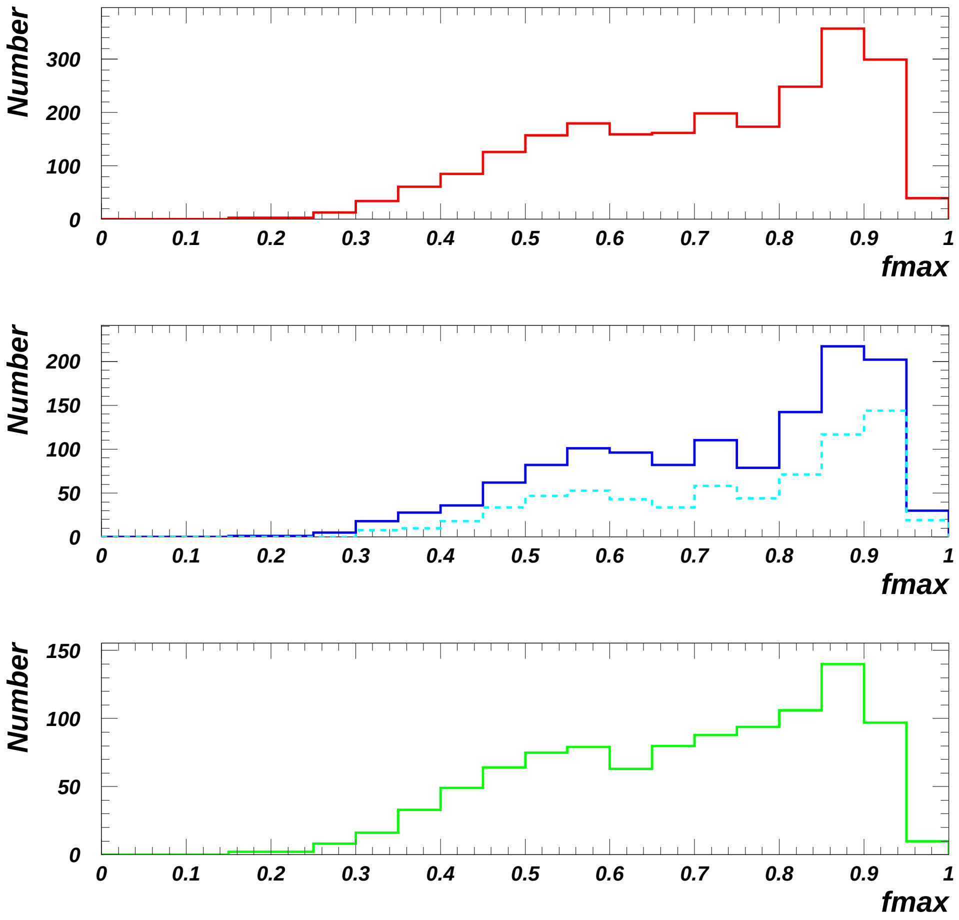

Figure 4.8: Prompt photon candidates in photoproduction [64]. Top : all candidates after $<\delta Z>$ cut to reduce η meson backgrounds, Middle : candidates after requiring a BPRE signal of less than 2.5 MIPS (solid) and candidates with BPRE signal of 0 MIPS (dashed), Bottom : candidates with BPRE signal greater than 2.5 MIPS.

event selection criteria are the same as those of 1996–1997 data analysis except for the uranium noise configuration in the ZEUS calorimeter. The details of the event selection procedure are presented in chapter 6. After event selection 2066 prompt photon candidates $E_T^\gamma > 5$ GeV in the region of pseudorapidity range $-0.7 < \eta^\gamma < 0.9$ remained.

The top plot in figure 4.8 shows the f_{max} distribution of prompt photon candidates after applying the $<\delta Z>$ cut; $<\delta Z> < 0.65$. From Monte Carlo studies, photons should peak strongly at high f_{max}, while π^0s exhibit an almost flat distribution with some peaking at values of about 0.6 and 0.9. The middle figure shows the f_{max} distribution after requiring a BPRE signal of less than 2.5 MIPS (solid line). Also shown (dashed line) is the distribution from 0 MIPS (no BPRE signal). The bottom plot is the resulting f_{max} distribution when the BPRE signal is greater than 2.5 MIPS. Note that the peak at high f_{max} is enhanced by the low BPRE MIP requirement while being suppressed by the high MIP cut.

A correlation between the BPRE signal and calorimeter–based variables designed to isolate prompt photon is seen. It is anticipated that in future prompt photon analyses, the BPRE will be used to enhance the ability to separate photons from π^0s, resulting in a larger prompt photon signal to π^0 background ratio.

Chapter 5

Monte Carlo Simulation

The aim of the measurements in this thesis is to make a comparison between measured data and the theoretical predictions. The theoretical calculation of the physics processes is achieved by the use of Monte Carlo event generators which simulate the leading–order hard subprocess and the effects of leading–logarithmic parton–showers. Monte Carlo event generators also include non–perturbative physics by use of appropriate phenomenological models and parameterisations of parton density functions in the calculation.

Monte Carlo techniques are not only used to simulate the physics processes, but are also required in describing the experimental measurement. In order to make a direct comparison between data and Monte Carlo model the measured data have to be corrected for detector acceptance and smearing effects before the comparison to the hadron level calculations. Knowing the true hadron level and detector level properties of the Monte Carlo events, such a correction can be made for the effect of the detector on the measured data. To simulate the detector response, events from the Monte Carlo generators are processed by the detector simulation program.

In this chapter the general features of Monte Carlo models and methods used in the study are discussed.

5.1 Event Generators

The main theoretical justification for QCD Monte Carlo simulation lies in the factorization theorems for hard QCD processes. The scheme of a Monte Carlo event generation for lepton–hadron collisions at HERA can be factorized into the following subprocesses;

- Hard Scattering Subprocess :

  This can be calculated analytically to fixed order in perturbation theory. The hard subprocess momentum transfer scale Q sets the boundary conditions for the initial and final state parton showers. At present, the matrix elements are implemented only to the first order in α_s, leading–order 2–to–2 processes, in current Monte Carlo models.

- Parton Showers :

  The perturbative parton emissions (gluon and photon) from the incoming and outgoing partons could give rise to potentially large corrections to the exact fixed–order matrix element treatment. These corrections become increasingly important as the available energy rises.
  In the Parton Shower approach, only the leading–log Q^2 approximation of the DGLAP evolution equation is used, which in turn allows us to simulate higher–orders. The parton shower evolution is terminated at a lower cut–off threshold, Q_0, which is typically ~ 1 GeV^2 for QCD radiation.

- Hadronization Process :

  In order to construct a realistic simulation one needs to convert the partons into hadrons. The hadronisation process takes place at low momentum transfer scale, and pQCD does not apply due to the large strong coupling constant, α_s at this scale. Instead a phenomenological hadronization model must be used to associate partons with hadrons.
  The main models at present are **string** and **cluster** hadronization models and are used in the Pythia and Herwig Monte Carlo event generators, respectively. In both cases, a parton shower initiated by the hard process evolves perturbatively, according to the DGLAP equation, until the scale of parton virtualities has fallen to some low value $Q_0 \sim 1$ GeV, whereupon the non-perturbative processes are assumed in the model to take over.

Two leading–logarithm parton shower Monte Carlo models, Pythia and Herwig, were used in this study. Both comprise a LO matrix element accompanied by higher order effects in the initial and final states together with hadronization. The main differences between the two LO Monte Carlo models lie in the evolution of the parton shower and the hadronisation model used.

5.2 The PYTHIA Monte Carlo Model

PYTHIA [65] is a general–purpose Monte Carlo event generator for particle production in e^+e^-, ep and pp interactions. Together it contains theory and models for a number of physics processes, including hard and soft interactions, parton distributions, initial and final state parton showers, multiple interactions, fragmentation and decay.

In PYTHIA, the evolution of the parton–shower is governed by the virtuality, Q^2. The angular ordering property of colour coherence is simulated by prohibiting non–ordered emission. In the case of photoproduction it uses the Weizsačker Williams Approximation (WWA) [10] to generate the photon spectrum for both direct and resolved processes.

The Lund string model [66] as implemented in JETSET [67] is used by PYTHIA to fragment partons into hadrons. This model is based on the dynamics of a relativistic string, representing the colour flux stretched between the initial $q\bar{q}$ produced in an e^+e^- collision. The string produces a linear confinement potential and an area law for matrix elements. The string breaks up into hadrons via $q\bar{q}$ pair production in its intense colour field. Gluons produced in the parton shower give rise to 'kinks' on the string. The model has extra parameters for the transverse momentum distribution and heavy particle suppression. It has some problems describing baryon production, but less than the cluster model.

The PYTHIA 5.7 and 6.1 MC versions are used for the inclusive prompt photon analysis in chapter 8 and for photon + jet analysis in chapter 9, respectively.

5.3 The HERWIG Monte Carlo Model

HERWIG (Hadron Emission Reactions With Interfering Gluons) [68] is a multi–purpose Monte Carlo event generator for high energy hadronic processes, with particular emphasis on the detailed simulation of QCD parton showers.

It uses the parton–shower approach using a coherent branching algorithm for initial–state and final–state QCD radiation in hard subprocesses. This parton shower algorithm implemented in HERWIG takes into account interference between soft gluons which gives rise to colour coherence in the parton shower. The coherence is included through the choice of evolution variables, ordering in which naturally restricts the branching phase space to an angular ordered region.

The HERWIG uses a cluster hadronization model with longitudinal splitting of high–mass clusters and soft underlying event to form a hadron. It is local in

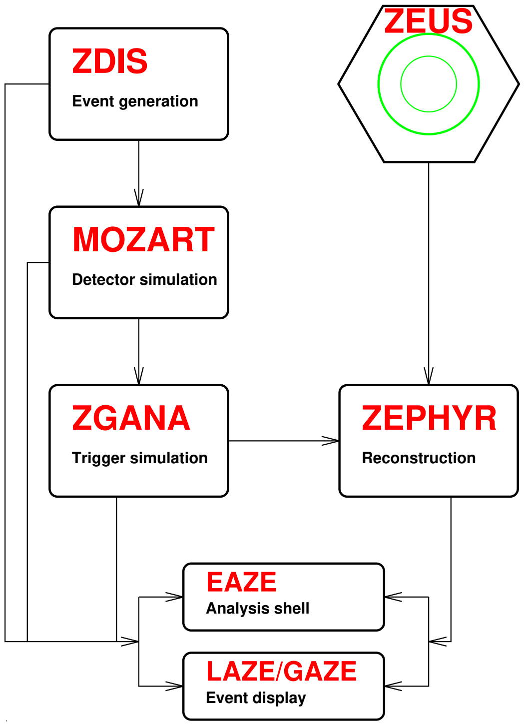

Figure 5.1: ZEUS offline and Monte Carlo chain

colour and independent of the hard process and the energy. After the perturbative parton shower, all outgoing gluons are split into quark–antiquark or diquark–antidiquark pairs. Then, all quarks are combined with their nearest neighbouring antiquark or diquark, to form a colour singlet cluster. The clusters thus formed are fragmented into hadrons. Light clusters are simply taken to be hadrons while heavier clusters decay isotropically into lighter hadrons.

The HERWIG 5.9 Monte Carlo is used throughout this thesis to check the Monte Carlo model–dependence.

5.4 Detector Simulation

The events from Monte Carlo generators have to be processed by the detector simulation and offline reconstruction chain before they can be compared with measured data. At ZEUS the detector simulation is carried out by MOZART (MOnte Carlo for ZEUS Analysis, Reconstruction and Trigger) which is based on the CERN GEANT [63] program package. It contains a detailed description of all the detector component materials and positions. MOZART simulates the passage of generated particles through the ZEUS detector including particle decay, energy loss into dead material and multiple scattering. To describe the development of hadronic showers, the program package GHEISHA is implemented. The ZEUS trigger decision on the signals is simulated by the ZGANA program [69].

Figure 5.1 shows the schematic diagram of processes which make up the ZEUS offline and Monte Carlo chain. Raw data from ZEUS detector or ZEUS detector (MOZART) and trigger (ZGANA) simulation programs is passed through the ZEUS physics reconstruction program (ZEPHYR) in order to reconstruct physics variables. The reconstruction of events runs through three phases:

1. Reconstruction of individual detector components.
2. Global track matching and vertex finding algorithm.
3. Particle identification.

The ADAMO (Aleph DAta MOdel) system is used in ZEUS event reconstruction and analysis for the design of data structure. Events are structured by grouping ADAMO tables into logical records called dataflows.

5.5 Monte Carlo Samples

Three types of Monte Carlo samples were employed in this analysis to simulate: (1) the LO QCD prompt photon processes, (2) dijet processes in which an outgoing quark radiated a hard photon (radiative events), and (3) single particles (γ, π^0, η) at high E_T. These are all subprocesses described in chapter 2. All generated events were passed through a full detector simulation chain, as described in the previous section, in order to simulate the ZEUS detector and trigger in the 1996–1997 running periods.

The PYTHIA 5.7/6.1 and HERWIG 5.9 Monte Carlo generators were both used to simulate the direct and resolved prompt photon processes. These generators include LO QCD subprocesses and higher–order processes modelled by initial and final–state parton showers. The MRSA proton parton density function (pdf) and the GRV–LO photon pdf were used. The minimum p_T of the hard scatter was set to 2.5 GeV and the maximum Q^2 set to 4 GeV^2. Initial and final–state QCD and QED radiation were employed. Multi–parton interactions were not implemented in the resolved samples since they are not expected to have a significant effect in the prompt photon photoproduction at HERA. The radiative event samples were likewise produced using direct and resolved photoproduction generators within PYTHIA and HERWIG.

	direct	resolved	radiative (dir)	radiative (res)
PYTHIA 5.7	136.1 pb^{-1}	138.5 pb^{-1}	127.6 pb^{-1}	54.4 pb^{-1}
HERWIG 5.9	146.7 pb^{-1}	150.9 pb^{-1}	62.9 pb^{-1}	41.5 pb^{-1}

Table 5.1: Integrated luminosity of the generated prompt photon Monte Carlo events.

	Single γ	Single π^0 meson	Single η meson	Single e^+
PYTHIA	100000	100000	100000	50000

Table 5.2: Single particle Monte Carlo samples.

The equivalent integrated luminosities of the prompt photon Monte Carlo samples generated by PYTHIA 5.7 and HERWIG 5.9 are listed in table 5.1. The Monte Carlo statistics are approximately four times that of the data.

In modelling the overall photoproduction process, the event samples produced for the separate direct, resolved and radiative processes were combined according to their total cross sections as calculated by the generators. A major difference between PYTHIA and HERWIG is the smaller radiative contribution in the HERWIG Monte Carlo model. Details of the result are given in chapter 8.

In order to reduce the Monte Carlo event generation time in the detector simulation, a special physics filter was introduced to select the prompt photon candidate events which are within an interesting kinematic region for the analysis. Photons with $E_T^\gamma > 3.5$ GeV and $|\eta^\gamma| < 2.0$ were selected. These requirements are safe enough to keep all prompt photon events which remain as a result of the offline analysis.

Three Monte Carlo single–particle data sets were generated using JETSET 7.3, comprising large samples of γ, π^0 and η–mesons respectively. The single particles were generated uniformly over the acceptance of the BCAL and with a flat transverse energy distribution between 3 and 20 GeV; E_T–dependent exponential weighting functions were subsequently applied to reproduce the observed E_T distributions. This gives a resonable representation of the pseudorapidity distribution of the photon candidate events. These samples are used in making the separation of signal and background using shower shapes in the calorimeter (see chapter 7 for details), and are also used to study the detector response of the photon and neutral mesons, e.g. photon transverse energy correction (see chapter 6 for details). The statistics of the single particle Monte Carlo samples above are listed in table 5.2.

	$k_0 = 0.44$	$k_0 = 1.0$	$k_0 = 1.5$	$k_0 = 2.0$	$k_0 = 3.0$
direct	135.0 pb^{-1}	129.8 pb^{-1}	123.6 pb^{-1}	120.7 pb^{-1}	113.1 pb^{-1}
resolved	162.2 pb^{-1}	158.9 pb^{-1}	157.8 pb^{-1}	156.3 pb^{-1}	151.2 pb^{-1}

Table 5.3: Integrated luminosity of the generated k_T enhanced non–fragmentation prompt photon Monte Carlo events using PYTHIA 6.1 (for the 1996–1997 ZEUS detector configuration).

	$k_0 = 0.44$	$k_0 = 1.0$	$k_0 = 1.5$	$k_0 = 2.0$	$k_0 = 3.0$
direct	328.0 pb^{-1}	315.0 pb^{-1}	328.0 pb^{-1}	323.0 pb^{-1}	310.0 pb^{-1}
resolved	38.9 pb^{-1}	36.4 pb^{-1}	38.7 pb^{-1}	36.9 pb^{-1}	34.8 pb^{-1}

Table 5.4: Integrated luminosity of the generated k_T enhanced fragmentation prompt photon Monte Carlo events using PYTHIA 6.1 (for the 1996–1997 ZEUS detector configuration).

5.5.1 Intrinsic k_T–enhanced Monte Carlo Samples

As different analyses are performed in chapter 9 in order to study the mean intrinsic parton transverse momentum, $<k_T>$, in the proton and the photon, additional prompt photon Monte Carlo sets with a higher intrinsic k_T values were generated using PYTHIA 6.1.

In the PYTHIA Monte Carlo model, the intrinsic $<k_T>$ of the partons in the proton and in the resolved photon can be parameterized by several functions ;

- Gaussian : $\mathrm{dN}/\mathrm{d}k_T^2 \propto e^{-k_T^2/k_0^2}$
- exponential : $\mathrm{dN}/\mathrm{d}k_T \propto e^{-k_T/k_0}$
- power–law : $\mathrm{dN}/\mathrm{d}k_T^2 \propto 1/(k_T^2 + k_0^2)$

where k_0 is a parameter which determines the hardness of the k_T distribution. The PYTHIA default value of k_0 for both the proton and the resolved photon is 0.44 GeV. An option in PYTHIA allows events to be generated using a different functional form for the k_T distribution and a different value of $<k_T>$. This option has been used to generate events with a higher $<k_T>$ values.

To generate the intrinsic k_T enhanced Monte Carlo samples, we used a Gaussian formula and the parameter k_0 (two–dimensional Gaussian width) of the proton varied between 0.44 and 3 GeV, where the mean absolute value of the intrinsic

	resolved (non–fragmentation)	resolved (fragmentation)
k_0 = (1.0,1.0)	153.0 pb^{-1}	36.05 pb^{-1}
k_0 = (1.5,1.0)	153.5 pb^{-1}	36.35 pb^{-1}
k_0 = (1.5,1.5)	147.0 pb^{-1}	33.20 pb^{-1}
k_0 = (2.0,1.0)	150.3 pb^{-1}	35.80 pb^{-1}
k_0 = (2.0,1.5)	146.0 pb^{-1}	33.50 pb^{-1}
k_0 = (2.0,2.0)	144.0 pb^{-1}	30.11 pb^{-1}
k_0 = (3.0,1.0)	146.2 pb^{-1}	32.40 pb^{-1}
k_0 = (3.0,1.5)	143.0 pb^{-1}	30.50 pb^{-1}
k_0 = (3.0,2.0)	140.7 pb^{-1}	27.50 pb^{-1}
k_0 = (3.0,3.0)	137.7 pb^{-1}	22.62 pb^{-1}

Table 5.5: Integrated luminosity of the generated k_T enhanced resolved prompt photon Monte Carlo events using PYTHIA 6.1 (for the 1996–1997 ZEUS detector configuration). For example k_0 = (3.0,2.0) means 3 GeV k_0 in the proton and 2 GeV k_0 in the photon.

parton momentum, $<k_T>$, is given by $<k_T> = \sqrt{\pi/4}k_0$. The k_0 in the resolved photon was fixed at the PYTHIA 6.1 default value of 0.44 GeV. An additional upper cut–off value for the intrinsic k_T has been applied for each value of k_0. The Monte Carlo statistics of the intrinsic k_T enhanced samples are listed in table 5.3 and 5.4.

We also generated additional Monte Carlo sets with different combinations for the intrinsic k_T values for both the proton and photon. (see table 5.5)

Chapter 6

Reconstruction and Event Selection

In this chapter we present the details of the reconstruction and event selection procedure for the analysis presented in this thesis. The data were obtained from e^+p running in 1996–97 at HERA, with $E_e = 27.5$ GeV and $E_p = 820$ GeV, corresponding to a centre of mass energy of $\sqrt{s} = 300$ GeV.

The major detector components in the analysis are the central tracking detector (CTD) and the uranium calorimeter (UCAL). A description of the ZEUS detector can be found in detail in chapter 3. Prompt photons are detected in the barrel section of the calorimeter, as seen in figure 6.1 and 6.2. It enables a partial discrimination between single photon signals and the decay products of neutral mesons. A typical high–E_T photon signal is observed in a small cluster of BEMC cells, with no associated CTD track. Possible such signals are referred to as prompt photon candidates.

Examples of prompt photon candidates from direct and resolved processes, as recorded in the ZEUS detector are shown in figure 6.1 and 6.2 respectively. Here the energy and position measurements of the UCAL and CTD for the event are displayed in three different views, shown in a plane parallel on the left, a rapidity–azimuth lego plot of transverse energy on the upper right and a view along the beam axis on the lower right. The shaded areas in the calorimeter indicate energy deposits. The prompt photon candidate is clearly identified in the upper half of the segmented uranium calorimeter and well isolated.

The fundamental signature of data samples used in the present study consists of (1) the isolated high E_T photon candidate (Inclusive prompt photon samples) and (2) a prompt photon accompanied by a balancing high E_T jet (Prompt photon + jet samples).

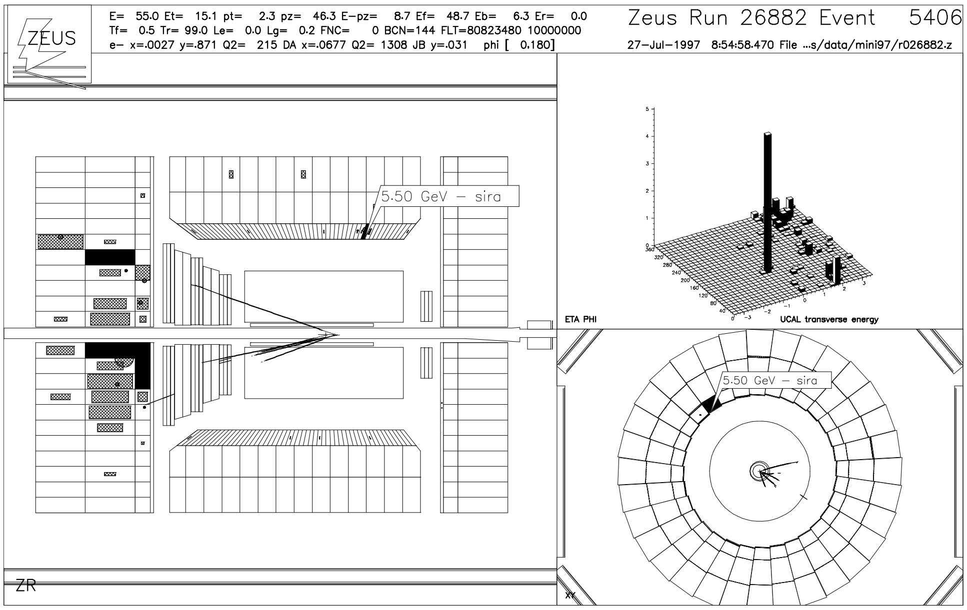

Figure 6.1: An example of a direct process prompt photon candidate. The prompt photon event is clearly identified in the uranium calorimeter and well isolated. The hadronic objects can be seen at the opposite ϕ direction to the photon. The energy flow around the FCAL beampipe is due to the proton remnant.

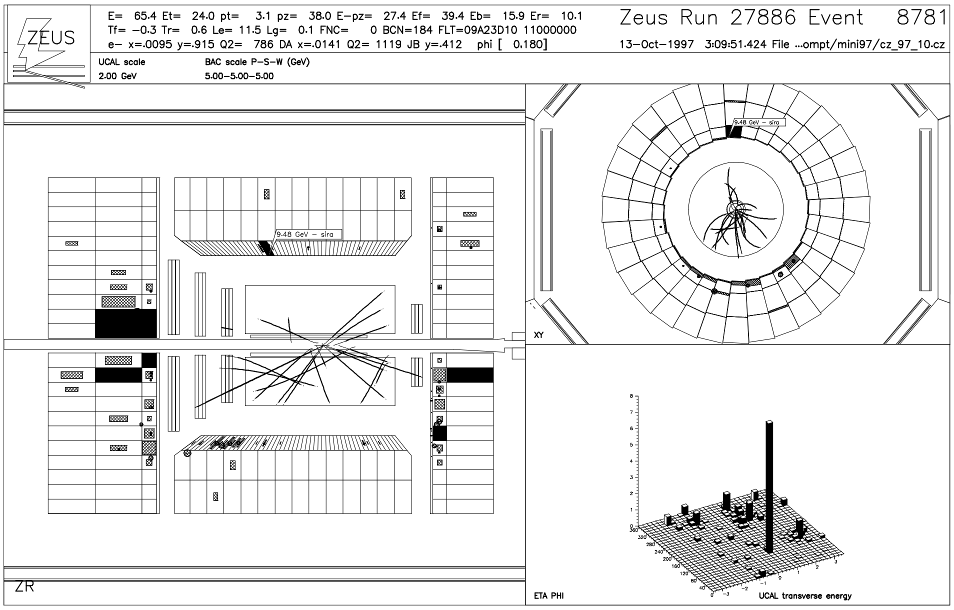

Figure 6.2: An example of a resolved process prompt photon candidate. The prompt photon event is clearly identified in the uranium calorimeter and well isolated. The energy flow around the FCAL and RCAL beampipe is due to the proton remnant and photon remnant respectively.

The algorithms used to find photons and jets are first discussed in section 6.1 and 6.2 respectively. In this chapter, we also discuss the event reconstruction and online / offline data selection criteria specific to this studies. In case of inclusive prompt photon analysis, the offline event selection cuts are the almost same as the photon + jet analysis except without the requirement of jet candidates.

6.1 Reconstruction of Photon

To identify the photon candidates in the offline analysis, the EEXOTICS [70] electron finder was used. This was selected as having been adapted from the ELEC5 [71] finder with the purpose of identifying deep inelastic scattered electrons in a wide energy region. Since the EEXOTICS finder does not require any track information, this electron finding algorithm can be used to identify the events with neutral electromagnetic shower characteristics such as a photon.

The virtue of the the EEXOTICS finder is good efficiency for finding photon signals in the kinematic region we are concerned with in this analysis.

6.1.1 Photon finding algorithm

The photon finding algorithm with the EEXOTICS finder collects the energy depositions from individual calorimeter cells and creates calorimeter objects using a cone algorithm. The EEXOTICS photon finding algorithm can be divided into the following steps ;

1. Seed cells finding :

The 10 highest energy EMC cells with energy above 1.0 GeV are considered "seed" cells, one for each photon. If the angle between two such cells was less than 12°, only the higher energy seed cell is further considered.

2. Cone assignments :

For each seed cell, the following cone assignments and cone cuts for assignment of calorimeter cells to a cluster are considered. The angles are measured relative to the seed cells.

- EMC inner region : EMC energy within a cone of radius 0.25 [rad]

- EMC outer region : EMC energy between cones of radii 0.25 and 0.4 [rad]
- HAC1 inner region : HAC1 energy within a cone of radius 0.3 [rad]
- HAC2 inner region : HAC2 energy within a cone of radius 0.3 [rad]

3. Calculation of e quality factor :

The following quantities are calculated for all remaining seed cells. These quantities were chosen and cone radii were tuned to distinguish between a compact electromagnetic shower and a broad hadronic shower.

- Energy weighted radius of EMC energy within a cone of radius 0.25 [rad]
- Ratio of EMC energy in an outer cone and inner cone.
- Ratio of HAC1 energy and EMC + HAC1 energy in an inner cone.
- Ratio of HAC2 energy and EMC + HAC2 energy in an inner cone.

The above 4 quantities were used to calculate an electron quality factor for a given candidates using the probability functions, P1, P2, P3 and P4. The electron quality factor is calculate as ;

$$\text{Quality factor} = \text{P1} \times \text{P2} \times \text{P3} \times \text{P4} \tag{6.1}$$

A candidate is rejected if its quality factor is less than 10^{-8}.

4. Selection of EM cluster :

The final candidates are selected if they satisfy the following conditions.

- Number of cells ≤ 35
- log_{10}(Quality factor) > -8
- $E_e = E_{EMC} + E_{HAC1} + E_{HAC2} > 2$ GeV
- $(E_{HAC1} + E_{HAC2})\ /\ E_e < 0.1$ for $0 <$ imbalance of seed cell < 0.2

Finally the position $(\eta,\ \phi)$ of the candidate is calculated based on energy sharing between cells and PMT energy imbalance within cells.

If there is more than one candidate surviving the cuts, they are ordered according to quality factor and are considered as prompt photon candidate events.

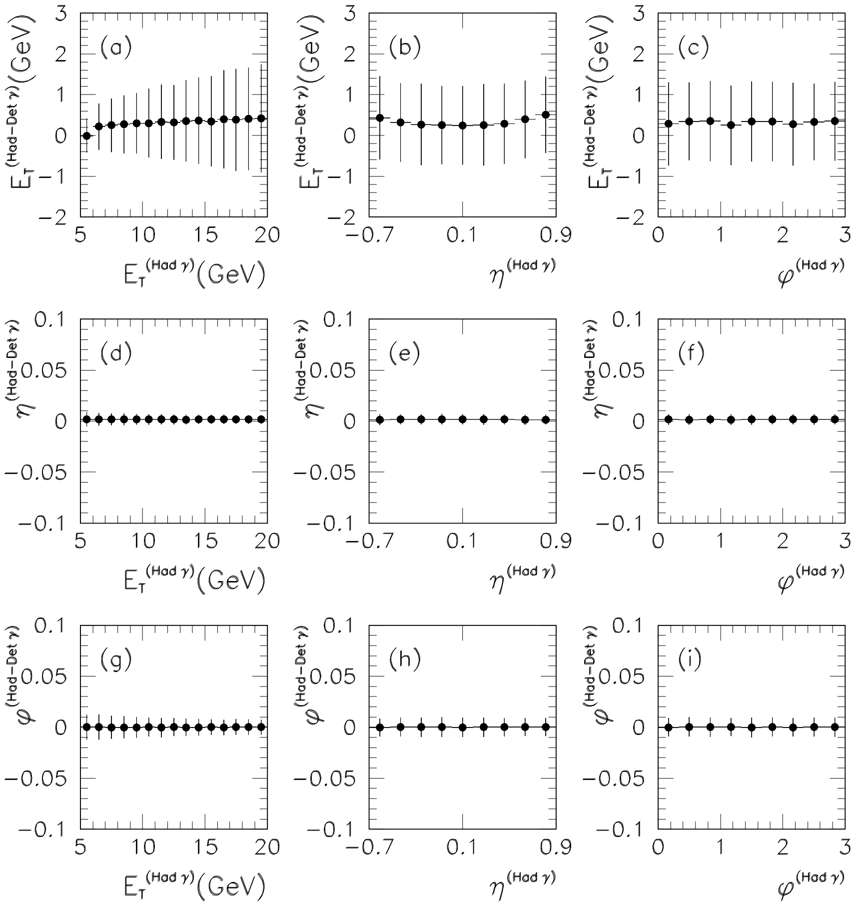

Figure 6.3: The correlation of the difference between detector and hadron level quantities with η, φ and E_T^{det} shown for PYTHIA events. (a), (b), (c) ΔE_T vs E_T^{det}, η, φ; (d), (e), (f) $\Delta\eta$ vs E_T^{det}, η, φ; (g), (h), (i) $\Delta\varphi$ vs E_T^{det}, η, φ. The points show the mean of the distributions and the error on the mean.

6.1.2 Photon transverse energy correction

The aim of the photon transverse energy correction is to correct the measured ZEUS data to hadron level, enabling comparisons with QCD predictions. Ideally, a detector would be able to measure particle positions and energies exactly. However detectors have finite angular and energy resolutions and other factors such as energy losses in dead materials in the detector. Such incompleteness of the detector makes the physical variables reconstructed with the raw calorimeter information different from the true hadronic variables.

A correction to the measured photon energy was established by means of a MC comparison between the generated and detected energies of single photons distributed over the calorimeter. Figure 6.3 show the correlation of the difference

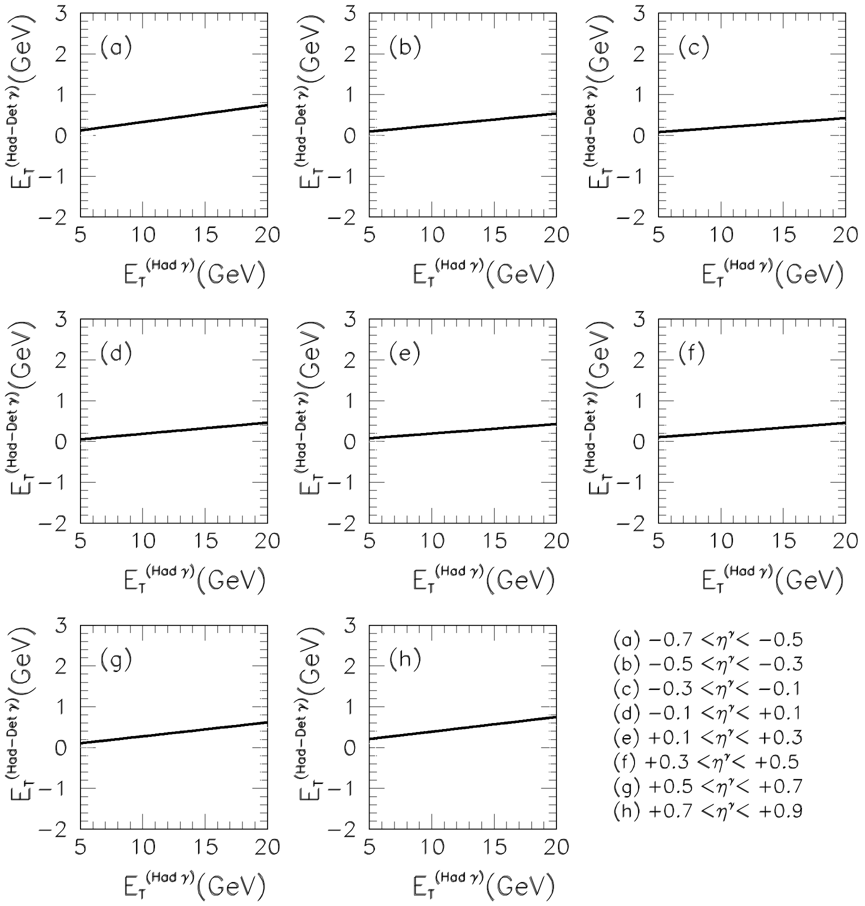

Figure 6.4: The profile of the transverse energy differences between hadron level and detector level photon and fit to the profile. $E_T^{had-det}$ vs E_T^{had} fitted by a function $E_T^{det} = A + B\dot{E}_T^{had}$ to obtain the photon energy correction functions.

between η, ϕ and E_T for matching pairs of detector and hadron level photons. The angular variables (η, ϕ) are well correlated between detector and hadron level photons in η, ϕ and E_T with no systematic shift. No corrections are required for these angular variables.

Figure 6.3 (a)–(c), however, shows that the photon E_T measured in the calorimeter is systematically lower than the true value. Such a systematic shift on the detector level photon E_T must be corrected to the hadron level.

In figure 6.4, the quantity E_T^{had}–E_T^{det} is plotted as a function of E_T^{had}, where E_T^{had} and E_T^{det} refer to the photon E_T at the hadron and detector level respectively. The event sample is divided into 8 bins of photon pseudorapidity according to the resolution. In each bin of photon pseudorapidity the distributions are fitted with a function of the linear form ;

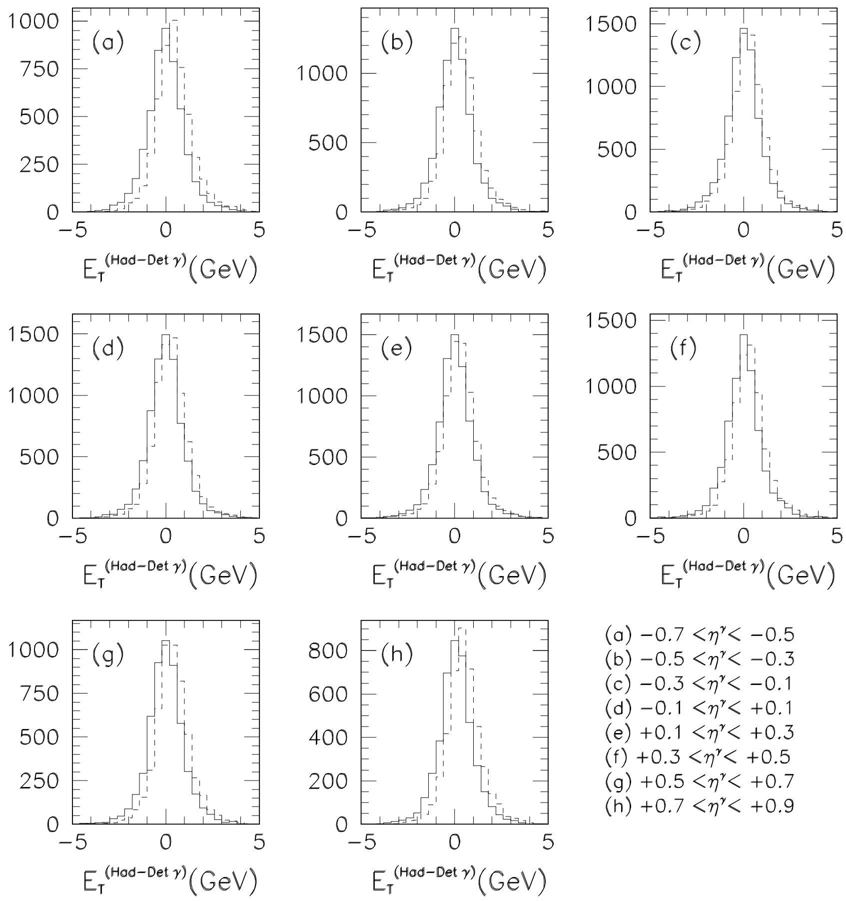

Figure 6.5: The distribution of E_T^{had} - E_T^{cor} (solid line) and E_T^{had} - E_T^{det} (dotted line). The E_T correction procedure was applied for prompt photon MC (PYTHIA). The eight profile plots correspond to each bin of photon rapidity. The scale of E_T is in GeV.

$$E_T^\gamma(had) - E_T^\gamma(det) = A \times E_T^\gamma(had) + B \tag{6.2}$$

from which the corrected E_T of photon, referred to as $E_T^\gamma(cor)$, is obtained ;

$$E_T^\gamma(cor) = \frac{E_T^\gamma(det)}{1-A} + \frac{B}{1-A} \tag{6.3}$$

Figure 6.4 also shows that reasonably good fits to the distributions are obtained. This correction amounted typically to 200–400 MeV in the $-0.7 < \eta^\gamma < 0.9$. Figure 6.5 shows the plots of E_T^{had}–E_T^{cor} and E_T^{had}–E_T^{det} in different bins of photon pseudorapidity and displays two different lines, a solid line for after the photon E_T correction and a dotted line for before the photon E_T correction. It shows that E_T^{cor} is closer to E_T^{had} than E_T^{det}. This photon E_T correction affects the acceptance correction slightly. As a result we get correction factors which are a little closer to 1.0. The resolutions for each bin of photon pseudorapidity show how well the hadron level photon E_T is reproduced by the corrected photon E_T using the methods described above.

After the photon energy correction the events were retained for final analysis if a photon candidate with transverse energy $E_T^{\gamma} > 5$ GeV was found in the kinematic region of pseudorapidity $-0.7 < \eta^{\gamma} < 0.9$.

6.2 Reconstruction of Jet

Since a jet is not a fundamental QCD object it is necessary to find an exact definition. Jets observed in hadronic final states are features of the event which are expected to correspond closely to the kinematics of the final state partons produced in the hadronic interaction. Experimentally a final state quark or a gluon forms an observable jet in the detector.

To enable comparison of results between experimental data and theory it is important to use standard jet finding algorithms. The 1990 Snowmass Workshop [72] stated that any jet definition should be simple to implement in an experimental analysis and in theoretical calculations, should be defined at any order of perturbation theory, and should yield a finite cross section at any order of perturbation theory that is also relatively insensitive to hadronisation.

On the experimental side, jets can be found by means of standard jet finding algorithms and then reconstructed using the information from calorimeter cells or (and) tracks in the tracking detector. In theoretical calculations, jets can be found from partons in the the hard subprocess (parton level) or, using events from hadronisation shower MC models, final state hadrons (hadron level). In order to compare experimental data meaningfully with theoretical predictions it is essential to have a good correspondence between jets at all levels. An important aspect of this is that the chosen jet definition should be applied to experimental and theoretical quantities in a consistent way.

6.2.1 Jet finding Algorithms

Two types of algorithm are available to define a jet: a cone algorithm in accordance with the Snowmass Convention and a clustering algorithm which combines objects with small relative transverse energy into jets. Detailed discussions of each of these can be found elsewhere [73], so only a brief description of two jet finding algorithms is given below.

The longitudinally invariant K_T clustering algorithm KTCLUS has been used in this analysis as it is well defined and free of singularities to all orders.

Cone Algorithms

Cone algorithms search for a jet by looking at a cone of fixed radius, R_0, in the $\eta - \varphi$ plane which contains a maximum transverse energy of hadrons or calorimeter cells. These are the type of jet finding algorithms used in hadron–hadron collisions. The Snowmass Convention defines the jet recombination scheme for the transverse energy and the angular variables, $\eta - \varphi$, of a jet as:

$$E_T^{jet} = \sum_i E_{Ti}$$

$$\eta^{jet} = \frac{1}{E_T^{jet}} \sum_i E_{Ti}\eta_i$$

$$\varphi^{jet} = \frac{1}{E_T^{jet}} \sum_i E_{Ti}\varphi_i$$

where the sum runs over all hadrons, and calorimeter cells within the jet cone radius, R_0, defined as ;

$$R_i = \sqrt{(\eta_i - \eta_{jet})^2 + (\varphi_i - \varphi_{jet})^2} \leq R_0$$

Here φ_i and η_i are the azimuthal angle and pseudorapidity of the cell. In general a jet cone radius of R_0=1 is taken for the cone algorithms, although the detailed properties of jet merging and seed finding are not defined with the Snowmass Convention.

EUCELL [74] is an adaptation of another cone jet algorithm used at ZEUS. It uses the concept of pre–clustering. In EUCELL, clusters are determined using a grid in $\eta - \phi$ space. The size of the cells that make up the grid is determined such that $\Delta\eta^{gridcell} \approx \Delta\phi^{gridcell} \approx R/2$. By then sliding a 3×3 cell window over the grid, potential pre–clusters are formed. The Snowmass parameters are calculated. A cone of radius R is then placed around the pre–cluster and an iterative process is performed. The first jet is defined as the cone with the highest transverse energy. Successive jets are then determined from the remaining objects by the same procedure until there exist no more cones above a certain energy threshold.

Clustering Algorithms

Clustering algorithms have been widely used for many years in e^+e^- collisions and differ significantly from cone algorithms. The cone algorithms as discussed above can lead to ambiguities. The treatment of overlapping jets is not defined within the Snowmass convention, nor is the question of seed finding for the initial jets. This leads to theoretical ambiguity with respect to jet merging in the final state and the process is not always infra–red safe at NNLO without modification [75].

These problems are avoided by the use of the K_T clustering algorithm, as the merging criterion is completely defined for any given final state. As such, in the present analyses we avoid the problems inherent in the use of the cone algorithm and use only the K_T algorithm [76].

For a cluster algorithm we must specify some distance measure which determines which particles will be merged, together with a recombination scheme which defines how they will be merged. In photoproduction we run the algorithm in the laboratory frame using the inclusive recombination scheme of Ellis and Soper [77] in a mode which is invariant under longitudinal boosts, the recombination scheme being similar to that of the Snowmass Convention (the so-called "p_T" mode). The algorithm depends on a chosen parameter R which is analogous to a cone radius.

To decide which particles should be merged, for each particle i we form the quantity,

$$d_i = E_{T,i}^2$$

and for each pair of particles, ij, we form the quantity

$$d_{ij} = \min(E_{T,i}^2, E_{T,j}^2)\left[(\eta_i - \eta_j)^2 + (\phi_i - \phi_j)^2\right]/R^2.$$

The d_i is the limiting case of small angles of the "distance" between particle i and a large mass remnant travelling along the z direction.

If the smallest of all the d values is a d_{ij}, the particles i and j are merged into a single object, k. If however, the smallest value is a d_i then this particle is considered "complete" and is removed from further clustering. This process is then repeated until all the objects have been removed, producing an E_T ordered list of objects.

The scheme for merging the objects is similar to the Snowmass Convention, and is,

$$E_{Tij} = E_{Ti} + E_{Tj}$$

$$\eta_{ij} = \frac{E_{Ti}\eta_i + E_{Tj}\eta_j}{E_{Tij}}$$
$$\varphi_{ij} = \frac{E_{Ti}\varphi_i + E_{Tj}\varphi_j}{E_{Tij}}$$

Therefore the scheme assigns objects to jets in a well-prescribed manner, and as each quantity $E_T, \Delta\eta, \Delta\phi$ in the distance parameter is invariant under longitudinal boosts, so the property of boost invariance of the jet finding itself is retained.

6.2.2 Jet reconstruction methods

There are several different jet reconstruction modes for running the KTCLUS algorithm. To investigate the momentum balance between a photon and a jet system for the study of parton behaviour in the proton and photon, (see chapter 9.10) it is necessary to treat the jet as a strictly relativistic object. In other words, the jet algorithm has to be applied correctly to the four–momenta of the true final state hadrons or of the outgoing partons from a hard interaction. Then it can be used in the calculations for intrinsic k_T–sensitive kinematic variables.

There are two different recombination schemes of a jet. In the "energy scheme", the 4–momentum of a jet is the sum of the four momenta of the particles in it. The jet is therefore massive. In the "p_T scheme", the jet mass is normally ignored. To look at the difference between "energy"and "p_T" in the recombination scheme, both schemes were tested as a systematic check for jet finding. (See chapter 9.10 for details)

In our analysis we used the "p_T scheme" to get the jet E_T properly and hence to correct the jet energy. However the momentum components of the objects comprising the jet were summed to obtain the total momentum vector in order to avoid any effects due to the Snowmass averaging. For greater accuracy jets were then reconstructed using energy flow objects, ZUFOS [78], which combines information from the calorimeter cells and tracks. The ZUFOS calculation matches track to calorimeter cell clusters and uses the track energy instead of that of the matched calorimeter cells when the track energy is better measured.

6.2.3 Jet transverse energy correction

In order to estimate the correction of the reconstructed jet transverse energy, the η^{jet}, ϕ^{jet} and E_T^{jet} variables for the hadron and detector level jet in PYTHIA

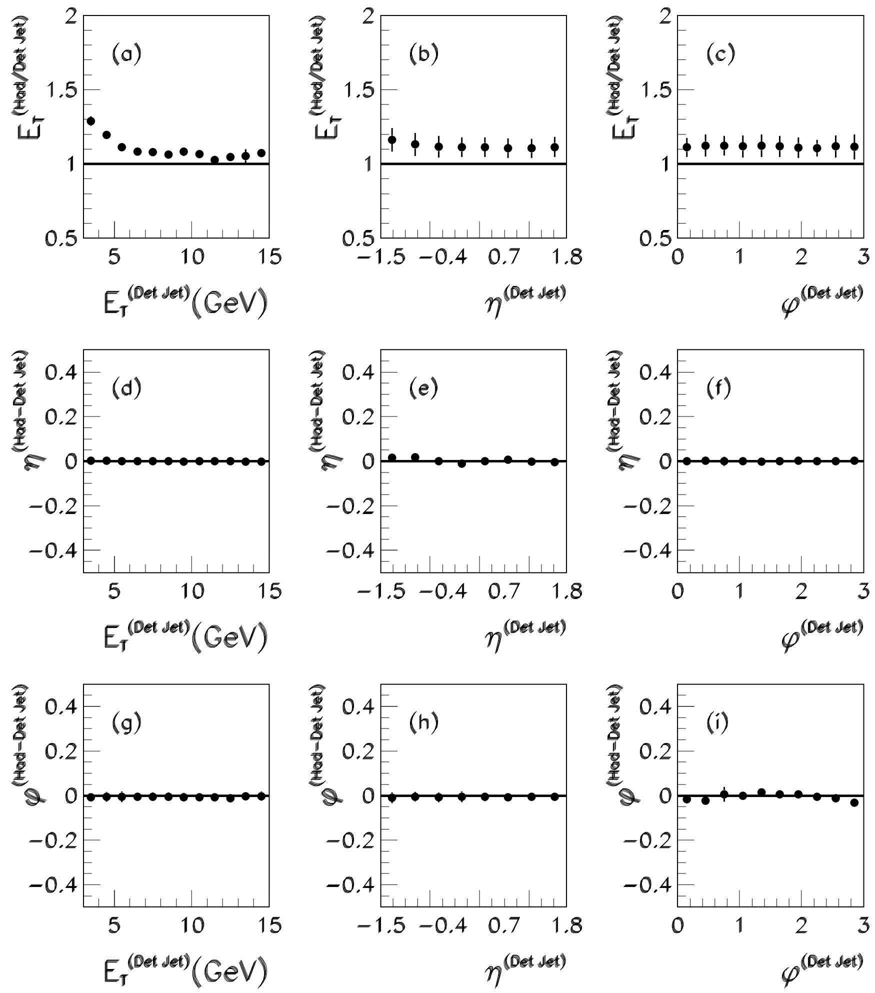

Figure 6.6: The correlation of the difference between detector and hadron level quantities with η, φ and E_T^{det} shown for PYTHIA events. (a), (b), (c) ΔE_T vs E_T^{det}, η, φ; (d), (e), (f) $\Delta\eta$ vs E_T^{det}, η, φ; (g), (h), (i) $\Delta\varphi$ vs E_T^{det}, η, φ. The points show the mean of the distributions and the error on the mean.

MC samples have been compared. The KTCLUS algorithm was applied in the inclusive mode, to the ZUFOS. Jets accompanying a photon were selected at both hadron and detector level of;

- $5 < E_T^{\gamma} < 10$ GeV and $-0.7 < \eta^{\gamma} < 0.9$
  $E_{T,det}^{jet} > 3$ GeV and $-1.5 < \eta^{jet} < 1.8$
- $5 < E_T^{\gamma} < 10$ GeV and $-0.7 < \eta^{\gamma} < 0.9$
  $E_{T,had}^{jet} > 5$ GeV and $-1.5 < \eta^{jet} < 1.8$

In this way the E_T^{jet} correction is obtained from events which are representative of the final selection for the analysis. The detector level jets and hadron level jets

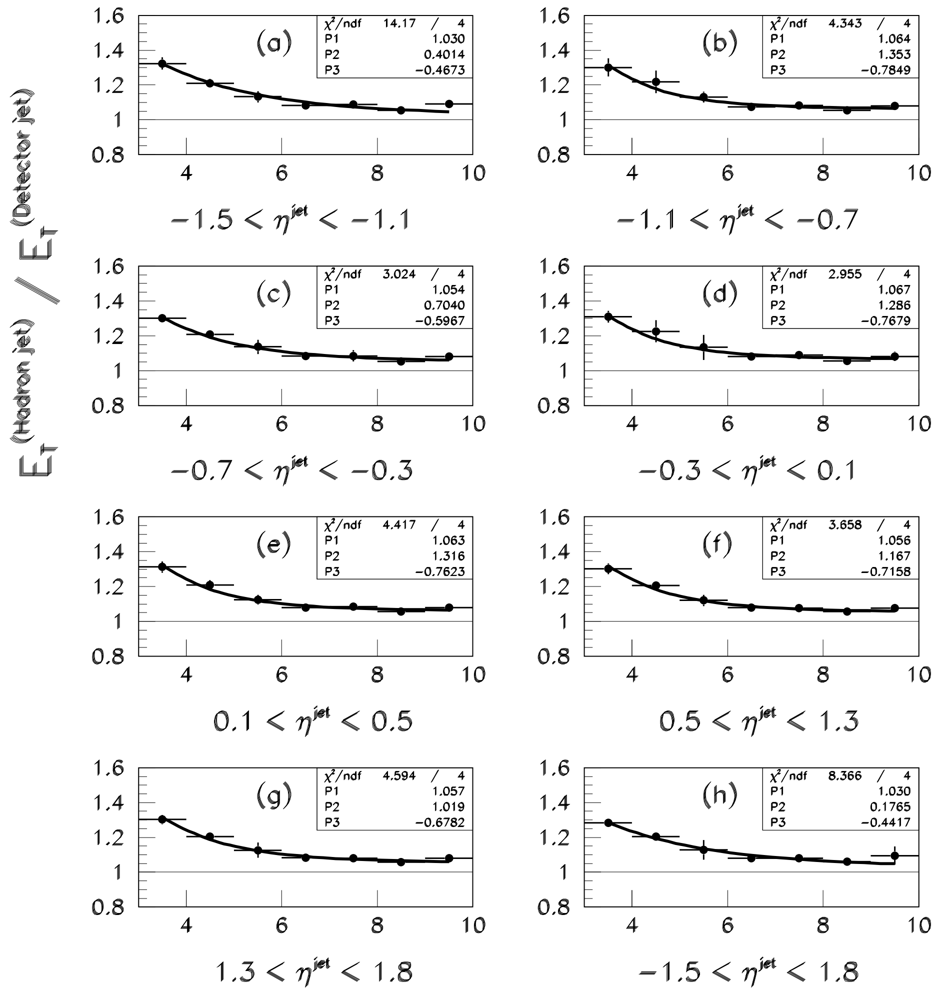

Figure 6.7: E_T^{had}/E_T^{det} in bins of E_T^{det} fitted by a function $E_T^{cor}(E_T^{det}, \eta^{det}) = C(E_T^{det}, \eta^{det}) \cdot E_T^{det}$ to obtain the jet energy correction functions from PYTHIA events. Points are plotted at the mean of the bin.

are then matched in (η–ϕ) space when

$$\Delta R(\eta, \phi) \equiv \sqrt{(\eta^{cal} - \eta^{had})^2 + (\phi^{cal} - \phi^{had})^2} \tag{6.4}$$

is a minimum and $\Delta R(\eta, \phi)$ is less than one.

Once pairs of matched detector and hadron level jets have been found the differences in the angular and energy variables can be studied. Figure 6.6 show the correlation of the difference between η, ϕ and E_T for matching pairs of detector and hadron level jets. The angular variables (η, ϕ) are well correlated between detector and hadron level jets on η, ϕ and E_T with no systematic shift. No corrections are required for these angular variables. The figure 6.6 (a)–(c), however,

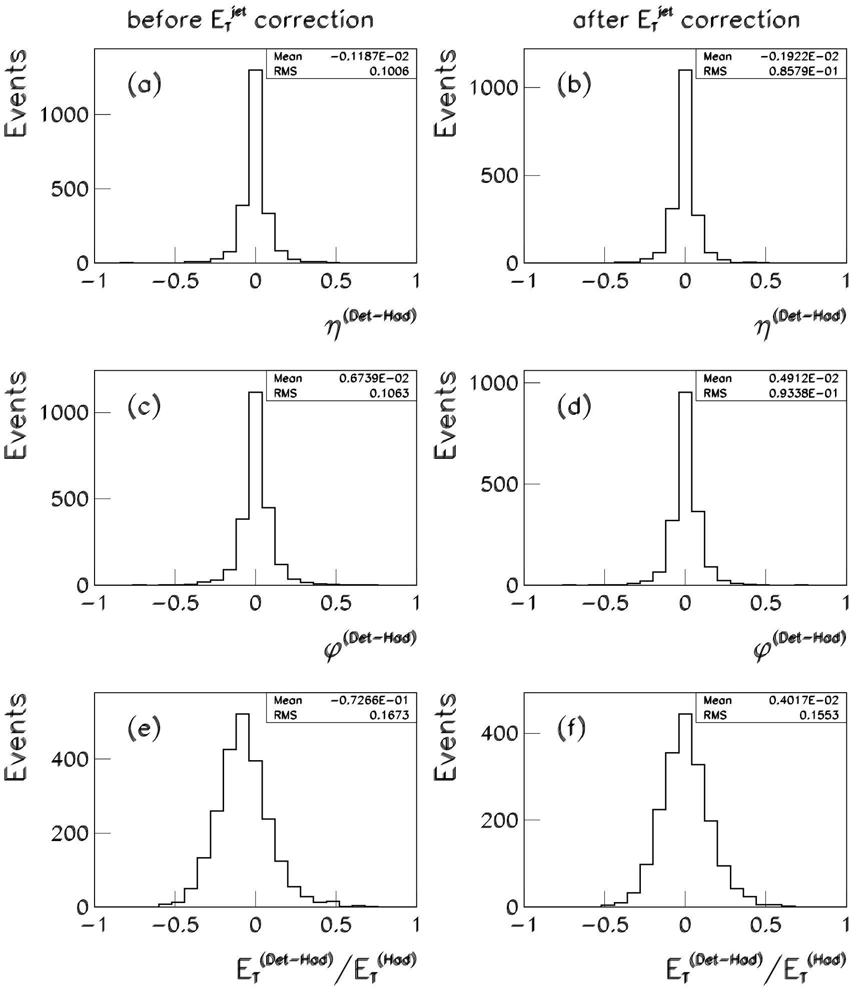

Figure 6.8: Correspondence between hadron and detector level η, φ and E_T of jet. Resolutions for (a) η, (c) φ and (e) E_T before jet energy correction. Resolutions for (b) η, (d) φ and (f) E_T after jet energy correction.

showed that the jet E_T measured in the calorimeter is systematically lower than the true value, presumably due to the energy loss in dead material in front of the calorimeter and in the FCAL–BCAL and RCAL–BCAL boundaries.

Figures 6.8 (a), (c) and (e) show the resolution plots before the jet transverse energy correction, indicating how well the quantities for hadron level jets are reproduced by the detector variables. Again it can be seen that the angular variables η and ϕ are well correlated between the detector and hadron level with no systematic shift and good resolution. The jet transverse energy, on the other hand, shows a systematic shift as seen in figure 6.7 (a)–(c). The resolution for jet E_T is about 16 %. Such a systematic shift on the detector level jet E_T must be corrected to that of hadron level.

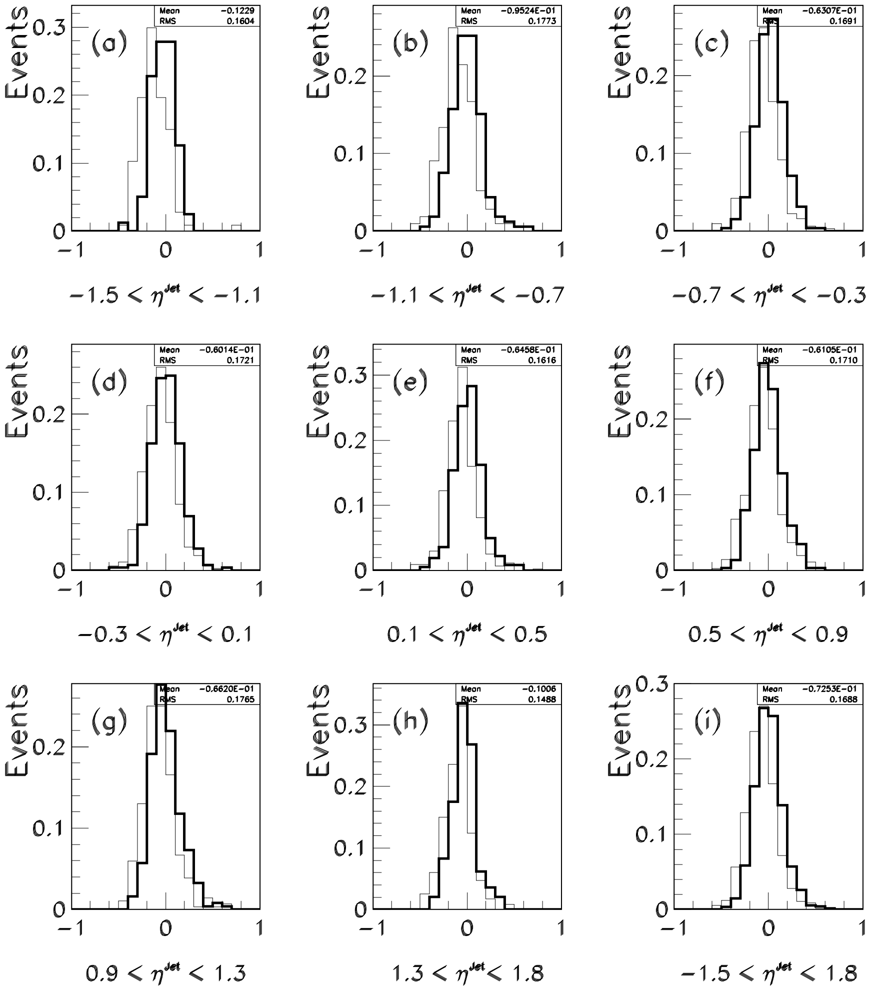

Figure 6.9: The distribution of E_T^{had} - E_T^{cor} (solid line) and E_T^{had} - E_T^{det} (dotted line). The E_T correction procedure was applied for prompt photon MC (PYTHIA). The eight profile plots correspond to each bin of photon rapidity. The scale of E_T is in GeV.

Since the jet transverse energy varies with the jet pseudorapidity and jet energy, correction factors to the measured jet transverse energies were evaluated through the use of Monte Carlo event samples with the following form ;

$$E_T^{cor}(E_T^{det}, \eta^{det}) = C(E_T^{det}, \eta^{det}) \cdot E_T^{det} \tag{6.5}$$

where E_T^{cor} is the corrected transverse energy of the jet.

In Figure 6.7, E_T^{had}/E_T^{det} quantity is plotted as a function of E_T^{had} in bins of jet pseudorapidity for matched detector and hadron level jets, where E_T^{had} and The E_T^{det} refer to the jet E_T at hadron and detector level respectively. For a given bin in jet pseudorapidity, the distributions are fitted with a function of the form ;

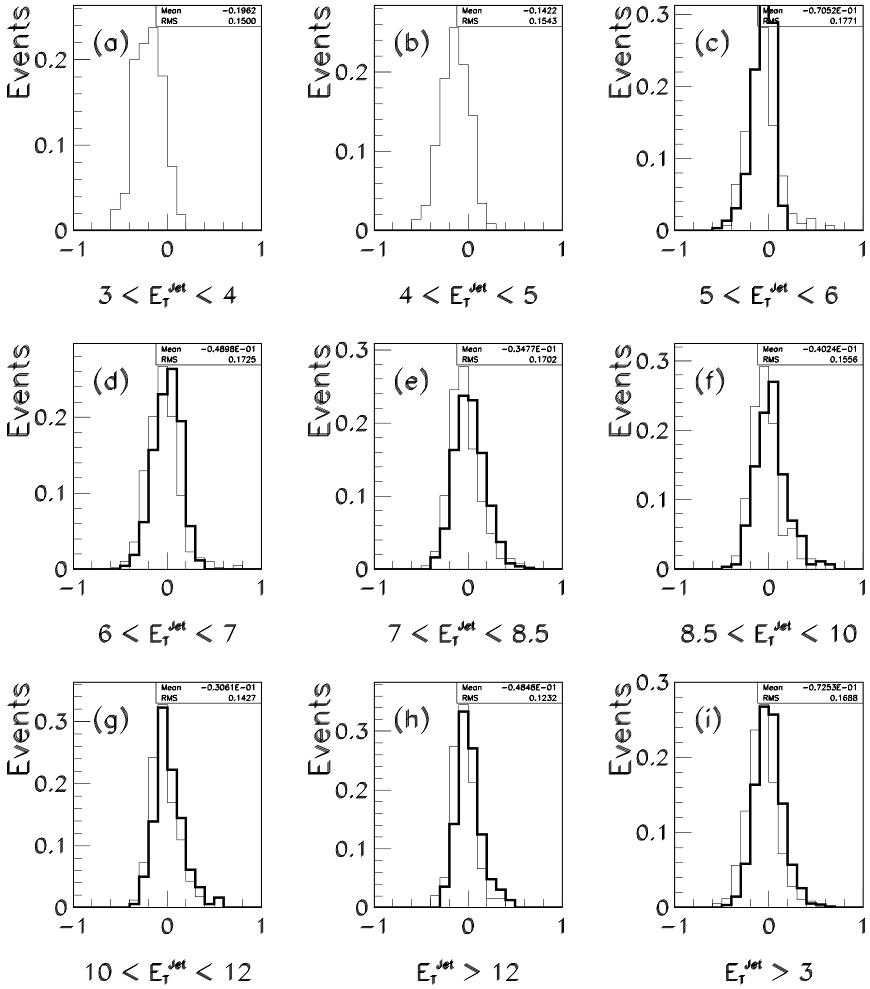

Figure 6.10: The distribution of E_T^{had} - E_T^{cor} (solid line) and E_T^{had} - E_T^{det} (dotted line). The E_T correction procedure was applied for prompt photon MC (PYTHIA). The eight profile plots correspond to each bin of photon E_T. The scale of E_T is in GeV.

$$C(E_T^{det}, \eta^{det}) \equiv A + exp(B + C \cdot E_T^{det}) \tag{6.6}$$

Figure 6.7 also shows that reasonably good fits to the distributions are obtained. This correction amounted typically to 1 GeV in the $-1.5 < \eta^{\gamma} < 1.8$.

The normalised distribution of E_T^{had}–E_T^{det} can be seen in figure 6.9 and 6.10. It shows the jet E_T resolution (a) before (thin line) and (b) after (thick line) application of the jet E_T correction obtained in figure 6.7. In figure 6.9, the resolutions for each bin of jet pseudorapidity demonstrate how well the hadron level jet E_T is reproduced by the corrected jet E_T using the methods described above. The scale of jet E_T is GeV. In addition, figure 6.10 shows the same

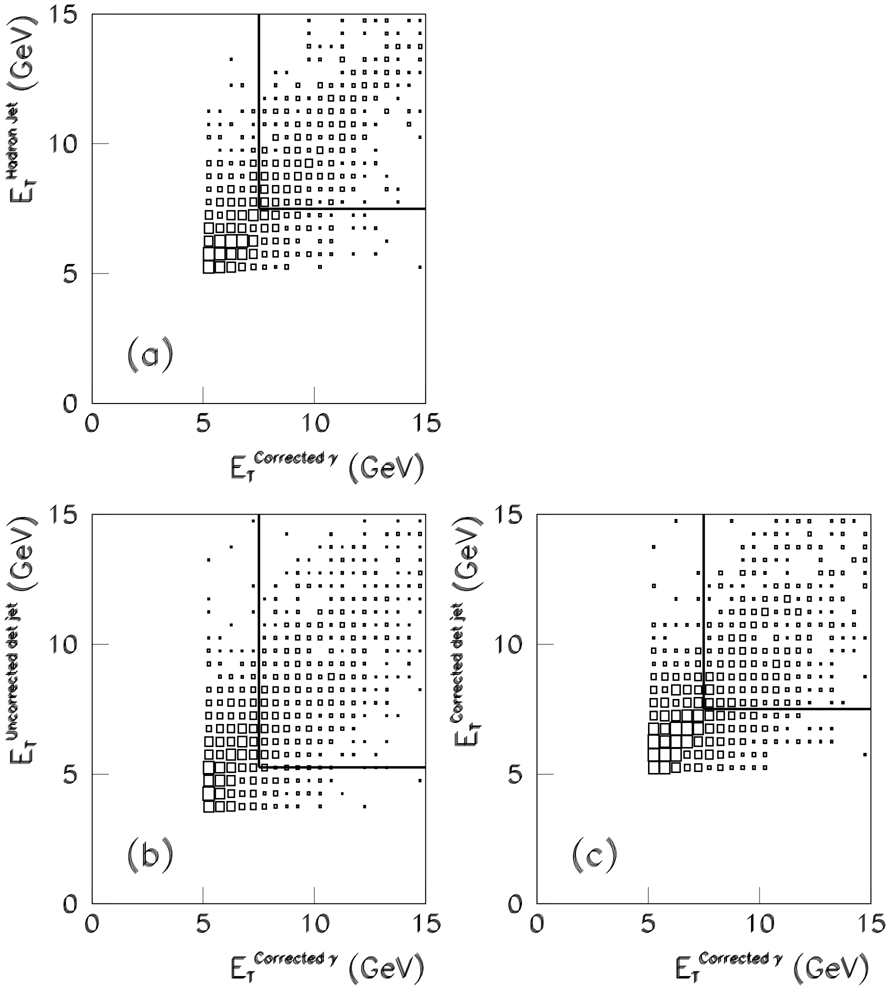

Figure 6.11: The transverse energy correlations between photons and jets; (a) E_T^{γ} vs hadron level E_T^{jet}, (b) E_T^{γ} vs detector level E_T^{jet} before E_T^{jet} correction and (c) E_T^{γ} vs detector level E_T^{jet} after E_T^{jet} correction.

distributions for each bin of jet E_T. Due to the hadron level selection cut for E_T of the jet ($E_{T,had}^{jet} > 5$ GeV), the distributions after the jet E_T correction are not shown for the first two bins in E_T^{had}.

The transverse energy correlations between photons and jets are shown in figure 6.11; (a) E_T^{γ} vs hadron level E_T^{jet}, (b) E_T^{γ} vs detector level E_T^{jet} before E_T^{jet} correction and (c) E_T^{γ} vs detector level E_T^{jet} after E_T^{jet} correction. These plots show that there is good correspondence between detector and hadron level quantities after transverse energy corrections for both photons and jets.

6.3 Online Event Selection

The ZEUS three–level trigger system [61] is used to select prompt photon candidate events. Cuts applied on the different levels of triggers are discussed in this section. In particular the third–level trigger made use of a standard ZEUS electron finding algorithm to select prompt photon candidate with an electromagnetic cluster of transverse energy $E_T > 4$ GeV in the BCAL, with no further tracking requirements at this stage. These represent the basic sample of prompt photon event candidates.

6.3.1 First Level Trigger (FLT)

Basically the prompt photon events are selected online by requiring an `OR` of the FLT slots 28, 40, 41, 42 and 43. The events with one good track and satisfying one of four thresholds at the Calorimeter FLT (CFLT) were selected in the FLT level. The four CFLT thresholds are ;

- BCAL EMC energy $>$ 3.404 GeV
- RCAL EMC energy $>$ 2.032 GeV
- Total EMC energy $>$ 10.068 GeV
- Total CAL energy $>$ 14.968 GeV

In addition the timing information observed in the two C5 counters and SRTD is used to reject the beam–gas background. In order to reject further the background events, only events with `TrKclass > 2` were accepted. These are events with a relatively high ratio of vertex to total number of tracks. The exact value of the ratio is dependent on the number of vertex and non-vertex tracks, but is approximately $>$ 25–30 %. The tracking demand requires the event to have at least one track found by the CTD–FLT coming from the nominal interaction region, -50 cm $< z_{vertex}$ (CTD FLT) $<$ 80 cm.

6.3.2 Second Level Trigger (SLT)

Events which pass the FLT selection proceed to the SLT , the so–called "HPP high–E_T" trigger, designed for hard photoproduction events. The following SLT conditions are required ;

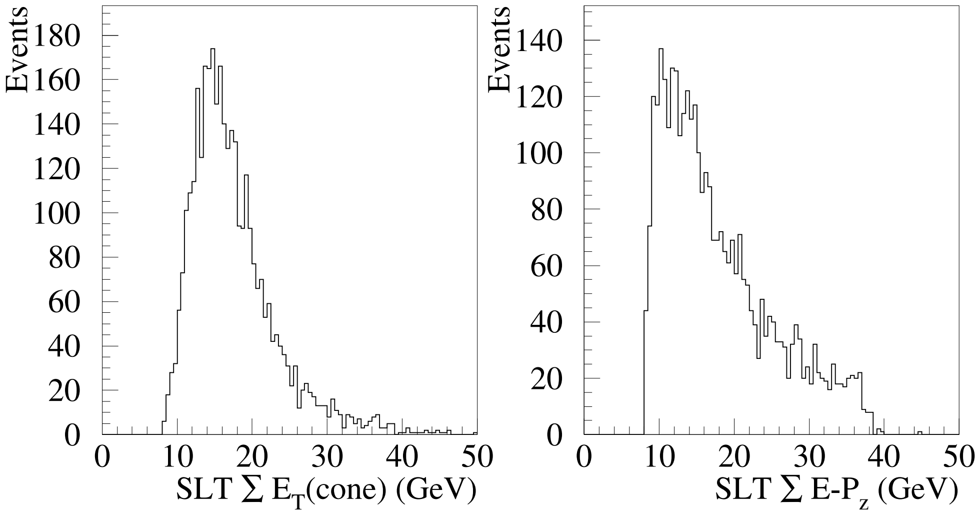

Figure 6.12: SLT $E_T(box)$ and $E - P_z$ distribution of prompt photon final candidates.

- SLT global Veto requirements
- -60 cm $< z_{vertex}$ (CTD SLT) < 60 cm
- At least 1 vertex track
- $E - P_z > 8.0$ GeV
- $E_T(box) > 8.0$ GeV
- $E - Pz > 12.0$ GeV `OR` $Pz/E < 0.95$

The $E_T(box)$ is defined as the sum of transverse energy on the calorimeter cells, excluding the first ring around the FCAL beam pipe (outside a value of about $\eta = 3$). It reduces proton beam gas background. The SLT $E_T(box)$ and $E-P_z$ distribution is shown in figure 6.12 for the prompt photon final candidates. Since the samples already satisfy the $E_T(box) > 8GeV$ and $E - P_z > 8GeV$ requirements at SLT level, it can be expected the efficiency of these requirements is close to 100 %. MC study shows that the efficiency of $E_T(box) > 8GeV$ and $E - P_z > 8GeV$ are 100.0 % and 99.7 % for the offline analysis respectively.

6.3.3 Third Level Trigger (TLT)

At the TLT level, all HPP TLT filters have the following common cuts.

- -60 cm $< z_{vertex} < 60$ cm
- At least 1 vertex track
- $E - P_z < 75.0$ GeV
- Number of bad tracks < 6
  A bad track is defined if the following conditions are not met.
  - $P_T \geq 0.2$ GeV
  - $-3.13 < \eta < 1.75$
  - The number of hits used in CTD axial superlayers > 5
  - The number of hits used in CTD stereo superlayers > 5
  - z value at distance of closest approach ≤ -75 cm

To select the prompt photon candidate events with an electromagnetic cluster with $E_T > 4$ GeV, the prompt photon trigger bit (HPP 16) is used.

- $\sum_{CAL} E_T^{cone} > 8.0$ GeV, where $\sum_{CAL} E_T^{cone}$ is the sum of E_T of all calorimeter cells outside of 10° cone around FCAL beam pipe
- $E_T^{\gamma} > 4.0$ GeV `AND` $-3.0 < \eta^{\gamma} < 1.5$ by ELEC5 electron finder

At the first stage the event samples used were chosen from events passed by the DST prompt photon bit. The trigger required (1) the preliminary identification of an electron or high E_T photon using the track and calorimetry information and (2) more than 8 GeV of summed E_T in the calorimeter away from the beam pipe. In addition, the trigger used for the photon + Jet analysis made use of the HPP dijet trigger in the TLT, which demanded two jets with $E_T^{jet} \geq 4$ GeV and $\eta^{jet} \leq 2.5$.

6.4 Offline Event Selection

In this section we describe the further event selection criteria applied offline to select the prompt photon candidate events. The standard calorimeter rescaling factors to the BCAL (5%) and RCAL (2.5%) have been applied. The noise suppression routine, NOISE96, has been used to minimise the effect of uranium and PMT noise in the ZEUS calorimeter. We have looked at the noise spectra for 96/97 data. It is found that the EMC isolated cell distribution has good agreement between data and MC, as in the previous studies for 95 data analysis. In both cases the MC has a little more noise than the data. Both procedures were applied to the data before commencing the offline analysis of an event.

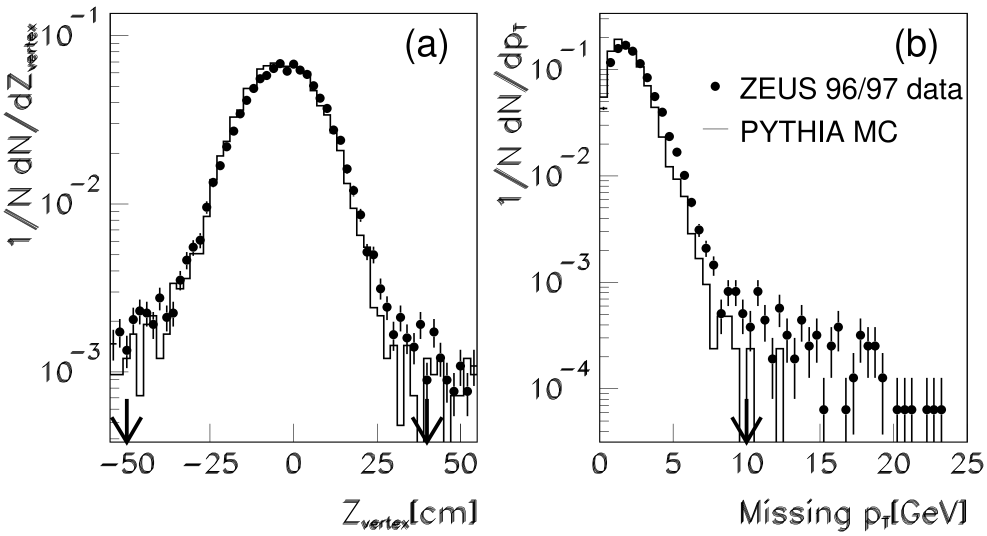

Figure 6.13: Distributions of (a) the z position of the vertex and (b) the missing p_T Points are for the data and histogram is for the PYTHIA prompt photon MC.

6.4.1 Cleaning cuts

After the three–level trigger filter conditions, there is still some contamination from non–ep collisions (beam–gas interactions, Cosmic radiation and halo muons) and deep inelastic neutral current interactions in the data sample. To remove these backgrounds, the following cuts are applied.

- –50 cm $< Z_{vertex} <$ 40 cm

Figure 6.13 (a) shows the reconstructed z position of the vertex for data (dot) and for PYTHIA MC (histogram). The simulated Z_{vertex} distribution describes the data well. In order to remove the remaining background due to beam–gas backgrounds or cosmic rays, the above cut is applied on vertex position.

- $\not{p}_T <$ 10 GeV

The missing p_T ($\not{p}_T$) is defined as the vector sum of the total calorimeter energy depositions. The distribution from data is shown in figure 6.13 (b). Overlaid on the data is the result from prompt photon MC (direct+resolved). The data are peaked at zero with a tail extending to 25 GeV. The prompt photon MC events lie almost exclusively in the $\not{p}_T <$ 10 GeV region.

In the case of PMT sparks, Cosmic rays and the final state neutrino in a charged current DIS events ($ep \to \mu X$), these tend to have large $\not{p}_T$, while the

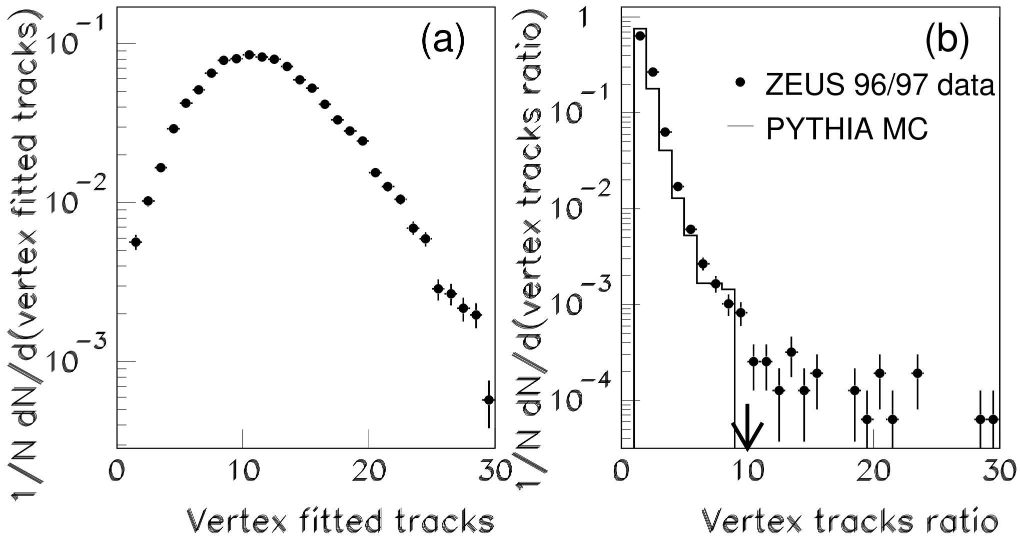

Figure 6.14: (a) Number of vertex fitted tracks and (b) the distribution of non–vertex tracks to vertex tracks. Points are for the data and histogram is for the prompt photon MC.

prompt photon events have small $\not{p}_T$ since the E_T of a photon is well balanced with that of a jet. Therefore we have selected the events with $\not{p}_T < 10$ GeV to remove these backgrounds.

- The ratio of non–vertex tracks to vertex tracks < 10

The "vertex fitted tracks" and "non–vertex fitted tracks" means tracks which are and are not associated to the primary vertex position respectively. The number of tracks fitted to the vertex is shown in figure 6.14 (a). A requirement of at least 3 vertex fitted tracks is made to remove wide angle bremsstrahlung (Compton) events of the kind $ep \rightarrow ep\gamma$.

Figure 6.14 (b) shows the ratio of vertex unfitted / fitted tracks. The prompt photon MC result (histogram) is overlaid on the data (dot). The beam–gas backgrounds usually tend to have many tracks which do not come from a single interaction point. Therefore the data show a larger tail extending to 30 than the prompt photon MC.

6.4.2 Isolated photon finding methods

An algorithm for finding electromagnetic clusters was applied to the data, and events were retained for the final analysis if (1) a photon candidate with $E_T > 5$

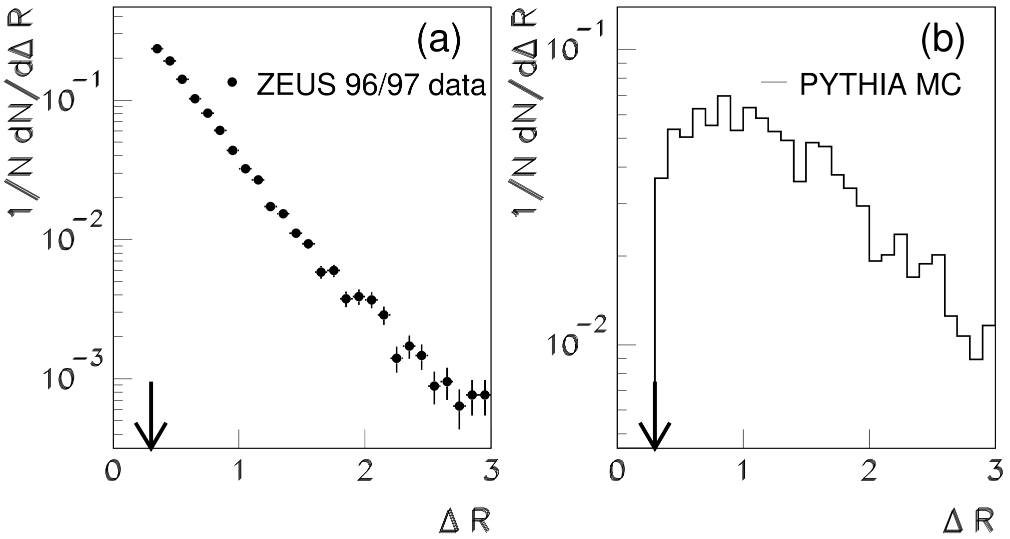

Figure 6.15: The ΔR distributions for (a) data and (b) prompt photon PYTHIA Monte Carlo.

GeV was found in the BCAL region and (2) all cells in the cluster are those of BCAL . The BCAL requirement restricts photon candidates to the approximate pseudorapidity range $-0.7 < \eta^{\gamma} < 0.9$ in the ZEUS laboratory frame.

- Track Isolation Cone

A photon candidate was rejected if a reconstructed CTD track pointed within 0.3 radians of an angle, ΔR, defined as ;

$$\Delta R = \sqrt{(\theta^{cluster} - \theta^{track})^2 + (\phi^{cluster} - \phi^{track})^2}$$

The angle between the cluster and the track was defined at the inner measured point of the vertex track in CTD. If any matching CTD track within a cone of $\Delta R = 0.3$ radians around the cluster was found, that candidate was rejected. This removed almost all high-E_T positrons and electrons, including the majority of those that had suffered hard radiation in the material between the interaction point and the BCAL, since the soft remaining positron track would still point towards the calorimeter cluster if taken at its inner measured point.

Figure 6.15 shows the normalised distributions of ΔR for prompt photon candidates in the (a) data (dots) as well as (b) prompt photon PYTHIA MC. The data peaks at a small value of ΔR compared to the prompt photon MC. Since there is still contamination from DIS events after the cleaning cut, most of

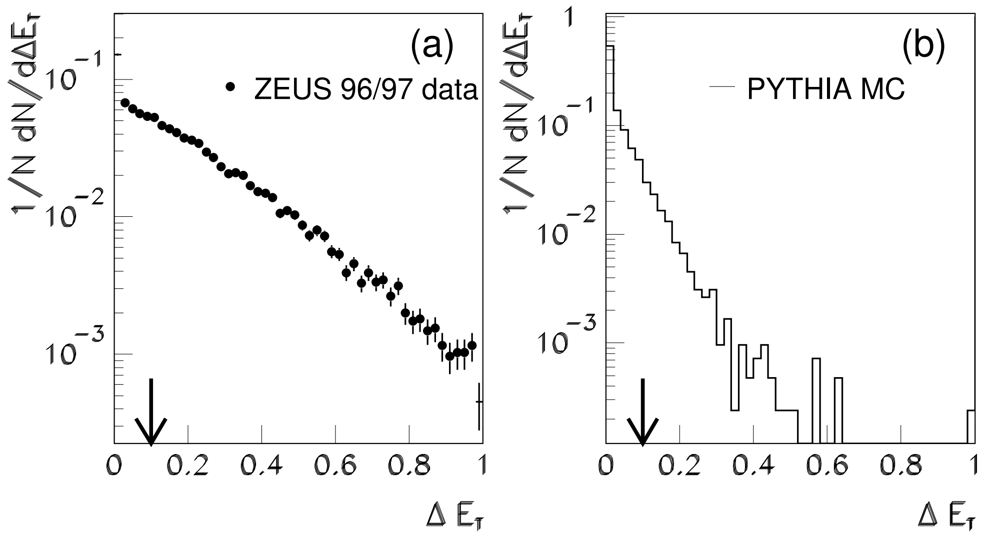

Figure 6.16: The ΔE_T(around γ) distributions for (a) data and (b) prompt photon PYTHIA Monte Carlo.

clusters have a matching track as seen in figure 6.15 (a). About 5 % of prompt photons convert in the detector into an e^+e^- pair. This feature is shown as peaks at $\Delta track$ near to zero in figure 6.15 (b). Therefore the $\Delta R > 0.3$ cut increases the signal to background ratio.

- Energy Isolation Cone

High E_T photons can be emitted by radiation from a final state quark in QCD diagrams; the so–called "direct and resolved fragmentation processes" (See figure 2.1 (c) and (d)). Such photons are likely to be found in or near jets. In addition, the neutral mesons such as π^0 and η whose calorimeter signals resemble those of photons are also formed in association with jets.

To reduce such neutral meson backgrounds, an energy isolation cone was imposed around the photon candidate: within a cone of unit radius in (η, ϕ), the total E_T from other particles was required not to exceed $0.1E_T^\gamma$. This was calculated by summing the E_T in each calorimeter cell within the isolation cone. Additional contributions from the charged tracks were added to ΔE_T assuming a track corresponds to a massless particle, when their directions were within the cone at the interaction point but were curved out at the calorimeter surface.

$$\Delta E_T \equiv \sum E_T^{calo+tracks} < 0.1 \times E_T^\gamma \tag{6.7}$$

This energy isolation cone requirement greatly reduces backgrounds from dijet events with part of one jet misidentified as a single photon (π^0, η, etc). In addition it removes most dijet events in which a high E_T photon radiates from a final–state quark. A remainder of such events is included as part of the signal in the data and the theoretical calculations.

The ΔE_T distributions of (a) the data and (b) the combined direct and resolved prompt photon MC are shown in figure 6.16. The data are peaked at zero with a tail extending to large value of ΔE_T due to dijet backgrounds in which the photon candidate is part of a jet. The MC distribution is much less sharply peaked at zero than the data distribution. The cut at 0.1 retains the large majority of prompt photon events.

6.4.3 DIS event rejection

Events with an identified deep inelastic scattered (DIS) positron were removed by the following means, restricting the acceptance of the present analysis to incoming photons of virtuality $Q^2 \lesssim 1$ GeV^2.

- $0.15 < y^{meas} < 0.7$

The quantity

$$y^{meas} = \frac{\sum(E - P_z)}{2E_e} \tag{6.8}$$

was calculated, where the sum is over all calorimeter cells, E is the energy deposited in the cell, and $p_Z = E\cos\theta$. When the outgoing positron is not detected in the UCAL, y^{meas} is a measure of $y = E_{\gamma,in}/E_e$, where $E_{\gamma,in}$ is the energy of the incident photon. In general most DIS events are to a good approximation completely contained within the ZEUS detector. Thus $y^{meas} \approx 1$.

The usual requirement of $0.15 < y^{meas} < 0.7$ on photoproduction analysis was imposed. The lower cut removed some residual proton–gas backgrounds and cosmic ray backgrounds while the upper cut removed remaining DIS events, including any with a prompt photon candidate that was actually a misidentified DIS positron. In addition wide–angle Compton scattering events ($ep \to e\gamma p$) were also excluded by this cut (see details in next subsection).

This range of accepted y^{meas} values corresponds approximately to the true y range $0.2 < y < 0.9$, equivalent to a true centre-of-mass γp energy range

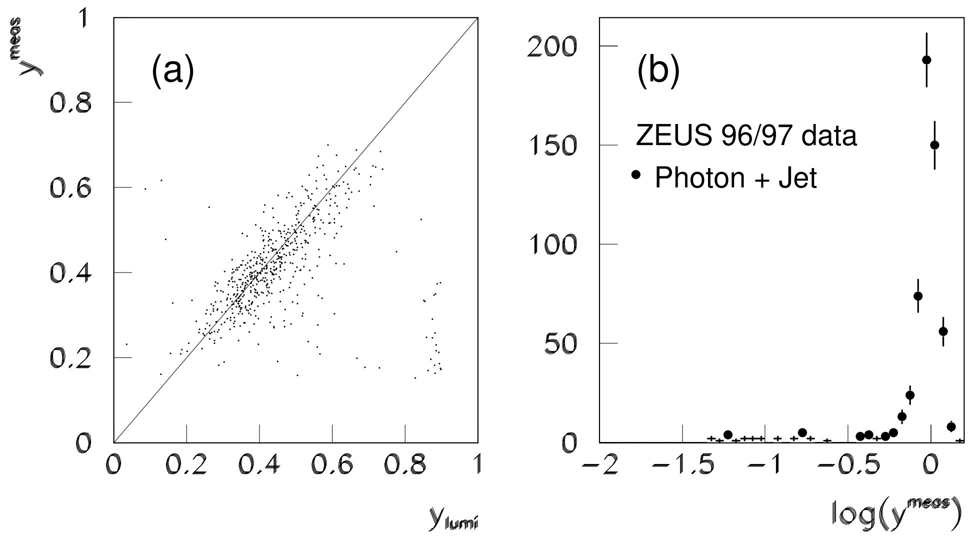

Figure 6.17: (a) y measured using the 35 m tagger vs y^{meas} for events at final stages of selection. (b) $\ln y^{meas}$ calculated for tagged events including the tagging electron.

$120 < W < 274$ GeV. At the offline level, y^{meas} was re–evaluated using energy–flow objects, and was corrected for energy losses.

Figure 6.17 (a) shows the good correlation between the value of y obtained from the 35 m luminosity tagger (x–axis) and the value of y^{meas} (y–axis). This is for all tagged events in the final sample. The agreement is demonstrated in a different way in figure 6.17 (b). Here the tagging electron energy is included in the calculation of y^{meas}. It shows a peak near unity in the logarithm distribution. The width of the peak due to the detector resolution should tell us what cut to impose on y^{meas} to remove contained events. A cut at 0.7, ln(0.7) = –0.36 is found to be indicated here as expected.

- Remove event if there are any electromagnetic clusters with $y_{el} < 0.75$ except prompt photon candidates

For events containing at least one scattered positron candidate, y_{el}, defined as,

$$y_{el} \equiv 1 - (\frac{E_e^{'}}{2E_e})(1 - \cos\theta_e^{'}) \tag{6.9}$$

was calculated in order to reject remaining DIS events in the sample. It is calculated for each electromagnetic cluster found by EEXOTIC finder using the energy ($E_e^{'}$) and angle of the cluster. If a cluster corresponds to the scattered

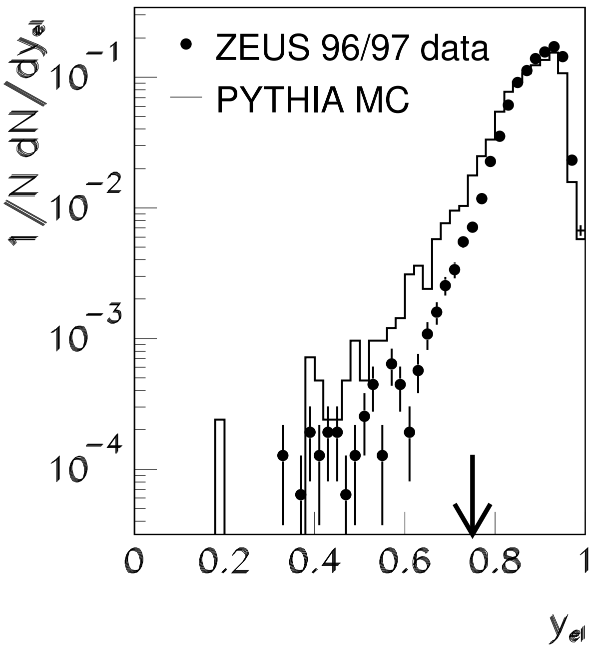

Figure 6.18: The y_{el} distributions of second electromagnetic cluster.

positron, it tends to have a low value of y_{el}. For photoproduction events in which the scattered positron escapes undetected down the beam pipe, y_{el} tends to have a high value.

The y_{el} distribution for the data sample after trigger and cleaning cuts described above is shown in figure 6.18. Overlayed on the data is the result from the prompt photon MC (direct+resolved). It is clear that the peak in the data at high y_{el} comes predominantly from photoproduction events. A cut of $y_{el} > 0.75$ for events containing an 'electron' selects almost pure photoproduction events with a minimum of DIS background.

6.4.4 QED Compton / PMT spark events rejection

QED Compton Events

An elastic QED Compton event, $e + p \to e + p + \gamma$, has the radiative photon and the scattered electron without any other particles in the final state. The following requirement was applied for the events which have two electromagnetic clusters.

- $\frac{E_1+E_2}{\text{Total energy of the event}} < 0.95$ if there are two electromagnetic clusters

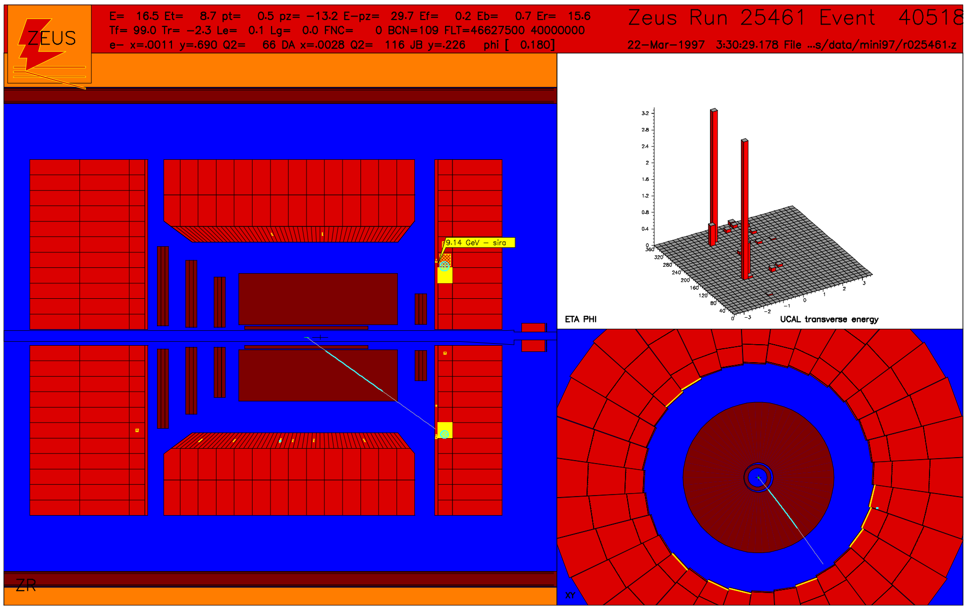

Figure 6.19: Typical example of elastic QED Compton event, $e + p \to e + p + \gamma$. The isolated γ and e in the final state is clearly identified in the uranium calorimeter and well isolated.

The quantity $(E_1 + E_2)$ defines the energy sum of the first and second electromagnetic clusters. It is found that QED Compton events show a clear peak around a unit value of the above ratio. Figure 6.19 shows a typical example of an elastic QED Compton event. The isolated γ and e in the final state are clearly identified in the UCAL and well isolated.

The QED Compton rejection algorithm QEDC [79] was also used to find QED Compton events. The algorithm searches for 2 good electrons in the calorimeter using the SIRA95 electron finder based on a neural network and requires them to be back–to–back, balanced in p_T. The energy deposits in the calorimeter have to be at least 90 % in the EMC.

PMT Spark Events

Additional cuts on the BCAL timing and the energy fraction of the electromagnetic cluster were applied to reject the events in which a PMT spark mimics a prompt photon signal. The typical example of PMT spark event in the ZEUS detector is shown in figure 6.20.

Most of the PMT sparks are already removed by looking at the energy imbalance between two PMTs in NOISE96. In the case that one of the PMTs is dead,

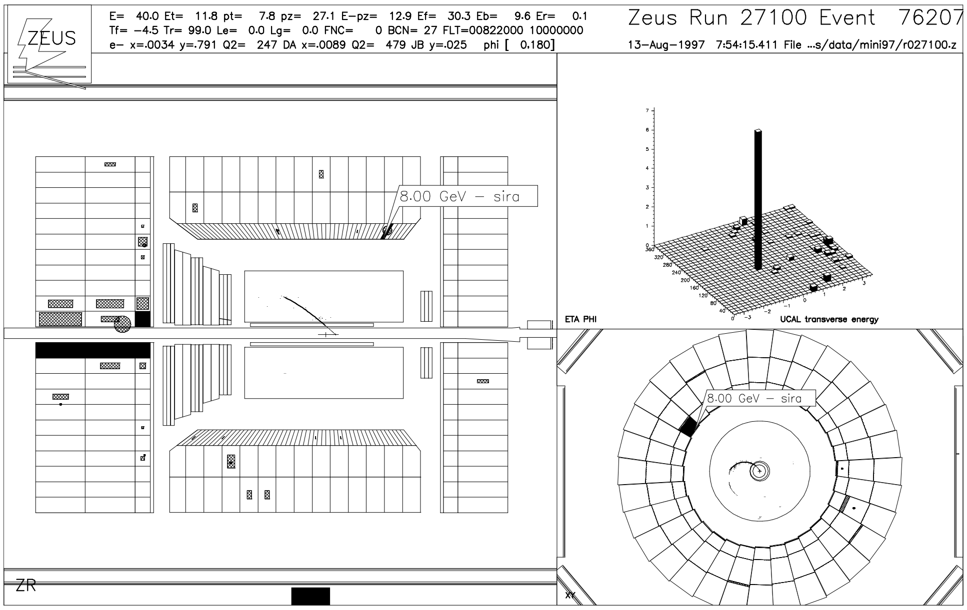

Figure 6.20: Typical example of PMT spark event at ZEUS detector.

however, the energy imbalance cannot be estimated. The BCAL timing and the energy fraction of the electromagnetic cluster were used to reject the PMT spark events.

- $-10 <$ BCAL timing < 10 ns

The BCAL timing from data is shown in figure 6.21 and compared to prompt photon MC, which are peaked at the centre without a tail. The small tail in the timing distribution of data is from the non–physics events, such as PMT sparks and cosmic rays, while the real physics events originated in the electron–proton interaction show timing which concentrate on around 0 ns.

- When one PMT of the most energetic cell in a cluster was dead, the cluster should be made from more than one cell.

The ratio of the energy deposited in one cell to the total energy of the cluster is also used to classify the PMT spark which makes a cluster by only one cell. After applying the above conditions, 2 events in the 1996 data and 10 events in the 1997 data were removed by the cut.

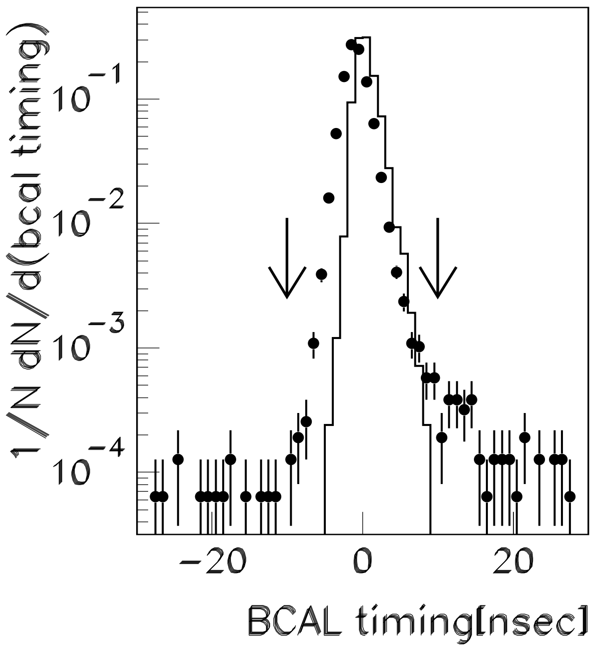

Figure 6.21: The distribution of BCAL timing.

6.5 Summary of Event Selections

In summary, at detector level after all the online and offline selection criteria described in this chapter, approximately 6000 prompt photon candidate events with $E_T^\gamma > 5$ GeV in the region of pseudorapidity range $-0.7 < \eta^\gamma < 0.9$ remained. Details of the events obtained after selection are given below. These events are used in the physics analysis.

6.5.1 Inclusive Prompt Photon Sample

Figure 6.22 shows the distributions of final prompt photon candidates after selection cuts on data for both the inclusive and the photon + jet events ; (a) E_T, (b) pseudorapidity, (c) azimuth and (d) y^{meas} of prompt photon candidates.

6.5.2 Prompt Photon + jet Sample

For jet identification, the longitudinally invariant K_T clustering algorithm, KTCLUS, was used in the inclusive mode. Correction factors to the measured jet energies were evaluated through the use of Monte Carlo event samples, and were typically 1.05–1.10 for the jet, as discussed in section 6.2. After correction, excluding the prompt photon itself, jets were required to have $E_T^{jet} > 5$ GeV and $-1.5 < \eta^{jet} < 1.8$. If more than one such jet was found in an event, that with the highest transverse energy was used in the analysis. About 40% of inclusive prompt photon candidates in the BCAL have an accompanying jet. This is shown in figure 6.22.

The jet distributions of photon + jet candidates, E_T^{jet}, η^{jet}, ϕ^{jet} and x_γ, where x_γ is the fraction of the incident photon energy that contributes to the resolved QCD subprocesses (see details in chapter 9.2.1), are also shown in figure 6.23.

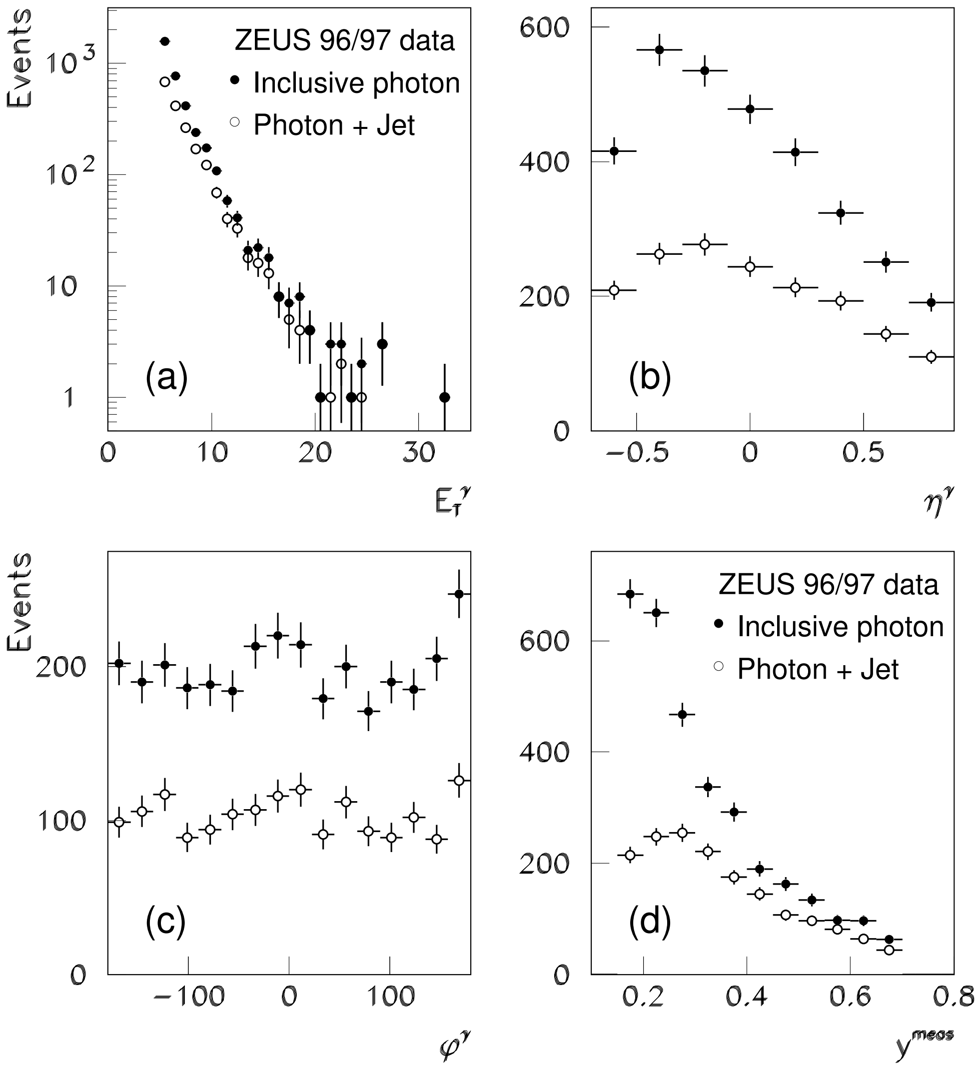

Figure 6.22: Distributions of final prompt photon candidates after selection cuts on data for both the inclusive and the photon + jet events ; (a) transverse energy, (b) pseudorapidity, (c) azimuth angle and (d) y^{meas} of prompt photon candidates. The inclusive events are shown by black circles and the white circles represent the events of the photon + jet sample.

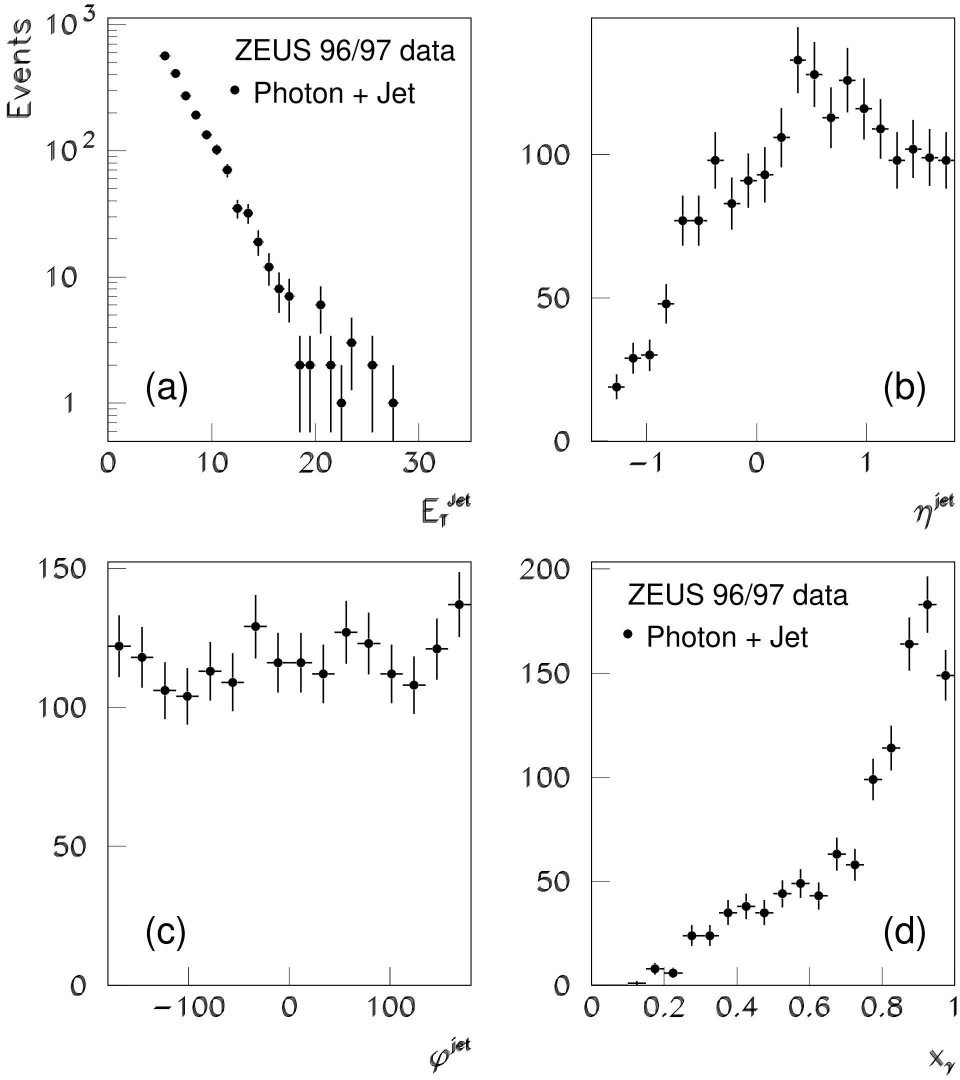

Figure 6.23: Jet distributions of final sample after selection cuts on data for photon + jet events ; (a) transverse energy, (b) pseudorapidity and (c) azimuth angle of jet candidates accompanied by balancing photon, (d) x_γ of prompt photon candidate events before background subtraction.

Chapter 7

Evaluation of the Photon Signal

In this chapter we describe the separation of the photon signal from the background. After the event selection procedure, as discussed in chapter 6, the final sample of prompt photon candidates consists of true high–E_T photons and also a remaining π^0 and η meson background. The shower shape variables used to discriminate between photons and neutral mesons are discussed in this chapter. The neutral meson background is statistically subtracted by fitting the measured shower shape quantities in the data with Monte Carlo shower shape distributions.

The result of the background subtraction procedure for the kinematical variables is compared to LO Monte Carlo prediction.

7.1 Characteristics of Neutral Mesons

A number of neutral mesons decay into multi–photon final states. Typically most π^0 mesons decay into two photons and η mesons decay ultimately into two or more photons in its neutral modes which have a 71.6 ± 0.4 % decay probability in the full set of η meson decay channels. The relevant decay modes and branching ratios for these neutral mesons are as follows [80].

$$\pi^0 \to \gamma\gamma \quad (98.798 \pm 0.032\ \%)$$

$$\eta \to \gamma\gamma \quad (39.33 \pm 0.25\ \%)$$

$$\eta \to \pi^0\pi^0\pi^0 \quad (32.24 \pm 0.29\ \%)$$

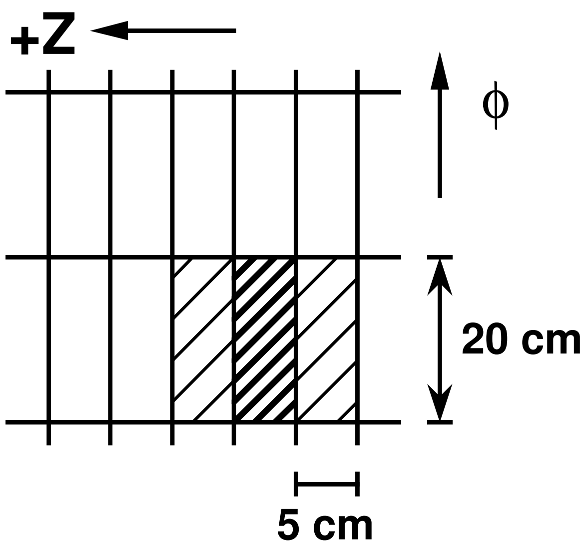

Figure 7.1: Layout of the BEMC cells. Each rectangle represents a calorimeter cell, while the shaded areas denote energy deposits from a photon.

When a π^0 meson decays into the two photon final state, the opening angle, α, of the two photons with energies E_1 and $(E_{\pi^0} - E_1)$ resulting from the decay of a π^0 with energy E_{π^0} is given by

$$\alpha = 2 \cdot sin^{-1}\left[\frac{m_{\pi^0}}{2 \cdot \sqrt{E_1(E_{\pi^0} - E_1)}}\right] \tag{7.1}$$

where m_{π^0} is the mass of the π^0 meson. It has a minimum value if each photon from the π^0 meson decay has the same energy.

To look at the relationship between the transverse EM shower development of the neutral mesons and the general granularity of the calorimeter cells, the minimum distance, ΔM, between two photons from the π^0 decay at the BEMC surface is introduced and is given by the following equation from the geometry.

$$\begin{aligned}\Delta M &= 2 \times \frac{123.2}{\sin\theta_{\pi^0}} \times \tan\left[\sin^{-1}\left(\frac{m_{\pi^0} \times \sin\theta_{\pi^0}}{E_T^{\pi^0}}\right)\right] \\ &\sim 246.4 \times \frac{m_{\pi^0}}{E_T^{\pi^0}} \qquad [cm]\end{aligned} \tag{7.2}$$

According to equation 7.2 the ΔM in the BCAL between the photons from a decaying 5–10 GeV π^0 is 6.7–3.3 cm. For a decaying 5–10 GeV η meson, ΔM is from 27.2 to 13.5 cm.

Figure 7.1 shows the geometry of the BEMC cells in the Z direction, 5 $\times$ 20 cm. Each rectangle represents a calorimeter cell, while the shaded area denotes energy deposits. We can use the shower shape information to see the different pattern of energy deposition between photons and neutral mesons such as π^0 and η mesons.

However it is not possible to distinguish photons and π^0 and η mesons on an event–by–event basis because all the decay products of a neutral meson are sometimes contained within a single BEMC cell. Therefore the evaluation of the photon signals from neutral meson backgrounds is done statistically.

7.2 Identification of Photon Signal

As mentioned above, a typical high-E_T photon candidate in the BEMC consists of a cluster of 4–5 cells selected by the electron finder. On average the π^0 and η mesons have a larger shower width in the BEMC because they dominantly decay into multi–photon final states. To utilize the difference of shower development in the calorimeter between photon and neutral mesons, two topological shower shape quantities were studied in order to reject events in which a neutral meson gives a photon candidate, and to enable the further step, the background subtraction procedure. These were (i) the energy weighted mean width $<\delta Z>$ of the BEMC cluster in Z direction and (ii) the fraction f_{max} of the cluster energy found in the most energetic cell in the BEMC cluster. The quantity $<\delta Z>$ is defined as

$$\langle \delta Z \rangle = \frac{\sum E_{cell} |Z_{cell} - \overline{Z}|}{\sum E_{cell}} \tag{7.3}$$

summing over the cells in the cluster, where $\overline{Z}$ is the energy-weighted mean Z value of the cells. The $<\delta Z>$ is expressed in units of the BEMC cell width in the Z direction, (i.e. $<\delta Z> = 1 = 5$ cm, see figure 7.1.)

Another quantity f_{max} is defined as

$$f_{max} = \frac{\text{Energy in the most energetic cell in the cluster}}{\text{Total energy of the cluster}} \tag{7.4}$$

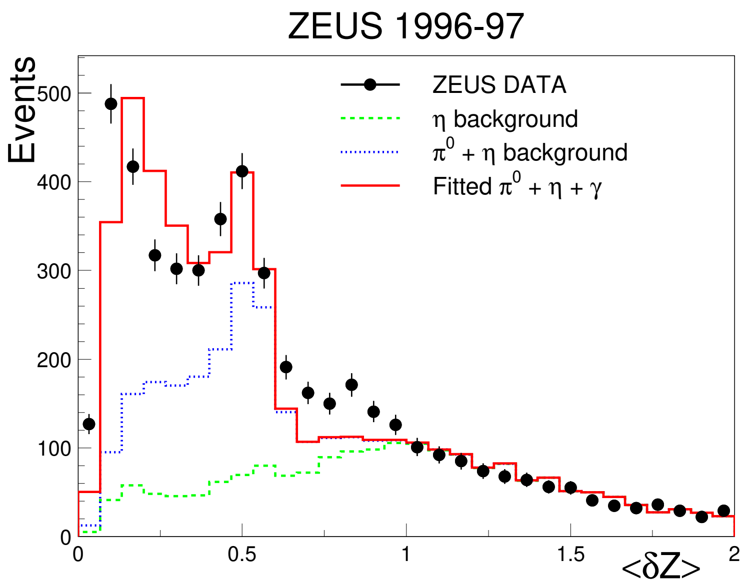

Figure 7.2: Distribution of mean width of cluster $<\delta Z>$ for the final selection of prompt photon candidate events in the inclusive analysis. The plotted unit is the BEMC block width (5.45 cm). Also plotted are fitted Monte Carlo curves ; Points = data; dashed = MC (η); doted = MC ($\eta + \pi^0$); dotted-dashed = MC ($\eta + \pi^0 + \gamma$).

Figure 7.2 shows the distribution of $<\delta Z>$ for the inclusive prompt photon data, with the finally selected sample of photon candidates, and the Monte Carlo samples of single γ, π^0s and η mesons, which were generated in the E_T range 3–20 GeV with a similar kinematic requirement to the experimental prompt photon candidates. A zero value in $<\delta Z>$ means the entire energy is in one calorimeter cell. The peak at 0.5 comes mainly when the energy is distributed in about two cells. The experimental data were fitted to a sum of the three single particle MC distributions.

The figure shows two peaks at low values of $<\delta Z>$ which are identified with photons and π^0 mesons, respectively. The photon contribution is peaked at low values of $<\delta Z>$ and that of π^0 is peaked at rather higher value around 0.5, while the distribution of $<\delta Z>$ contains a tail at higher value of BEMC cell width. This tail quantified the η meson background for the higher mass and multiple decay modes. Events with $<\delta Z> > 0.65$ were removed from the subsequent analysis because there are only few photons and π^0s candidates in this region. The remaining candidates after the cut on $<\delta Z>$ at 0.65 are taken to consist of genuine high E_T photons, π^0 mesons and a small admixture of η mesons.

Figure 7.3 shows the distribution of $<\delta Z>$ for the event sample with a prompt photon candidates accompanied by a jet. Also shown is the good agreement

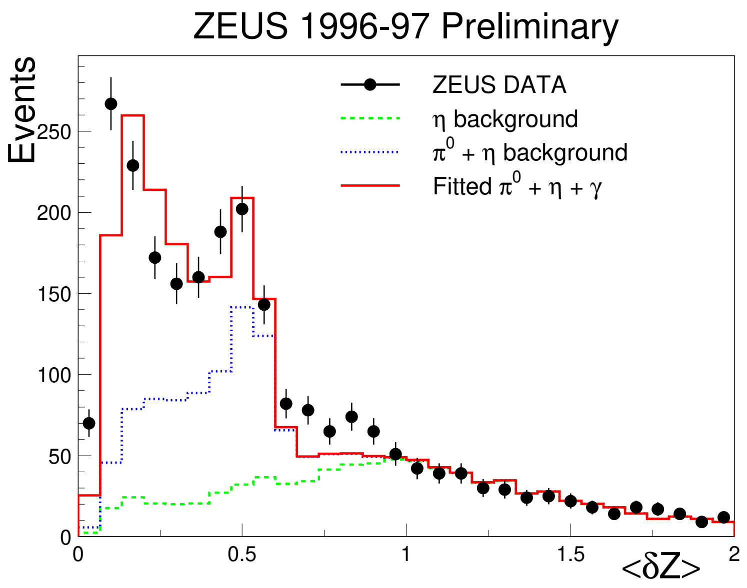

Figure 7.3: Distribution of mean width of cluster $<\delta Z>$ for the final selection of prompt photon candidate events in the photon + jet analysis. The plotted unit is the BEMC block width (5.45 cm). Also plotted are fitted Monte Carlo curves ; Points = data; dashed = MC (η); doted = MC ($\eta + \pi^0$); dotted-dashed = MC ($\eta + \pi^0 + \gamma$).

between data and fitted MC prediction (solid–line). The displacement of the photon peak from the MC $<\delta Z>$ distribution does not affect the present analysis and the poor fit in the region 0.6–1.0 is taken into account in the systematic errors. In general, it is assumed to have similar properties to the π^0 and η contributions.

7.3 Correction of MC f_{max} Distributions

Figure 7.4 shows the distribution of f_{max}, the fraction of the photon candidate energy in the BEMC cell with maximum energy, for inclusive photon candidates. The MC curves are taken from a combined fit of the portion of figure 7.2 for the $<\delta Z> < 0.65$ condition to a sum of the single particle MC samples. In both the data and the single particle MCs, events with $<\delta Z> < 0.65$ have been removed. All single particle MC f_{max} distributions were then scaled by a factor in f_{max} to get the positions of the peaks to match. The scaling factor here is 1.025 ± 0.05 which is estimated from DIS positron data and MC, and those of prompt photon.

In figure 7.4, however, such a simple constant correction applied to all MC f_{max} distributions is not good enough to fit to the data. A small rapidity–dependent discrepancy was found to exist between the experimental f_{max} distribution and

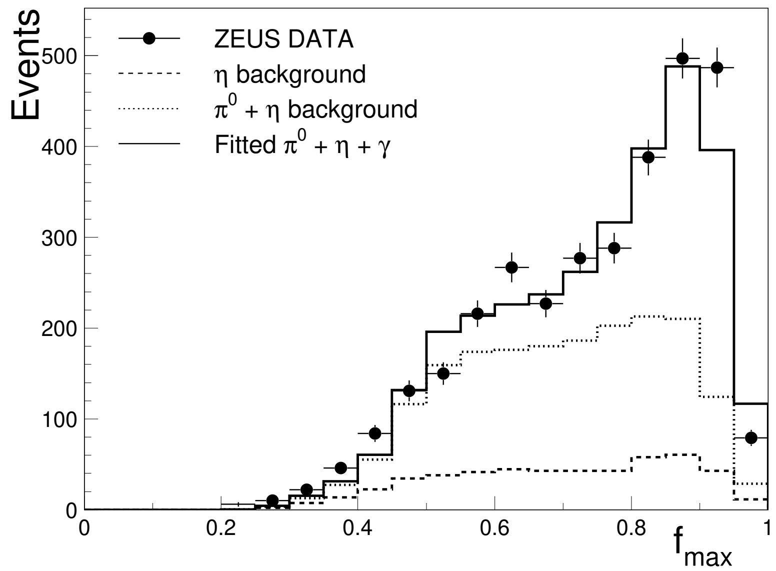

Figure 7.4: Distribution of f_{max} for prompt photon candidates in selected events, after cutting on $<\delta Z>$. Also plotted are fitted Monte Carlo curves for photons, π^0 and η mesons with similar selection cuts as for the observed photon candidates. Points = data; dashed = MC (η); doted = MC ($\eta + \pi^0$); dotted-dashed = MC ($\eta + \pi^0 + \gamma$).

those given by the single–particle MC simulations. This discrepancy differed for photons and for neutral mesons. It was also found that the shower shapes of the data become narrower than those of the MC at the central region of BCAL and become broader than the MC at the edge of the BCAL region. Therefore correction factors which describe the rapidity dependence of the f_{max} variable are needed.

The simple scaling correction leads approximately to a 20% systematic effect on the hadron level cross section. To reduce such a systematic effect, we have examined several f_{max} correction formulas with various values of f_{max} correction factor χ, where χ is estimated by (1) DIS e^+ data/MC samples, (2) prompt photon data/MC samples, (3) neutral mesons in $\rho^\pm$ enriched MC samples and (4) $\pi^0 + \eta$ anti–isolation background from neutral current (NC) samples.

From a comparison of such data with the simulations using the various correction schemes, rapidity–dependent correction factors in the range 0.95–1.05 were applied to the MC f_{max} distribution for the different types of single particle. The best f_{max} correction factor was found using a chi–squared method. In the next two sub–sections we present the study of the MC f_{max} correction methods for photons and for π^0 / η mesons, respectively.

7.3.1 Correction of the photon f_{max} in MC

As mentioned above, a separation of the photon signal from the mesonic background largely depends on the MC simulation of shower shapes in the EM clusters. In this sub–section the correction method for the photon f_{max} distribution is presented using (1) photon candidate samples with allowance made for the neutral meson components and (2) experimental DIS e^+ data and MC samples.

- **Shower shape study using prompt photon candidates**

In order to estimate the difference of the f_{max} distributions between the data and the sum of single particle MCs, the single photon MC f_{max} distributions were scaled by a factor which is varied from 0.95 to 1.10 as in the following formula.

$$f_{max}^{cor} = f_{max} \times factor \tag{7.5}$$

A total of 61 single photon MC f_{max}^{cor} distributions were taken. The prompt photon candidate events were then fitted to a sum of the three MC distributions. To evaluate the optimum value of the f_{max} factor, a minimum–χ^2 calculation was performed for each psedorapidity bin by the following definition ;

$$\chi^2 = \sum_{i=1}^{20} \frac{(N_{data}^i - N_{MC}^i)^2}{{\sigma_{data}^i}^2 + {\sigma_{MC}^i}^2} \tag{7.6}$$

where i denotes the bins of the f_{max} distributions.

Figure 7.5 shows the χ^2 distributions from prompt photon candidates as a function of f_{max} factor for each rapidity bin of photon ((a) $\sim$ (h)). All χ^2 distributions show a reasonable shape and a second order polynomial fit to each χ^2 point was used to find the best f_{max} factor. The number of degree of freedom in the χ^2 fit is nine.

As seen in figure 7.7 the best correction factor estimated from such procedure (black upper triangles) shows that it tends to be larger in the region of central rapidity and to be smaller at the edge of the BCAL region. It confirms that there is a rapidity dependence in the photon f_{max} distribution, and the effect was finally taken into account in the modelling of the photon shower shape.

The same procedure was repeated to look at the E_T dependence and it was found that there is no such behaviour as a function of photon transverse energies. The estimated f_{max} correction factors were within the range from 1.02 to 1.03. These values corresponds to the average value of the rapidity–dependent factors.

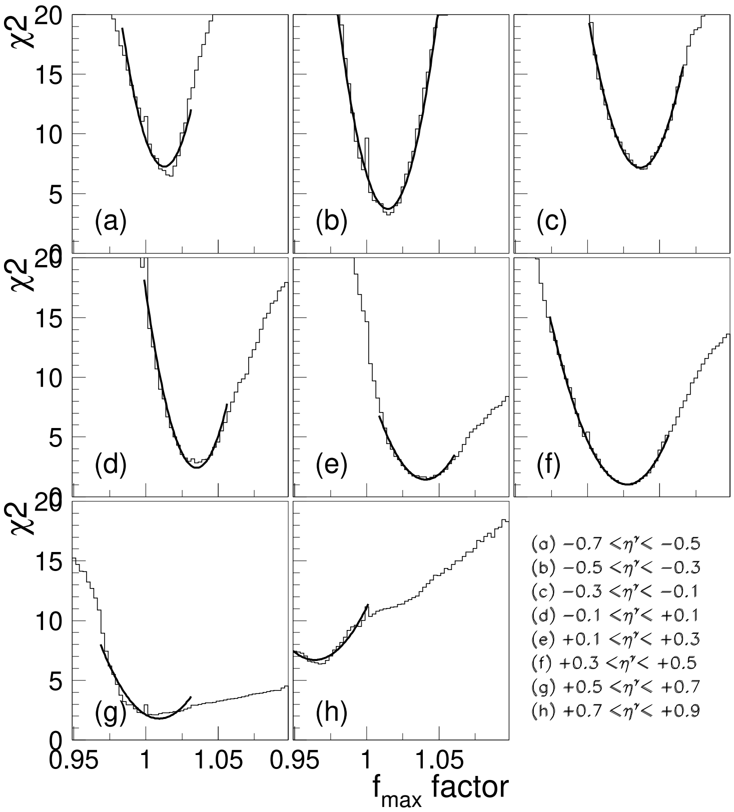

Figure 7.5: The χ^2 distributions from prompt photon candidates as a function of f_{max} factor in each bin of photon pseudorapidity; (a)–(h).

- **Shower shape study using DIS e^+ samples**

One advantage of using the DIS e^+ sample in order to estimate the f_{max} factor of the photon is the existence of enough statistics. Ideally we need to look at the behaviour of the photon shower shape using photon signals, but the shower shape behaviour from the DIS e^+ data and the MC samples look very similar to those of photons.

The same procedure as for the prompt photon sample was repeated for the DIS e^+ data and MC. The values of χ^2 were estimated in the same way as in the previous study. This can be seen in the figure 7.6 and figure 7.7 (black lower triangles). The errors are estimated from the points with (smallest χ^2 + 1).

- **Tuning of photon f_{max} distribution**

As seen in figure 7.7, there is a small difference between two samples. It may be due to the difference between the photon and e^+ shower shape in the EM

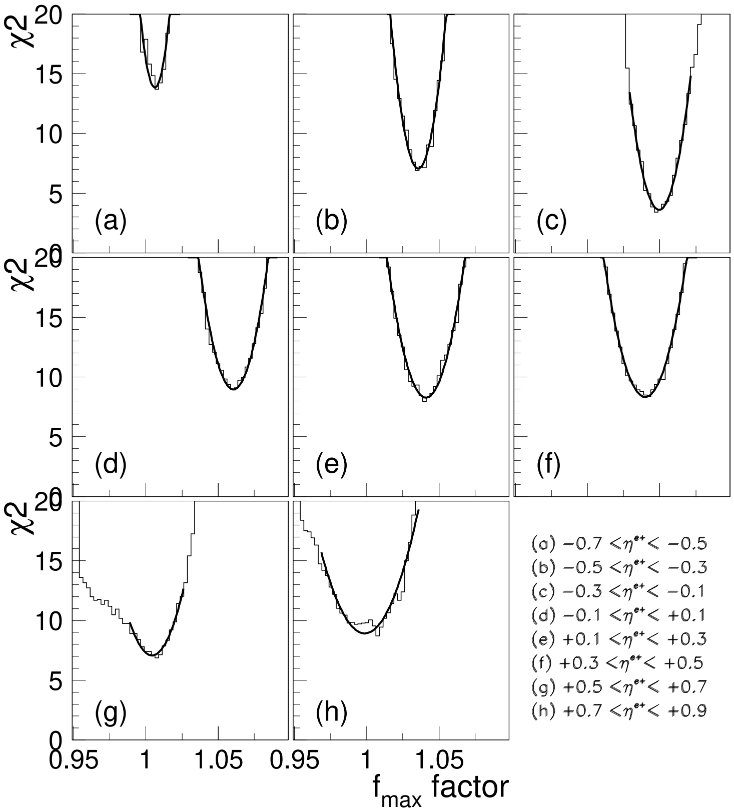

Figure 7.6: The χ^2 distributions from DIS e^+ samples as a function of f_{max} factor in each bin of e^+ pseudorapidity; (a)–(h).

cluster. The average points of both samples are used to estimate the f_{max} factors, as shown in the figure as black circles. Such averaged values were parameterised by a second–order polynomial fit (thick line). The uncertainty due to the resulting fit procedure is estimated to be $\pm$ 0.009 from the root mean square deviations of both samples.

The formula for the f_{max} correction applied for the single photon MC in this analysis is

$$f_{max}^{cor} = f_{max}^{uncor} \cdot \chi_1 \tag{7.7}$$

$$\chi_1 = -0.104 \cdot \eta^2 + 0.002 \cdot \eta + 1.046 \pm 0.009 \tag{7.8}$$

The f_{max} distribution reasonably agrees between the data and MC after applying this correction factor (see figure 7.8).

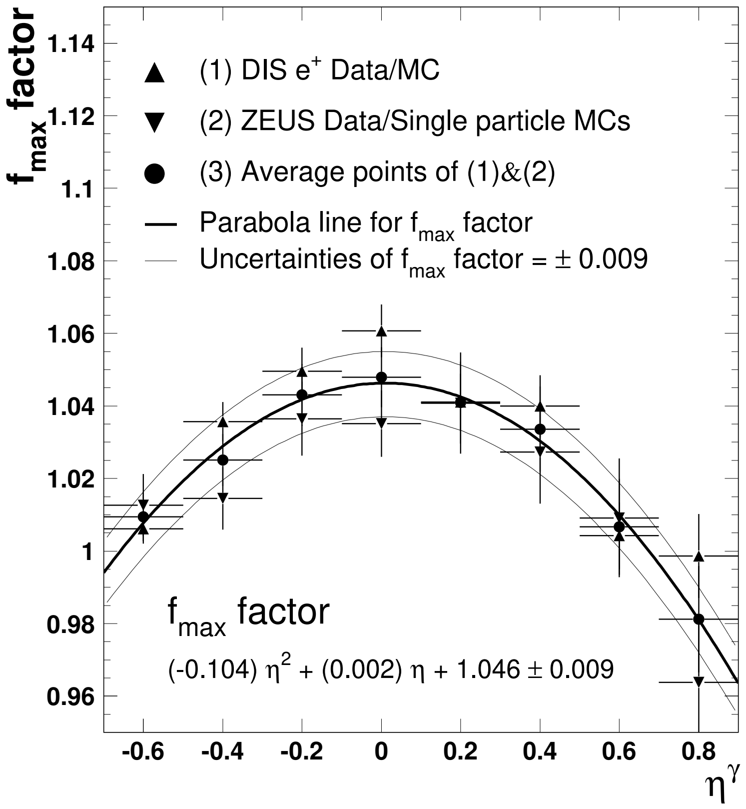

Figure 7.7: The rapidity dependence of the factors with smallest χ^2. The upper–triangles are the result from DIS e^+. The lower–triangles are the results from the prompt photon candidates. The circles are the average of the DIS e^+ and prompt photon candidates. The solid line is the fitted results to the circles.

7.3.2 Correction of the π^0 f_{max} in MC

A description of the correction method for the π^0 f_{max} distribution in the MC, a brief account of which is given in below, can be found in detail elsewhere [81].

Since the width of the BEMC cells in the z direction is too large to resolve the two photons from neutral meson decays, mainly π^0, and to reconstruct the π^0, the $\rho^\pm \to \pi^0 + \pi^\pm$ channel is used as a π^0 enriched sample to estimate the f_{max} correction factor for the π^0 and η meson MC which is expected to have a rapidity dependence. After event selection criterion the invariant mass $\mathrm{M}(\pi^0\pi^\pm)$ was reconstructed by assuming the π^0 and $\pi^\pm$ meson masses. A peak was observed at around 769 MeV, identified with the $\rho^\pm$ meson. The events with 695 MeV $<$ $\mathrm{M}(\pi^0\pi^\pm)$ $<$ 845 MeV were then selected as $\rho^\pm \to \pi^0 + \pi^\pm$ candidates for the further study.

It was found that there is no sensitivity to distinguish whether the π^0 and η meson backgrounds need a different f_{max} correction factor. Therefore the same f_{max} correction factor was used for the π^0 and η meson MC samples. To estimate the correction factor of π^0 and η meson f_{max} distributions, finally, the following formula was applied into π^0 enriched samples, which takes into account the characteristics of neutral meson decay, as described in section 7.1. The equation 7.9 is, therefore, different from those of single photon f_{max} distribution, equation 7.7. In particular the correction is not applied to the calorimeter cluster with $f_{max} \leq 0.4$.

$$f_{max}^{cor} = f_{max} + \frac{1.8 \times (\chi_1 - 1)}{f_{max} - 0.4} \tag{7.9}$$

The minimum values of χ^2 for each rapidity bins were estimated by the same way as described in the equation 7.6. The χ_1 obtained by a parabola fit is as follows.

$$\chi_1 = (-0.047 \cdot \eta^2) + 1.01 \pm 0.014 \tag{7.10}$$

The uncertainty due to the resulting fit procedure is estimated to be $\pm$ 0.014 from the root mean square deviations of the sample. As a cross check the π^0 + η anti–isolation background sample was tested as well.

7.3.3 Corrected f_{max} distributions

As described above, the f_{max} distribution of the three single particle MC samples was corrected in order to reproduce the shape of data. The results are given in figure 7.8 (for the inclusive photon sample) and 7.9 (for photon + jet sample). Only events which have $<\delta Z>$ $<$ 0.65 are considered. The data were fitted to a sum of single particle MC distributions and has a peak at high value of f_{max}, corresponding to an energy deposit with a narrow shower width. One can see that the η and π^0 f_{max} distributions are similar in shape, whereas the photon f_{max} distribution has a sharp peak above 0.75. The fit to the experimental f_{max} distribution is good, and above 0.75 the data are dominated by a substantial photon component. A clean photon contribution can be seen in the f_{max} distribution as a peak near 0.9. Furthermore the corrected MC f_{max} distributions shows a better fit to the data than using a simple constant correction as shown in figure 7.4.

For the cross section measurements of inclusive prompt photons, the $<\delta Z>$ and f_{max} distributions are presented in 8 different regions of the pseudorapidity of the photons and in 6 different regions of the transverse energy of the photons. The results are plotted in the figure 7.10 and figure 7.11. The fit results indicate

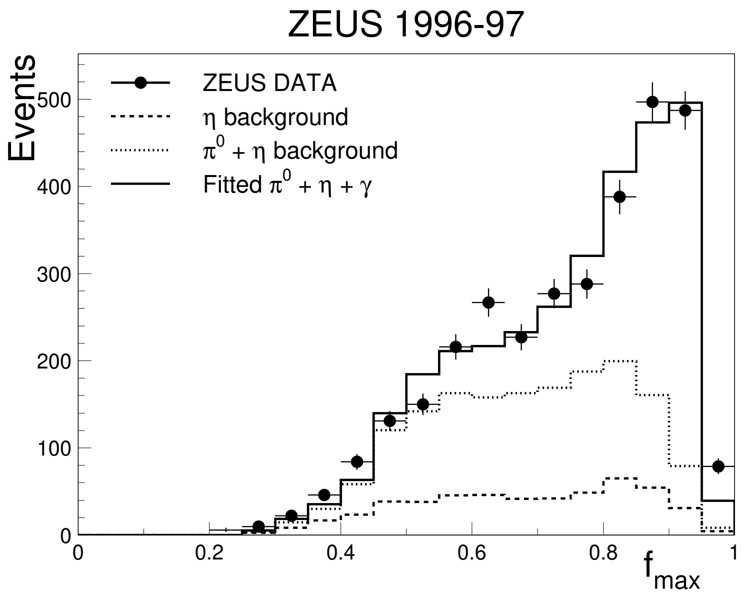

Figure 7.8: Distribution of f_{max} for prompt photon candidates in selected events (inclusive sample), after cutting on $<\delta Z>$. Also plotted are fitted Monte Carlo curves for photons, π^0 and η mesons with similar selection cuts as for the observed photon candidates. Samples with $f_{max} > 0.75$ and $f_{max} < 0.75$ are enriched in the photon signal and in the meson background, respectively.

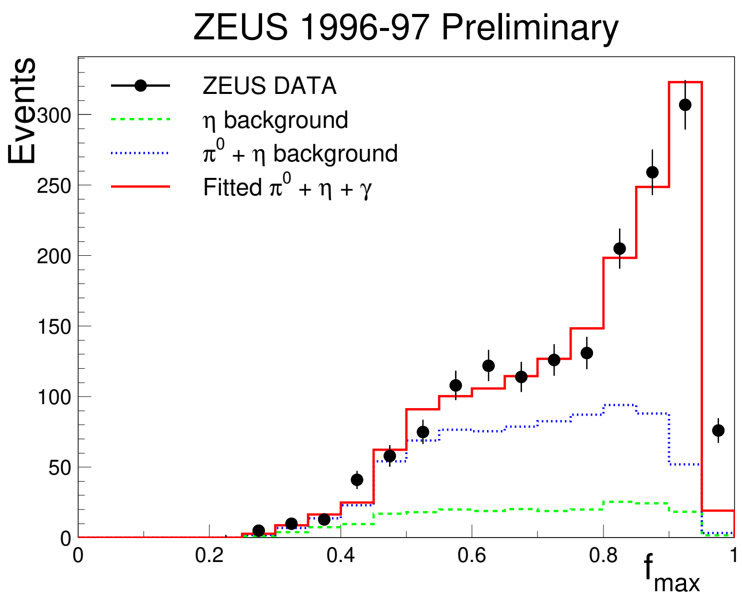

Figure 7.9: Distribution of f_{max} for prompt photon candidates in selected events (photon + jet sample), after cutting on $<\delta Z>$. Also plotted are fitted Monte Carlo curves for photons, π^0 and η mesons with similar selection cuts as for the observed photon candidates. Samples with $f_{max} > 0.75$ and $f_{max} < 0.75$ are enriched in the photon signal and in the meson background, respectively.

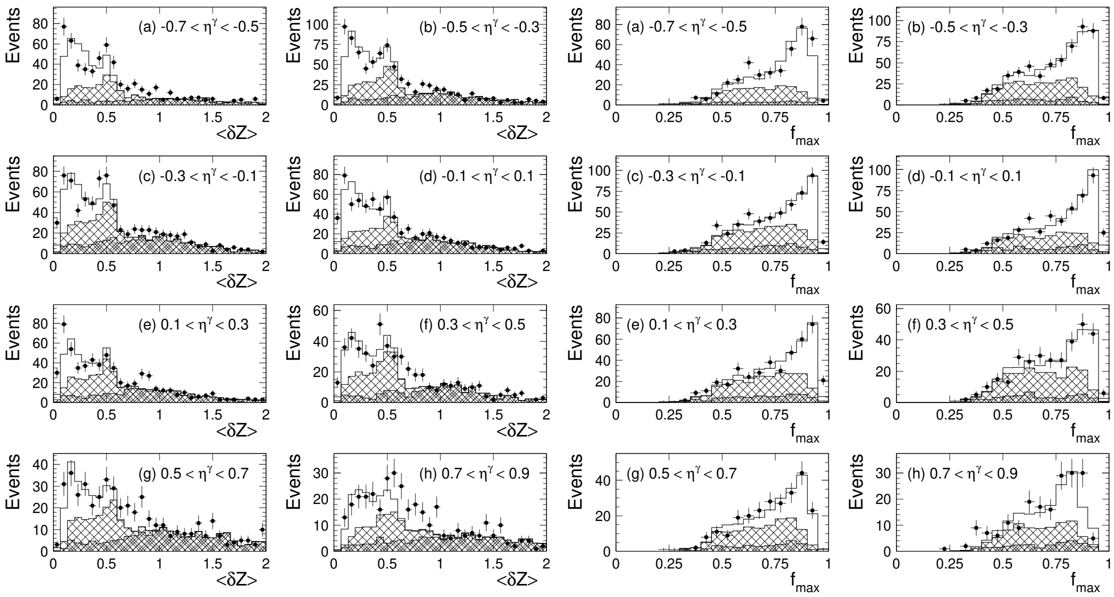

Figure 7.10: The $<\delta Z>$ and f_{max} distributions of the final prompt photon candidates for the inclusive prompt photon analysis. The distributions are fitted by using single particle MCs. Plotted are fitted MC curves ; Points = ZEUS 96+97 data ; dashed = MC (η) ; dotted = MC ($\eta+\pi^0$) ; dotted-dashed = MC ($\eta+\pi^0+\gamma$). The pseudorapidity ranges are from $-0.7 < \eta^\gamma < -0.5$; (**topleft**) to $0.7 < \eta^\gamma < 0.9$; (**bottomright**).

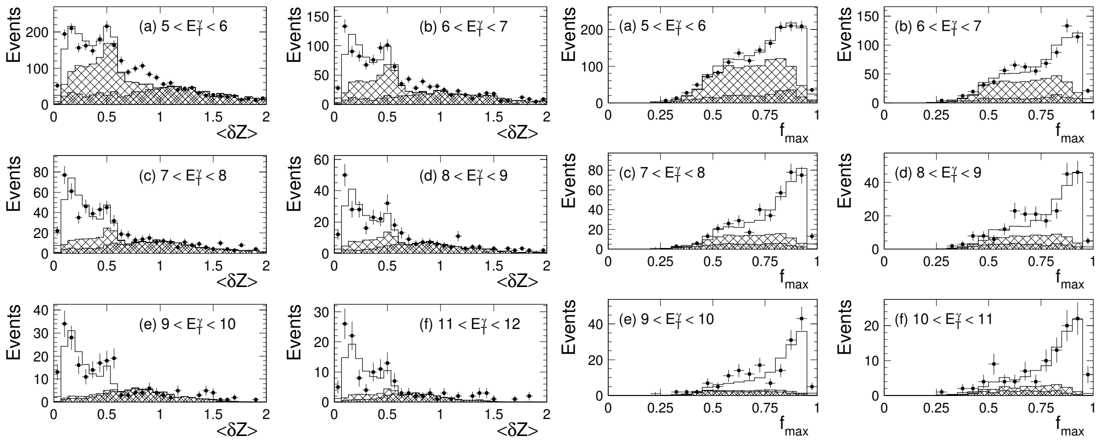

Figure 7.11: The $<\delta Z>$ and f_{max} distributions of the final prompt photon candidates for the inclusive prompt photon analysis. The distributions are fitted by using single particle MCs. Plotted are fitted MC curves ; Points = ZEUS 96+97 data ; dashed = MC (η) ; dotted = MC ($\eta + \pi^0$) ; dotted-dashed = MC ($\eta + \pi^0 + \gamma$). The E_T^γ ranges are from $5 < E_T^\gamma < 6$ GeV ; (**topleft**) to $10 < E_T^\gamma < 11$ GeV ; (**bottomright**).

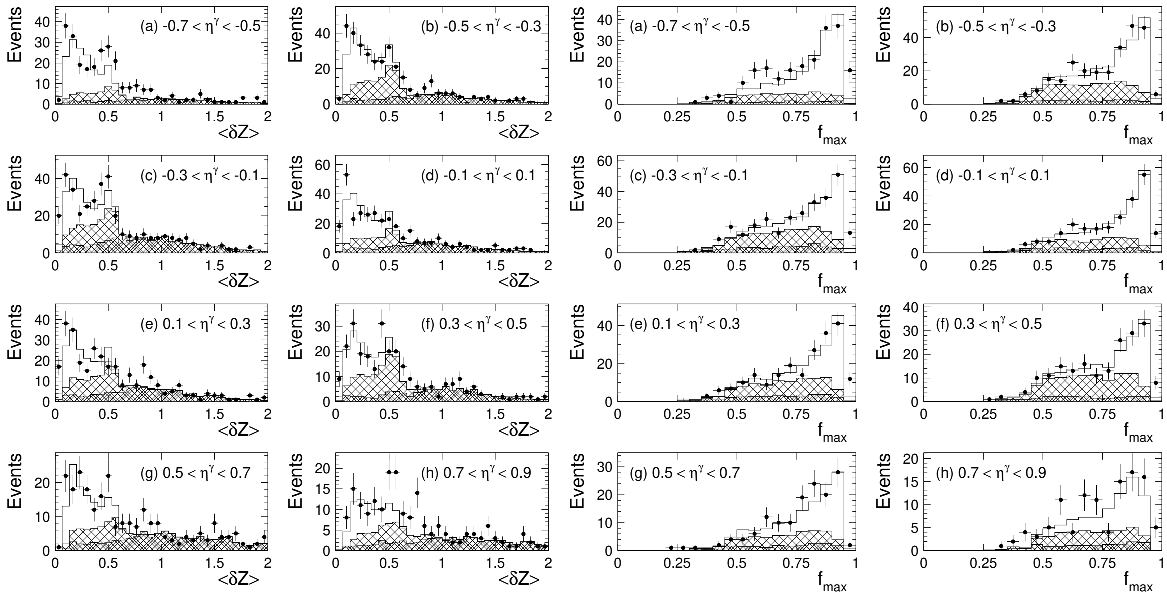

Figure 7.12: The $<\delta Z>$ and f_{max} distributions of the final prompt photon candidates for the photon + jet analysis. The distributions are fitted by using single particle MCs. Plotted are fitted MC curves ; Points = ZEUS 96+97 data ; dashed = MC (η) ; dotted = MC ($\eta + \pi^0$) ; dotted-dashed = MC ($\eta + \pi^0 + \gamma$). The pseudorapidity ranges are from $-0.7 < \eta^\gamma < -0.5$; (**topleft**) to $0.7 < \eta^\gamma < 0.9$; (**bottomright**).

that the data can be reasonably described by the sum of single photon and neutral meson backgrounds in each bin.

Figure 7.12 shows the distribution of $<\delta Z>$ and f_{max} for the event sample with prompt photon candidates accompanied by jet. Also shown is the good agreement between data and fitted MC prediction in each bin as well as those of inclusive prompt photon sample.

7.4 Signal/Background Separation

After the $<\delta Z>$ cut the remaining candidates consisted of true high E_T photons and the remaining π^0 and η backgrounds. Above $f_{max} = 0.75$ the sample typically contains about 50% photons; below it is dominated by neutral meson backgrounds. With the use of the corrected f_{max} distributions of simulated photon, π^0 and η signals, it is possible to perform a background subtraction. The extraction of the photon signal from the mixture of photons and a neutral meson background, as described in previous section, was done by means of the f_{max} distributions.

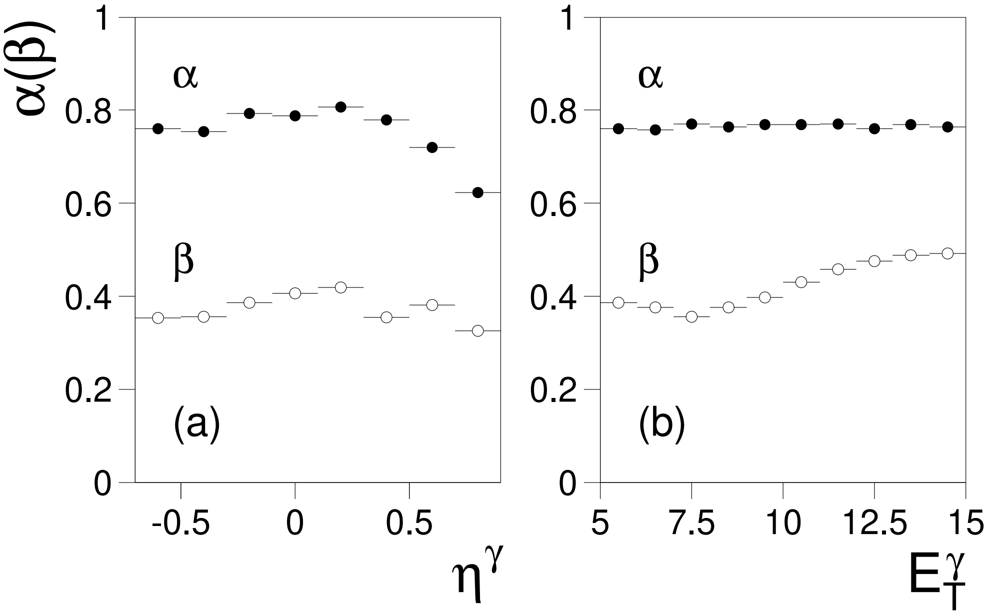

Figure 7.13: The (a) pseudorapidity and (b) transverse energy dependence of the probability that the single particle MC events satisfy the condition $f_{max} \geq 0.75$. The black circles and white circles represent the probability for the single photon and the mixture of single π^0 and η meson MC respectively.

From the f_{max} distribution for the final selection of prompt photon candidate events, the data in each measured bin was divided into two subsamples, consisting of events whose photon candidate has $f_{max} \geq 0.75$, which is enriched in photons, and $f_{max} < 0.75$, which is dominated by mesons, respectively. These will be referred to as "good" (n_{good}) and "poor" (n_{poor}) subsamples. The values of n_{good} and n_{poor} in a bin may be written:

$$\begin{aligned} n_{good} &= \alpha n_{sig} + \beta n_{bgd} \\ n_{poor} &= (1-\alpha) n_{sig} + (1-\beta) n_{bgd} \end{aligned} \tag{7.11}$$

where n_{sig}, n_{bgd} are the numbers of signal (*i.e.* photon) and background (*i.e.* π^0 or η) events in the bin. The coefficient α is the probability that a photon events satisfy the condition $f_{max} \geq 0.75$, and the α is evaluated from the known shapes of the MC f_{max} distributions of the photons. The coefficient β is the probability that a background event satisfied the condition $f_{max} \geq 0.75$, and is estimated by using the fitted $\pi^0 + \eta$ backgrounds. For given observed values of n_{good} and n_{poor} it is now straightforward to solve equation 7.11 for the values of n_{sig} and n_{bgd}, and to evaluate their errors.

The probability of the single photon, π^0 and η meson satisfying the condition $f_{max} \geq 0.75$ are shown in figure 7.13 as a function of (a) η^γ and (b) E_T^γ. As seen in figure 7.13 (b) the single photon MC events show little E_T dependence up to $\sim$ 15 GeV. On the other hand, the single π^0 + η MC events show significant E_T dependence. The showers of π^0 and η mesons become narrower at higher E_T. This means the separation power between photons and neutral mesons is reduced in the high E_T region. This is because more multi–photon clusters which tend to have smaller f_{max} values can survive the $<\delta Z>$ cut at higher E_T region. The ratio $N_\eta/(N_{\pi^0} + N_\eta)$ is evaluated from the results of the $<\delta Z>$ fit for each distribution and the obtained ratio is about 0.25 with a fluctuation of $\pm$ 0.10 for each η^γ and E_T^γ bins. In the analysis, the E_T^γ range is restricted up to 15 GeV. In the η^γ analysis, the E_T^γ range is restricted up to 10 GeV.

7.5 Inclusive Prompt Photon Signals

The signals and backgrounds from the inclusive prompt photon sample are calculated in each bin of any quantity of interest. The results of the signal/background separation procedure are shown in figure 7.14. The quantities plotted are detector–level distributions and are for (a)–(b) photon pseudorapidity, η^γ, and (c)–(d) photon transverse energy, E_T^γ. Both signal and background distributions are of similar magnitude in each bins of η^γ and E_T^γ.

7.6 Prompt Photon + Jet Signals

The signals and backgrounds from the prompt photon + jet sample are also calculated in each bin of any quantity of interest. The results from the signal/background separation procedure are shown in figure 7.15 and figure 7.16 and the values for the separation variables (i.e. n_{good}, n_{poor}, α, β, n_{sig} and n_{bgd}) are listed in table 7.1 and 7.2. The quantities plotted are detector–level distributions, and are x_γ in figure 7.15 and (a)–(b) photon pseudorapidity, η^γ, and (c)–(d) photon transverse energy, E_T^γ, in figure 7.16. Here the x_γ is the fraction of the incident photon energy that contributes to the resolved QCD subprocesses and is described in detail in chapter 9.2.1. In figure 7.16, both signal and background distributions were found to be of a similar shape to those in figure 7.14.

In particular the events with $x_\gamma^{meas} > 0.9$ are predominantly from direct photoproduction processes, and the restriction to high x_γ^{meas} also minimises the effects of hard gluon radiation from the recoil quark. Therefore the signal distribution in figure 7.15 (a) shows a pronounced peak at high x_γ^{meas} values, while the background distribution in figure 7.15 (b) peaks at a lower value.

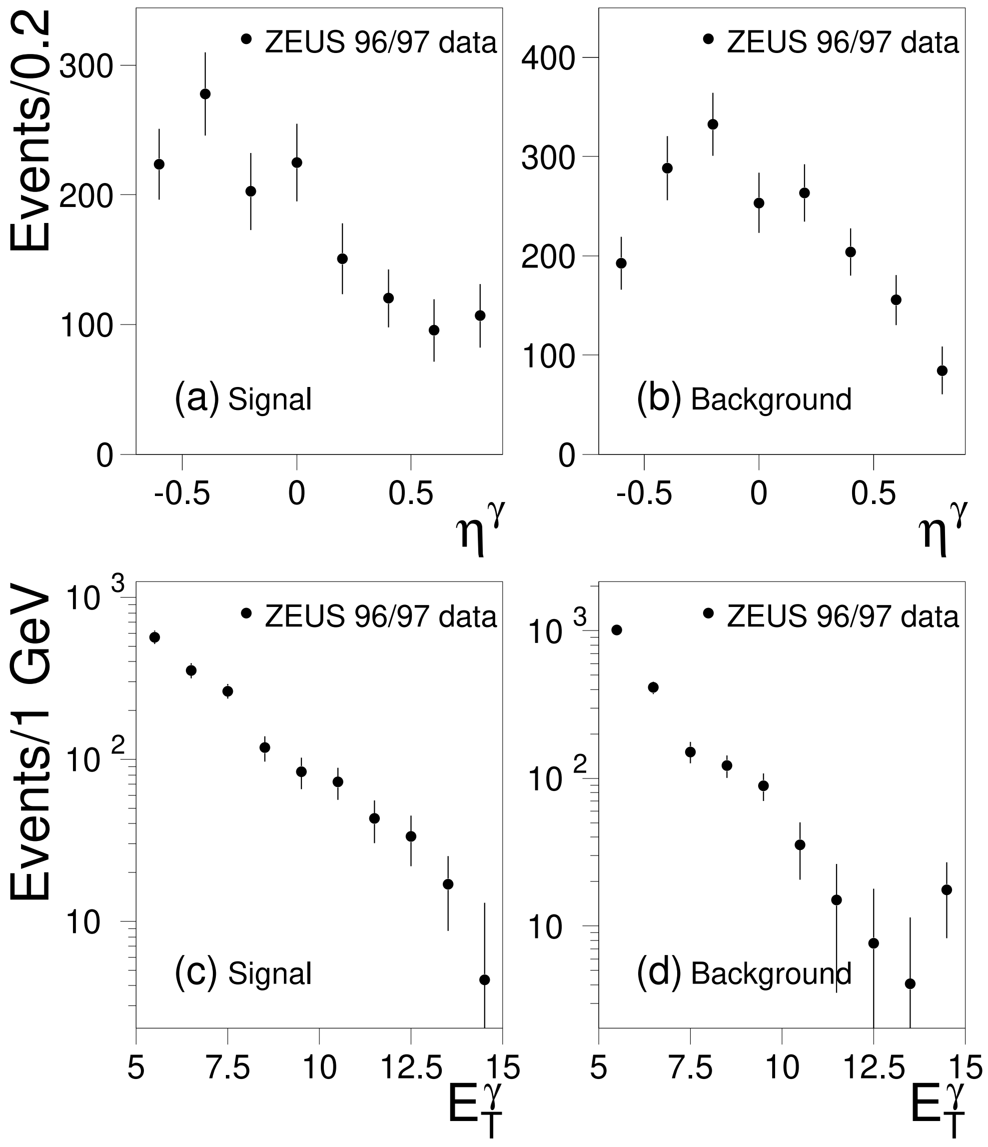

Figure 7.14: The signal and background distributions of kinematic quantities observed in inclusive prompt photon production at ZEUS. The quantities plotted are the detector–level quantities and are: (a)–(b) photon pseudorapidity, η^γ, and (c)–(d) photon transverse energy, E_T^γ.

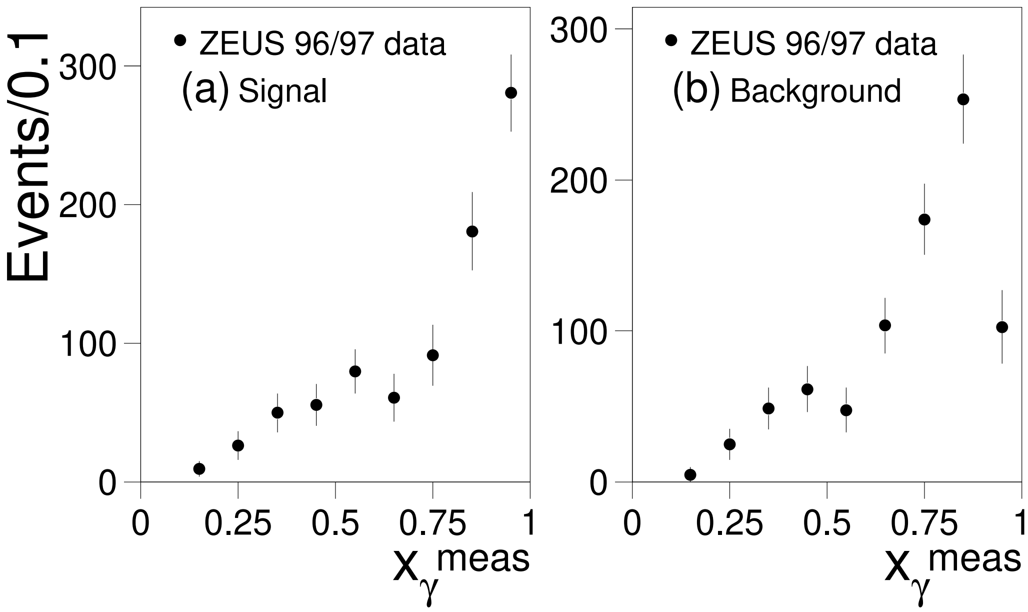

Figure 7.15: The signal and background distributions of x_γ observed in prompt photon + jet production at ZEUS. The x_γ plotted are the detector level quantities and are: (a) signals and (b) backgrounds.

Figure 7.17 shows signal/background distributions of the k_T–sensitive kinematic quantities in the full x_γ region. The quantities plotted are calculated in the plane transverse to the beam direction and are (a) perpendicular momentum component of the photon relative to the axis of the jet ($p_\perp$), (b) longitudinal momentum imbalance (photon–jet) along the axis of the jet ($p_{||}$), (c) absolute momentum component of the photon relative to that of the jet (Q_T) and (d) difference in azimuthal angle between the photon and jet directions ($\Delta\phi$). The occasional negative value arises statistically from the background subtraction procedure. The results from the signal/background separation procedure are listed in table 7.3 to 7.6. A more detailed description of these kinematic quantities follows in chapter 9.2. Figure 7.18 shows the same distributions of kinematic quantities, as discussed in figure 7.17, of the prompt photon + jet system, for events selected with $x_\gamma^{meas} > 0.9$. It shows that the signal distribution has higher statistics than the background distribution after the cut on $x_\gamma^{meas} > 0.9$.

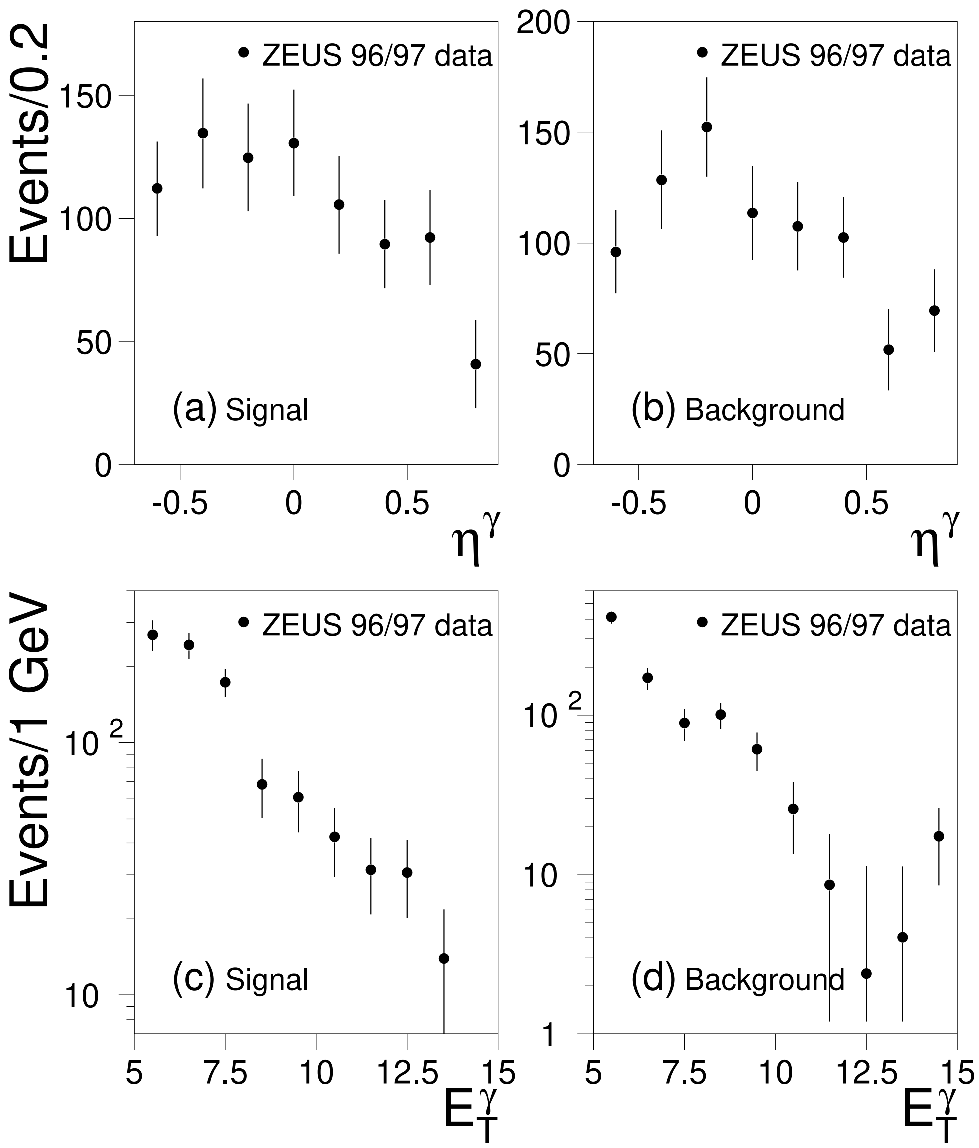

Figure 7.16: The signal and background distributions of kinematic quantities observed in prompt photon + jet production at ZEUS. The quantities plotted are the detector level quantities and are: (a)–(b) photon pseudorapidity, η^γ, and (c)–(d) photon transverse energy, E_T^γ.

x_γ	N_{good}	N_{poor}	α	β	N_{signal}	N_{bgd}
$[0.0, 0.1]$	0.0	0.0	0.0	0.0	0.0 ± 0.0	0.0 ± 0.0
$[0.1, 0.2]$	9	2	0.76	0.41	13.0 ± 5.4	-2.0 ± 3.7
$[0.2, 0.3]$	15	11	0.77	0.40	12.6 ± 7.4	13.4 ± 7.4
$[0.3, 0.4]$	37	27	0.78	0.40	30.2 ± 11.1	33.8 ± 11.3
$[0.4, 0.5]$	55	31	0.78	0.40	54.6 ± 13.3	31.4 ± 12.4
$[0.5, 0.6]$	67	48	0.78	0.40	55.3 ± 14.7	59.7 ± 14.8
$[0.6, 0.7]$	76	64	0.78	0.40	52.0 ± 16.0	88.0 ± 17.1
$[0.7, 0.8]$	149	123	0.78	0.40	105.1 ± 22.4	166.9 ± 23.8
$[0.8, 0.9]$	184	138	0.79	0.40	143.2 ± 24.4	178.8 ± 25.1
$[0.9, 1.0]$	109	44	0.79	0.40	123.5 ± 17.6	29.5 ± 14.7

Table 7.1: The results of the signal/background separation in each x_γ bin ; N_{good}, N_{poor} are subsamples consisting of events with $f_{max} \geq 0.75$ and $f_{max} < 0.75$. N_{sig}, N_{bgd} are numbers of signal and background in x_γ bin. The coefficients α, β are the probabilities that a signal, background event will end up in the good subsample.

η^γ	N_{good}	N_{poor}	α	β	N_{signal}	N_{bgd}
$[-0.7, -0.5]$	93	53	0.80	0.40	86.3 ± 16.3	59.7 ± 15.5
$[-0.5, -0.3]$	102	81	0.77	0.38	84.2 ± 18.4	98.8 ± 18.8
$[-0.3, -0.1]$	120	84	0.80	0.39	99.1 ± 18.8	104.9 ± 19.0
$[-0.1, +0.1]$	107	68	0.79	0.41	92.2 ± 18.2	82.8 ± 18.0
$[+0.1, +0.3]$	93	63	0.81	0.42	70.4 ± 17.1	85.6 ± 17.45
$[+0.3, +0.5]$	82	63	0.79	0.37	67.4 ± 15.4	77.6 ± 15.8
$[+0.5, +0.7]$	64	33	0.76	0.44	66.7 ± 15.8	30.3 ± 14.6
$[+0.7, +0.9]$	40	43	0.71	0.42	19.0 ± 15.7	64.0 ± 17.1

Table 7.2: The results of the signal/background separation in each η^γ bin ; N_{good}, N_{poor} are subsamples consisting of events with $f_{max} \geq 0.75$ and $f_{max} < 0.75$. N_{sig}, N_{bgd} are numbers of signal and background in η^γ bin. The coefficients α, β are the probabilities that a signal, background event will end up in the good subsample.

$p_\perp$	N_{good}	N_{poor}	α	β	N_{signal}	N_{bgd}
$[0.0, 1.0]$	326	211	0.78	0.40	289.3 ± 32.1	247.7 ± 31.4
$[1.0, 2.0]$	243	152	0.78	0.40	223.2 ± 27.8	171.8 ± 26.9
$[2.0, 3.0]$	146	113	0.78	0.40	111.0 ± 22.0	148.0 ± 22.8
$[3.0, 4.0]$	91	87	0.79	0.40	51.5 ± 17.8	126.5 ± 19.8
$[4.0, 5.0]$	70	54	0.78	0.40	53.2 ± 15.4	70.8 ± 15.9

Table 7.3: The results of the signal/background separation in each $p_\perp$ bin ; N_{good}, N_{poor} are subsamples consisting of events with $f_{max} \geq 0.75$ and $f_{max} < 0.75$. N_{sig}, N_{bgd} are numbers of signal and background in $p_\perp$ bin. The coefficients α, β are the probabilities that a signal, background event will end up in the good subsample.

$p_{\parallel}$	N_{good}	N_{poor}	α	β	N_{signal}	N_{bgd}
$[-9.0, -0.7]$	5.5	7.0	0.78	0.40	1.2 ± 4.6	11.3 ± 5.6
$[-0.7, -0.5]$	13.0	8.5	0.79	0.40	11.4 ± 6.4	10.1 ± 6.3
$[-0.5, -0.3]$	33.5	29.0	0.79	0.401	22.0 ± 10.6	40.6 ± 11.5
$[-0.3, -0.1]$	77.5	60.5	0.78	0.40	58.4 ± 16.0	79.6 ± 16.7
$[-0.1, +0.1]$	950.0	43.5	0.78	0.40	103.2 ± 16.8	35.3 ± 14.6
$[+0.1, +0.3]$	41.5	27.0	0.78	0.41	36.3 ± 11.7	31.8 ± 11.5
$[+0.3, +0.5]$	9.5	4.0	0.78	0.40	10.7 ± 5.3	2.8 ± 4.5

Table 7.4: The results of the signal/background separation in each $p_{\parallel}$ bin ; N_{good}, N_{poor} are subsamples consisting of events with $f_{max} \geq 0.75$ and $f_{max} < 0.75$. N_{sig}, N_{bgd} are numbers of signal and background in $p_{\parallel}$ bin. The coefficients α, β are the probabilities that a signal, background event will end up in the good subsample.

Q_T	N_{good}	N_{poor}	α	β	N_{signal}	N_{bgd}
$[0.0, 0.5]$	40.0	8.0	0.78	0.40	54.4 ± 10.4	-6.4 ± 6.9
$[0.5, 1.5]$	96.0	51.0	0.78	0.40	97.1 ± 17.1	49.9 ± 15.7
$[1.5, 3.5]$	125.5	78.0	0.78	0.40	114.8 ± 19.9	88.7 ± 19.2
$[3.5, 6.0]$	48.4	40.8	0.78	0.40	33.2 ± 12.8	56.0 ± 13.7
$[6.0, 9.0]$	15.1	11.4	0.79	0.40	11.67 ± 7.0	14.9 ± 7.3
$[9.0, 15.]$	4.7	3.1	0.78	0.40	4.2 ± 3.8	3.6 ± 3.8

Table 7.5: The results of the signal/background separation in each Q_T bin ; N_{good}, N_{poor} are subsamples consisting of events with $f_{max} \geq 0.75$ and $f_{max} < 0.75$. N_{sig}, N_{bgd} are numbers of signal and background in Q_T bin. The coefficients α, β are the probabilities that a signal, background event will end up in the good subsample.

$\Delta\phi$	N_{good}	N_{poor}	α	β	N_{signal}	N_{bgd}
$[100, 120]$	19.0	16.0	0.78	0.40	13.0 ± 8.1	22.0 ± 8.6
$[120, 140]$	41.5	28.0	0.78	0.40	35.8 ± 11.5	33.7 ± 11.4
$[140, 160]$	105.0	91.0	0.78	0.40	69.4 ± 19.0	126.7 ± 20.4
$[160, 170]$	248.0	154.0	0.78	0.40	228.5 ± 28.0	173.5 ± 27.0
$[170, 180]$	380.0	232.0	0.78	0.40	336.7 ± 34.2	265.3 ± 33.1

Table 7.6: The results of the signal/background separation in each $\Delta\phi$ bin ; N_{good}, N_{poor} are subsamples consisting of events with $f_{max} \geq 0.75$ and $f_{max} < 0.75$. N_{sig}, N_{bgd} are numbers of signal and background in $\Delta\phi$ bin. The coefficients α, β are the probabilities that a signal, background event will end up in the good subsample.

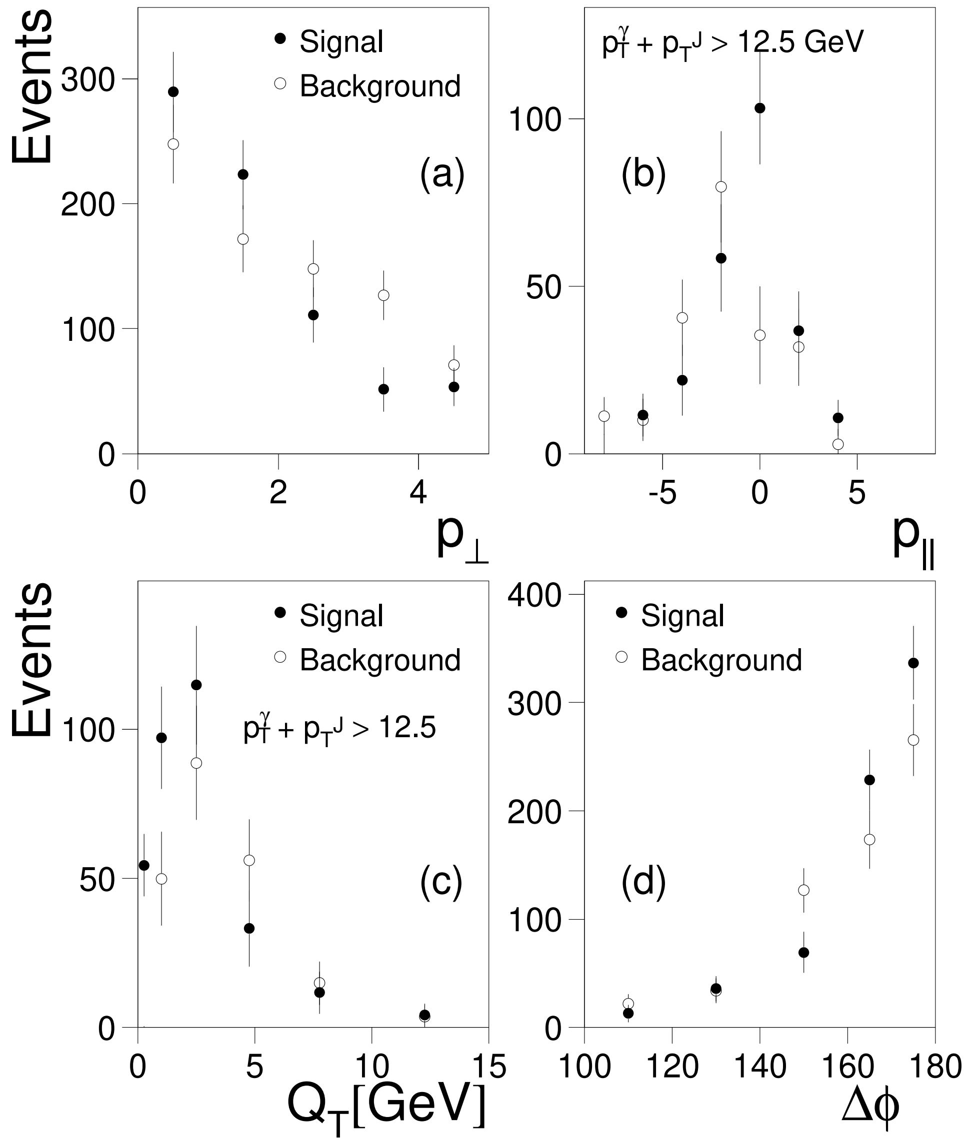

Figure 7.17: The signal and background distributions of kinematic quantities observed in prompt photon production at ZEUS. The quantities plotted are calculated in the plane transverse to the beam direction and are: (a) perpendicular momentum component of the photon relative to the axis of the jet, (b) longitudinal momentum imbalance (photon–jet) along the axis of the jet, (c) absolute momentum component of the photon relative to that of the jet, (d) difference in azimuthal angle between the photon and jet directions.

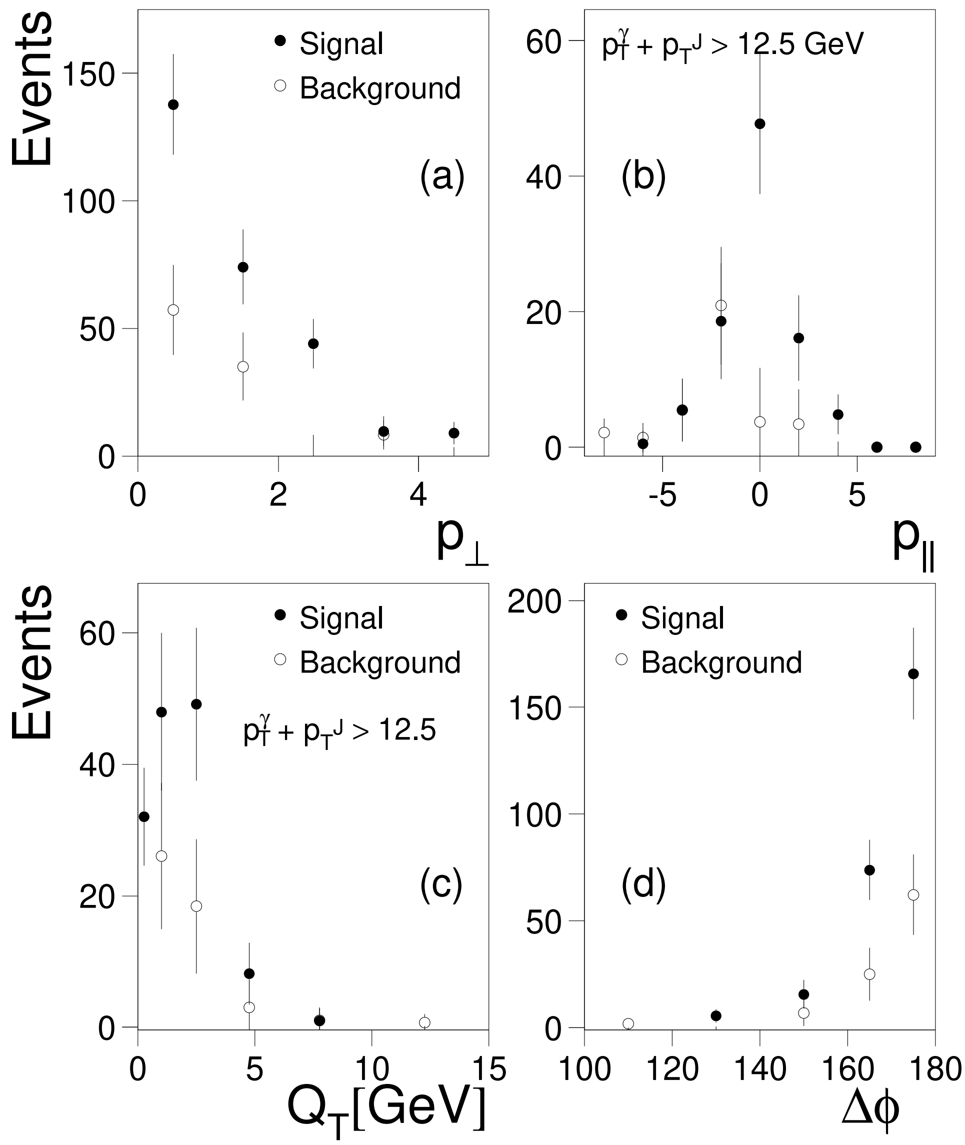

Figure 7.18: The signal and background distributions of kinematic quantities observed in prompt photon production at ZEUS. Only events with $x_\gamma^{meas} > 0.9$ are used. The quantities plotted are calculated in the plane transverse to the beam direction and are: (a) perpendicular momentum component of the photon relative to the axis of the jet, (b) longitudinal momentum imbalance (photon–jet) along the axis of the jet, (c) absolute momentum component of the photon relative to that of the jet, (d) difference in azimuthal angle between the photon and jet directions.

Chapter 8

Cross section Measurement of Inclusive Prompt Photons

The photoproduction of isolated prompt photons within the kinematic range $0.2 < y < 0.9$, equivalent to incident γp centre-of-mass energies W of 134–285 GeV, has been measured in the ZEUS detector at HERA, using an integrated luminosity of 38.4 pb^{-1}. Inclusive cross sections for $\gamma p \to \gamma + X$ are presented as a function of E_T^γ for the photoproduction of isolated prompt photons in the pseudorapidity range $-0.7 < \eta^\gamma < 0.9$, and as a function of η^γ for photons with $5 < E_T^\gamma < 10$ GeV. The latter results are given for the full y range and three partial ranges. The systematic uncertainties are discussed. Comparisons are made with predictions from Monte Carlo models containing leading-logarithm parton showers, and with next–to–leading–order QCD calculations, using currently available parameterisations of the photon structure.

8.1 Hadron Level Kinematic Region

In order to compare the data with theoretical calculations, the number of events measured at the detector level should be corrected back to the hadron level quantity. Hadron level cross sections for the inclusive prompt photon in hard photoproduction are measured within the following kinematic ranges.

- $5 < E_T^\gamma < 15$ GeV and $-0.7 < \eta^\gamma < 0.9$ for $d\sigma/dE_T^\gamma$
  $5 < E_T^\gamma < 10$ GeV and $-0.7 < \eta^\gamma < 0.9$ for $d\sigma/d\eta^\gamma$
- $\sum E_T^{calo+tracks} < 0.1 \times E_T^\gamma$
- $0.2 < y < 0.9$

In addition the virtuality of the incident photon is restricted to the range $Q^2 \lesssim 1$ GeV^2, with a median value of approximately 10^{-3} GeV^2.

8.2 Corrected Data

In this section we present a study of a procedure based on Monte Carlo events which is able to correct measured ZEUS data to the hadron level. The PYTHIA 5.7 and HERWIG 5.9 MC samples described in chapter 5 were used. A bin–by–bin correction method was applied to the detector–level measurements, in the specified kinematic intervals calculated in terms of the final state hadron system.

8.2.1 Efficiencies and Purities

There are two steps in measuring the cross section corrected to the hadron level. The correction of photon transverse energies and other quantities which give good correspondence between detector and hadron level was discussed in chapter 6. The next step, presented in this sub–section, is the correction for the detector acceptance to the events to be measured.

The bin efficiency, defined as,

$$\text{Efficiency (i)} = \frac{\text{\# of Event generated \& reconstructed in a bin (i)}}{\text{\# of Event generated in a bin (i)}} \tag{8.1}$$

is of interest since it gives the fraction of 'true' hadron level events which are reconstructed at detector level in the same bin. The higher the efficiency, the greater the fraction of hadron level events which are measured by the experiment in the same bin of the distribution. This minimises the extrapolation of the measurement into unmeasured regions.

The bin purity is defined as,

$$\text{Purity (i)} = \frac{\text{\# of Event generated \& reconstructed in a bin (i)}}{\text{\# of Event reconstructed in a bin (i)}} \tag{8.2}$$

and gives the fraction of the events reconstructed experimentally which actually have a corresponding 'true' hadron level event in the same bin of the distribution. High purities indicate that the contamination of the sample from events migrating from other bins is small.

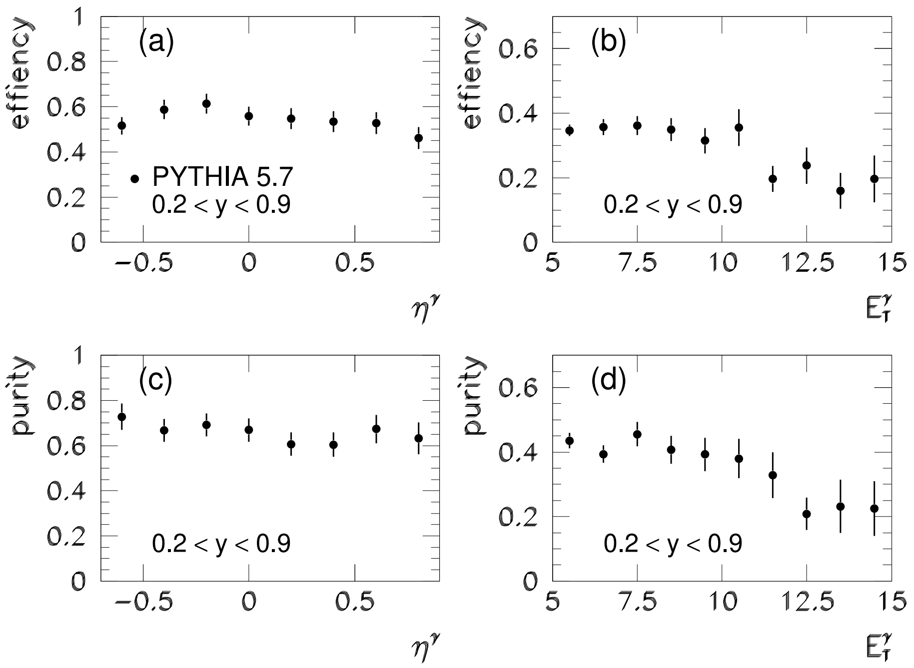

Figure 8.1: (a) efficiency and (c) purity for PYTHIA events as a function of η^γ. (b) efficiency and (d) purity for PYTHIA events as a function of E_T^γ

Figure 8.1 shows the efficiency and purity as a function of η^γ and E_T^γ for events passing the inclusive photon event selection detailed above. The efficiency varies between 45% and 60% in η^γ bins, and 20% and 45% in E_T^γ bins, being lower at high E_T^γ. The purity is around 70% in (c) η^γ bins and and 45% and 60% in (d) E_T^γ bins. The main reason for the loss of the purity and efficiency comes from the smearing of the E_T^γ measurement. Smaller efficiency at forward region is due to the y^{meas} cut.

The same quantities for events with restricted y ranges are also shown in figure 8.2. The efficiencies in the three partial y ranges are around 45%. The purities are around 50% in the lower y range ((d) : $0.2 < y < 0.32$), and approximately flat in the higher y ranges ((e),(f)) and around 60%.

8.2.2 Correction factors

A measured distribution can be corrected from detector to hadron level by applying the MC based bin–by–bin method provided that the MC describes the data and can account for migrations between bins.

The combination of the efficiency and purity gives the correction factor to

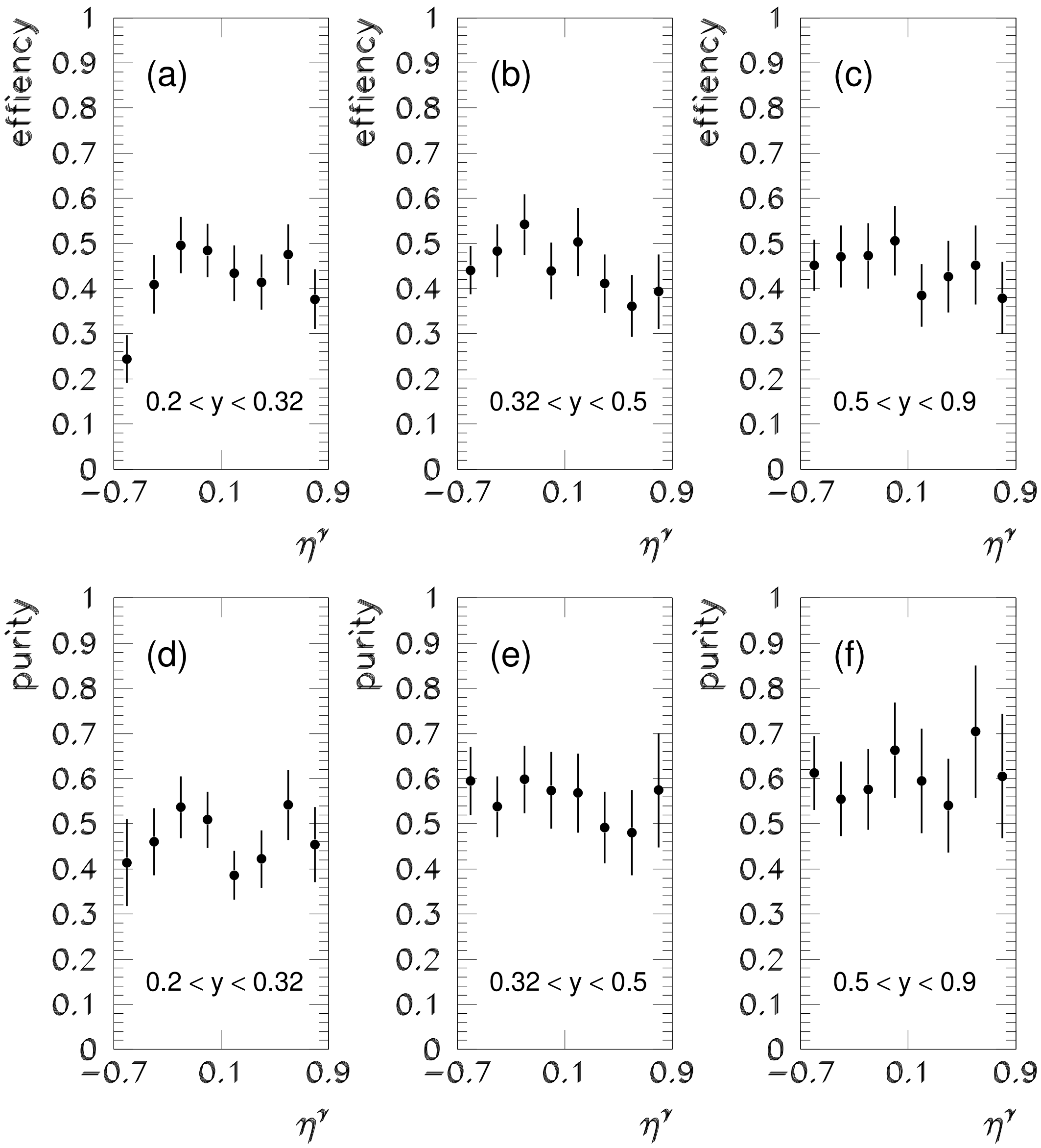

Figure 8.2: Efficiency and purity for PYTHIA events as a function of η^γ. The plots are for the three partial y (y^{meas}) ranges ; (a),(d) $0.2 < y < 0.32$ ($0.15 < y^{meas} < 0.25$), (b),(e) $0.32 < y < 0.5$ ($0.24 < y^{meas} < 0.4$) and (c),(f) $0.5 < y < 0.9$ ($0.4 < y^{meas} < 0.7$). The corresponding W ranges are 134–170 GeV, 170–212 GeV and 212–285 GeV.

compensate for the detector acceptance. The relation between the purity, efficiency and correction factor is defined as ;

$$\text{Acceptance correction factor (i)} = \frac{\text{Purity (i)}}{\text{Efficiency (i)}} \tag{8.3}$$

Figure 8.3 shows the correction factors which should be applied to the data distributions to obtain hadron level cross sections. The correction factor for the inclusive prompt photon η^γ distribution is within the range between 1.2 to 1.4 (see (a)). Also plotted in (c) $\sim$ (e) are the correction factors as a function of η^γ for each restricted y range. The correction factors for η^γ vary for the most part between 1.1–1.4 except in the lowest bin of (c) and the highest bin of (d),(e). The correction factors for E_T^γ are also relatively flat except in the higher E_T^γ regions (above 11 GeV) and around 1.2.

8.2.3 Cross–section Calculation

The differential cross sections for the inclusive prompt photon production as a function of E_T^γ and η^γ were obtained by a bin–by–bin correction method according to the formulae ;

$$\frac{d\sigma}{d\eta^\gamma} = \frac{N(\eta^\gamma) \cdot C(\eta^\gamma)}{\Gamma(\eta^\gamma) \cdot \int \mathcal{L}\, dt} \tag{8.4}$$

$$\frac{d\sigma}{dE_T^\gamma} = \frac{N(E_T^\gamma) \cdot C(E_T^\gamma)}{\Gamma(E_T^\gamma) \cdot \int \mathcal{L}\, dt} \tag{8.5}$$

where $N(\eta^\gamma)$ and $N(E_T^\gamma)$ are the number of events measured in η^γ and E_T^γ bin respectively. The terms $C(\eta^\gamma)$ and $C(E_T^\gamma)$ are multiplicative factors to correct for detector acceptance, $\int \mathcal{L}\, dt = 38.4\ \text{pb}^{-1}$ is the integrated luminosity of the data analysed. The $\Gamma(\eta^\gamma)$ and $\Gamma(E_T^\gamma)$ comes from dividing by bin–width.

8.3 Study of Systematic Uncertainties

The systematic uncertainty in the cross section measurement was studied by making changes in the event selection and data correction procedures. The sources of systematic uncertainties were grouped into the following categories; calorimeter energy scale, modelling of the shower shape, $\eta/(\eta + \pi^0)$ ratio, kinematic cuts, model dependence of detector corrections. For each check, the full analysis was

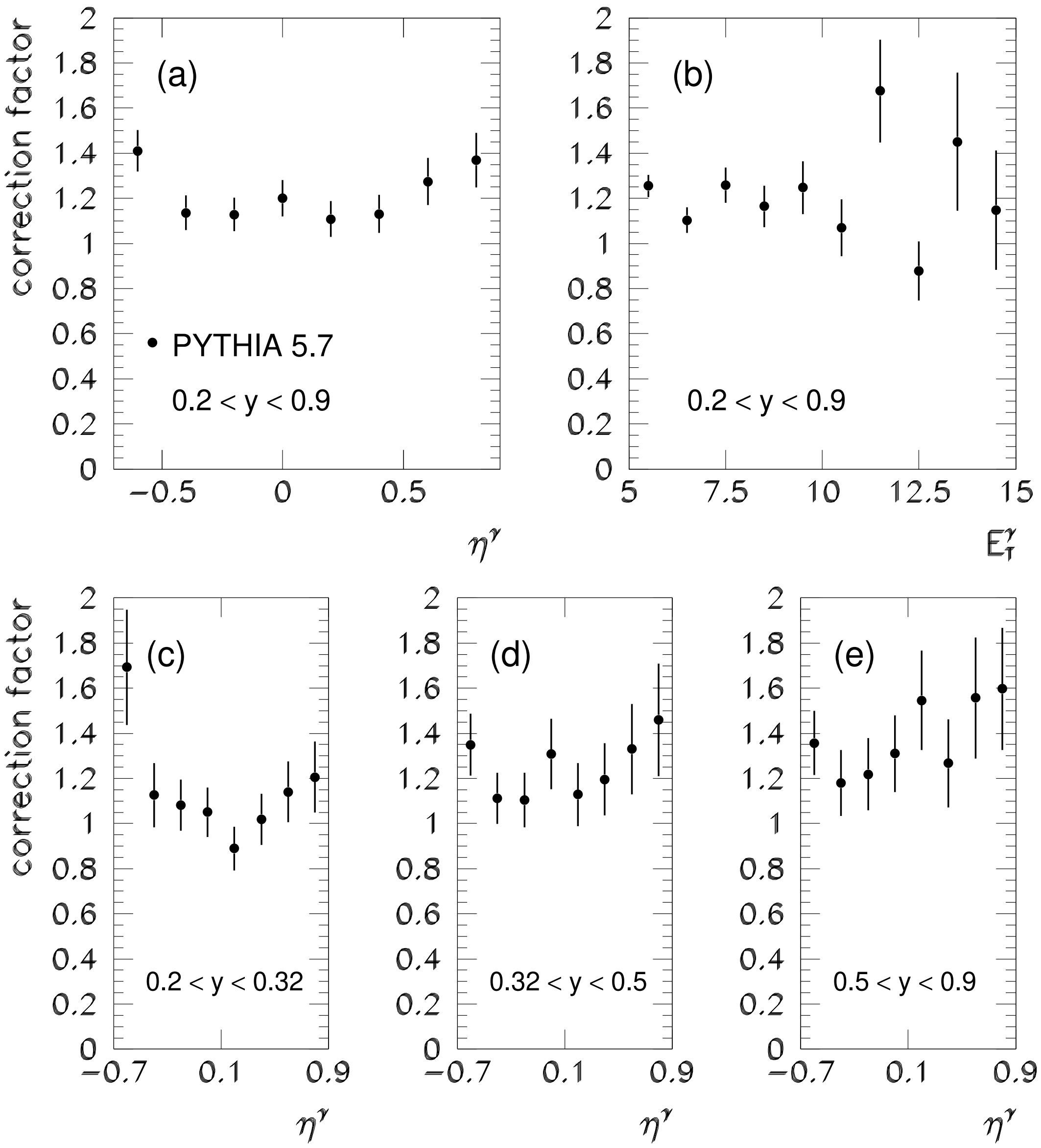

Figure 8.3: Detector to Hadron level correction factors obtained from PYTHIA events as a function of (a) η^γ and (b) E_T^γ for the full y (y^{meas}) ranges; $0.2 < y < 0.9$ ($0.15 < y^{meas} < 0.7$). The (c) $\sim$ (e) are for the three partial y (y^{meas}) ranges; (c) $0.2 < y < 0.32$ ($0.15 < y^{meas} < 0.25$), (d) $0.32 < y < 0.5$ ($0.24 < y^{meas} < 0.4$) and (e) $0.5 < y < 0.9$ ($0.4 < y^{meas} < 0.7$); the corresponding W ranges are 134–170 GeV, 170–212 GeV and 212–285 GeV.

repeated. The first three classes were attributed to the experimental systematic error. The results of this study are shown in figure 8.4 to figure 8.5 for the data points obtained in the following ways.

Calorimeter energy scale :

1. Change of the calorimeter energy scale by + 3%
2. Change of the calorimeter energy scale by – 3%

The energy scale of the calorimeter was varied for the extracted hadronic final state by $\pm 3\%$. This was done to account for a possible uncertainty in the absolute energy scale of the calorimeter. The uncertainty of the simulation of the calorimeter response [82] gives rise to an uncertainty on the cross sections of $\pm$ 7–10%.

Modelling of the shower shape :

1. f_{max} correction factor of the single photon MC raised by + 0.009
2. f_{max} correction factor of the single photon MC lowered by – 0.009
3. f_{max} correction factor of the π^0 and η MC raised by + 0.014
4. f_{max} correction factor of the π^0 and η MC lowered by – 0.014
5. Change of the E_T slope of the single particle MC

As discussed in chapter 7 the uncertainties from the modelling of the shower shape were evaluated for the fits used to estimate the correction factors applied to the single particle MC f_{max} distributions. The systematic uncertainties due to the resulting fit procedure were $\pm$ 0.009 and $\pm$ 0.014 for MC f_{max} distribution of single photon and π^0/η meson backgrounds respectively (see equation 7.8 and 7.10). These were taken into account as systematic sources. These gave rise to a systematic error averaging $\pm 8\%$ on the final cross sections.

The single particle MC events were E_T weighted according to e^{-aE_T} to reproduce the E_T shapes seen in the data. The systematic effect on the slope of the E_T distribution of the single particle MC was checked by varying the constant, a, in the weighting formulae and this contributed as uncertainty of up to 1%.

$\eta/(\eta+\pi^0)$ **ratio :**

1. Ratio of η meson to the background events set to 15%.
2. Ratio of η meson to the background events set to 35%.

The η meson contribution to the background was estimated from the fit of the $<\delta Z>$ distribution in each physical bin. The fitted value was typically 25% with $\pm$ 10% uncertainty. Variations of the ratio (to 15% and 35% respectively), allowing for the imperfect fit to the distribution, led to cross section variations of $\sim \pm 2\%$.

Correction factor :

1. HERWIG used for acceptance correction.
2. Cross–section of the radiative MC halved.
3. Cross–section of the radiative MC doubled.
4. Cross–section of the direct photon MC raised by 20%.
   Cross–section of the resolved photon MC lowered by 10%.

Hadron level correction factors were also evaluated using the HERWIG MC model to investigate the MC model dependence. Both MC models gave a reasonable description of the shape of measured E_T cross sections; the average cross section using HERWIG was lower by $\sim \pm 1\%$.

In addition, studies were made of the effects of varying the composition of the MC simulation in terms of direct, resolved and radiative processes. The fraction of the different processes contributing to the combined MC samples were varied by amounts corresponding to their estimated uncertainties. The cross sections were insensitive to this, changing by at most 1%.

Kinematic selection cuts :

1. $E_T^\gamma > 5$ GeV $\rightarrow 5.5$ GeV
2. $y^{meas} > 0.15 \rightarrow 0.18$
3. $y^{meas} < 0.7 \rightarrow 0.6$
4. $\sum E_T^{calo+tracks} < 0.1E_T^\gamma \rightarrow 0.05E_T^\gamma$
5. $\sum E_T^{calo+tracks} < 0.1E_T^\gamma \rightarrow 0.15E_T^\gamma$
6. $\Delta R \equiv \sqrt{(\Delta\phi)^2 + (\Delta\theta)^2} < 0.3 \rightarrow \sqrt{(\Delta\phi)^2 + (\Delta\theta)^2} < 0.2$

7. $\Delta R \equiv \sqrt{(\Delta\phi)^2 + (\Delta\theta)^2} < 0.3 \rightarrow \sqrt{(\Delta\phi)^2 + (\Delta\theta)^2} < 0.4$
8. $<\delta Z> < 0.65 \rightarrow 0.75$
9. z–vertex cuts; $(-50, +40$ cm$) \rightarrow (-20, +20$ cm$)$

These systematic sources show the effect of events migrating into the data sample from outside the kinematic range of interest. The cuts defining the accepted kinematic range at the detector level were varied by amounts corresponding to the resolution on the variables. For each check the full analysis was repeated. Changes of up to 5% in the cross section were observed.

Total systematic uncertainty :

Figures 8.4 and 8.5 show the deviation from the central cross section values in the analysed η^γ and E_T^γ bins respectively, for the different systematic checks. The numbers on the x–axis refer to the systematic sources detailed above and the line at zero refers to the position of the nominal value. The major systematic effect on the cross section measurement comes from the calorimeter energy scale in the detector simulation and the modelling of the shower shape.

All systematic errors were combined in quadrature to give the total systematic error. The final systematic uncertainty in the inclusive prompt photon cross sections are around 15%. For the differential cross sections $d\sigma/d\eta^\gamma$ and $d\sigma/dE_T^\gamma$ for prompt photon production, they were added in quadrature to the statistical errors and are indicated as the outer error bars in figure 8.7 to 8.10.

8.4 Measured Cross Sections

It is of interest to consider the feasibility of distinguishing between different models of the photon structure (see chapter 2 for details). To look at such a possibility from the experimental point of view, differential cross sections as a function of pseudorapidity and transverse energy of the photon within the defined set of hadron level kinematic cuts are compared with predictions from leading–logarithm parton–shower Monte Carlos and next–to–leading order QCD calculations using currently available models of the photon structure. The measurement can be also used to test NLO pQCD calculations.

The obtained differential cross sections are presented in the tables (see Appendix C); $d\sigma/dE_T^\gamma$ (Table 1) and $d\sigma/dE_T^\gamma$ (Table 2) for the range $0.2 < y < 0.9$. The $d\sigma/d\eta^\gamma$ for the three partial y ranges are presented in table 2; for the $0.2 < y < 0.32$, $0.32 < y < 0.5$ and $0.5 < y < 0.9$, respectively.

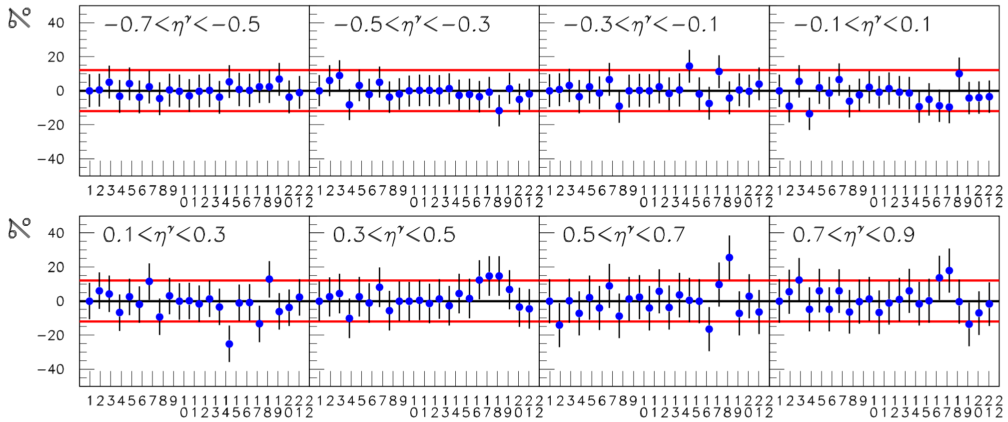

Figure 8.4: Summary of systematic uncertainties for $d\sigma/d\eta^{\gamma}$. Sources of systematic uncertainties are grouped into the three areas; experimental, detector level selection cuts and correction factor. The experimental uncertainty is subdivided into; (1–2) calorimeter energy scale, (3–6) modelling of shower shape, (7–8) $\eta/(\eta+\pi^0)$ ratio and (9) varying the E_T-distribution applied to the single-particle samples.

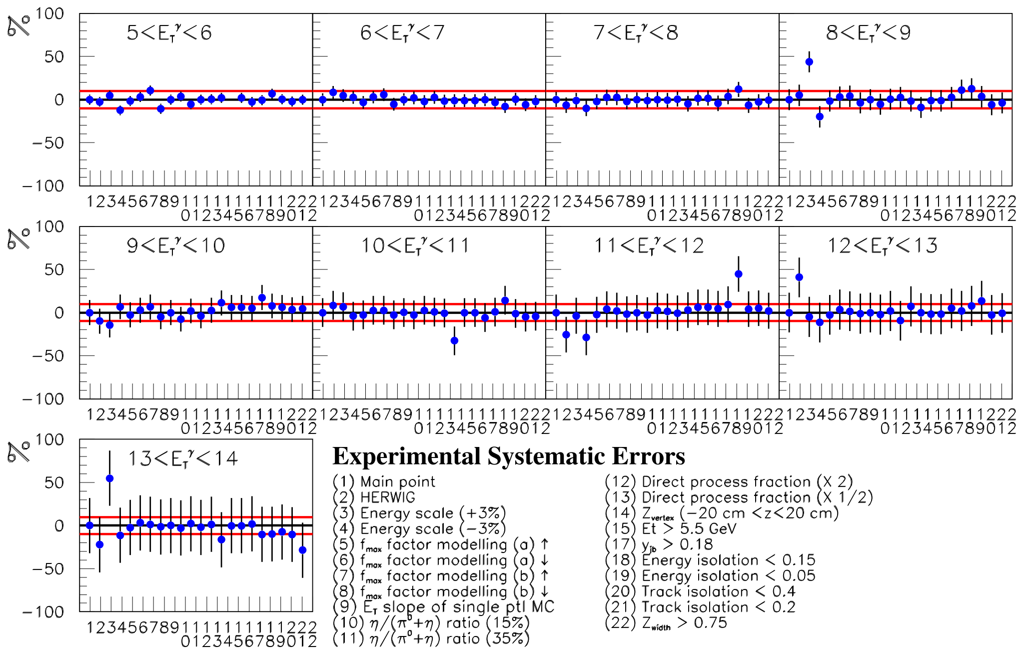

Figure 8.5: Summary of systematic uncertainties for $d\sigma/dE_T^{\gamma}$. Sources of systematic uncertainties are grouped into the three areas; experimental, detector level selection cuts and correction factor. The experimental uncertainty is subdivided into; (1–2) calorimeter energy scale, (3–6) modelling of shower shape, (7–8) $\eta/(\eta+\pi^0)$ ratio and (9) varying the E_T-distribution applied to the single-particle samples.

8.5 Theoretical Calculations

In presenting cross sections, comparison is made with two types of theoretical calculation, in both of which the photon and proton parton density function (pdf) can be varied. There is, however, little sensitivity to the proton parton densities.

8.5.1 Leading–logarithm parton shower MC models

PYTHIA 5.7 and HERWIG 5.9 calculations evaluated at the final state hadron level, were outlined in Chapter 5. These comprise LO matrix elements accompanied by higher order effects in the initial and final states together with hadronization. Differences between the two LO MC models lie in the treatment of the contributions from perturbative radiation and the non–perturbative fragmentation. The general features of the two MC models are discussed in Chapter 5. All prompt photon processes were combined finally according to their relative cross sections.

8.5.2 NLO parton–level calculations

Theoretical NLO pQCD calculations for prompt photon photoproduction have been made available from two theoretical groups :

- Gordon (LG) [22, 83]
- Krawczyk and Zembrzuski (K&Z) [84]

These calculations include point–like and hadronic diagrams at the Born level, together with virtual (loop) corrections and terms taking into account three–body final states. The radiative terms are in both cases included by means of fragmentation functions obtained from experiment. The renormalization and factorisation scales (QCD scale) in both calculations are taken to be equal to the photon transverse momentum, $Q^2 = (P_T^\gamma)^2$. In both calculations, the isolation criterion for the prompt photon was applied at the parton level.

The two NLO calculations differ in several respects [85], for instance in the way of power–counting of the strong coupling constant, α_s, and in the treatment of higher order corrections. In figure 8.6 a diagrammatic comparison is made between two NLO parton–level calculations in detail. The LG calculation treats the

DIAGRAM	GORDON	KRAWCZYK ET AL.
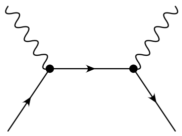	$O(\alpha^2)$ LO+NLO	$O(\alpha^2)$ LO+NLO
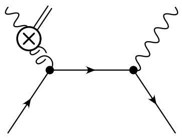	$O(\alpha\alpha_s)O(\alpha/\alpha_s)=O(\alpha^2)$ LO+NLO	$O(\alpha\alpha_s)O(\alpha)=O(\alpha^2\alpha_s)$ (N)LO
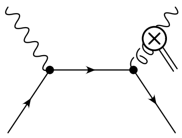	$O(\alpha\alpha_s)O(\alpha/\alpha_s)=O(\alpha^2)$ LO+NLO	$O(\alpha\alpha_s)O(\alpha)=O(\alpha^2\alpha_s)$ (N)LO
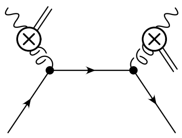	$O(\alpha_s^2)O(\alpha^2/\alpha_s^2)=O(\alpha^2)$ LO+NLO	$O(\alpha_s^2)O(\alpha^2)=O(\alpha^2\alpha_s^2)$ (NN)LO
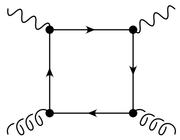	$O(\alpha^2\alpha_s^2)$ --	$O(\alpha^2\alpha_s^2)$ NNLO

Figure 8.6: Diagrammatic comparison of two prompt photon QCD calculations [85]. Gordon calculates the NLO corrections to the direct, single–resolved, and double–resolved contributions, whereas Krawczyk et al. only calculate the corrections to the direct contribution. On the other hand, Krawczyk takes into account the box diagram that arises at NNLO and contributes at the 7% level. The classifications differ although the calculation in principle do not.

photon structure and fragmentation functions as order of $\mathcal{O}(\alpha/\alpha_s)$ from considering the asymptotic limit and calculates the NLO corrections to all subprocesses in figure 8.6. The K&Z calculation, however, treats the photon structure and fragmentation functions as order of $\mathcal{O}(\alpha)$ and calculates the NLO corrections only to the direct process. As a result the resolved term and direct fragmentation term contributes at $\mathcal{O}(\alpha^2\alpha_s)$ and the resolved fragmentation process contribute at $\mathcal{O}(\alpha^2\alpha_s^2)$. Therefore the resolved fragmentation process is regarded as NNLO process. As a result a higher order correction to the resolved terms is excluded, while a box diagram contribution for the process $\gamma g \to \gamma g$ [86] is included in the calculation.

In LG a value of $\Lambda_{\overline{\rm MS}} = 200$ MeV (5 flavours) is used, while in K&Z $\Lambda_{\overline{\rm MS}}$ is chosen to be 320 MeV (4 flavours) so as to reproduce a fixed value of $\alpha_S = 0.118$ at the Z^0 mass. Both NLO calculations use higher order (HO) versions of the GRV [16] and GS [87] photon pdf sets. In particular the GS calculation used CTEQ4M for the proton pdf, while in K&Z GRV is chosen for the proton pdf.

8.6 Comparisons with Theoretical Calculations

The aim of the present section is to make a quantitative comparison between measured inclusive prompt photon cross sections in photoproduction at HERA and the corresponding LO and NLO QCD predictions. Such a comparison can be used as a quantitative test of pQCD and may also provide a new perspective on the present theoretical modelling of the hadronic structure of the photon.

The comparisons of the inclusive prompt photon data with the theoretical predictions were made as follows.

- Differential cross sections $d\sigma/dE_T^\gamma$ for prompt photons produced over $-0.7 < \eta^\gamma < 0.9$ were compared with the LO MC models and with the LG and K&Z NLO predictions.
- Differential cross sections $d\sigma/d\eta^\gamma$ for prompt photons with $5 < E_T^\gamma < 10$ GeV, for $134 < W < 285$, were compared with the LO MC models and with the LG and K&Z NLO predictions.
- Differential cross sections $d\sigma/d\eta^\gamma$, for prompt photons with $5 < E_T^\gamma < 10$ GeV, were compared with the LO PYTHIA model and with the LG and K&Z NLO predictions, in the varying W ranges (1) 134–170 GeV, (2) 170–212 GeV and (3) 212–285 GeV.

8.6.1 Differential cross section $d\sigma/dE_T^\gamma$

Figure 8.7 gives the inclusive cross section $d\sigma/dE_T^\gamma$ for the production of isolated prompt photons in the range $-0.7 < \eta^\gamma < 0.9$. The inner (thick) error bars are statistical, the outer include systematic errors added in quadrature. All the theoretical models describe the shape of the data well; however the predictions of PYTHIA and especially HERWIG are lower than the data. Both MC distributions are the sum of the corresponding subprocesses for prompt photon

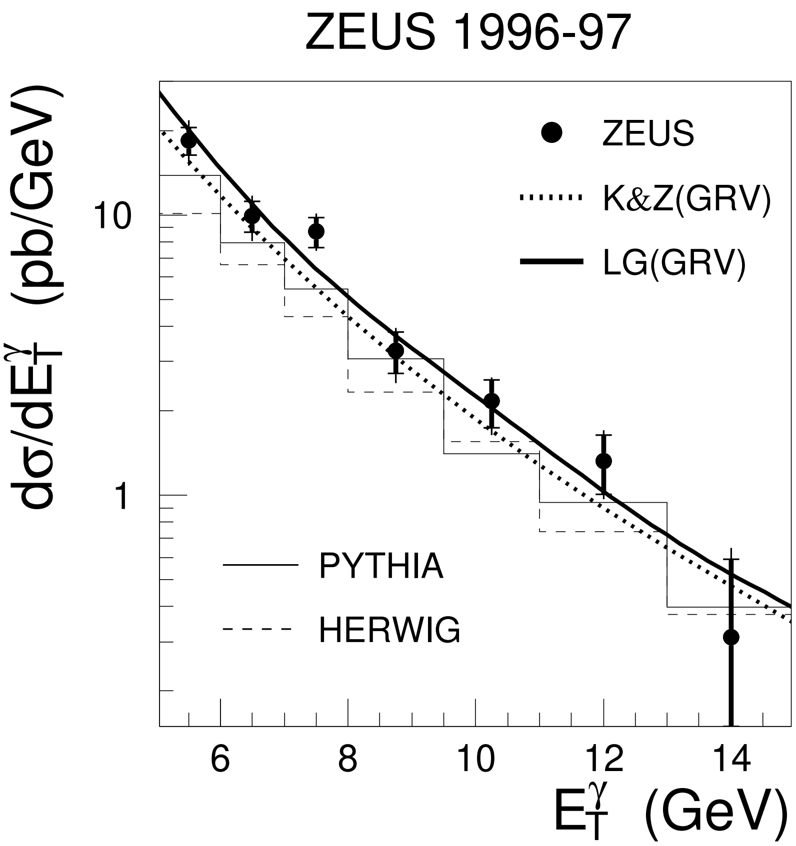

Figure 8.7: Differential cross section $d\sigma/dE_T^\gamma$ for prompt photons produced over $-0.7 < \eta^\gamma < 0.9$. The inner (thick) error bars are statistical; the outer include systematic errors added in quadrature. Predictions are shown from PYTHIA, HERWIG (histograms) and LG, K&Z (curves). In K&Z, the default 4-flavour NLO $\Lambda_{\overline{\mathrm{MS}}}$ value of 320 MeV is used.

production at HERA and are normalised to the same integrated luminosity as the data. The results from the two NLO calculations, LG and K&Z, are also overlaid on the plot. In the K&Z calculation, the default 4–flavour NLO $\Lambda_{\overline{\mathrm{MS}}}$ value of 320 MeV is used, while in the LG a value of $\Lambda_{\overline{\mathrm{MS}}} = 200$ MeV (5–flavours) is used. The NLO calculations are in better agreement with the data, and are indistinguishable from each other within the present experimental uncertainties.

8.6.2 Differential cross–section $d\sigma/d\eta^\gamma$ for full y range

Figure 8.8 (a)–(d) give the inclusive cross section $d\sigma/d\eta^\gamma$ for isolated prompt photons in the range $5 < E_T < 10$ GeV with $0.2 < y < 0.9$, compared to the theoretical models. The measured cross section rises at negative photon rapidity and decreases with increasing photon rapidity. The two different predictions from leading logarithm parton shower Monte Carlo models, PYTHIA 5.7 and HERWIG 5.9 are shown in figure 8.8 (a). Using the GRV–LO photon parton distribution, PYTHIA 5.7 gives a good description of the data for forward pseudorapidities, but is low in the rear region. The HERWIG distribution, while similar in shape to that of PYTHIA, is lower throughout; this is attributable chiefly to the lower value of the radiative contribution in HERWIG. Figure 8.9 confirms this interpretation. Overlaid on the measured cross section in figure 8.9 (a) and (b) are the contributions of the subprocesses to the inclusive prompt photon production predictions from PYTHIA and HERWIG respectively. The difference between the two MCs mainly comes from the radiative contribution in the fragmentation processes.

The K&Z and LG calculations using GRV are similar to each other and to PYTHIA as seen in figure 8.8 (b) which also illustrates the effects of varying the photon parton densities, comparing the results using GRV with those using GS. The ACFGP parton set [88] gives results similar to GRV. All NLO calculations describe the data well for $\eta^\gamma > 0.1$, as does PYTHIA, while being low at more backward η^γ values. The K&Z calculation using GRV and $\Lambda_{\overline{\mathrm{MS}}} = 320$ MeV gives the best description overall, which is still low for negative η^γ.

The effects of varying some of the quantities in the K&Z calculation relative to their standard values (NLO, 4 flavours, $\Lambda_{\overline{\mathrm{MS}}} = 320$ MeV, GRV photon pdf) are shown in figure 8.8 (c). Changing $\Lambda_{\overline{\mathrm{MS}}}$ to 200 MeV (for comparison with LG) lowered the cross sections by 9%. Reducing the the number of flavours in the calculation to three ($\Lambda_{\overline{\mathrm{MS}}} = 365$ MeV) reduced the cross sections by 35–40% across the η^γ range, confirming the need for a charm contribution in the calculation. A LO calculation (evaluated with $\Lambda_{\overline{\mathrm{MS}}} = 120$ MeV and a NLO radiative contribution) was approximately 25% lower than the standard NLO. Variations of the QCD scale between $0.25E_T^2$ and $4E_T^2$ gave cross section variations of approximately $\pm 3\%$.

In figure 8.8 (d), the effect was investigated of varying the magnitude of the photon pdf's in the K&Z calculation. Both two times and three times the photon parton densities in the resolved component for the high x_γ range (i.e. $x_\gamma > 0.8$) increase the cross section in the backward rapidity region, $-0.7 < \eta^\gamma < -0.4$, while keeping the lines within experimental uncertainties in the forward rapidity region. This is of course very artificial but may indicate a need to reexamine the theoretical modelling of the high–x_γ resolved photon.

Finally the theoretical calculations characterise the data normalization and shape in the positive rapidity region, however, it appears to systematically underestimate the measured cross section in the negative rapidity region.

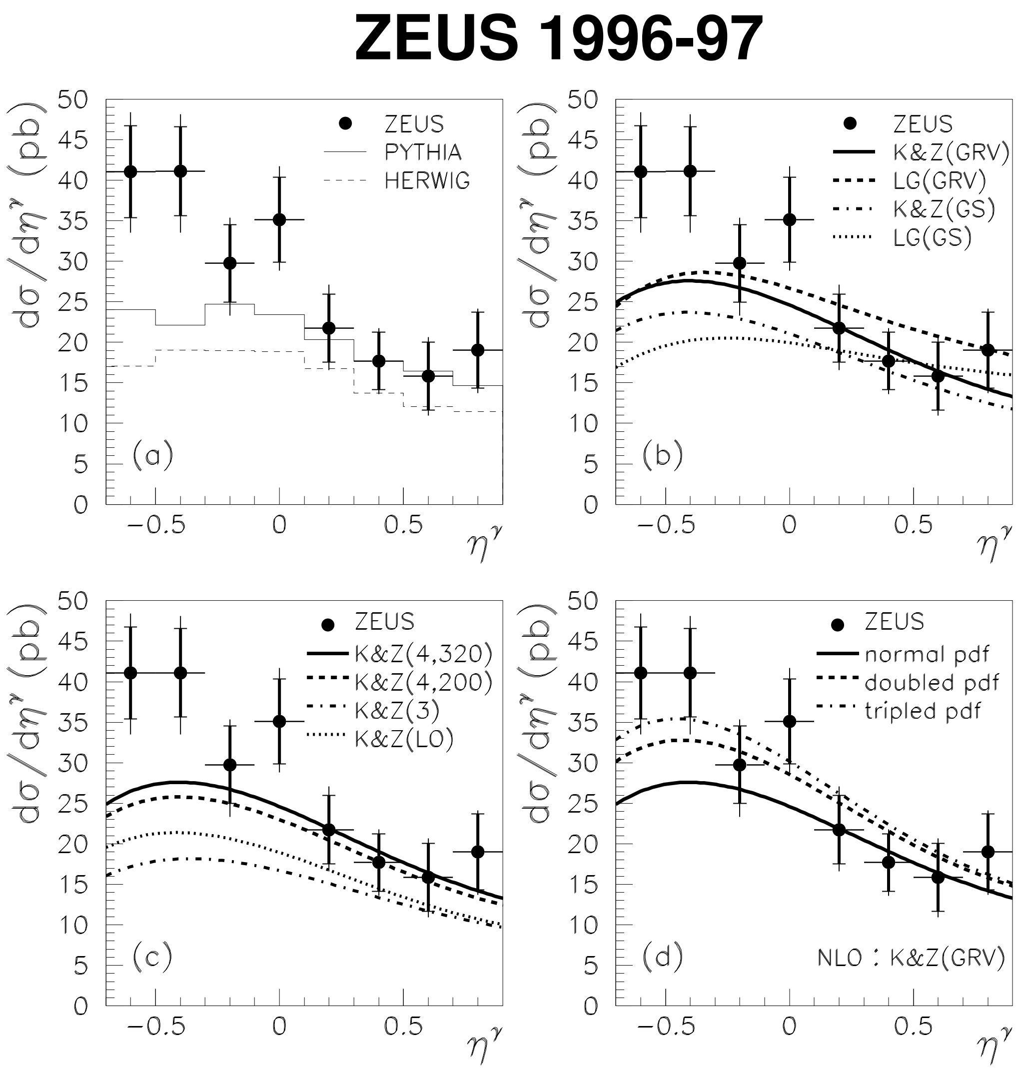

Figure 8.8: Differential cross section $d\sigma/d\eta^{\gamma}$, for prompt photons with $5 < E_T^{\gamma} < 10$ GeV, for $0.2 < y < 0.9$ ($134 < W < 285$ GeV). The inner (thick) error bars are statistical, outer include systematic errors added in quadrature. Also plotted are (a) PYTHIA and HERWIG predictions using the GRV(LO) photon parton densities; (b) LG and K&Z NLO predictions using GRV(HO) and GS photon parton densities; (c) K&Z predictions using GRV(HO) photon parton densities: NLO (4 flavours, $\Lambda_{\overline{\rm MS}} =$ 320 and 200 MeV), LO (4 flavours, $\Lambda_{\overline{\rm MS}} = 120$ MeV, GRV(LO) parton densities), and NLO (3 flavours, $\Lambda_{\overline{\rm MS}} = 365$ MeV); (d) K&Z predictions using doubled and tripled photon parton densities at $x_{\gamma} > 0.8$.

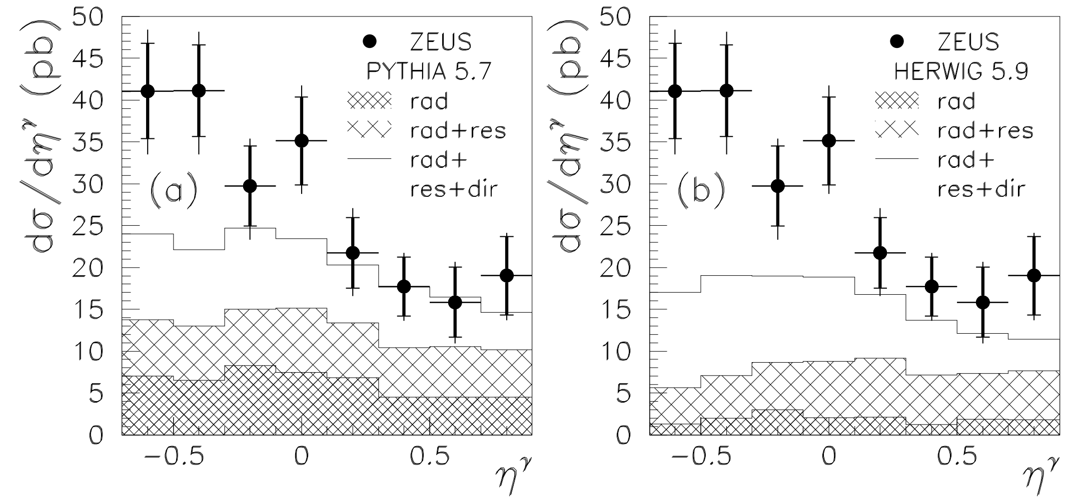

Figure 8.9: Differential cross section $d\sigma/d\eta^\gamma$, for prompt photons with $5 < E_T^\gamma < 10$ GeV, for $0.2 < y < 0.9$ ($134 < W < 285$ GeV). The inner (thick) error bars are statistical, outer include systematic errors added in quadrature. Also plotted are (a) PYTHIA and HERWIG predictions using the GRV(LO) photon parton densities; (b) LG and K&Z NLO predictions using GRV(HO) and GS photon parton densities

To confirm our understanding of topological characteristics in prompt photon production mechanism, the same cross sections were recalculated with the additional requirement of a jet in the event with a transverse energy of at least 5 GeV in the rapidity range $(-1.5, 1.8)$. The main features are seen to be similar to those of figure 8.7 and figure 8.8 (a)–(d), and give rise to similar conclusions. The results will be shown in the next chapter.

8.6.3 Differential cross sections $d\sigma/d\eta^\gamma$ for restricted y ranges

The discrepancy between data and theory at low η^γ is found to be proportionately strongest at low values of y. Figure 8.10 shows the inclusive cross section $d\sigma/d\eta^\gamma$ as in figure 8.8, but evaluated for the three restricted y ranges $0.2 < y < 0.32$, $0.32 < y < 0.5$ and $0.5 < y < 0.9$ using detector–level cuts on y^{meas} at $0.15 < y^{meas} < 0.25$, $0.25 < y^{meas} < 0.4$ and $0.4 < y^{meas} < 0.7$. The corresponding W ranges are 134–170 GeV, 170–212 GeV and 212–285 GeV. Tables for these measurements can be found in Appendix C.

Measured cross sections are compared with the PYTHIA, K&Z and LG calculations using the standard theoretical input parameters. Also shown in figure 8.10

are the corresponding MC predictions for contributions from the different subprocesses for prompt photon production at HERA: (i) dijet processes in which the photon is radiated from a final state quark (termed “radiative”), (ii) radiative plus resolved process, (iii) and summed also with direct process. These are calculated using PYTHIA 5.7, with the proton and photon structure functions given by the MRSA and GRV(LO) parton density sets respectively.

The results shows that the difference between data and theory is relatively large in the low y region, $0.2 < y < 0.32$. As seen in the full y range result in figure 8.8, the data tend to be higher in the negative rapidity region. For negative η^γ values, and bearing in mind the larger statistical errors, the experimental cross sections now lie approximately 50% above the highest available theoretical predictions. In the highest y range (figure 8.10 (c)), there is good agreement between the data, PYTHIA and K&Z, but LG appears high. As y increase, the events with high x_γ become boosted to negative η^γ values, eventually leaving the measurement acceptance.

The kinematic region where the discrepancy is most strongly observed corresponds mainly to x_γ values in the approximate range 0.8–1, where x_γ is the fraction of the incident photon energy that contributes to the QCD subprocess. Low theoretical predictions with respect to data have also recently been reported in the photoproduction of high–E_T jet pairs at HERA [89], although the discrepancy here appears associated with all values of x_γ. By varying the theoretical parameters, the discrepancy was found to correspond in the K&Z calculation to insufficient high x_γ partons in the resolved photon. (see figure in details)

8.6.4 Further kinematic distributions

As shown above, it is found that the measured cross section of inclusive prompt photons is much higher than the various theoretical calculations at negative rapidity region in the laboratory frame. This discrepancy can be partially unfolded by evaluating results approximately in the incident γp centre of mass frame.

The new kinematic quantities, η^* and η' (defined in equations 8.6 and 8.7) in the incident γp centre of mass frame were studied in order to prove the assumption that the excess of data over theory will be seen where the photon appears in the rear direction in the γp frame. It is scattered forwards.

As discussed in [90], the inclusive photons away from threshold are not sensitive to particular values of the proton parton energy. This implies that the prompt photon measurement is sensitive to the integrated quark density, and to

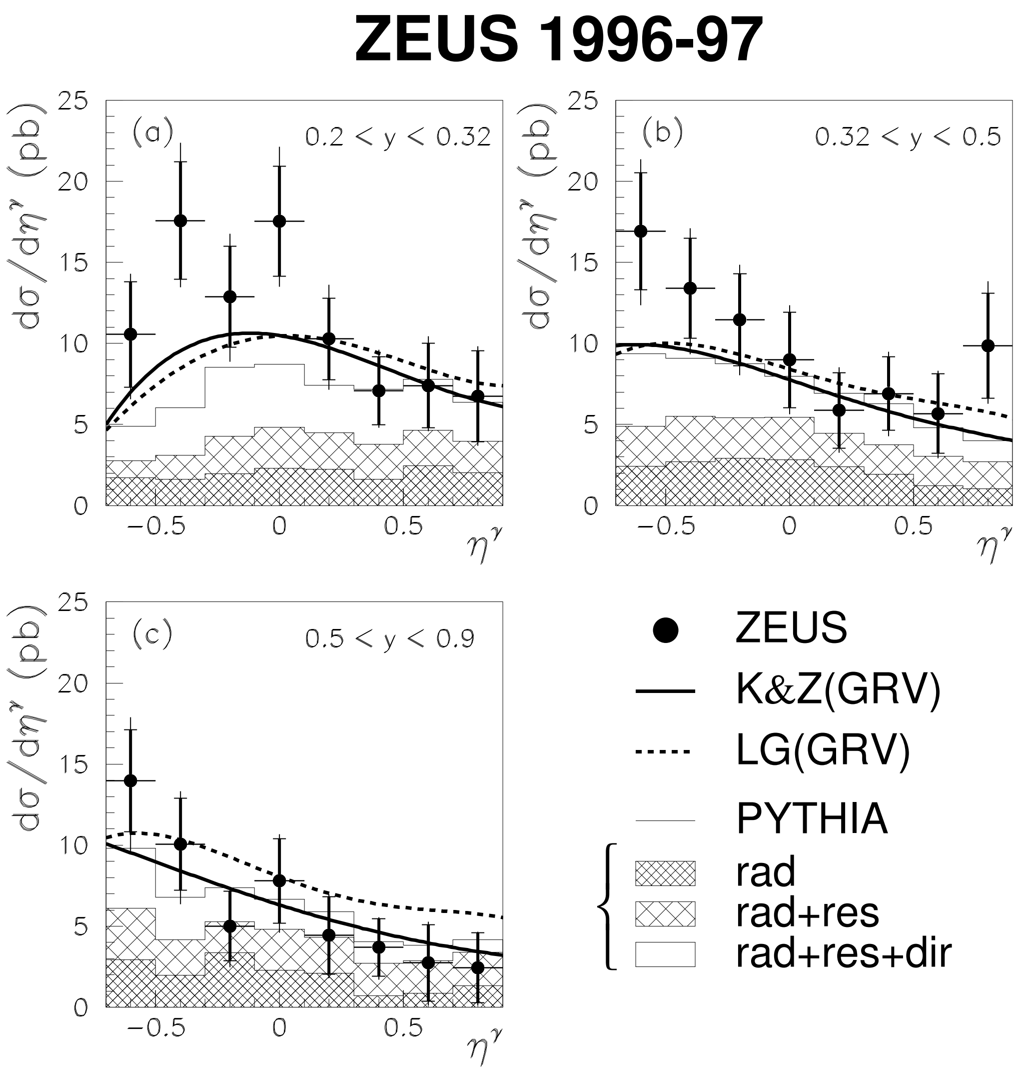

Figure 8.10: Differential cross section $d\sigma/d\eta^{\gamma}$, for prompt photons with $5 < E_T^{\gamma} < 10$ GeV, compared with PYTHIA, LG and K&Z NLO predictions using GRV photon parton densities. The inner (thick) error bars are statistical; the outer include systematic errors added in quadrature. The plots are for the y (W) ranges (a) 0.2–0.32 (134–170 GeV), (b) 0.32–0.50 (170–212 GeV), (c) 0.50–0.90 (212–285 GeV). Also plotted are PYTHIA predictions at the detector level. Thick hatch = MC radiative; thin hatch = MC radiative + resolved; solid = MC radiative + resolved + direct.

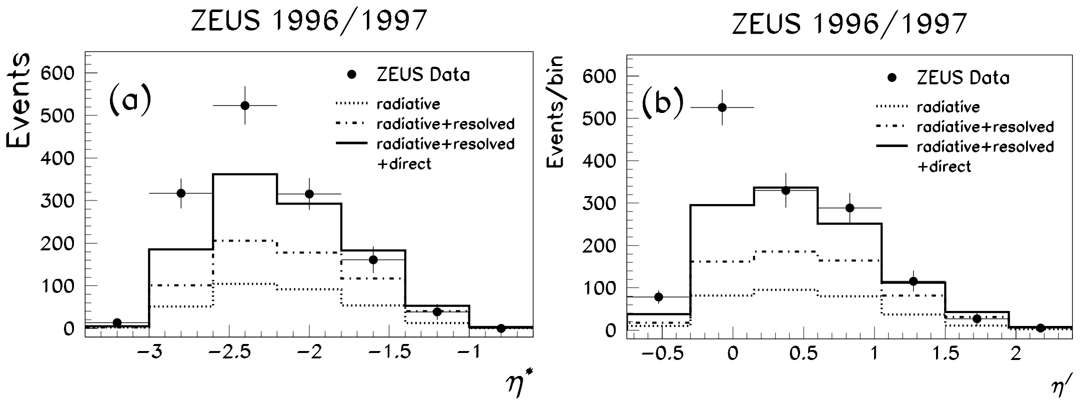

Figure 8.11: (a) Distribution of events of bin as a function of η^* for isolated prompt photons with $5 < E_T^\gamma < 10$ GeV and $0.15 < y^{meas} < 0.7$. (b) Distribution of events of bin as a function of η' for isolated prompt photons with $5 < E_T^\gamma < 10$ GeV and $0.15 < y^{meas} < 0.7$. Also plotted are fitted Monte Carlo curves ; Points = data; dashed–dotted = MC radiative; dotted = MC radiative + resolved; dashed = MC radiative + resolved + direct. Statistical error only.

a lesser extent the integrated gluon density, in the proton. In particular, the η' is an approximate formula for –ln x_γ a quantity which may be sensitive to the hadronic modelling and behaviour of the photon, as well as being measurable [90]. It is meant to be in the frame of the photon and the quark in the proton.

These quantities are defined as below ;

$$\eta^* = \eta^\gamma - 0.5 \ln(E_p/k_y y^{meas} E_e) \tag{8.6}$$

$$\eta' = \eta^\gamma - \ln(E_T^\gamma/k_y y^{meas} E_e) \tag{8.7}$$

where the factor k_y denotes the mean value of y/y^{meas}; a value of 1.25, with no significant y variation, was taken on the basis of PYTHIA studies. The same event selection requirements as described in chapter 6 were applied to select the prompt photon candidates. Then prompt photon candidates are boosted into the γp centre–of–mass system by the equation 8.6 and 8.7 respectively. The backgrounds are subtracted for each bin of η^* and η' as described in chapter 7.

Figure 8.11 (a) and (b) shows the distribution of prompt photon signals as a function of η^* and η' at the detector level, compared with results from PYTHIA, for the detector–level range $0.15 < y^{meas} < 0.7$. A pronounced discrepancy is again observed in the lower part of the η^* and η' ranges, in the remaining region the agreement is good. Within the PYTHIA model, the individual contributions from the direct, resolved and radiative processes are also indicated. No one of these dominates in the region of the discrepancy.

The discrepancy between data and PYTHIA at negative η^* is also found to be relatively strongest at low y^{meas} ranges due to the different size of the boost as indicated in the equation 8.6.

8.7 Conclusions

The photoproduction of isolated prompt photons within the kinematic range $0.2 < y < 0.9$, equivalent to incident γp centre–of–mass energies W of 134–285 GeV, has been measured in the ZEUS detector at HERA, using an integrated luminosity of 38.4 pb^{-1}. Inclusive cross sections for $ep \to \gamma + X$ are presented as a function of E_T^γ for the production of isolated prompt photons in the pseudorapidity range $-0.7 < \eta^\gamma < 0.9$, and as a function of η^γ for photons with $5 < E_T^\gamma < 10$ GeV. The latter results are given for the full y range and three partial ranges.

Comparisons are made with predictions from leading–logarithm parton shower Monte Carlos (PYTHIA and HERWIG), and from next–to–leading order parton–level calculations. The models are able to describe the data well for forward (proton direction) values of photon pseudorapidity, but are low in the rear direction. None of the available variations of the model parameters was found to be capable of removing the discrepancy with the data. The disagreement is strongest within the W interval 134–170 GeV, and not seen within the measurement acceptance for $W > 212$ GeV. Given the discrepancies also seen in recent dijet results at HERA [89], there would appear a need to review the present theoretical modelling of the photon parton structure.

Chapter 9

Measurement of Prompt Photon + Jet Production

In this chapter we present a study of the photoproduction of isolated prompt photons accompanied by jets, within the incident γp centre–of–mass energies W of 120–274 GeV, using an integrated luminosity of 38.4 pb^{-1}, as in the previous chapter.

The kinematical properties of events with a measured jet as well as a prompt photon are used to study the parton behaviour in the proton and photon. The presence of the jet enables the type of underlying QCD process to be identified more clearly, and allows a study of its dynamics. The results are compared with predictions from leading–logarithm parton–shower Monte Carlo models calculated with differing values of the mean intrinsic transverse momentum $<k_T>$ of the partons in both proton and the photon, with the goal of searching for evidence for parton $<k_T>$ effects. The results are also compared with recent prompt–photon measurements from TeVatron colliders and fixed target experiments, which have suggested high values of parton $<k_T>$ inside the proton.

9.1 Experimental Motivation

In recent years a pattern of deviations has been observed between measured prompt photon cross sections and pQCD calculations (both LO and NLO) [21]. Our work is motivated by the observations in a number of previous experiments [35, 38, 39, 30, 91], summarised in the chapter 2.4, that the production of inclusive prompt photons in hadronic reactions sometimes appears to be unexpectedly high in lower regions of transverse energy (see figure 2.6). The discrepancy is particularly striking in the recently published higher–statistics data from

TeVatron E706 experiment [30]. The E706 observed large deviations between NLO calculations and data, for both prompt photon and π^0 inclusive cross sections, for 530 and 800 GeV/c proton beams and a 515 GeV/c π^- beam incident on Be targets (see figure 2.4).

As discussed in chapter 2.4, a discrepancy of this kind could arise from the intrinsic transverse momentum, k_T, of the parton in the incoming hadron or from multiple initial–state soft gluon radiation which can enhance the effective $<k_T>$ value of the parton as it interacts.

Nowdays theoretical efforts of explaining the inclusive prompt photon production rate is in progress with the help of MC techniques which take these effects into account, with several simple mathematical models, for instance Gaussian smearing. In particular, programs such as PYTHIA and HERWIG that include a variable treatment of k_T smearing, and the LO cross section for high p_T particle production, are available and can be used in the study of prompt photon production.

The aim of the present measurements is to determine kinematically whether the partons in the proton possess high values of $<k_T>$ when they interact with a high energy photon. This is facilitated by the use of event samples in which the 'direct photoproduction' process dominates, i.e. in which the entire incoming photon interacts with a quark in the proton. This minimises the effect of the hadronic behaviour of the photon. At leading order, the Compton process $\gamma q \rightarrow \gamma q$ is the only direct prompt photon process in photoproduction.

9.2 Kinematics of the Event Topology

Correlations between a photon and a jet probe aspects of the hard–scatter not easily accessible via inclusive prompt photon production, and can be used to investigate the transverse momentum of the parton $<k_T>$ prior to the hard scatter. In this section we discuss the topology of events with a photon plus a jet at HERA and describe the definitions of relevant kinematic quantities whose contributions will be finally compared with theoretical predictions.

9.2.1 HERA kinematic quantities, x_γ and x_p

We first look at two basic kinematical variables, x_γ^{meas} and x_p^{meas}, of the photon plus jet system at HERA. As with the photoproduction of a dijet final state [92], the information from the prompt photon and the measured jet can be used to measure a value of x_γ, the fraction of the incoming photon energy which participates in the hard interaction. The fraction of the incoming proton momentum entering the QCD hard process is estimated by evaluating the quantity x_p. "Measured" values of x_γ and x_p at the detector level were evaluated as :

$$x_\gamma^{meas} = \sum_{\gamma,jet} (E - p_Z) / 2E_e y_{JB} \tag{9.1}$$

$$x_p^{meas} = \sum_{\gamma,jet} (E + p_Z) / 2E_p \tag{9.2}$$

where the sums are over the photon candidate and the detector level object which form the jet, each object being treated as equivalent to a massless particle of energy E and longitudinal momentum component p_Z. The y^{meas} is evaluated similarly. The x_γ^{meas} distribution peaks at values close to unity for direct photoproduction events, in which the whole photon energy takes part in the hard subprocess. It takes smaller values for resolved events, where the photon acts as a source of partons, one of which takes part in the hard subprocess.

9.2.2 Momentum imbalances of γ–jet

The momentum imbalances of the photon relative to the jet in the (x,y) plane can be used to investigate the sensitivity to intrinsic k_T effects. Three such kinematical quantities have been examined, defined as [93] :

$$p_\perp = |\boldsymbol{p}_{xy}^{\gamma} \times \boldsymbol{p}_{xy}^{jet}| \Big/ p_T^{jet} \tag{9.3}$$

$$p_{||} = -\boldsymbol{p}_{xy}^{\gamma} . \boldsymbol{p}_{xy}^{jet} \Big/ p_T^{jet} - p_T^{jet} \tag{9.4}$$

$$Q_T = \sqrt{p_\perp^2 + p_{||}^2} \tag{9.5}$$

The quantities $p_\perp$ and $p_{||}$ are the perpendicular and longitudinal momentum components of the photon relative to those of the jet, respectively, which are used since the photon is better measured experimentally than the jet. The quantity Q_T is the total momentum imbalance of the photon–jet system. Figure 9.1 show a schematic diagram of kinematic quantities, $p_\perp$ and $\Delta\phi$ (see section 9.2.3)

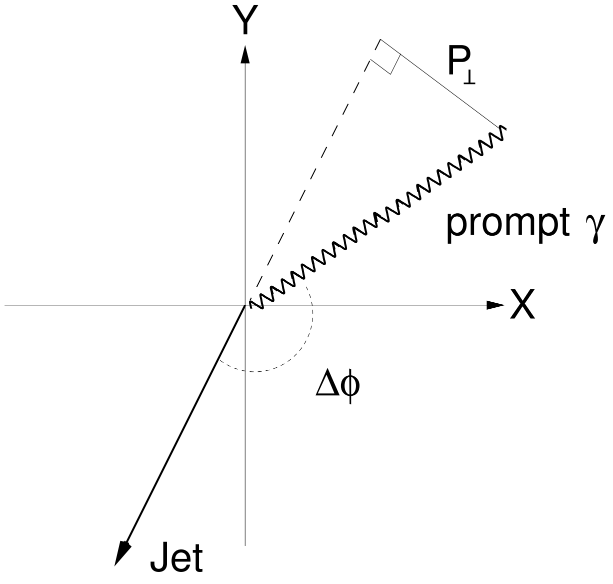

Figure 9.1: A schematic diagram showing a kinematics of the event topology. The plotted quantities describe the momentum imbalance of the photon-jet system in the (X, Y) plane, and denote the momentum component $p_{\perp}$ of the photon relative to the jet, and the collinearity $\Delta\phi$. The quantity $\Delta\phi$ also shown in the diagram.

In leading order pQCD, the differential cross section $d\sigma/\, dQ_T$ for the photon + jet production peaks at Q_T=0. Only in higher–order QCD does the two–object system receive a p_T push which results in a shift of the peak of $d\sigma/\, dQ_T$ to a non–zero value. The distribution of this quantity is therefore a good test of higher–order effects and can provide a direct measurement of the intrinsic $<k_T>$ of colliding partons.

For each quantity in the equations above the vector $\boldsymbol{p}_{xy}$ is (p_x, p_y), and $p_T = \sqrt{p_x^2 + p_y^2}$. Thus p_T^{jet} is not identical to the Snowmass quantity E_T^{jet}, defined as the sum of the E_T values of the individual particles in the jet, but is the true momentum component of the jet as a whole.

Figure 9.2 shows that after corrections the transverse energy of the photon and the jet are approximately equal. Now, since most of the events are at low value of p_T, the portion of the experimental acceptance at the bottom left corner tries to force each $p_{||}$ distribution, as seen in the figure, to be near zero. The corner of the plot, therefore, was removed in plotting $p_{||}$ to get a more unbiased distribution by requiring the condition of $(p_T^{jet} + p_T^{\gamma}) > 12.5$ GeV. Several choices of the minimum $(p_T^{jet} + p_T^{\gamma})$ requirement, for instance 10, 11, 12, 12.5 and 13 GeV, were tested to clarify the effects of this cut.

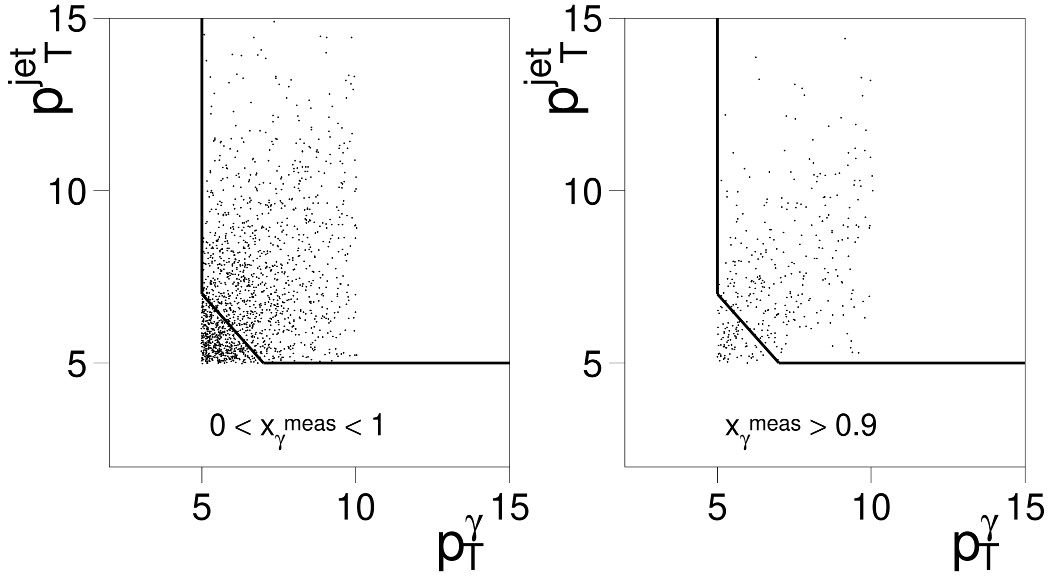

Figure 9.2: The correlation between p_T^γ and p_T^{jet}, (a) for the full x_γ^{meas} and (b) for the $x_\gamma^{meas} > 0.9$, for photon + jet events passing the above final event selection cuts. The tick lines define the region of interest for the quantities, $p_{||}$ and Q_T, as described in the text.

9.2.3 Azimuthal angle between γ–jet

In the leading order QCD diagram, a high–E_T prompt photon is balanced, back–to–back in the plane perpendicular to the beam direction, by a jet. Thus the azimuthal angle difference between a photon and a jet should be ideally $\Delta\phi = 180°$. In practice $\Delta\phi$ does not show precise back–to–back characteristics for the following reasons ;

- The detector resolution and hadronization effects might smear the original direction of the parton.
- The virtuality of the photon is not exactly zero, which provides some transverse momentum to the initial photons.
- The effects of the initial state radiation (ISR) of the gluons off the incoming partons in the hard sub–processes.
- The effect of the intrinsic transverse momentum $<k_T>$ of the partons in both the proton and the photon.

The $\Delta\phi$ distribution has the advantage of being insensitive to the measured photon and jet energies and also is relatively unbiased with respect to longitudinal fragmentation effects.

9.3 Event Selection

The data used here were obtained from e^+p running in 1996–97 at HERA, with $E_e = 27.5$ GeV, $E_p = 820$ GeV. These data correspond to an integrated luminosity of 38 pb^{-1}, which is more than six times that available in the first analysis of prompt photon plus jet photoproduction performed by ZEUS using 1995 data [18]. The 1996–97 data shows similar features to that of 1995.

The same offline selection criterion and isolation condition, as described in chapter 6, are applied to identify candidate photon signals in BCAL and to reduce the neutral mesonic backgrounds, and the contribution from high–energy photons radiated from outgoing quarks, respectively. In particular both calorimeter cells and tracks are taken into account in evaluating the isolation condition.

For the reconstruction of jets in the present analysis the longitudinally invariant K_T clustering algorithm, KTCLUS [76], was used in the inclusive mode, by means of energy flow objects, ZUFOS, which combine information from the calorimeter cells and tracks. Further details of the ZUFOS and KTCLUS are given in chapter 6.

Correction factors to the measured photon and jet energies were evaluated through the use of Monte Carlo event samples, and were typically 1.05–1.10 for both the photon and the jet. After correction, photons were required to have $5 < E_T^\gamma < 10$ GeV and $-0.7 < \eta^\gamma < 0.9$ to minimize neutral meson backgrounds, while jets were required to have $E_T^{jet} > 5$ GeV and $-1.5 < \eta^{jet} < 1.8$. These cuts confined both types of outgoing object to be within well–measured kinematic regions. The momentum components of the objects comprising the jet were summed to obtain the total jet momentum vector.

9.4 Study of Systematic Uncertainties

The systematic uncertainty on the measurements was studied by taking into account the following sources, which were grouped into the following categories: calorimeter energy scale, modelling of the shower shape, $\eta/(\eta + \pi^0)$ ratio, kinematic cuts. The results of this study are shown in figure 9.3 and 9.4 for the data points obtained in the following ways.

1. Standard analysis selection

   Calorimeter energy scale :

2. Change of the calorimeter energy scale by +3%
3. Change of the calorimeter energy scale by −3%

Modelling of the shower shape :

4. f_{max} correction factor of the single photon MC raised by +0.009
5. f_{max} correction factor of the single photon MC lowered by −0.009
6. f_{max} correction factor of the π^0 and η MC raised by +0.014
7. f_{max} correction factor of the π^0 and η MC lowered by −0.014
8. Change of the E_T slope of the single particle MC

$\eta/(\eta+\pi^0)$ **ratio :**

9. Ratio of η meson to the background events are fixed to 15%
10. Ratio of η meson to the background events are fixed to 35%

Kinematic cuts :

11. Photon rapidity cut was varied by $-0.5 < \eta^\gamma < 0.7$
12. x_γ^{meas} cut lowered to $x_\gamma^{meas} > 0.85$

The effect of the discussed variations on measured quantities, $1/NdN/dp_\perp$ and $1/NdN/d\Delta\phi$, in each bins is shown in the figures 9.3 to 9.4.

Figure 9.3 shows the difference in percent between each systematic item and the nominal result of $1/NdN/dp_\perp$ in each bin of $p_\perp$. The numbers on the x–axis refer to the systematic sources detailed previously and the line at zero refers to the position of the nominal value. The calorimeter energy scale uncertainties should have a negligible effect since they change only the magnitude of the distribution and not the shape of normalised distributions. As described in chapter 7, uncertainties in evaluating the correction factors applied to the MC f_{max} distributions for both photon and π^0/η mesons were taken into account. In addition the fitted value of $\eta/(\eta+\pi^0)$ ratio was varied in the range 15–35%. As expected the uncertainties from the modelling of the shower shape and $\eta/(\eta+\pi^0)$ ratio has not a significant effect on the normalised distributions. On the other hand it shows that the shape of the $p_\perp$ distribution is slightly sensitive at low $p_\perp$ to the variation of kinematic cuts. Further investigations for each effect on a typical MC predictions will be discussed in section 9.8.3.

The same pattern is observed in figure 9.4 which show the systematic uncertainties for $1/NdN/d\Delta\phi$.

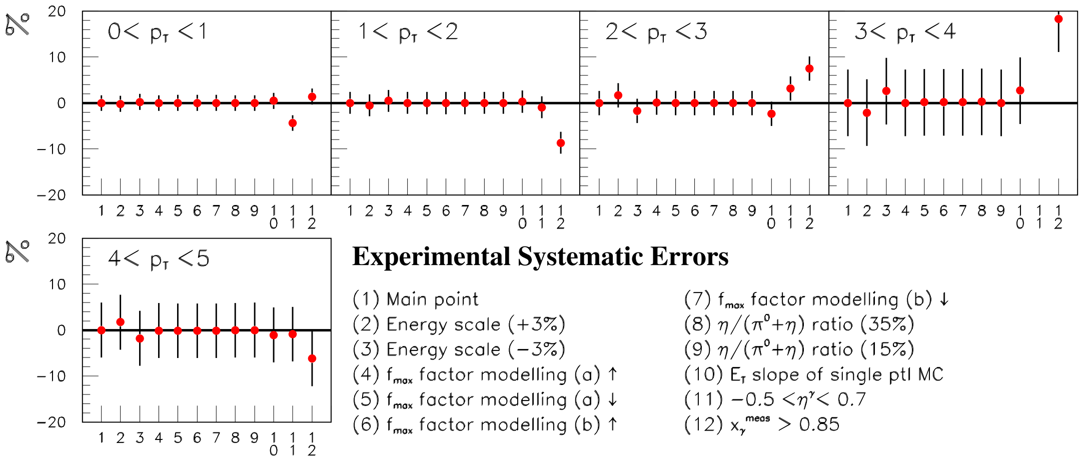

Figure 9.3: Summary of systematic uncertainties for the normalised $1/NdN/dp_{\perp}$ distribution of $p_{\perp}$ quantity. The systematic uncertainty is subdivided into: (2–3) calorimeter energy scale, (4–7) modelling of shower shape, (8–9) $\eta/(\eta+\pi^0)$ ratio, (10) varying the E_T–distribution applied to the single–particle samples and (11–12) kinematic cuts.

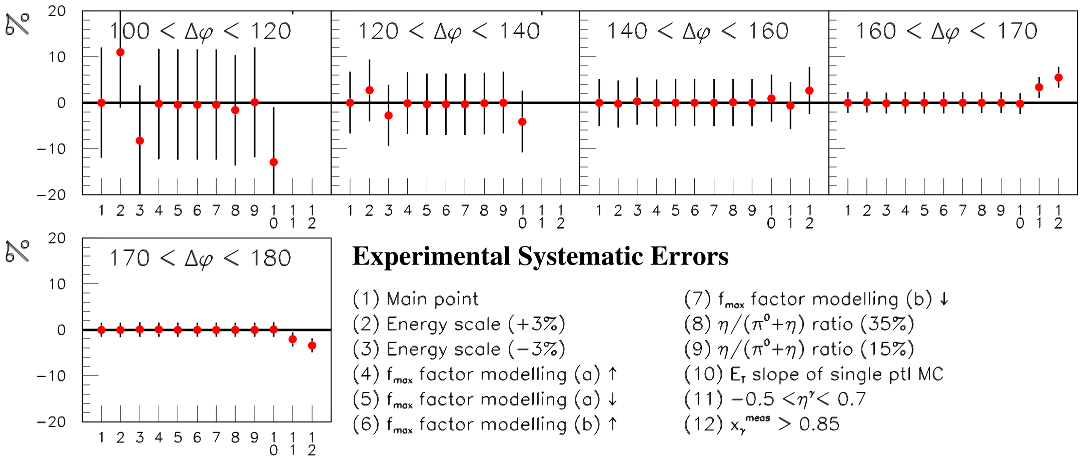

Figure 9.4: Summary of systematic uncertainties for the normalised $1/NdN/d\Delta\phi$ distribution of $\Delta\phi$ quantity. The systematic uncertainty is subdivided into: (2–3) calorimeter energy scale, (4–7) modelling of shower shape, (8–9) $\eta/(\eta+\pi^0)$ ratio, (10) varying the E_T–distribution applied to the single–particle samples and (11–12) kinematic cuts.

In summary, the systematic uncertainties on the data point in the most populated bin in several kinematic quantities were typically at the 1–2% level. Proportionally larger effects were seen in some of the other bins, but always within the level of the statistical uncertainty. The dominant uncertainties were associated with variation of the kinematic range used in making the measurement.

9.5 Phenomenological Calculation

The preliminary version of an NLO pQCD calculation has been performed by members of the Durham group [93]. They calculated the p_{Tout} distribution for the direct component, $x_\gamma \sim 1$, of prompt photon + jet events as measured at HERA. Here p_{Tout} is a positive quantity called acoplanarity, representing the transverse momentum imbalance between the emitted photon and the jet, and is the same quantity as we term $p_\perp$. In their calculation an unintegrated parton distribution is used to incorporate the initial transverse momentum $<k_T>$ of a quark. Even with the leading order $2 \to 2$ subprocess, they have a non–zero prediction for the p_{Tout} distribution because of the initial state $<k_T>$ effect.

The p_{Tout} distribution does depend strongly on the two parameters, $\overline{\mu}$ and $\overline{x}$, in the theoretical approximation. Here the $\overline{\mu}$ is the hard factorization scale and $\overline{x}$ is the longitudinal momentum fraction.

Figure 9.5 shows the theoretical calculations for $\overline{x}$= 0.01 and for three illustrative scales $\overline{\mu}$= 10 GeV, 5 GeV and 2.5 GeV. The strong scale $\overline{\mu}$ dependence in the gradient of the straight line parts is seen in the theoretical calculation. This effect is clearly seen in the logarithmic plot (not shown).

Figure 9.6 also shows the dependence on $\overline{x}$ for the fixed value of $\overline{\mu}$=10 GeV. The variation is fairly modest.

9.6 Intrinsic k_T–insensitive Distributions

Figure 9.7 shows the distributions of kinematic quantities, x_γ^{meas} and η^γ, measured in prompt photon plus jet photoproduction. The distributions are at detector level after evaluation of the photon signals as described in chapter 7. The errors on the data are statistical only and no corrections have been applied to the data.

The x_γ^{meas} distribution of the signal is shown in figure 9.7 (a). A clear peak is seen near $x_\gamma \sim 1$ corresponding to the direct Compton process, $\gamma q \to \gamma q$. It is evident that both direct and resolved processes are present in the distribution.

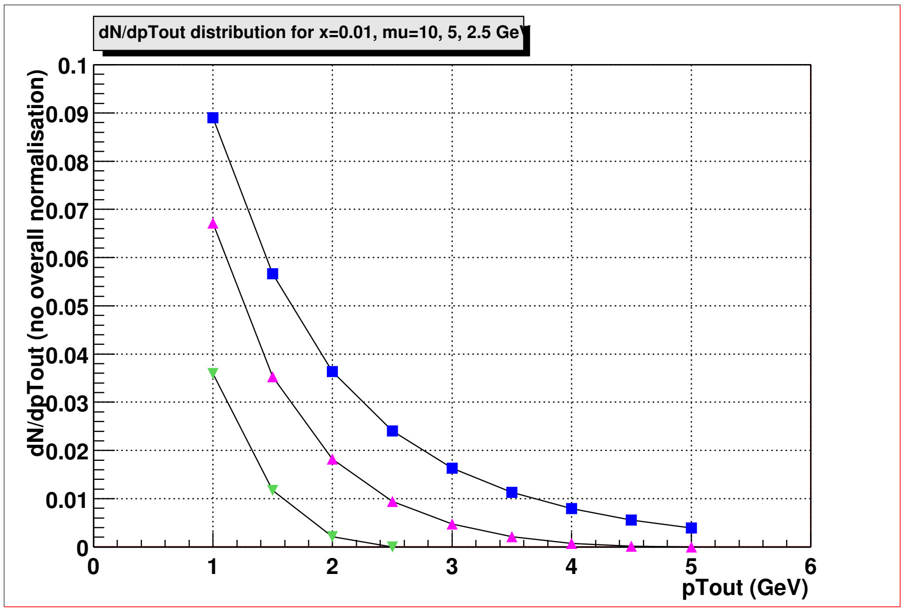

Figure 9.5: Theoretical calculations of the quantity p_{Tout} for $\overline{x}$= 0.01 and various scales $\overline{\mu}$; $\overline{\mu}$= 10 GeV (squares), 5 GeV (upper triangles) and 2.5 GeV (lower triangles).

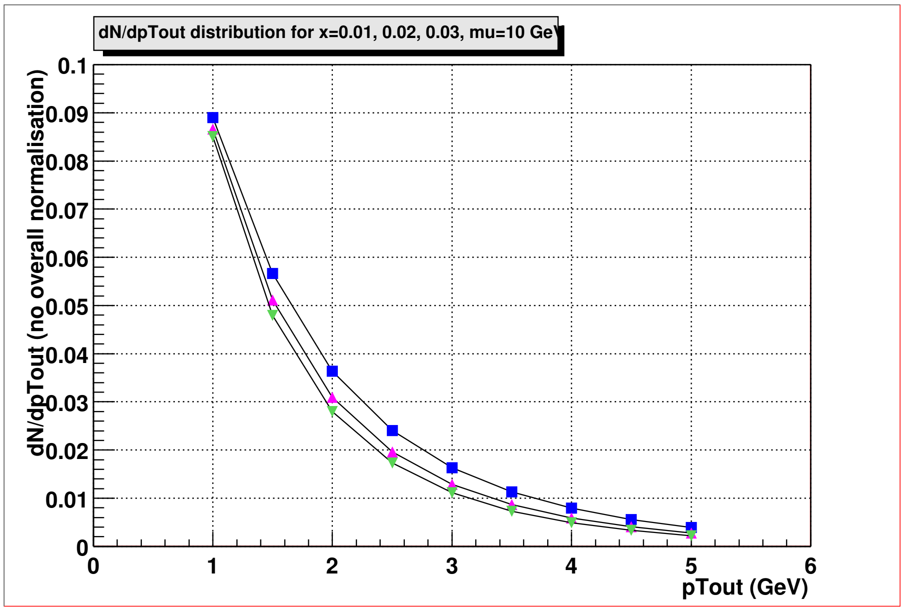

Figure 9.6: Theoretical calculations of the quantity p_{Tout} for scale $\overline{\mu}$= 10 GeV and various $\overline{x}$ values ; $\overline{x}$= 0.01 (squares), 0.02 (upper triangles) and 0.03 (lower triangles).

Comparisons are made with predictions from the MC model, PYTHIA 6.1, using default values of the intrinsic transverse momentum of the partons in both the proton and photon. The parton density function used is MRSA [94] and GRV [16] for the proton and photon respectively.

The PYTHIA distributions include events from direct and resolved prompt–photon photoproduction at lowest order in QCD, together with radiative dijet events in which an outgoing quark from a hard QCD scatter radiates a high–E_T photon which passes the present experimental selections. The MC distribution agrees with the shape of the data, although it systematically tends to underestimate the data in magnitude. QCD radiation, hadronization outside the jet cone and detector effects lower the peak position slightly from its expected value of unity. There is also a contribution of entries extending over lower x_γ values. These correspond to resolved photoproduction events, whose observed numbers are consistent with the level expected from the MC. The predicted radiative contribution is not negligible compared to the resolved contribution.

Further details are presented in the figure 9.8, which shows the various combinations of corresponding processes for the prompt photon photoproduction at HERA ;

- direct process $\Rightarrow$ QCD Compton process ($\gamma q^p \to \gamma q$)
- resolved process $\Rightarrow$ *e.g)* $q^\gamma g^p \to \gamma q$, $q^\gamma q^p \to \gamma g$, $g^\gamma q^p \to \gamma q$
- radiative process (direct) $\Rightarrow$ $\gamma q^p \to qg \to q\gamma g$
- radiative process (resolved) $\Rightarrow$ *e.g)* $q^\gamma g^p \to qg \to q\gamma g$

These x_γ^{meas} distributions indicate that the requirement $x_\gamma^{meas} > 0.9$ selects a clean sample of events strongly enriched in direct photoproduction. To investigate the parton behaviour in the proton and the photon, we therefore use the direct–enriched sample and resolved–enriched sample, respectively, for this purpose, making a cut at $x_\gamma^{meas} > 0.9$ (see section 9.8.2) and $x_\gamma^{meas} < 0.9$ (see section 9.9.1), respectively.

Figure 9.7 (b) shows the pseudorapidity distribution of the photons, the presence of a jet being required. The agreement with PYTHIA is qualitatively satisfactory although the predictions tend to lie below the data. This discrepancy is particularly evident at negative η^γ values, where a lack of theoretical modelling of the photon parton structure is expected to have greater impact. This is also

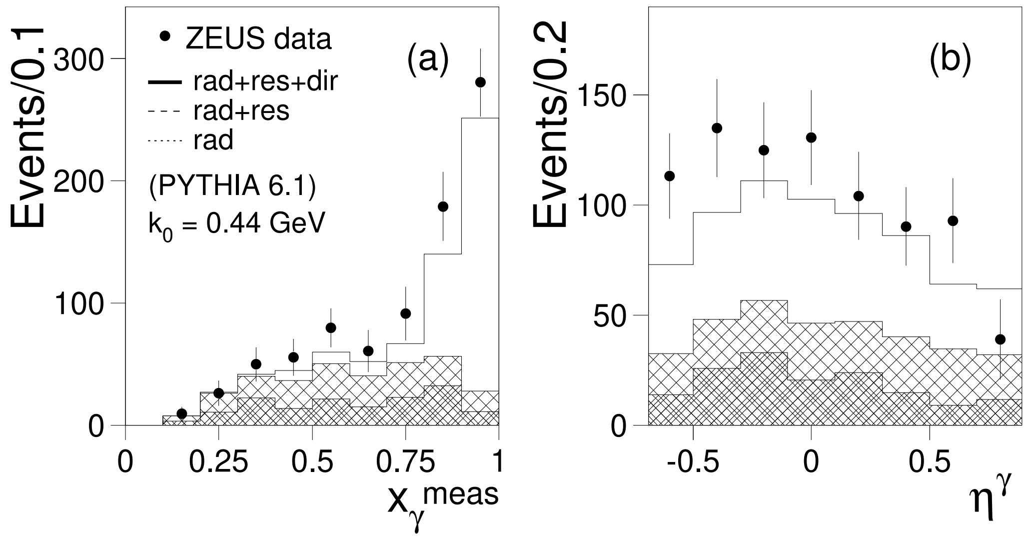

Figure 9.7: Observed distributions (a) in x_γ^{meas} and (b) in photon pseudorapidity, for prompt photon events at ZEUS in which a jet is also observed, compared with predictions from PYTHIA6.1. Errors are statistical only. The PYTHIA histograms indicate contributions from dijet events where a final-state quark radiates a photon, resolved prompt photon events, and direct prompt photon events. The PYTHIA6.1 default $<k_T>$ values in the proton and photon are used. The Monte Carlo is normalised to the integrated luminosity of the data.

observed in the inclusive prompt photon distributions. Further details of the inclusive prompt photon distributions are given in chapter 8.

It should be noted that there is little sensitivity to the choice of possible intrinsic $<k_T>$ values of the proton in these kinematic quantities. In figure 9.9, the detector–level data shown in figure 9.7 is compared with PYTHIA predictions with the $<k_T>$ value for the proton varied. This variation does not produce strong effects on the predicted event rate in this variable and is not able to generate significantly higher cross sections in the negative pseudorapidity range.

Since the photon signals and backgrounds were evaluated statistically in each bin of any measured quantity, as discussed in chapter 7, we looked at the rebinned x_γ^{meas} distribution in events per 0.05 bin in order to see the effect on statistical fluctuations to each bin. The resulting distributions are compared with PYTHIA 6.1 predictions (not shown) [95]. The PYTHIA 6.1 predictions indicate the effects of varying the default $<k_T>$ values for the proton, with that of the photon fixed at its normal value. Reasonable agreement is seen, and again a dominant peak near unity indicates clearly the presence of the direct process.

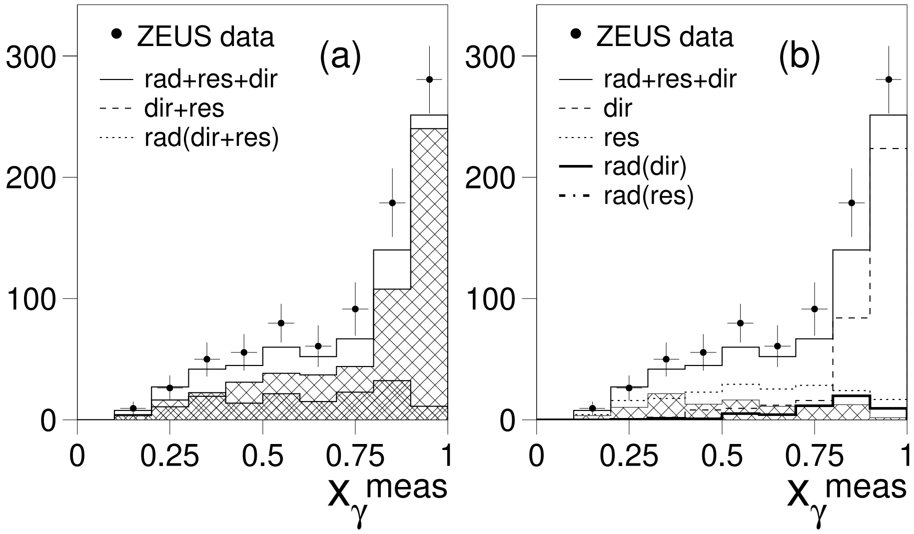

Figure 9.8: Observed distributions in x_γ^{meas} for prompt photon events in which a jet is also observed, compared with predictions from PYTHIA6.1. Errors are statistical only. Also plotted are PYTHIA predictions at the detector level. (a); Thick hatch = radiative, thin hatch = radiative + resolved, solid = radiative + resolved + direct. (b); Thin hatch = radiative resolved, thick solid = radiative direct, dotted =resolved, dashed = direct, solid = radiative + resolved + direct.

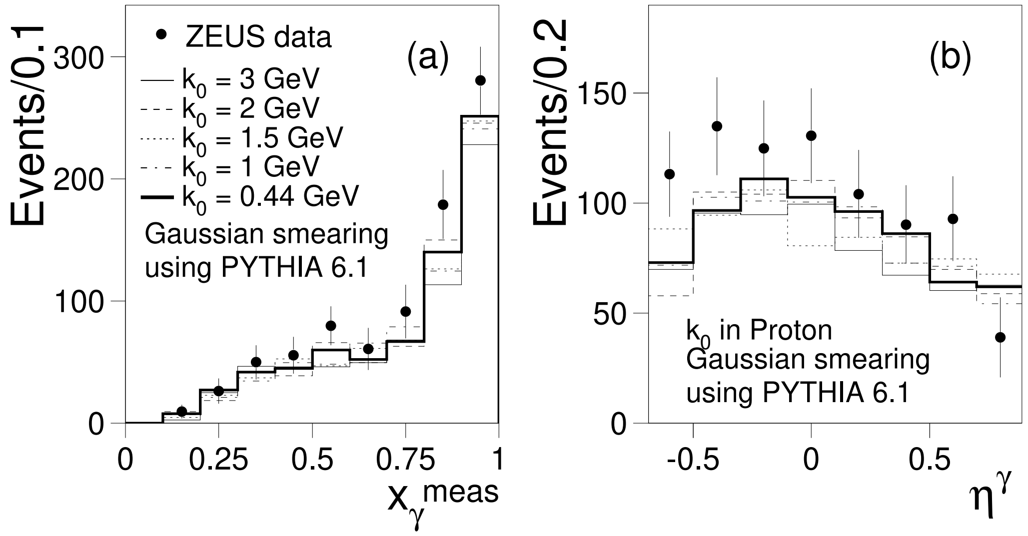

Figure 9.9: Observed distributions (a) in x_γ^{meas}, (b) in photon pseudorapidity, for prompt photon events at ZEUS in which a jet is also observed, compared with predictions from PYTHIA6.1. Errors are statistical only. The PYTHIA predictions indicate the effects of varying the default <k_T> values for the proton, with that of the photon fixed at its normal value. The Monte Carlo is normalised to the integrated luminosity of the data.

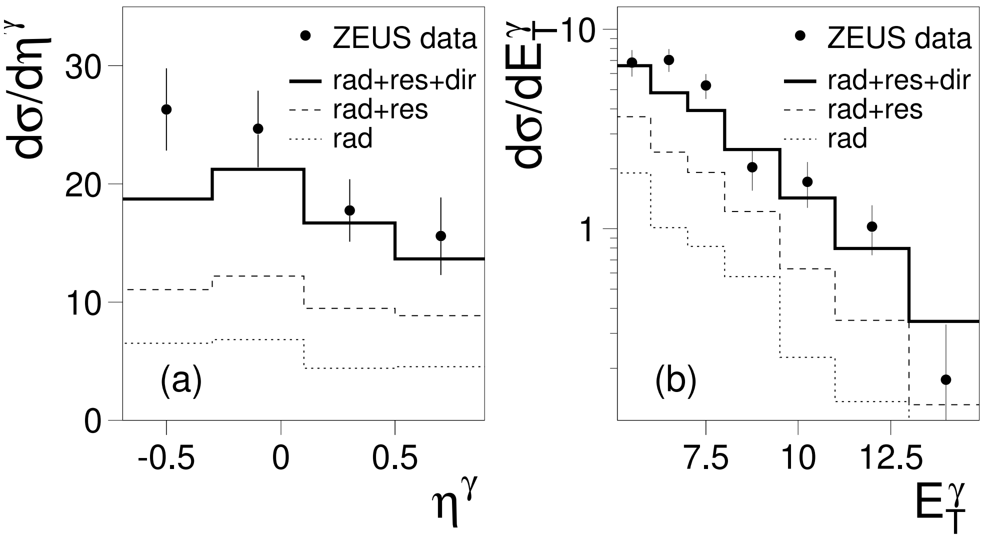

Figure 9.10: Differential cross sections (a) $d\sigma/d\eta^{\gamma}$ for prompt photons with $5 < E_T^{\gamma} < 10$ GeV and (b) $d\sigma/dE_T^{\gamma}$ for prompt photons produced over $-0.7 < \eta^{\gamma} < 0.9$ for $134 < W < 285$ GeV. Errors are statistical only. Also plotted are PYTHIA 6.1 predictions at the hadron level using the GRV(LO) photon parton densities. In PYTHIA 6.1, the default $<k_T>$ values of 0.44 GeV is used. Dotted line = MC radiative; dash–dotted line = MC radiative + resolved; thick solid = MC radiative + resolved + direct.

9.7 Measured Cross Sections

As a check on the inclusive prompt photon results in chapter 8, the same cross sections were recalculated with the additional requirement of a jet. We evaluate cross sections for prompt photon production corrected by means of PYTHIA 6.1 using GRV photon structures [16]. A bin–by–bin factor is applied to the detector–level measurements using ZUFOS so as to correct to cross sections in the specified kinematic intervals calculated in terms of the final state hadron system photoproduced in the range $0.16 < y^{true} < 0.8$. The virtuality of the incoming photon is restricted to the range $Q^2 < 1$ GeV^2. The detector–level jets were corrected to hadron–level jets in the kinematic range $E_T^{jet} > 5$GeV, $-1.5 < \eta^{jet} < 1.8$.

Figure 9.10 shows corresponding cross sections for the prompt photon accompanied by at least one jet. The differential cross section $d\sigma/d\eta^{\gamma}$ for prompt photons in the range $5 < E_T^{\gamma} < 10$ GeV is shown in figure 9.10 (a) and compared with prediction from LO parton–shower MC model, PYTHIA 6.1, using the proton and photon structure functions given by the MRSA and GRV(LO) parton density sets respectively. Only statistical errors are shown. Reasonable agreement between data and MC is seen at forward values of pseudorapidity, but the data tend to lie above the MC at negative pseudorapidity. The agreement appears to be better than in the inclusive prompt photon distributions. Both the measured and theoretical distributions were found to be of a similar shape to those of inclusive prompt photons, as discussed in chapter 8.

In figure 9.10 (b) the differential cross section $d\sigma/dE_T^\gamma$ for the production of a photon accompanied by a jet in the kinematic range $-0.9 < \eta^\gamma < 0.7$ are compared to the PYTHIA model. The PYTHIA result describes the shape of the data well but is slightly low in magnitude. Similar features were seen in the inclusive distribution. Also shown are the corresponding MC expectations for the contributions from subprocesses; (i) radiative, (ii) radiative + resolved process and (iii) summed also with direct process.

9.8 Study of Parton Behaviour in the Proton

In this section we examine the effects of varying the intrinsic $<k_T>$ in the proton independently of the photon. The various kinematic quantities, as described in section 9.2, are presented (1) for the full range of x_γ^{meas} values, (2) for a direct–enriched event sample with $x_\gamma^{meas} > 0.9$, and (3) for a resolved–enriched event sample with $x_\gamma^{meas} < 0.9$. The distributions are at detector level after evaluation of the photon signals using the neutral meson background subtraction. Further details of the background subtraction method are given in chapter 7. The errors on data are statistical only. No hadron–level corrections have been applied to the data. This approach has been adopted since most hadron–level corrections would cancel out on normalising the distributions; one would effectively be correcting mainly for migration effects between the bins. It seems best for present purposes not to introduce further systematic errors by attempting this.

9.8.1 Intrinsic k_T effect for the full range of x_γ^{meas}

Figure 9.11 shows distributions of the kinematic quantities described above in the full x_γ region. The azimuthal acollinearity $\Delta\phi$ between the prompt photon and the accompanying jet is well peaked at 180° as expected. There was a minimum requirement of $(p_T^{jet} + p_T^\gamma) > 12.5$ GeV in plotting both (b) $p_{||}$ and (c) Q_T variables, to prevent the distribution from being dominated by the many events with transverse energy just above the lower cuts, which are approximately $p_{||}$–balanced by definition.

Comparison is made with predictions from PYTHIA 6.1, calculated with differing values of the two–dimensional Gaussian width, k_0, of the partons in the proton, where a Gaussian formula for the spread in $<k_T>$ is employed. The mean absolute value of the intrinsic parton momentum, $<k_T>$ is given by $<k_T> = \sqrt{\pi/4}k_0$ [46]. The k_0 value for partons in the photon is fixed at 0.44 GeV, which is the default value in the PYTHIA model. Here and in figures 9.12 to 9.15, the MC distributions are normalised to the same integrated luminosity as the data for the comparison of shape between data and MC predictions. The error bars on the data points are statistical only.

Figure 9.11 (a) shows that $p_\perp$ peaks at zero with a fall–off around 2 GeV. The $p_{||}$ distribution is well peaked around zero, falling off around $\pm$ 2 GeV and is reasonably reproduced by MC. A small asymmetry towards the positive direction is observed on the $p_{||}$ distribution (figure 9.11 (b)), which may be attributed to higher–order processes in which not quite all the recoiling system is included in the defined jet and is strongly affected by E_T resolution effects. There is insufficient resolution in $p_{||}$ to distinguish the different PYTHIA models of $<k_T>$ variations, since the $p_{||}$ distribution is more sensitive than the other to the definition of the jet. The $(p_T^{jet}+p_T^{\gamma}) > 12.5$ GeV cut also reduces the statistics in this quantity. The Q_T distribution (Figure 9.11 (c)) is less sensitive to the intrinsic k_T effects and the data again provides little discrimination between the various $<k_T>$ values.

It is evident that a $<k_T>$ value of 3 GeV is excluded by the distributions in $p_\perp$ and $\Delta\phi$, which favour a value in the range 1–2 GeV. The distributions are also in poor agreement with the PYTHIA 6.1 default value of 0.44 GeV. In later editions of the program, this default value has been increased to around 1 GeV; it may be noted that the initial–state parton showering in PYTHIA is not evolved below a scale of 1 GeV^2, so that it is necessary to impose an appropriate $<k_T>$ value by hand [96].

The distribution of the azimuthal angle between the photon and the jet is shown in figure 9.11 (d) for events with full range of x_γ^{meas} value. Ideally balanced photon–jet pairs would have $\Delta\phi = 180^\circ$. As discussed in section 9.2, however, a deviation from the back–to–back configuration is seen due to several reasons and such deviation increases with increasing intrinsic k_T of the partons in the proton as seen in the MC predictions. The results indicate that we have experimental resolution of an useful kind in $\Delta\phi$ which suggests again that the $<k_T>$ of the quarks in the proton is 1–2 GeV, rather than the PYTHIA default of 0.44 GeV and at the other extremely higher value of $<k_T> \sim 3$ GeV, which appear to be excluded. $\Delta\phi$ is of course strongly correlated with $p_\perp$.

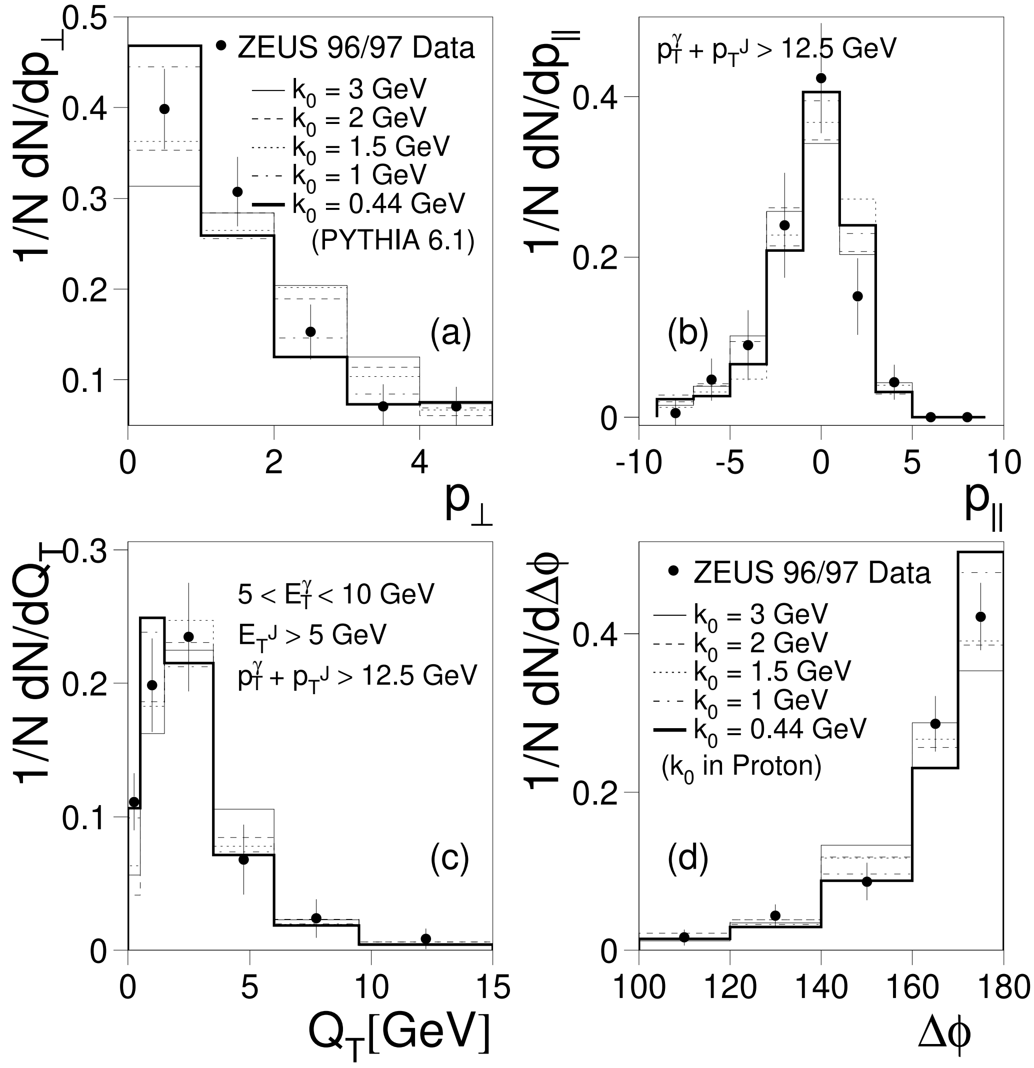

Figure 9.11: Normalised distributions of kinematic quantities observed in prompt photon production at ZEUS, compared with predictions from PYTHIA6.1 calculated with differing values of the mean intrinsic transverse momentum $<k_T>$ of the partons in the photon. The quantities plotted are calculated in the plane transverse to the beam direction and are: (a) perpendicular momentum component of the photon relative to the axis of the jet, (b) longitudinal momentum imbalance (photon–jet) along the axis of the jet, (c) absolute momentum component of the photon relative to that of the jet, (d) difference in azimuthal angle between the photon and jet directions. Statistical errors are shown, the systematic uncertainties may be neglected in comparison.

9.8.2 Intrinsic k_T effect for $x_\gamma^{meas} > 0.9$

Figure 9.12 shows normalised distributions of kinematic quantities, as discussed in figure 9.11, of the prompt photon + jet system, for events selected with $x_\gamma^{meas} > 0.9$. The events with $x_\gamma^{meas} > 0.9$ are predominantly from the direct photoproduction processes, and the restriction to high x_γ^{meas} also minimises the effects of hard gluon radiation from the recoil quark in direct processes.

Also shown in the figures are the predictions from PYTHIA 6.1, which include the small contributions from resolved events with $x_\gamma^{meas} > 0.9$. The k_0 value for partons in the resolved photon was fixed at the PYTHIA 6.1 default value of 0.44 GeV, but its effects here are small since the selected events come predominantly from direct processes. The PYTHIA predictions are shown again for a variety of values of the two–dimensional Gaussian width k_0 of the partons in the proton, where $<k_T>$ is given by $<k_T> = \sqrt{\pi/4}k_0$.

Again the MC models with k_0 in the range 1–2 GeV more successfully reproduce the shape of the k_T–sensitive kinematical quantities than the PYTHIA 6.1 default. In addition k_0= 3 GeV is excluded by $p_\perp$ and $\Delta\phi$ distributions.

To evaluate the optimum value of $<k_T>$ in the proton, a minimum–χ^2 calculation was performed using the $p_\perp$ and $\Delta\phi$ data and MC distributions; (figure 9.13 (a) and (c)). A second order polynomial fit to the each χ^2 point was used to find the best value of $<k_T>$ in the proton. The resulting fitted values of $<k_T>$ are ;

- 1.39 $\pm$ 0.36 GeV (from $p_\perp$ distribution; first 4 bins used.)
- 1.28 $\pm$ 0.49 GeV (from $\Delta\phi$ distribution; last 3 bins used.)

Both kinematic quantities, $p_\perp$ and $\Delta\phi$, yield approximately the same value for $<k_T>$. These results confirm that the data are consistent with $<k_T>$ values in the range 1–2 GeV. The fitted result is shown in figure 9.13 (b) for the $p_\perp$ distribution. Since the result from $p_\perp$ is better defined, we regard the $\Delta\phi$ result just as a check.

9.8.3 Systematic checks for $<k_T>$ value in the proton

In figure 9.14, the $p_\perp$ and $\Delta\phi$ quantities are plotted (a),(b) for events with $x_\gamma^{meas} >$ 0.85, and (c),(d) for event with $x_\gamma^{meas} > 0.9$ in the range $-0.5 < \eta^\gamma < 0.7$, in order to check the systematic effects, as discussed in section 9.4. The variation in these

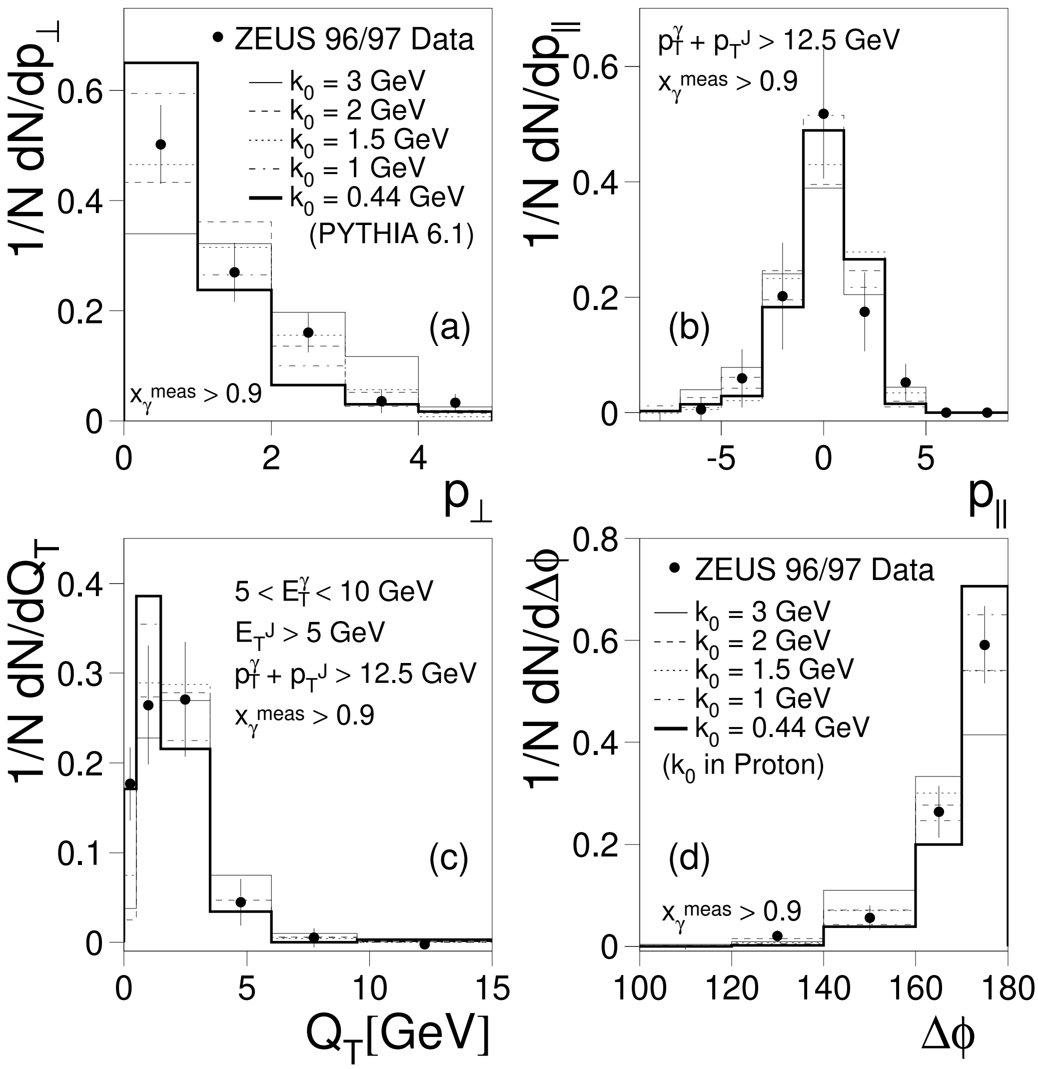

Figure 9.12: Normalised distributions of kinematic quantities observed in prompt photon production at ZEUS, compared with predictions from PYTHIA6.1 calculated with differing values of the mean intrinsic transverse momentum $<k_T>$ of the partons in the proton. Only events with $x_\gamma^{meas} > 0.9$ are used. The quantities plotted are calculated in the plane transverse to the beam direction and are: (a) perpendicular momentum component of the photon relative to the axis of the jet, (b) longitudinal momentum imbalance (photon – jet) along the axis of the jet, (c) absolute momentum component of the photon relative to that of the jet, (d) difference in azimuthal angle between the photon and jet directions. Statistical errors are shown, the systematic uncertainties may be neglected in comparison.

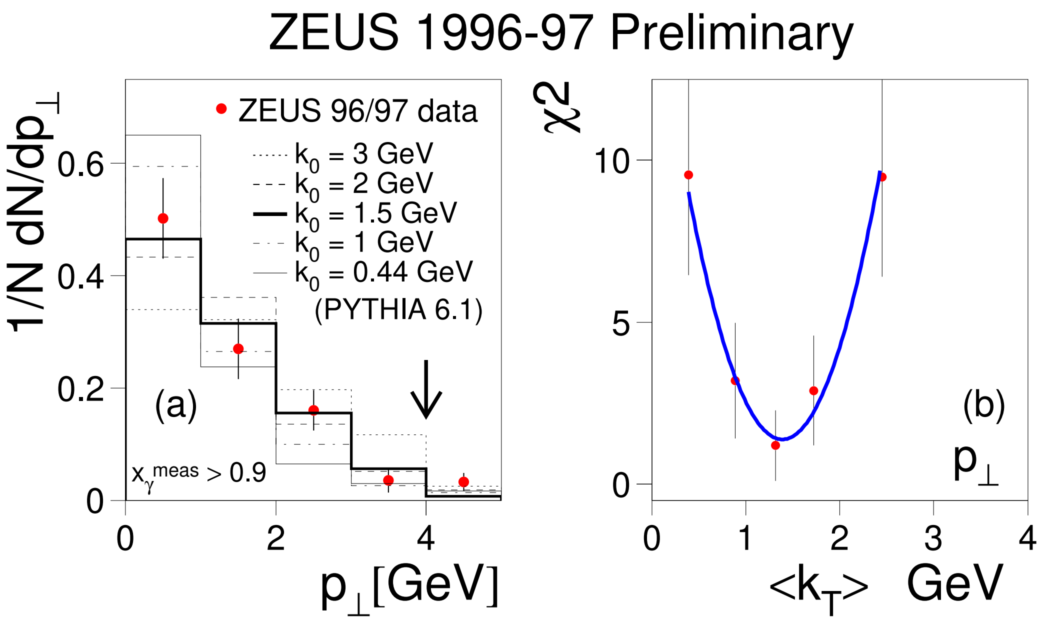

Figure 9.13: (a) Normalised distributions of kinematic quantities observed in prompt photon production at ZEUS, compared with predictions from PYTHIA6.1 calculated with differing values of the mean intrinsic transverse momentum $<k_T>$ of the partons in the proton. Only events with $x_\gamma^{meas} > 0.9$ are used. The quantities plotted are calculated in the plane transverse to the beam direction and is: perpendicular momentum component of the photon relative to the axis of the jet. (b) the optimum value of $<k_T>$ in the proton using a minimum–χ^2 calculation.

quantities allows for possible error in the modelling of the process. Comparisons with PYTHIA are again made with k_0 for the proton varying from 0.44 GeV to 3 GeV. As discussed in section 9.4 the other systematic sources led to final result variations typically at the 1–2% level, and are thus neglected compared to the other uncertainties in the present measurement.

The same χ^2 minimization procedure has been done not only to determine the best value of $<k_T>$ for each quantity, but also to evaluate the systematic effects of variations on kinematic cuts. The results are ;

- 1.16 ± 0.39 GeV (from $x_\gamma^{meas} > 0.85$; figure 9.14 (a))
- 1.51 ± 0.41 GeV (from $-0.5 < \eta^\gamma < 0.7$; figure 9.14 (c))

The resulting fitted value of $<k_T>$ was $1.39 \pm 0.36\ ^{+0.12}_{-0.23}$ GeV using the $p_\perp$ data and MC histograms. Taking systematic uncertainties into account, the values of 0.44 GeV and 3 GeV are excluded at the 2% and 0.5% levels respectively. The fit using the $\Delta\phi$ data gave a similar result with a larger statistical error.

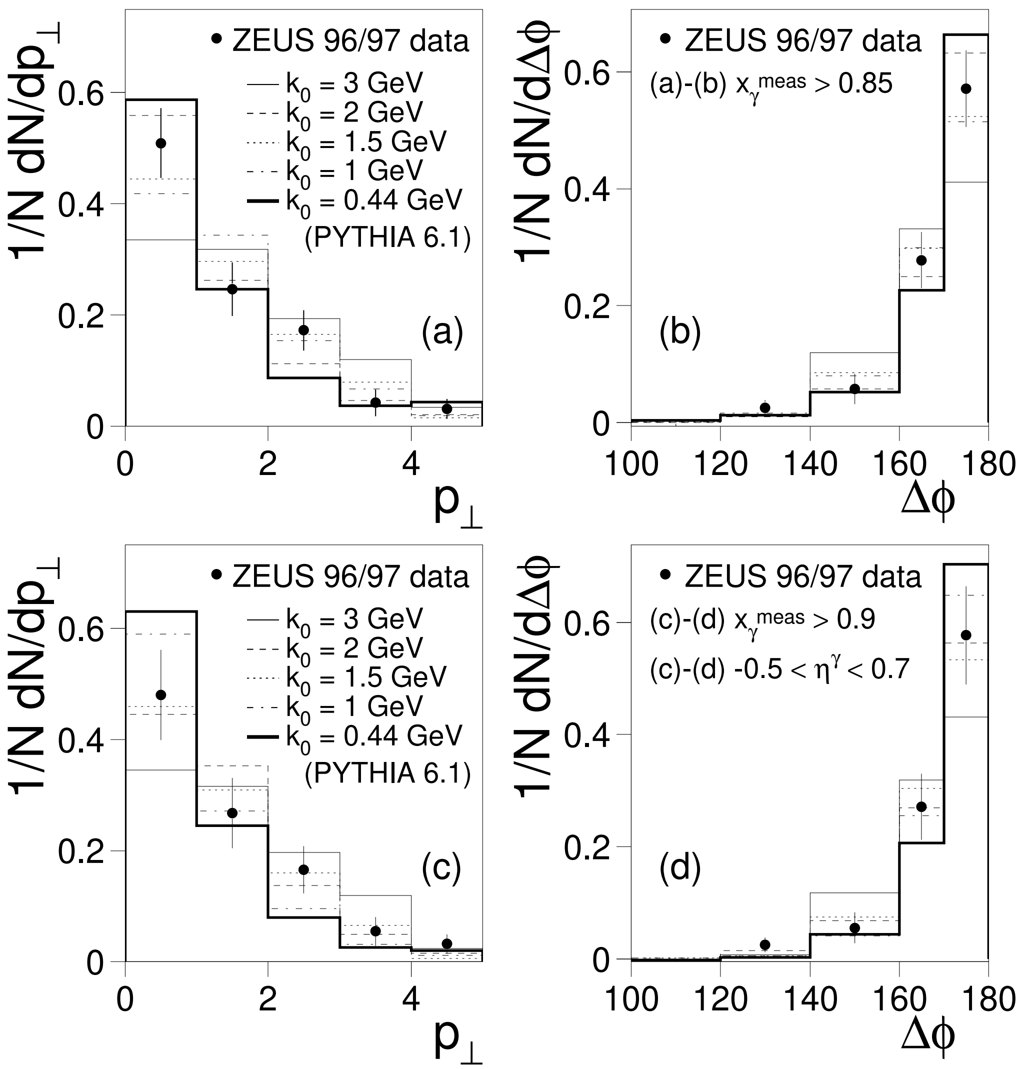

Figure 9.14: Normalised distributions of kinematic quantities observed in prompt photon production at ZEUS, compared with predictions from PYTHIA6.1 calculated with differing values of the mean intrinsic transverse momentum $<k_T>$ of the partons in the photon. Events with $x_\gamma^{meas} > 0.85$ are used in (a),(b) and event with $x_\gamma^{meas} > 0.9$ in the range $-0.5 < \eta^\gamma < 0.7$ are used in (c),(d). The quantities plotted are calculated in the plane transverse to the beam direction and are: (a),(c) perpendicular momentum component of the photon relative to the axis of the jet, and (b),(d) difference in azimuthal angle between the photon and jet directions. Statistical errors are shown.

Further discussion of the physics interpretation of this $<k_T>$ value will be given in section 9.11

9.9 Study of Parton Behaviour in the Photon

We looked at the intrinsic k_T effects in the proton independently of the photon with a variety of different combinations for proton intrinsic $<k_T>$ values. In this case obviously the direct photon diagram does not require any intrinsic $<k_T>$ values in the photon.

The ZEUS collaboration has previously observed that adjusting the intrinsic k_T of the partons in the photon is a way to improve the agreement between the data and MC predictions from the study of the photon remnant in resolved photoproduction process [97]. As a result a better agreement can be obtained by increasing the k_0 of the partons in the photon to about $k_0 = 0.66 \pm 0.22$ GeV, as compared to $k_0 = 0.44$ GeV for PYTHIA 6.1 with default parameters.

A similar behaviour of partons in the photon had been observed in the production of two photon process from e^+e^- collisions at LEP experiments [98]. The power–like distribution of the intrinsic transverse momentum of the struck photon greatly improves the hadronic final state distributions of both PYTHIA and HERWIG. From the recent measurement of the low–x behaviour of the photon structure function $F_2^\gamma(x, Q^2)$ by the OPAL experiment [99], the improved MC models have been used for the F_2^γ measurement to reduce a large model–dependent systematic uncertainty coming from the MC modelling of the hadronic final state of deep inelastic electron–photon scattering events. The HERWIG model implementing a modified k_T distribution for the quarks inside the photon was used for this purpose.

However recently H1 results from both the photon remnant and inclusive photoproduction of π^0 mesons [100] shows that the data are inconsistent with large values of an intrinsic $<k_T>$ in the photon. H1 used the PYTHIA model to look at the evidence for non–zero intrinsic $<k_T>$ of partons inside the photon using several choices of k_0 parametrizations ; a Gaussian, an exponential, and power law parametrizations. (see chapter 5 for details)

It would therefore be attractive to determine kinematically whether the partons in the hadronic photon possess high values of $<k_T>$ in resolved processes at HERA and to check the effects suggested by other experiments.

9.9.1 Intrinsic k_T effect for $x_\gamma^{meas} < 0.9$

In figure 9.15, the k_T–sensitive kinematic quantities are plotted for events with $x_\gamma^{meas} < 0.9$, where resolved photoproduction diagrams dominate. As modelled by PYTHIA there is a substantial fraction of radiative dijet events in this sample; like the prompt photon events themselves, these still arise from resolved processes. With the caveat that this fraction is not yet well determined experimentally, comparisons with PYTHIA are again made with k_0 for the proton varying from 0.44 GeV to 3 GeV.

In this distribution effects of possible inelasticities in the final state are evident: the asymmetry in $p_{||}$ indicates that the selected jet often has insufficient momentum to balance that of the photon. The sharp fall–off at negative $p_{||}$ remains in principle a good measure of the event kinematics. In these plots, moreover, a measurement of the photon $<k_T>$ is not possible with present statistics.

As discussed in the previous section, measuring the intrinsic $<k_T>$ in the proton with clean direct samples ($x_\gamma > 0.9$) shows that the data imply $<k_T>$ values in the range 1 – 2 GeV. A similar analysis is now performed for resolved photon processes, fixing the proton k_0 at 1.5 GeV, in order to study the parton behaviour inside the photon. The result from the PYTHIA model using the default parameters (k_0 = 0.44 GeV for both the proton and the photon) is also overlaid on the data to compare with PYTHIA predictions.

Figure 9.16 shows the k_T–sensitive distributions area normalised, for $x_\gamma^{meas} <$ 0.9. The data are compared to four PYTHIA models calculated with varying values of the intrinsic k_T of the partons in the proton, fixing $<k_T>$ values in the proton. The general agreement between the data and the various models is reasonably but does not allow a determination of $<k_T>$ for the present statistics.

9.10 Study of Jet Reconstruction Methods

As mentioned above, jets were reconstructed using energy flow objects, ZUFOS, which combine information from the calorimeter cells and tracks, by means of KTCLUS [76], in the inclusive mode. As further checks, four alternative strategies for identifying a jet were examined.

- Jet mode 1 : KTCLUS algorithm using calorimeter cells
- Jet mode 2 : KTCLUS algorithm using Zufos (default)

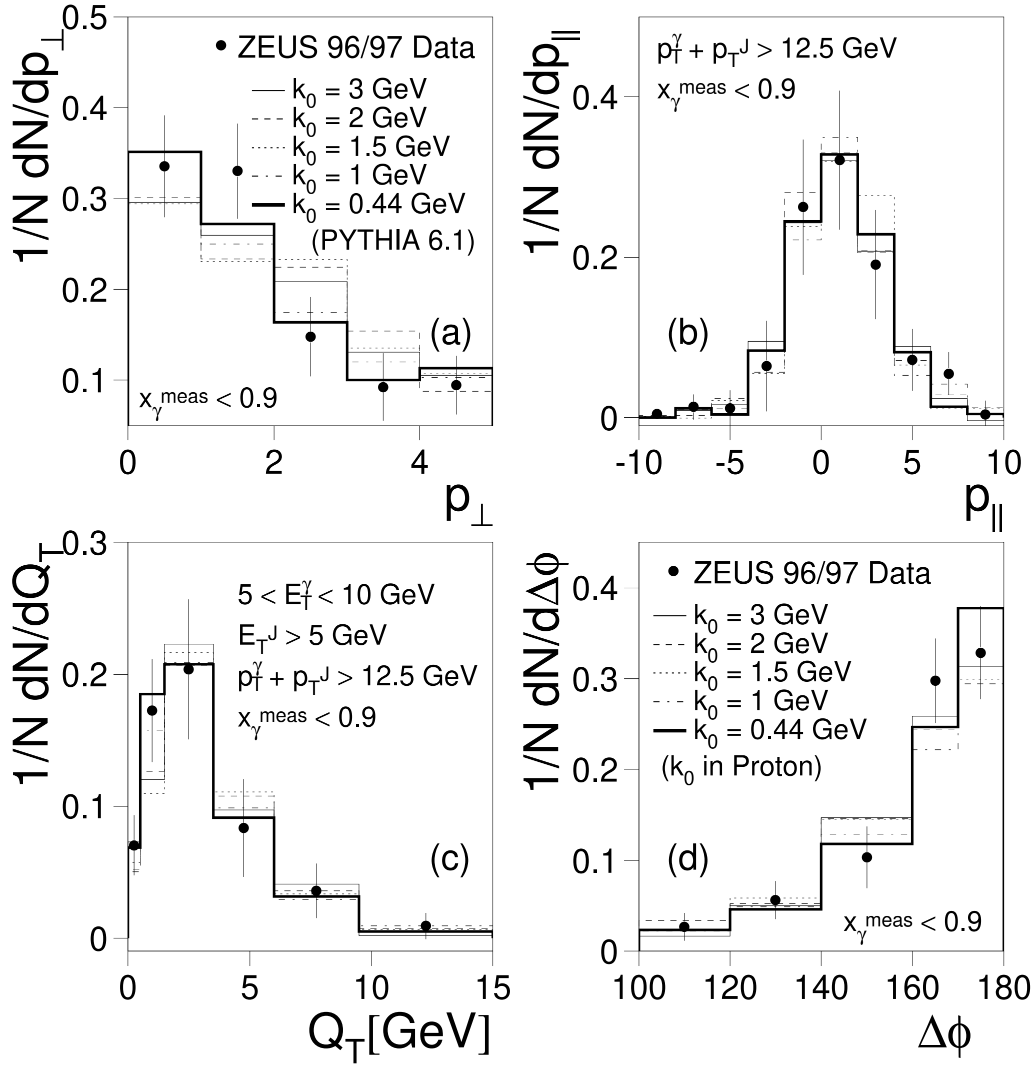

Figure 9.15: Normalised distributions of kinematic quantities observed in prompt photon production at ZEUS, compared with predictions from PYTHIA6.1 calculated with differing values of the mean intrinsic transverse momentum $<k_T>$ of the partons in the photon. The quantities plotted are calculated in the plane transverse to the beam direction and are: (a) perpendicular momentum component of the photon relative to the axis of the jet, (b) longitudinal momentum imbalance (photon – jet) along the axis of the jet, (c) absolute momentum component of the photon relative to that of the jet, (d) difference in azimuthal angle between the photon and jet directions. Statistical errors are shown, the systematic uncertainties may be neglected in comparison.

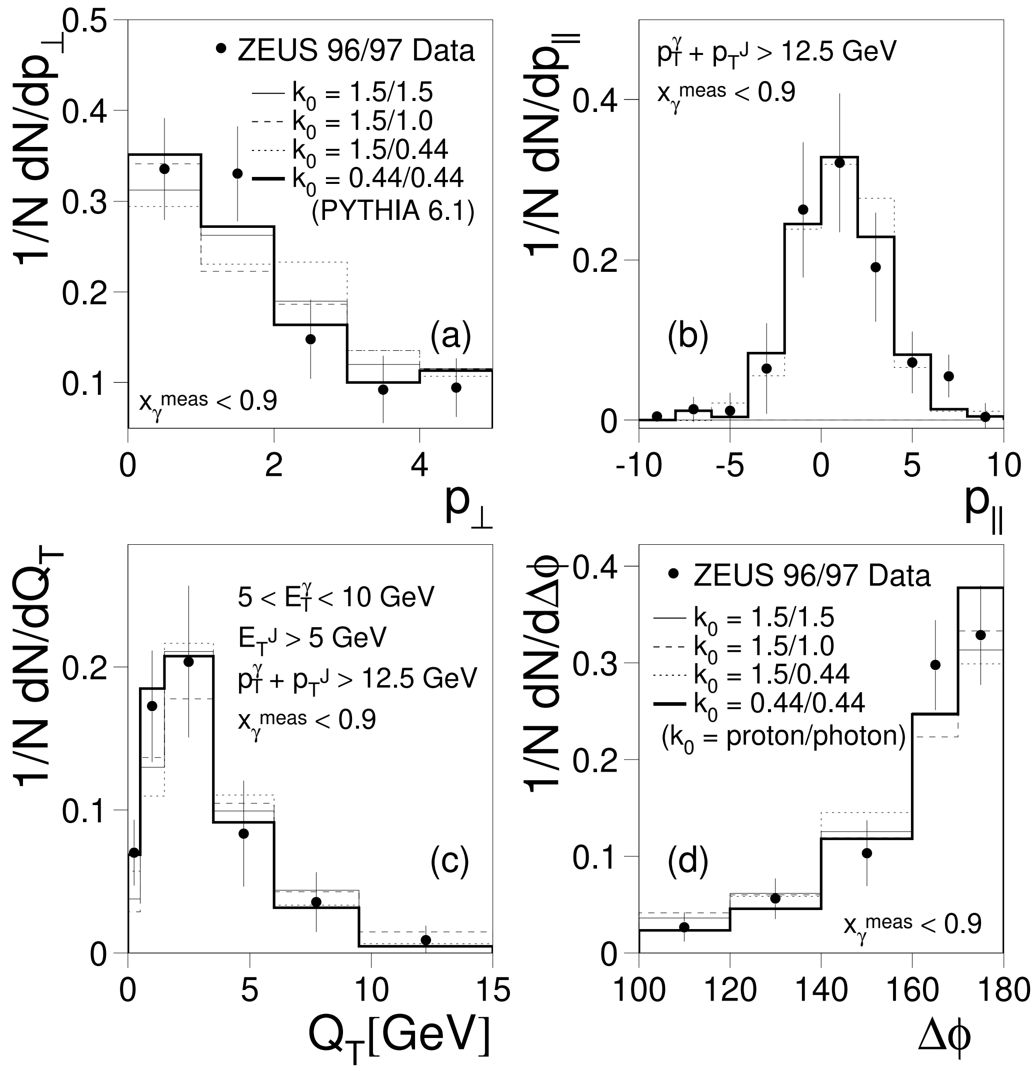

Figure 9.16: Normalised distributions of kinematic quantities observed in prompt photon production at ZEUS, compared with predictions from PYTHIA6.1 calculated with differing values of the mean intrinsic transverse momentum $<k_T>$ of the partons in the photon. Only events with $x_\gamma^{meas} < 0.9$ are used. The quantities plotted are calculated in the plane transverse to the beam direction and are: (a) perpendicular momentum component of the photon relative to the axis of the jet, (b) longitudinal momentum imbalance (photon – jet) along the axis of the jet, (c) absolute momentum component of the photon relative to that of the jet, (d) difference in azimuthal angle between the photon and jet directions. Statistical errors are shown, the systematic uncertainties may be neglected in comparison. Note) The first k_T value refers to the proton k_T and the second k_T value refers to the photon k_T.

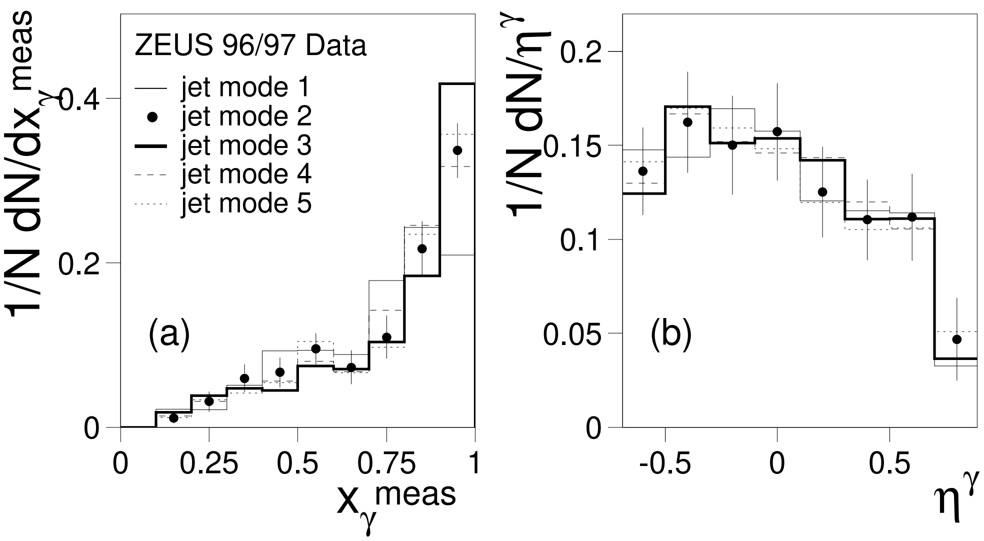

Figure 9.17: Normalised distributions in (a) x_γ^{meas} and (b) η^γ of prompt photon events, accompanied by balancing jets, after background subtraction. Shown in comparison are the same quantities from different methods of changing the jet search.

- Jet mode 3 : KTCLUS algorithm with larger radius parameter using Zufos
- Jet mode 4 : EUCELL algorithm, using Zufos
- Jet mode 5 : KTCLUS algorithm using energy weighted method

The results according to the different jet modes are plotted in figures 9.17 and 9.18, normalised distributions of kinematic quantities of the prompt photon + jet system. It should be noted that the Jet mode 2 is used as the default mode of jet finding method for the final results. The Jet mode 3 (increasing the jet–radius parameter by a factor 1.25) has sensitivity to the possible jet–broadening effects of hard final–state gluon radiation.

Figure 9.17 (a) and (b) shows the background subtracted x_γ^{meas} and η^γ distributions for the selected sample of photon plus jet events. The distribution is presented for the five different modes of jet reconstruction method, as discussed above. In order to facilitate the comparison of shapes between various jet reconstruction modes, all distributions are normalized to unit area.

The x_γ direct peak from 1 is poorly defined; method 3 gives a sharper, more inclusive peak as might be expected. It should be noted that much larger jet energy corrections are needed for method 1. Methods 2, 4, 5 give similar results.

The correlation of the photon + jet system is shown in figure 9.18 by normalised distribution as a function of several kinematic quantities sensitive to

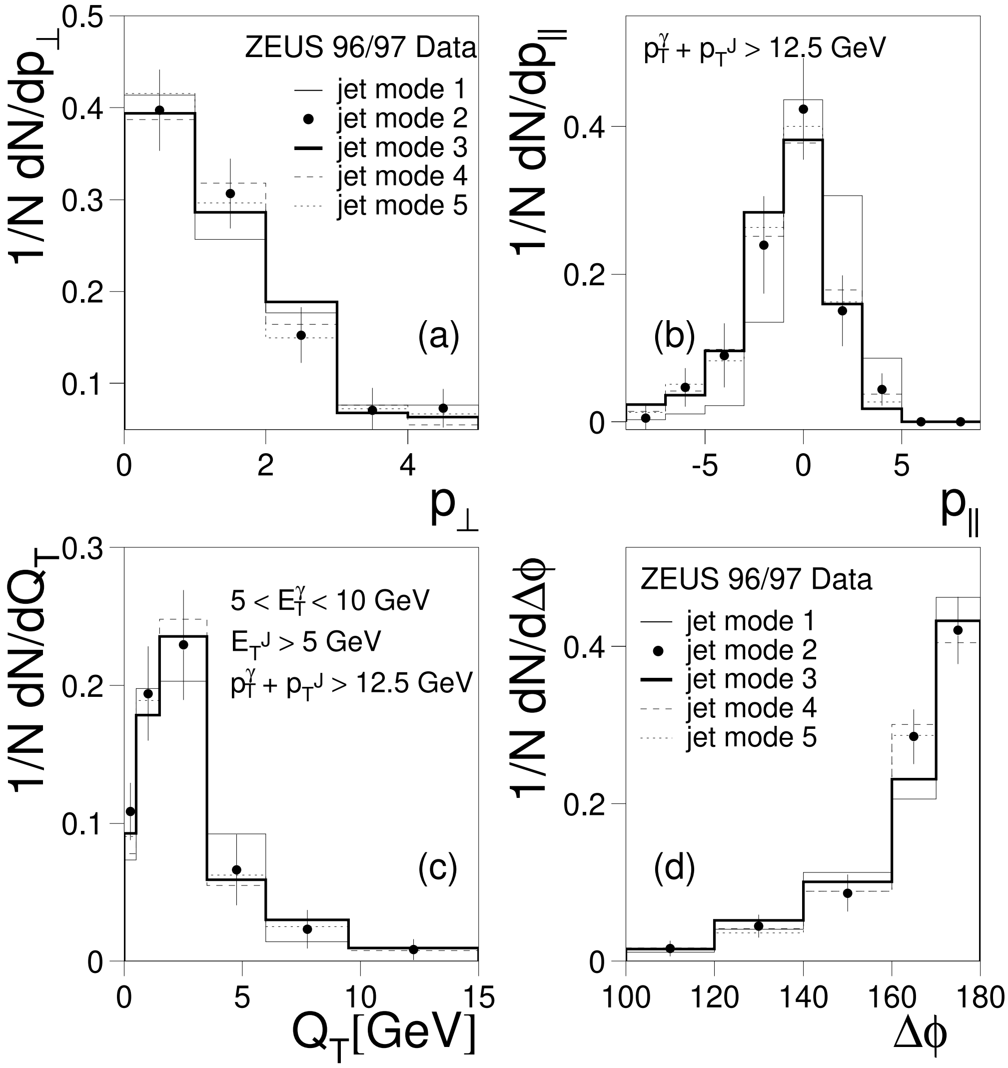

Figure 9.18: Normalised distributions in (a) $p_\perp$, (b) $p_{||}$, (c) Q_T and (d) $\Delta\phi$, of prompt photon events, accompanied by balancing jets, after background subtraction. Shown in comparison are the same quantities from different methods of changing the jet search.

intrinsic momentum, k_T, of initial state partons, namely, (a) $p_\perp$, (b) $p_\parallel$, (c) Q_T and (d) $\Delta\phi$, respectively. As before, the results from modes 2,4,5 are very similar. Mode 1 gives better aligned jets, but is not used in view of the poor direct x_γ peak and the large E_T jet corrections. Mode 3 would be a viable alternative method, but possibly is sensitive to higher–order QCD effects which are not connected to $<k_T>$. Further study on each jet reconstruction mode was performed using the kinematic quantities of the prompt photon data with $x_\gamma^{meas} > 0.9$, comparing with predictions from PYTHIA calculated with the favoured $k_0 = 1.5$ GeV in the proton. Again the results from all jet reconstruction modes were consistent with the main method within statistical uncertainties.

9.11 Comparisons with Other Experiments

Recently the TeVatron experiments highlighted serious limitations of current pQCD description of high p_T prompt photon production. One offered explanation is that the partons in the proton may have a considerably higher value of $<k_T>$ due to the soft gluon radiation at lower E_T region.

At the CDF and DØ experiments ($\sqrt{s} = 1.8$ TeV), Gaussian smearing of the intrinsic parton $<k_T>$ by 3.5 GeV can model the rise of prompt photon cross section at low E_T region. In addition, NLO with 2.5 GeV $<k_T>$ describe the CDF data very well at $\sqrt{s}$ =630 GeV. Using diphoton production, CDF has also measured the parton $<k_T>$ value directly; $<k_T> = 3.6 \pm 0.8$ GeV at $\sqrt{s} = 1.8$ TeV [101].

Recently the E706 at $\sqrt{s} = 20 \sim 30$ GeV observed large deviations between NLO calculations and data, for both prompt photon and π^0 inclusive cross sections. Their conclusion is that a simple implementation of supplemental parton k_T 1.2 GeV, in theoretical calculations is needed to provide a reasonable description of the inclusive cross sections. WA70 ($\sqrt{s} = 23.0$ GeV) and UA6 ($\sqrt{s} = 24.3$ GeV) actually measured the $<k_T>$ values, $<k_T> = 0.9 \pm 0.1 \pm 0.2$ GeV, based on the data for diphoton production and the values are expected to be slightly smaller than the value required for the E706 experiment [46].

These experimental measurements demonstrated that phenomenological $<k_T>$ model provides a better agreement with data than is available in the enhanced parton–shower model. In addition $<k_T>$ values seems to be increase approximately logarithmically with $\sqrt{s}$.

Evidence of significant $<k_T>$ effects has long been observed in measurements of dimuon, diphoton, and dijet pairs. A collection of measurements of the average transverse momentum of the pairs, $< Q_T >$, is presented in figure 2.7, for

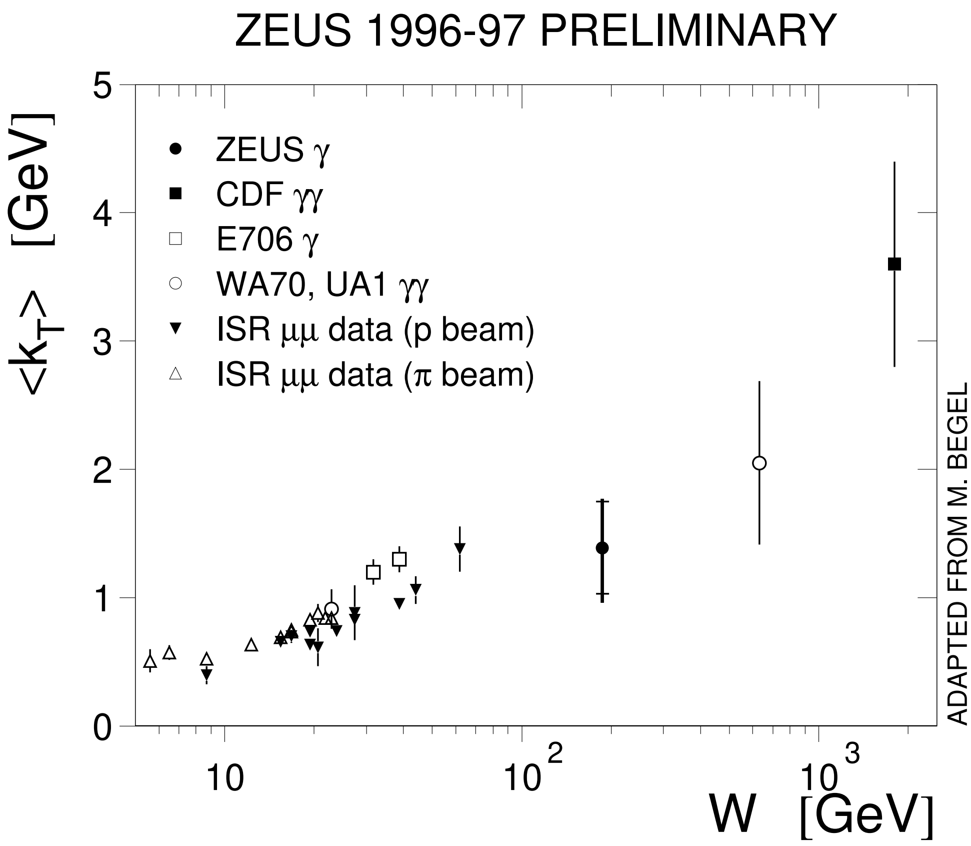

Figure 9.19: ZEUS result for $<k_T>$ compared with results from other experiments (inner error bar = statistical error, outer = statistical + systematic in quadrature). Other published results have been scaled by $\sqrt{2}$ as appropriate. The single prompt photon results from CDF and DØ are in agreement with the double prompt photon CDF point plotted [46]. Full references may be found in a recent FNAL report [101] from which the present figure has been adapted. The error bars from the ISR data [103] have been enlarged to cover the range of the published points. The horizontal axis denotes the centre-of-mass energy of the interacting system, which is the incoming γp system in the case of ZEUS.

a wide range of centre–of–mass energies ($\sqrt{s}$). In figure 9.19 the ZEUS result is shown in comparison with results from other experiments. For consistency, the quantity $<k_T>$ is plotted from the present ZEUS measurement and elsewhere where appropriate; it is nevertheless still not guaranteed that all the indicated measurements have been evaluated in exactly the same way. However, a rising trend with increasing centre–of–mass energy of the reaction is evident, as discussed most recently by Laenen et al. [48], and with which the present ZEUS data are fully consistent.

At γp centre–of–mass energies W of 120–274 GeV, we have observed such $<k_T>$ effects of the parton in the proton using prompt photon photoprodution. Our best $<k_T>$ value at HERA estimated by a minimum–χ^2 calculation is $<k_T>$ $= 1.39 \pm 0.36\ ^{+0.12}_{-0.23}$ GeV. This result confirms that the parton $<k_T>$ in the proton have increase approximately logarithmically.

9.12 Conclusions

The kinematical properties of prompt photons accompanied by recoil jets have been studied in photoproduction events using the ZEUS detector at HERA. Data were taken in an effective centre-of-mass γp energy range of $120 < W < 274$. As modelled within the PYTHIA Monte Carlo, the acollinearity of the photon + jet system was used to investigate the intrinsic $<k_T>$ of the quarks in the proton. Several distributions of the kinematic quantities for prompt photon production at HERA show that there is significant evidence for the presence of the intrinsic $<k_T>$ effects in such hard scattering process.

Values as high as $<k_T>\ = 3.0$ GeV in the proton, as suggested in an earlier high–energy $\bar{p}p$ experiment, are excluded under the present experimental conditions, as is the present PYTHIA default value of 0.44 GeV. The ZEUS prompt photon data are consistent with $<k_T>$ values inside proton in the range 1–2 GeV. A minimum-χ^2 calculation was performed to evaluate the best value of $<k_T>$ using the $p_\perp$ data and Monte Carlo histograms. A fit to the data gave a value of $<k_T>$ of $1.39 \pm 0.36\ ^{+0.12}_{-0.23}$ GeV. This result is consistent with a generally observed trend that the effective parton $<k_T>$ rises with the energy of the interacting hadronic system. For the parton $<k_T>$ effects in the photon side, however, the data do not provide a clear measurement with present statistics.

Chapter 10

Summary

In this thesis the differential cross sections of inclusive isolated prompt photon production, $e + p \to \gamma + X$, at HERA has been measured for the first time for hard photoproduction events using the ZEUS detector. The data were taken from e^+p collisions during the 1996 and 1997 HERA running period and correspond to an integrated luminosity of 38.4 pb^{-1}.

Inclusive cross sections within the kinematic range $0.2 < y < 0.9$, equivalent to incident γp centre–of–mass energies W of 134–285 GeV, are presented as a function of E_T^γ for the production of isolated prompt photons in the pseudorapidity range $-0.7 < \eta^\gamma < 0.9$, and as a function of η^γ for photons with $5 < E_T^\gamma < 10$ GeV. The latter results are given for the full W range and three partial ranges, $134 < W < 170$ GeV, $170 < W < 212$ GeV and $212 < W < 285$ GeV.

In presenting cross sections, comparisons are made with two types of theoretical calculation, in which the pdf sets taken for both the photon and the proton can be varied. These are (1) leading–logarithm parton shower Monte Carlo (PYTHIA and HERWIG) calculations evaluated at the final–state hadron level and (2) next–to–leading order parton–level calculations of Gordon and of Krawczyk and Zembrzuski.

The theoretical models are able to describe the data well for the forward (proton direction) values of photon pseudorapidity, but are low in the rear direction. None of the available variations of the model parameters was found to be capable of removing the discrepancy with the data. The disagreement is strongest within the W interval 134–170 GeV, and not seen within the measurement acceptance for $W > 212$ GeV. Together with the recent dijet results at HERA [89], the prompt photon results indicated a need to review the present theoretical modelling of the parton structure of the photon in the high x_γ regions.

We also present a first study of the mean parton intrinsic transverse momentum $<k_T>$ in the proton and photon using the kinematical properties of events with a measured jet as well as a prompt photon, with the goal of searching the evidence for parton $<k_T>$ effects in high–E_T prompt photon production at HERA. This work is motivated by the observation in a number of previous experiments that the production of inclusive prompt photons in hadronic reactions is unexpectedly high in lower regions of transverse energy. A discrepancy of this kind could arise from the intrinsic transverse momentum, $<k_T>$, of the parton in the incoming hadron or from multiple initial–state soft gluon radiation which can enhance the effective $<k_T>$ value of the parton as it interacts.

As modelled within the PYTHIA Monte Carlo, the acollinearity of the photon–jet system was used to investigate the intrinsic $<k_T>$ of the quarks in the proton at HERA. Several distributions for the kinematic properties of prompt photons accompanied by recoil jets show that there is significant evidence for the presence of the intrinsic $<k_T>$ effects in such hard scattering process. Values as high as $<k_T> = 3.0$ GeV in the proton, as suggested in an earlier high–energy $\bar{p}p$ experiment, are excluded under the present experimental conditions, as is the present PYTHIA 6.1 default value of 0.44 GeV. It can be interpreted as evidence of parton intrinsic transverse momentum $<k_T>$ effects in the proton via prompt photon photoproduction at HERA.

A fit to the data gave a value of $<k_T>$ of $1.39 \pm 0.36\ ^{+0.12}_{-0.23}$ GeV. This result is consistent with a generally observed trend that the effective parton $<k_T>$ rises with the energy of the interacting hadronic system. For the parton $<k_T>$ effects in the photon side, however, the data do not provide a clear measurement with present statistics. There is still a large statistical uncertainty in the present prompt photon data at HERA. More statistics on both data and Monte Carlo models, therefore, will allow for precision measurement of behaviour of the parton $<k_T>$ inside the proton and even the photon at HERA, and can in principle provide experimental guidance to a better theoretical modelling of possible soft gluon radiation effects.

In conclusion, prompt photon production at HERA still has much to tell us and future work promises to reveal further important information on QCD and partonic nature of matter.

Appendix A

Contribution to the Photon'99 Conference

The results presented here include measurements of inclusive prompt photons and prompt photons accompanied by jets, although the author's input has been mainly concerned.

Paper published in the Proceedings of International Conference on the Structure and Interactions of the Photon (Photon'99) held in Freiburg im Breisgau, Germany, 23-27 May 1999, ed. S. Söldner-Rembold, March 2000. This contribution has now been published in Nucl. Phys. Proc. Suppl., Vol. 82.

Prompt Photon Processes in Photoproduction at HERA

Sung Won Lee[a]

[a] Dept. of Physics and Astronomy, University of Glasgow, Glasgow, U.K.

We present results for the photoproduction of inclusive prompt photons and for prompt photons accompanied by jets, measured with the ZEUS detector at HERA. Cross sections as a function of pseudorapidity and transverse energy are presented for $5 < E_T^{\gamma} < 10$ GeV, $E_T^{jet} > 5$ GeV in the centre of mass energy range 120–270 GeV. Comparisons are made with predictions from leading logarithm parton shower Monte Carlos and next-to-leading order QCD calculations using currently available models of the photon structure. NLO QCD calculations describe the shape and magnitude of the measurements reasonably well.

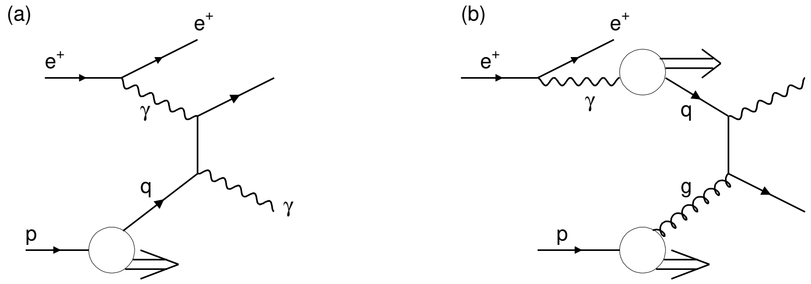

Figure A.1: Example of (a) direct (pointlike) (b) resolved (hadronic) processes in LO hard photoproduction producing an outgoing prompt photon.

A.1 Introduction

Isolated high transverse energy ("prompt") photon processes at HERA (figure A.1) could yield information about the quark and gluon content of the photon, together with the gluon structure of the proton [19]. The particular virtue of prompt photon processes is that the observed final state photon emerges directly from a QCD diagram without the subsequent hadronisation which complicates the study of high E_T quarks and gluons.

The ZEUS collaboration has recently published the first observation at HERA of prompt photons at high transverse momentum in photoproduction reactions [18], based on an integrated luminosity of 6.4 pb^{-1}. An NLO calculation by Gordon [22] was found to be in agreement with the ZEUS results, and indicates the feasibility of distinguishing between different models of the photon structure.

In the present study we extend our earlier study of prompt photon production from a data sample of 37 pb^{-1}. Differential cross sections are given for the final state containing a prompt photon, and a prompt photon accompanying jet as a function of pseudorapidity and of transverse photon energy.

Comparison is made with several LO and NLO (next to leading order) predictions, with the goal of testing different proposed hadronic structures of the incoming photon.

A.2 Event Selection

The data used here were obtained from e^+p running in 1996–97 at HERA, with E_e = 27.5 GeV, E_p = 820 GeV. The ZEUS experiment is described elsewhere [104]. The major components used in the analysis are the central tracking detector (CTD) and the uranium-scintillator calorimeter(UCAL). Prompt photons are detected in the barrel section of the calorimeter (BCAL), which consists of an electromagnetic section (BEMC) followed by two hadronic sections; the BEMC consists of pointing cells of ≈ 20 cm length and ≈ 5 cm width at a minimum radius 1.23m from the beamline. This width is not small enough to resolve the photons from the processes $\pi^0 \to 2\gamma$, $\eta \to 2\gamma$ and $\eta \to 3\pi^0$ on an event by event basis. It does, however, enable a partial discrimination between single photon signals and the decay product of neutral mesons.

A standard ZEUS electron finding algorithm was used to identify candidate photon signals in BCAL with measured $E_T^\gamma > 4.5$ GeV. The Energy loss in dead material to the measured photon energy has been corrected using MC generated single photons. This correction amounted typically to 200-300 MeV. After the photon energy correction the events were retained for final analysis if a photon candidates with transverse energy $E_T^\gamma > 5$ GeV was found in the BCAL. To identify jets, a cone jet finding algorithm [92] was used. Jet with $E_T^{jet} > 4.5$ GeV and pseudorapidity $-1.5 < \eta^{jet} < 1.8$ were accepted with a cone radius of 1 radian, where pseudorapidity is defined as $\eta = -\ln(\tan\theta/2)$. Events with an identified DIS positron were removed, restricting the acceptance of the present analysis to incoming photons of virtuality $Q^2 \leq 1$ GeV^2. The quantity y_{JB}, defined as the sum of $(E - p_Z)$ over all the UCAL cells divided by twice the positron beam energy E_e, provides a measure of the fractional energy $E_{\gamma 0}/E_e$ of the interacting quasi-real photon. A requirement of $0.15 < y_{JB} < 0.7$ was imposed, the lower cut removing some residual proton-gas backgrounds and the upper cut removing remaining DIS events. Wide–angle Compton scatters were also excluded by this cut.

A photon candidate was rejected if a CTD track pointed within 0.3 rad of it. An isolation cone was also imposed around photon candidates: within a cone of unit radius in (η, ϕ), the total E_T from other particles was required not to exceed $0.1E_T(\gamma)$. This greatly reduces backgrounds from dijet events with part of one jet misidentified as a single photon (π^0, η, etc). In addition, as discussed in [19], it removes most dijet events in which a high E_T photon radiating from a final state quark. A remainder of such events is included as part of the signal in the data and the theoretical calculations.

A.3 Signal/background separation

A typical high-E_T photon candidate in the BEMC consists of a cluster of 4-5 cells selected by the electron finder. Two shape-dependent quantities were

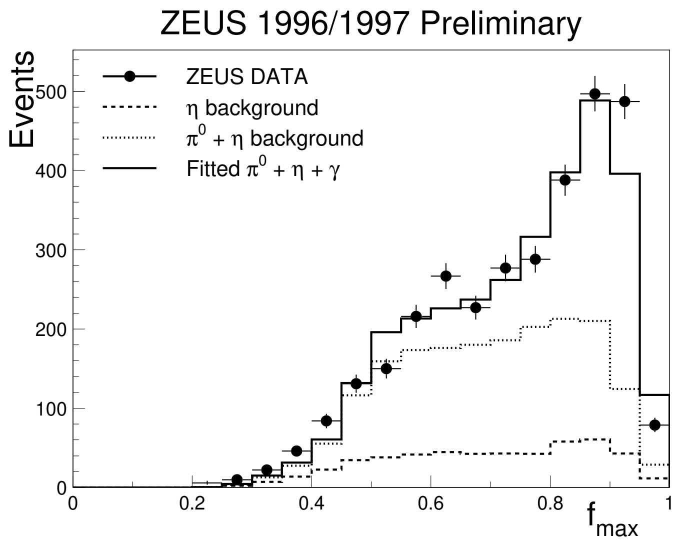

Figure A.2: Distribution of f_{max} for prompt photon candidates in selected events, after cutting on $<\delta Z>$. Also plotted are fitted Monte Carlo curves for photons, π^0 and η mesons with similar selection cuts as for the observed photon candidates.

studied in order to distinguish photon, π^0 and η signals. These were (i) the mean width $<\delta Z>$ of the BEMC cluster in Z and (ii) the fraction f_{max} of the cluster energy found in the most energetic cell in the cluster. $<\delta Z>$ is defined as the mean absolute deviation in Z of the cells in the cluster, energy weighted, measured from the energy weighted mean Z value of the cells in the cluster. Its distribution shows two peaks at low $<\delta Z>$ which are identified with photons and π^0 mesons, and a tail at higher values. This tail quantified the η background; photon candidates in this region were removed.

The remaining candidates consisted of genuine high E_T photons and π^0 and remaining η mesons. The numbers of candidates with $f_{max} \geq 0.75$ and $f_{max} < 0.75$ were calculated for the sample of events occurring in each bin of any measured quantity. From these numbers, and the ratios of the corresponding numbers for the f_{max} distributions of the single particle samples, the number of photon events in the given bin was evaluated. Further details of the background subtraction method are given in [18]. The distribution of f_{max} for prompt photon candidates in selected events is shown in figure A.2, well fitted to a sum of photon and background distributions.

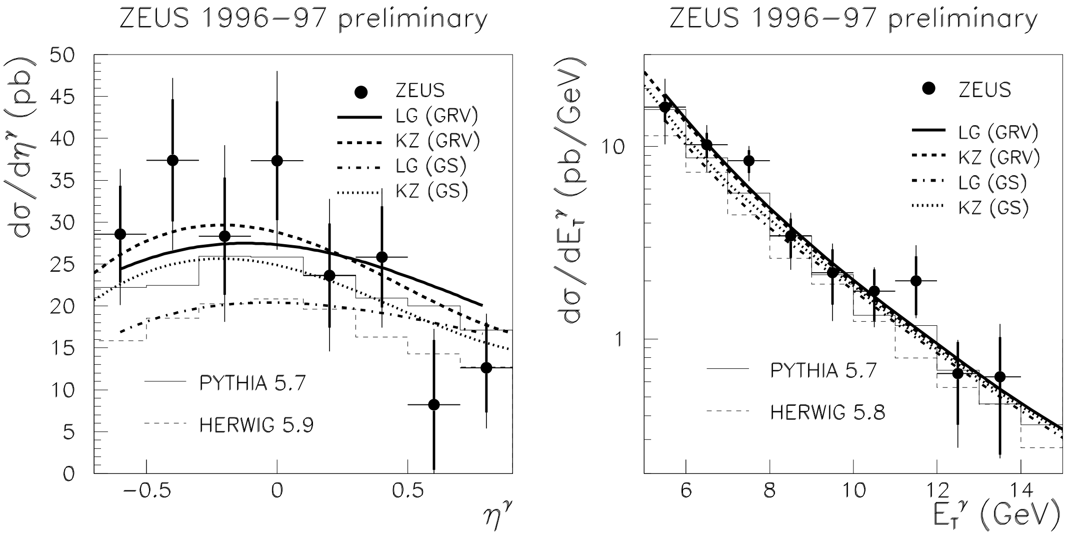

Figure A.3: Differential cross sections $d\sigma/d\eta^\gamma$ for prompt photons integrated over $5 < E_T^\gamma < 10$ GeV, $d\sigma/dE_T^\gamma$ for prompt photons integrated over $-0.7 < \eta^\gamma < 0.9$. Inner (thick) error bars are statistical, outer include systematic added in quadrature. Also plotted are PYTHIA, HERWIG and NLO calculations of LG and KZ with two different photon structures.

A.4 Results

We evaluate cross sections for prompt photon production corrected by means of PYTHIA using GRV photon structures [16]. A bin-by-bin factor is applied to the detector-level measurements so as to correct to cross sections in the specified kinematic intervals calculated in terms of the final state hadron system photoproduced in the range $0.16 < y^{true} < 0.8$, i.e. γp centre of mass energies in the range 120 – 270 GeV. The virtuality of the incoming photon is restricted to the range $Q^2 < 1$ GeV^2. When a jet was demanded, the hadron-level selections $E_T^{jet} > 5$ GeV, $-1.5 < \eta^{jet} < 1.8$ were imposed. The systematic error of 15% were taken into account and were finally combined in quadrature. The main contributions are from the energy scale on the calorimeter and the background subtraction.

Figure A.3 (left) shows an inclusive cross section $d\sigma/d\eta^\gamma$ for prompt photons in the range $5 < E_T^\gamma < 10$ GeV. Reasonable agreement between data and MC is seen at forward values of rapidity, but the data tend to lie above the MC at negative rapidity. The data are also compared with NLO calculations of Gordon(LG), Krawczyk and Zembrzuski(KZ) [22, 84] using the GS and GRV photon structures [16]. The curves are subject to a calculational uncertainty of 5%, and

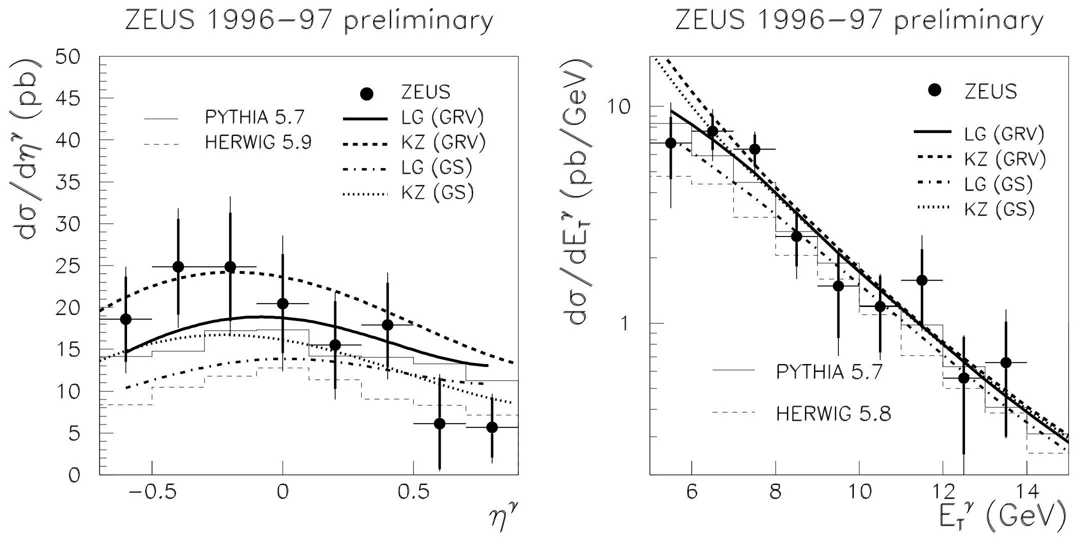

Figure A.4: Differential cross sections $d\sigma/d\eta^\gamma$, $d\sigma/dE_T^\gamma$ for prompt photons with a jet requirement. Also plotted are PYTHIA, HERWIG and NLO calculations of LG and KZ with two different photon structures.

uncertainties in the QCD scale could raise the numbers by up to $\approx 8\%$. Away from the most forward directions, the LG calculation using GS tend to lie low, while the LG implementation of the GRV photon structure give a reasonable description of the data. KZ calculation has detailed differences from LG including a box diagram contribution for the process $\gamma g \to \gamma g$ [86].

In figure A.3 (right) inclusive cross sections $d\sigma/dE_T^\gamma$ for prompt photons in the range $-0.9 < \eta^\gamma < 0.7$ are compared to the theoretical models. All six theoretical models describe the shape of the data well. However the HERWIG predictions is systematically low. The two NLO calculations are in better agreement with the data, and cannot be experimentally distinguished. Similar features can be seen in figure A.4 (right) which shows cross sections for the production of a photon accompanied by a jet in the kinematic range specified above. The KZ calculation is too high at low E_T^γ, attributable to the lack of a true jet algorithm in this approach [84].

Figure A.4 (left) shows corresponding cross sections for the photon accompanied by at least one jet. The results were corrected to hadron-level jets in the kinematic range $E_T^{jet} > 5$GeV, $-1.5 < \eta^{jet} < 1.8$. In a comparison with NLO calculations from [22, 84] the GS photon structure again provides a less good description of the data overall than that of GRV.

As with the photoproduction of a dijet final state [92], the information from the prompt photon and the measured jet can be used to measure a value of

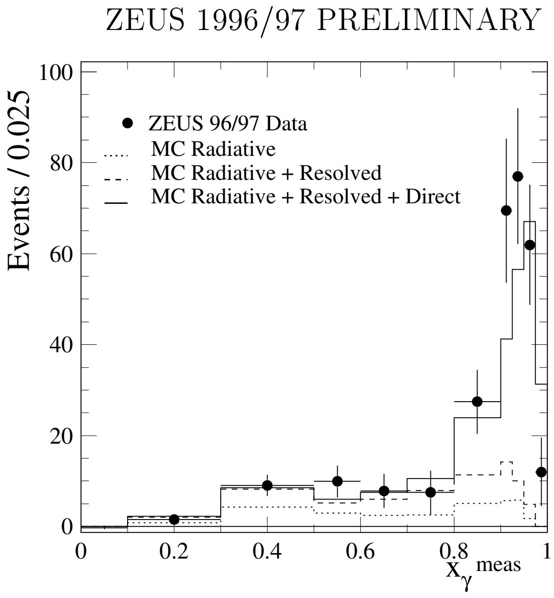

Figure A.5: x_γ^{meas} associated with the photon+jet final state at the detector level, compared with PYTHIA predictions. Points = data; dotted = MC radiative; dashed = MC radiative+resolved; solid line = MC radiative+resolved+direct.

x_γ, the fraction of the incoming photon energy which participates in the hard interaction. A "measured" value of x_γ at the detector level was evaluated as $x_\gamma^{meas} = \sum(E - p_Z)/2E_e y_{JB}$, where the sum is over the jet plus the photon. The resulting distribution is shown in figure A.5 compared with PYTHIA predictions. Reasonable agreement is seen, and a dominant peak near unity indicates clearly the presence of the direct process. Corrected to hadron level, the cross section integrated over $x_\gamma > 0.8$ is $15.4 \pm 1.6(stat) \pm 2.2(sys)$ pb. This may be compared with results from Gordon [22], which vary in the range 13.2 to 16.6 pb according to the photon structure taken and the QCD scale (approximately an 8% effect). Here, the experiment is in good agreement with the range of theoretical predictions but does not discriminate between the quoted models.

A.5 Conclusions

The photoproduction of inclusive prompt photons, and prompt photons accompanied by jets, has been measured with the ZEUS detector at HERA using an integrated luminosity of 37 pb^{-1}. Cross sections as a function of pseudorapidity and transverse energy have been measured for photon transverse energies in the range $5 < E_T^\gamma < 10$ GeV and for jet transverse energies in the range $E_T^{jet} > 5$ GeV. The results are compared with parton-shower Monte Carlo simulations of prompt photon processes and with NLO QCD calculations incorporating the currently available parameterisations of the photon structure. NLO QCD calculations describe the shape and magnitude of the measurements reasonably well.

Acknowledgments

We are grateful to L. E. Gordon, Maria Krawczyk and Andrzej Zembrzuski for helpful conversations, and for providing theoretical calculations.

Appendix B

Contribution to the DIS'2000 Conference

The results presented here include the first measurements of inclusive prompt photon cross sections in photoproduction at HERA. The author's input has been mainly concerned. This contribution will be published in the Proceedings of DIS'2000 held in Liverppol, UK, 25-30 April 2000, eds J. Gracey and T. Greenshaw.

Prompt Photon Processes in Photoproduction at HERA

Sung Won Lee[a]

[a] Dept. of Physics and Astronomy, University of Glasgow, Glasgow, U.K.

First inclusive measurements of isolated prompt photons in photoproduction at HERA have been made with the ZEUS detector. Cross sections are given as a function of the pseudorapidity and the transverse energy of the photon, for $E_T^\gamma >$ 5 GeV in the γp centre-of-mass energy range 134–285 GeV. Comparisons are made with predictions from LO Monte Carlo models and NLO QCD calculations. For forward η^γ (proton direction) good agreement is found, but in the rear direction all predictions fall below the data.

B.1 Introduction

Isolated high transverse energy ("prompt") photon processes at HERA could yield information about the quark and gluon content of the photon, together with the

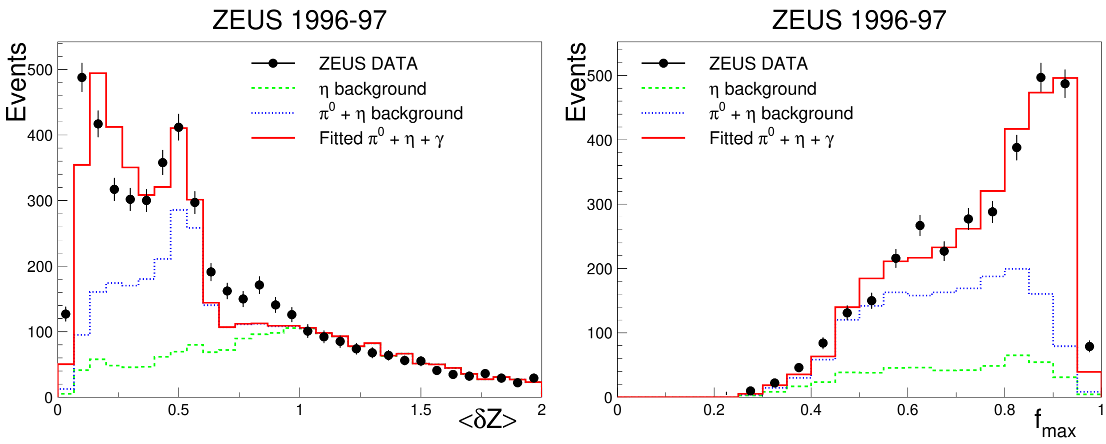

Figure B.1: Distribution of (a) $<\delta Z>$ and (b) f_{max} for prompt photon candidates in selected events. Also given in both cases are fitted MC distributions for γ, π^0 and η mesons.

gluon structure of the proton. The particular virtue of prompt photon processes is that the observed final state photon emerges directly from a QCD diagram without the subsequent hadronisation which complicates the study of high E_T quarks and gluons.

In a ZEUS paper [18] the observation of prompt photons was first confirmed at HERA. More recently [105], ZEUS collaboration has measured the cross sections of inclusive prompt photons in photoproduction reactions, using an integrated luminosity of 38.4 pb^{-1}. Comparisons are made with predictions from Monte Carlo models containing leading-logarithm parton showers, and with next-to-leading-order QCD calculations, using currently available parameterisations of the photon structure.

B.2 Evaluation of the photon signal

The data used here were obtained from e^+p running in 1996–97 at HERA, with $E_e = 27.5$ GeV, $E_p = 820$ GeV.

The major components in the analysis are the central tracking detector(CTD) and the uranium calorimeter(UCAL). Prompt photons are detected in the barrel section of the calorimeter, which consists of an electromagnetic section (BEMC) followed by two hadronic sections. It enable a partial discrimination between single γ signals and the decay product of neutral mesons. A typical high-E_T photon signal is observed in a small cluster of BEMC cells, with no associated CTD track. An isolation cone was also imposed around photon candidates within a cone of unit radius in (η, ϕ), to reduce backgrounds from dijet events with part of one jet misidentified as a single photon.

Two shape-dependent quantities were studied in order to further distinguish γ, π^0 and η signals. These were (1) the mean width $<\delta Z>$ of the BEMC cluster in Z and (2) the fraction f_{max} of the cluster energy found in the most energetic cell in the cluster. The $<\delta Z>$ distribution is shown in figure B.1 (a), in which peaks due to the γ and π^0 contributions are clearly visible. The tail quantified the η background; photon candidates in this region were removed.

The extraction of the photon signal from the mixture of photons and a neutral meson background was done by means of the f_{max} distribution. Figure B.1 (b) shows the shape of the f_{max} distribution for the final event sample, after the $<\delta Z>$ cut, fitted to the η component determined from the $<\delta Z>$ distribution and freely-varying γ and π^0 contributions. Above an f_{max} value of 0.75, the distribution is dominated by the photons; below this value it consists mainly of meson background. The numbers of candidates with $f_{max} \geq 0.75$ and $f_{max} < 0.75$ were calculated for the sample of events occurring in each bin of any measured quantity. From these numbers, and the ratios of the corresponding numbers for the f_{max} distributions of the single particle samples, the number of photon events in the given bin was evaluated. Further details of the background subtraction method are given in reference. [18, 105]

B.3 Results

We evaluate cross sections for prompt photon production corrected by means of PYTHIA using GRV photon structure functions [16]. A bin-by-bin correction factors were applied to the detector–level measurements so as to correct to cross sections in the γp centre–of–mass energy 134 – 285 GeV. The systematic error of 15% were taken into account and were finally combined in quadrature. The main contributions are from the energy scale of the calorimeter and the background subtraction. In presenting cross sections, comparison is made with two types of theoretical calculation, in which the pdf sets taken for both the photon and proton can be varied. These are (1) PYTHIA and HERWIG calculations evaluated at the final-state hadron level and (2) NLO parton–level calculations of Gordon [22](LG) and of Krawczyk and Zembrzuski [84](K&Z).

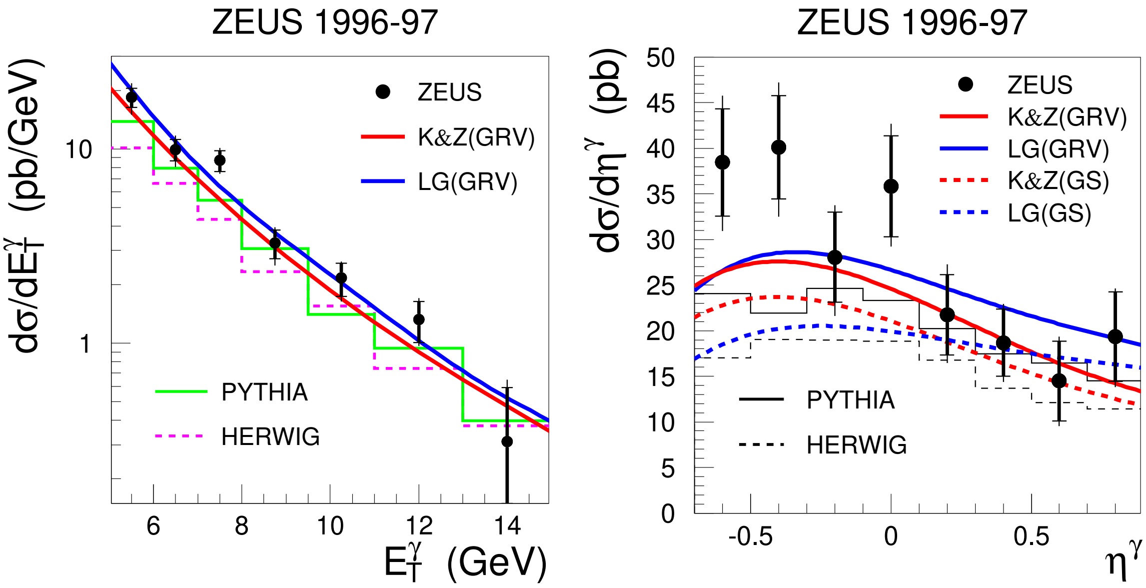

Figure B.2: Differential cross section (a) $d\sigma/dE_T^\gamma$ and (b) $d\sigma/d\eta^\gamma$ for isolated prompt photons produced over $-0.7 < \eta^\gamma < 0.9$.

Figure B.2 (a) gives the inclusive cross–section $d\sigma/dE_T^\gamma$ for isolated prompt photons in the range $-0.7 < \eta^\gamma < 0.9$. All the theoretical models describe the shape of the data well; however the predictions of PYTHIA and especially HERWIG are too low in magnitude. The LG and K&Z calculations give better agreement with the data.

The inclusive cross–section $d\sigma/d\eta^\gamma$ for isolated prompt photons in the range $5 < E_T^\gamma < 10$ GeV is shown in figure B.2 (b) and compared with theoretical calculations, using two sets of photon pdf, GS [87]and GRV. The LG and K&Z calculations gives a good description of the data for forward (proton direction) η^γ range and are similar to PYTHIA prediction. However all the calculations lie below the data in the lower η^γ range, where the curves using the GS parton densities give poorer agreement than those using GRV.

The discrepancy between data and theory at negative η^γ is found to be relatively strongest at low γp centre-of-mass energy range. In the lowest W range (134–170 GeV), both theory and data show a peaking at negative η^γ, but it is stronger in the data. In the highest W range (212–285 GeV), agreement is found between theory and data. The movement of the peak can be qualitatively understood by noting that for fixed values of E_T and x_γ, where x_γ is the fraction of the incident photon energy that contributes to the resolved QCD subprocesses, measurements at increasing y correspond on average to decreasing values of pseudorapidity. By varying the theoretical parameters, the discrepancy was found to correspond in the K&Z calculation to insufficient high x_γ partons in the resolved photon.

B.4 Conclusions

The photoproduction of isolated prompt photons within the γp centre-of-mass energy range 134–285 GeV has been measured in the ZEUS detector at HERA. Inclusive cross sections have been presented as a function of E_T^γ for photons in $-0.7 < \eta^\gamma < 0.9$, and as a function of η^γ for photons with $5 < E_T^\gamma < 10$ GeV.

Comparisons have been made with predictions from LO Monte Carlos, and from NLO calculations. The models are able to describe the data well for forward η^γ, but are low in the rear direction. None of the available variations of the model parameters was found to be capable of removing the discrepancy with the data. This result would appear to indicate a need to review the present theoretical modelling of the parton structure of the photon.

Acknowledgments

We are grateful to L. E. Gordon, Maria Krawczyk and Andrzej Zembrzuski for helpful conversations, and for providing theoretical calculations.

Appendix C

Contribution to the ZEUS Publication

This contribution has been published in Phys. Lett. B **472**, 175 (2000)

Measurement of inclusive prompt photon photoproduction at HERA

ZEUS Collaboration

Abstract

First inclusive measurements of isolated prompt photons in photoproduction at the HERA ep collider have been made with the ZEUS detector, using an integrated luminosity of 38.4 pb^{-1}. Cross sections are given as a function of the pseudorapidity and the transverse energy (η^γ, E_T^γ) of the photon, for $E_T^\gamma > 5$ GeV in the γp centre-of-mass energy range 134–285 GeV. Comparisons are made with predictions from Monte Carlo models having leading-logarithm parton showers, and with next-to-leading-order QCD calculations, using currently available parameterisations of the photon structure. For forward η^γ (proton direction) good agreement is found, but in the rear direction all predictions fall below the data.

13 January 2000

PHYSICS LETTERS B

ELSEVIER

Physics Letters B 472 (2000) 175–188

Measurement of inclusive prompt photon photoproduction at HERA

ZEUS Collaboration

J. Breitweg, S. Chekanov, M. Derrick, D. Krakauer, S. Magill, B. Musgrave, A. Pellegrino, J. Repond, R. Stanek, R. Yoshida

Argonne National Laboratory, Argonne, IL, USA [1]

M.C.K. Mattingly

Andrews University, Berrien Springs, MI, USA

G. Abbiendi, F. Anselmo, P. Antonioli, G. Bari, M. Basile, L. Bellagamba, D. Boscherini [2], A. Bruni, G. Bruni, G. Cara Romeo, G. Castellini [3], L. Cifarelli [4], F. Cindolo, A. Contin, N. Coppola, M. Corradi, S. De Pasquale, P. Giusti, G. Iacobucci, G. Laurenti, G. Levi, A. Margotti, T. Massam, R. Nania, F. Palmonari, A. Pesci, A. Polini, G. Sartorelli, Y. Zamora Garcia [5], A. Zichichi

University and INFN Bologna, Bologna, Italy [6]

C. Amelung, A. Bornheim, I. Brock, K. Coböken, J. Crittenden, R. Deffner, H. Hartmann, K. Heinloth, E. Hilger, H.-P. Jakob, A. Kappes, U.F. Katz, R. Kerger, E. Paul, J. Rautenberg [7], H. Schnurbusch, A. Stifutkin, J. Tandler, K.Ch. Voss, A. Weber, H. Wieber

Physikalisches Institut der Universität Bonn, Bonn, Germany [8]

D.S. Bailey, O. Barret, N.H. Brook [9], B. Foster [10], G.P. Heath, H.F. Heath, J.D. McFall, D. Piccioni, E. Rodrigues, J. Scott, R.J. Tapper

H.H. Wills Physics Laboratory, University of Bristol, Bristol, UK [11]

M. Capua, A. Mastroberardino, M. Schioppa, G. Susinno

Calabria University, Physics Department and INFN, Cosenza, Italy [6]

PII: S0370-2693(99)01450-1

H.Y. Jeoung, J.Y. Kim, J.H. Lee, I.T. Lim, K.J. Ma, M.Y. Pac [12]

Chonnam National University, Kwangju, South Korea [13]

A. Caldwell, W. Liu, X. Liu, B. Mellado, R. Sacchi, S. Sampson, F. Sciulli

Columbia University, Nevis Laboratories, Irvington on Hudson, NY, USA [14]

J. Chwastowski, A. Eskreys, J. Figiel, K. Klimek, K. Olkiewicz, M.B. Przybycień, P. Stopa, L. Zawiejski

Institute of Nuclear Physics, Cracow, Poland [15]

L. Adamczyk [16], B. Bednarek, K. Jeleń, D. Kisielewska, A.M. Kowal, T. Kowalski, M. Przybycień, E. Rulikowska-Zarębska, L. Suszycki, J. Zając

Faculty of Physics and Nuclear Techniques, Academy of Mining and Metallurgy, Cracow, Poland [15]

A. Kotański

Jagellonian University, Department of Physics, Cracow, Poland [17]

L.A.T. Bauerdick, U. Behrens, J.K. Bienlein, C. Burgard [18], K. Desler, G. Drews, A. Fox-Murphy, U. Fricke, F. Goebel, P. Göttlicher, R. Graciani, T. Haas, W. Hain, G.F. Hartner, D. Hasell [19], K. Hebbel, K.F. Johnson [20], M. Kasemann [21], W. Koch, U. Kötz, H. Kowalski, L. Lindemann [22], B. Löhr, M. Martínez, M. Milite, T. Monteiro [23], M. Moritz, D. Notz, F. Pelucchi, M.C. Petrucci, K. Piotrzkowski [23], M. Rohde, P.R.B. Saull, A.A. Savin, U. Schneekloth, F. Selonke, M. Sievers, S. Stonjek, E. Tassi, G. Wolf, U. Wollmer, C. Youngman, W. Zeuner

Deutsches Elektronen-Synchrotron DESY, Hamburg, Germany

C. Coldewey, H.J. Grabosch, A. Lopez-Duran Viani, A. Meyer, S. Schlenstedt, P.B. Straub

DESY Zeuthen, Zeuthen, Germany

G. Barbagli, E. Gallo, P. Pelfer

University and INFN, Florence, Italy [6]

G. Maccarrone, L. Votano

INFN, Laboratori Nazionali di Frascati, Frascati, Italy [6]

A. Bamberger, S. Eisenhardt [24], P. Markun, H. Raach, S. Wölfle

Fakultät für Physik der Universität Freiburg i. Br., Freiburg i. Br., Germany [8]

J. Breitweig, et al. / Physics Letters B 472 (2000) 175–188 177

P.J. Bussey, A.T. Doyle, S.W. Lee, N. Macdonald, G.J. McCance, D.H. Saxon, L.E. Sinclair, I.O. Skillicorn, R. Waugh

Department of Physics and Astronomy, University of Glasgow, Glasgow, UK [11]

I. Bohnet, N. Gendner, U. Holm, A. Meyer-Larsen, H. Salehi, K. Wick

Hamburg University, I. Institute of Experimental Physics, Hamburg, Germany [8]

A. Garfagnini, I. Gialas [25], L.K. Gladilin [26], D. Kçira [27], R. Klanner, E. Lohrmann, G. Poelz, F. Zetsche

Hamburg University, II. Institute of Experimental Physics, Hamburg, Germany [8]

R. Goncalo, K.R. Long, D.B. Miller, A.D. Tapper, R. Walker

Imperial College London, High Energy Nuclear Physics Group, London, UK [11]

U. Mallik, S.M. Wang

University of Iowa, Physics and Astronomy Department, Iowa City, USA [1]

P. Cloth, D. Filges

Forschungszentrum Jülich, Institut für Kernphysik, Jülich, Germany

T. Ishii, M. Kuze, K. Nagano, K. Tokushuku [28], S. Yamada, Y. Yamazaki

Institute of Particle and Nuclear Studies, KEK, Tsukuba, Japan [29]

S.H. Ahn, S.H. An, S.J. Hong, S.B. Lee, S.W. Nam [30], S.K. Park

Korea University, Seoul, South Korea [13]

H. Lim, I.H. Park, D. Son

Kyungpook National University, Taegu, South Korea [13]

F. Barreiro, G. García, C. Glasman [31], O. Gonzalez, L. Labarga, J. del Peso, I. Redondo [32], J. Terrón

Universidad Autónoma Madrid, Departamento de Física Teórica, Madrid, Spain [33]

M. Barbi, F. Corriveau, D.S. Hanna, A. Ochs, S. Padhi, M. Riveline, D.G. Stairs, M. Wing

McGill University, Department of Physics, Montréal, Que., Canada [34,35]

T. Tsurugai

Meiji Gakuin University, Faculty of General Education, Yokohama, Japan

178 J. Breitweig, et al. / Physics Letters B 472 (2000) 175–188

V. Bashkirov [36], B.A. Dolgoshein

Moscow Engineering Physics Institute, Moscow, Russia [37]

G.L. Bashindzhagyan, P.F. Ermolov, Yu.A. Golubkov, L.A. Khein, N.A. Korotkova, I.A. Korzhavina, V.A. Kuzmin, O.Yu. Lukina, A.S. Proskuryakov, L.M. Shcheglova, A.N. Solomin, S.A. Zotkin

Moscow State University, Institute of Nuclear Physics, Moscow, Russia [38]

C. Bokel, M. Botje, N. Brümmer, J. Engelen, E. Koffeman, P. Kooijman, A. van Sighem, H. Tiecke, N. Tuning, J.J. Velthuis, W. Verkerke, J. Vossebeld, L. Wiggers, E. de Wolf

NIKHEF and University of Amsterdam, Amsterdam, Netherlands [39]

B. Bylsma, L.S. Durkin, J. Gilmore, C.M. Ginsburg, C.L. Kim, T.Y. Ling, P. Nylander [40]

OH State University, Physics Department, Columbus, OH, USA [1]

S. Boogert, A.M. Cooper-Sarkar, R.C.E. Devenish, J. Große-Knetter [41], T. Matsushita, O. Ruske, M.R. Sutton, R. Walczak

Department of Physics, University of Oxford, Oxford, UK [11]

A. Bertolin, R. Brugnera, R. Carlin, F. Dal Corso, S. Dondana, U. Dosselli, S. Dusini, S. Limentani, M. Morandin, M. Posocco, L. Stanco, R. Stroili, C. Voci

Dipartimento di Fisica dell' Università and INFN, Padova, Italy [6]

L. Iannotti [42], B.Y. Oh, J.R. Okrasiński, W.S. Toothacker, J.J. Whitmore

Pennsylvania State University, Department of Physics, University Park, PA, USA [14]

Y. Iga

Polytechnic University, Sagamihara, Japan [29]

G. D'Agostini, G. Marini, A. Nigro

Dipartimento di Fisica, Università 'La Sapienza' and INFN, Rome, Italy [6]

C. Cormack, J.C. Hart, N.A. McCubbin, T.P. Shah

Rutherford Appleton Laboratory, Chilton, Didcot, Oxon, UK [11]

D. Epperson, C. Heusch, H.F.-W. Sadrozinski, A. Seiden, R. Wichmann, D.C. Williams

University of California, Santa Cruz, CA, USA [1]

J. Breitweig, et al. / Physics Letters B 472 (2000) 175–188 179

N. Pavel

Fachbereich Physik der Universität-Gesamthochschule Siegen, Germany [8]

H. Abramowicz [43], S. Dagan [44], S. Kananov [44], A. Kreisel, A. Levy [44]

Raymond and Beverly Sackler Faculty of Exact Sciences, School of Physics, Tel-Aviv University, Tel-Aviv, Israel [45]

T. Abe, T. Fusayasu, K. Umemori, T. Yamashita

Department of Physics, University of Tokyo, Tokyo, Japan [29]

R. Hamatsu, T. Hirose, M. Inuzuka, S. Kitamura [46], T. Nishimura

Tokyo Metropolitan University, Department of Physics, Tokyo, Japan [29]

M. Arneodo [47], N. Cartiglia, R. Cirio, M. Costa, M.I. Ferrero, S. Maselli, V. Monaco, C. Peroni, M. Ruspa, A. Solano, A. Staiano

Università di Torino, Dipartimento di Fisica Sperimentale and INFN, Torino, Italy [6]

M. Dardo

II Faculty of Sciences, Torino University and INFN - Alessandria, Italy [6]

D.C. Bailey, C.-P. Fagerstroem, R. Galea, T. Koop, G.M. Levman, J.F. Martin, R.S. Orr, S. Polenz, A. Sabetfakhri, D. Simmons

University of Toronto, Department of Physics, Toronto, Ont., Canada [34]

J.M. Butterworth, C.D. Catterall, M.E. Hayes, E.A. Heaphy, T.W. Jones, J.B. Lane, B.J. West

University College London, Physics and Astronomy Department, London, UK [11]

J. Ciborowski, R. Ciesielski, G. Grzelak, R.J. Nowak, J.M. Pawlak, R. Pawlak, B. Smalska, T. Tymieniecka, A.K. Wróblewski, J.A. Zakrzewski, A.F. Żarnecki

Warsaw University, Institute of Experimental Physics, Warsaw, Poland [15]

M. Adamus, T. Gadaj

Institute for Nuclear Studies, Warsaw, Poland [15]

O. Deppe, Y. Eisenberg [44], D. Hochman, U. Karshon [44]

Weizmann Institute, Department of Particle Physics, Rehovot, Israel [48]

180 J. Breitweig, et al. / Physics Letters B 472 (2000) 175–188

W.F. Badgett, D. Chapin, R. Cross, C. Foudas, S. Mattingly, D.D. Reeder, W.H. Smith, A. Vaiciulis [49], T. Wildschek, M. Wodarczyk

University of Wisconsin, Department of Physics, Madison, WI, USA [1]

A. Deshpande, S. Dhawan, V.W. Hughes

Yale University, Department of Physics, New Haven, CT, USA [1]

S. Bhadra, J.E. Cole, W.R. Frisken, R. Hall-Wilton, M. Khakzad, S. Menary, W.B. Schmidke

York University, Department of Physics, Toronto, Ont., Canada [34]

Received 20 October 1999; accepted 3 December 1999
Editor: K. Winter

Abstract

First inclusive measurements of isolated prompt photons in photoproduction at the HERA *ep* collider have been made with the ZEUS detector, using an integrated luminosity of 38.4 pb^{-1}. Cross sections are given as a function of the pseudorapidity and the transverse energy (η^{γ}, E_T^{γ}) of the photon, for $E_T^{\gamma} > 5$ GeV in the γp centre-of-mass energy range 134–285 GeV. Comparisons are made with predictions from Monte Carlo models having leading-logarithm parton showers, and with next-to-leading-order QCD calculations, using currently available parameterisations of the photon structure. For forward η^{γ} (proton direction) good agreement is found, but in the rear direction all predictions fall below the data.

[1] Supported by the US Department of Energy.
[2] Now visiting scientist at DESY.
[3] Also at IROE Florence, Italy.
[4] Now at University of Salerno and INFN Napoli, Italy.
[5] Supported by Worldlab, Lausanne, Switzerland.
[6] Supported by the Italian National Institute for Nuclear Physics (INFN).
[7] Drafted to the German military service.
[8] Supported by the German Federal Ministry for Education and Science, Research and Technology (BMBF), under contract numbers 057BN19P, 057FR19P, 057HH19P, 057HH29P, 057SI75I.
[9] PPARC Advanced fellow.
[10] Also at University of Hamburg, Alexander von Humboldt Research Award.
[11] Supported by the Particle Physics and Astronomy Research Council.
[12] Now at Dongshin University, Naju, Korea.
[13] Supported by the Korean Ministry of Education and Korea Science and Engineering Foundation.
[14] Supported by the US National Science Foundation.
[15] Supported by the Polish State Committee for Scientific Research, grant No. 115/E-343/SPUB/P03/154/98, 2P03B03216, 2P03B04616, 2P03B10412, 2P03B03517, and by the German Federal Ministry of Education and Science, Research and Technology (BMBF).
[16] Supported by the Polish State Committee for Scientific Research, grant No. 2P03B14912.
[17] Supported by the Polish State Committee for Scientific Research (grant No. 2P03B08614 and 2P03B06116).
[18] Now at Barclays Capital PLC, London.
[19] Now at Massachusetts Institute of Technology, Cambridge, MA, USA.
[20] Visitor from Florida State University.

1. Introduction

One of the primary aims of photoproduction measurements in ep collisions at HERA is the elucidation of the hadronic behaviour of the photon. The measurement of jets at high transverse energy has provided much information in this area [1,2]. In the study of inclusive jets, next-to-leading order (NLO) QCD calculations are able to describe the experimental data over a wide range of kinematic conditions, although the agreement is dependent on the jet algorithm [3]. However, significant discrepancies between data and NLO theories are found in dijet measurements [4]. A further means to study photoproduction is provided by final states with an isolated high-transverse-energy photon. These have the particular merit that the photon may emerge directly from the hard QCD subprocess (''prompt'' photons), and also can be investigated without the hadronisation corrections needed in the case of quarks or gluons. In a previous measurement by ZEUS at HERA [5], it was shown that prompt photons, accompanied by balancing jets, are produced at the expected level in photoproduction and with the expected event characteristics. This work is extended in the present paper through the use of a much larger event sample taken in 1996-97, corresponding to an integrated ep luminosity of 38.4 pb^{-1}. This allows a measurement of inclusive prompt photon distributions as a function of pseudorapidity η^{γ} and transverse energy E_T^{γ} of the photon, and a comparison with LO and NLO QCD predictions.

2. Apparatus and trigger

During 1996-97, HERA collided positrons with energy $E_e = 27.5$ GeV with protons of energy $E_p =$ 820 GeV. The luminosity was measured by means of the bremsstrahlung process $ep \rightarrow e\gamma p$.

A description of the ZEUS apparatus and luminosity monitor is given elsewhere [6]. Of particular importance in the present work are the uranium calorimeter (CAL) and the central tracking detector (CTD).

The CAL [7] has an angular coverage of 99.7% of 4π and is divided into three parts (FCAL, BCAL, RCAL), covering the forward (proton direction), central and rear angular ranges, respectively. Each part consists of towers longitudinally subdivided into electromagnetic (EMC) and hadronic (HAC) cells. The electromagnetic section of the BCAL (BEMC)

[21] Now at Fermilab, Batavia, IL, USA.
[22] Now at SAP A.G., Walldorf, Germany.
[23] Now at CERN.
[24] Now at University of Edinburgh, Edinburgh, U.K.
[25] Visitor of University of Crete, Greece, partially supported by DAAD, Bonn - Kz. A/98/16764.
[26] On leave from MSU, supported by the GIF, contract I-0444-176.07/95.
[27] Supported by DAAD, Bonn - Kz. A/98/12712.
[28] Also at University of Tokyo.
[29] Supported by the Japanese Ministry of Education, Science and Culture (the Monbusho) and its grants for Scientific Research.
[30] Now at Wayne State University, Detroit.
[31] Supported by an EC fellowship number ERBFMBICT 972523.
[32] Supported by the Comunidad Autonoma de Madrid.
[33] Supported by the Spanish Ministry of Education and Science through funds provided by CICYT.
[34] Supported by the Natural Sciences and Engineering Research Council of Canada (NSERC).
[35] Supported by the FCAR of Québec, Canada.
[36] Now at Loma Linda University, Loma Linda, CA, USA.
[37] Partially supported by the German Federal Ministry for Education and Science, Research and Technology (BMBF).
[38] Supported by the Fund for Fundamental Research of Russian Ministry for Science and Education and by the German Federal Ministry for Education and Science, Research and Technology (BMBF).
[39] Supported by the Netherlands Foundation for Research on Matter (FOM).
[40] Now at Hi Techniques, Inc., Madison, WI, USA.
[41] Supported by the Feodor Lynen Program of the Alexander von Humboldt foundation.
[42] Partly supported by Tel Aviv University.
[43] An Alexander von Humboldt Fellow at University of Hamburg.
[44] Supported by a MINERVA Fellowship.
[45] Supported by the German–Israeli Foundation, the Israel Science Foundation, the US-Israel Binational Science Foundation, and by the Israel Ministry of Science.
[46] Present address: Tokyo Metropolitan University of Health Sciences, Tokyo 116-8551, Japan.
[47] Now also at Università del Piemonte Orientale, I-28100 Novara, Italy.
[48] Supported by the MINERVA Gesellschaft für Forschung GmbH, the German Israeli Foundation, and by the Israel Ministry of Science.
[49] Now at University of Rochester, Rochester, NY, USA.

consists of cells of ~ 20 cm length azimuthally and mean width 5.45 cm in the Z direction [50], at a mean radius of ~ 1.3 m from the beam line. These cells have a projective geometry as viewed from the interaction point. The profile of the electromagnetic signals observed in clusters of cells in the BEMC provides a partial discrimination between those originating from photons or positrons, and those originating from neutral meson decays.

The CTD [8] is a cylindrical drift chamber situated inside a superconducting solenoid which produces a 1.43 T field. Using the tracking information from the CTD, the vertex of an event can be reconstructed with a resolution of 0.4 cm in Z and 0.1 cm in X,Y. In this analysis, the CTD tracks are used to reconstruct the event vertex, and also in the selection criteria for high-E_T photons.

The ZEUS detector uses a three-level trigger system, of which the first- and second-level triggers used in this analysis have been described previously [5]. The third-level trigger made use of a standard ZEUS electron finding algorithm [9] to select events with an electromagnetic cluster of transverse energy $E_T >$ 4 GeV in the BCAL, with no further tracking requirements at this stage. These events represent the basic sample of prompt photon event candidates.

3. Event selection

The offline analysis was based on previously developed methods [5]. An algorithm for finding electromagnetic clusters was applied to the data, and events were retained for final analysis if a photon candidate with $E_T > 5$ GeV was found in the BCAL. A photon candidate was rejected if a CTD track, as measured at the vertex, pointed to it within 0.3 radians; this removed almost all high-E_T positrons and electrons, including the majority of those that underwent hard radiation. The BCAL requirement restricts the photon candidates to the approximate pseudorapidity [51] range $-0.75 < \eta^\gamma < 1.0$.

Events with an identified deep inelastic scattered (DIS) positron in addition to the BCAL photon candidate were removed, thus restricting the acceptance to incident photons of virtuality $Q^2 \lesssim 1$ GeV^2. The quantity $y^{\mathrm{meas}} = \Sigma(E - p_Z)/2E_e$ was calculated, where the sum is over all calorimeter cells, E is the energy deposited in the cell, and $p_Z = E\cos\theta$. When the outgoing positron is not detected in the CAL, y^{meas} is a measure of $y = E_{\gamma,\mathrm{in}}/E_e$, where $E_{\gamma,\mathrm{in}}$ is the energy of the incident photon. If the outgoing positron is detected in the CAL, $y^{\mathrm{meas}} \approx 1$. A requirement of $0.15 < y^{\mathrm{meas}} < 0.7$ was imposed; the lower cut removed some residual proton-gas backgrounds while the upper cut removed remaining DIS events, including any with a photon candidate that was actually a misidentified DIS positron. Wide-angle Compton scattering events $(ep \to e\gamma p)$ were also excluded by this cut. This range of accepted y^{meas} values corresponds approximately to the true y range $0.2 < y < 0.9$.

An isolation cone was imposed around the photon candidate: within a cone of unit radius in (η, ϕ), the total E_T from other particles was required not to exceed $0.1 E_T^\gamma$. This was calculated by summing the E_T in each calorimeter cell within the isolation cone. Further contributions were included from charged tracks which originated within the isolation cone but curved out of it; the small number of tracks which curved into the isolation cone were ignored. The isolation condition much reduces the dijet background by removing a large majority of the events where the photon candidate is closely associated with a jet and is therefore either hadronic (e.g. a π^0) or else a photon radiated within a jet. In particular, the isolation condition removes most dijet events in which a photon is radiated from a final-state quark. Approximately 6000 events with $E_T^\gamma > 5$ GeV remained after the above cuts.

Studies based on the single-particle Monte Carlo samples showed that the photon energy measured in

[50] The ZEUS coordinate system is right-handed with positive-Z in the proton beam direction and an upward-pointing Y axis. The nominal interaction point is at $X = Y = Z = 0$.

[51] All kinematic quantities are given in the laboratory frame. Pseudorapidity η is defined as $-\ln\tan(\theta/2)$, where θ is the polar angle relative to the Z direction, measured from the Z position of the event vertex.

the CAL was on average less than the true value, owing to dead material in front of the CAL. To compensate for this, an energy correction, typically 0.2 GeV, was added.

4. Monte Carlo simulations

In describing the hard interaction of photons of low virtuality with protons, two major classes of diagram are important. In one of these the photon couples in a pointlike way to a $q\bar{q}$ pair, while in the other the photon interacts via an intermediate hadronic state, which provides quarks and gluons which then take part in the hard QCD subprocesses. At leading order (LO) in QCD, the pointlike and hadronic diagrams are distinct and are commonly referred to as direct and resolved processes, respectively.

In the present analysis, three types of Monte Carlo samples were employed to simulate: (1) the LO QCD prompt photon processes, (2) dijet processes in which an outgoing quark radiated a hard photon (radiative events), and (3) single particles (γ, π^0, η) at high E_T. All generated events were passed through a full GEANT-based simulation [10] of the ZEUS detector.

The PYTHIA 5.7 [11] and HERWIG 5.9 [12] Monte Carlo generators were both used to simulate the direct and resolved prompt photon processes. These generators include LO QCD subprocesses and higher-order processes modelled by initial- and final-state parton showers. The parton density function (pdf) sets used were MRSA [13] for the proton, and GRV(LO) [14] for the photon. The minimum p_T of the hard scatter was set to 2.5 GeV. No multi-parton interactions were implemented in the resolved samples. The radiative event samples were likewise produced using direct and resolved photoproduction generators within PYTHIA and HERWIG.

In modelling the overall photoproduction process, the event samples produced for the separate direct, resolved and radiative processes were combined in proportion to their total cross sections as calculated by the generators. A major difference between PYTHIA and HERWIG is the smaller radiative contribution in the HERWIG model.

Three Monte Carlo single-particle data sets were generated, comprising large samples of γ, π^0 and η. The single particles were generated uniformly over the acceptance of the BCAL and with a flat E_T distribution between 3 and 20 GeV; E_T-dependent exponential weighting functions were subsequently applied to reproduce the observed distributions. These samples were used in separating the signal from the background using shower shapes.

5. Evaluation of the photon signal

Signals in the BEMC that do not arise from charged particles are predominantly due to photons, π^0 mesons and η mesons. A large fraction of these mesons decay into multiphoton final states, the π^0 through its 2γ channel and the η through its 2γ and $3\pi^0$ channels. For π^0, η produced with E_T greater than a few GeV, the photons from the decays are separated in the BEMC by distances comparable to the BEMC cell width in Z. Therefore the discrimination between photons and neutral mesons was performed on the basis of cluster-shape characteristics, thus avoiding any need to rely on theoretical modelling of the background.

A typical high-E_T photon candidate consists of signals from a cluster of 4–5 BEMC cells. Two shape-dependent quantities were used to distinguish γ, π^0 and η signals [5]. These were (i) the mean width $\langle \delta Z \rangle$ of the cell cluster in Z, which is the direction of finer segmentation of the BEMC, and (ii) the fraction f_{max} of the cluster energy found in the most energetic cell in the cluster. The quantity $\langle \delta Z \rangle$ is defined as $\Sigma\left(E_{cell}|Z_{cell} - \bar{Z}|\right)/\Sigma E_{cell}$, summing over the cells in the cluster, where $\bar{Z}$ is the energy-weighted mean Z value of the cells. The $\langle \delta Z \rangle$ distribution for the event sample is shown in Fig. 1(a), in which peaks due to the photon and π^0 contributions are clearly visible. [52] The Monte Carlo samples of single γ, π^0 and η were used to establish a cut on $\langle \delta Z \rangle$ at 0.65 BEMC cell widths, such

[52] The displacement of the photon peak from the Monte Carlo prediction does not affect the present analysis; the poor fit in the region $\langle \delta Z \rangle = 0.6$–$1.0$ is taken into account in the systematic errors.

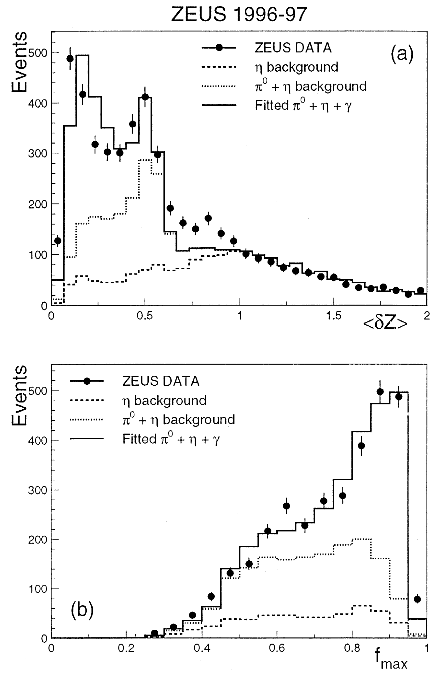

Fig. 1. (a) Distribution of $\langle \delta Z \rangle$ for prompt photon candidates in selected events. (b) Distribution of f_{max} for prompt photon candidates in selected events after cutting on $\langle \delta Z \rangle$. Also given in both cases are fitted Monte Carlo distributions for photons, π^0 and η mesons with similar selection requirements as for the observed photon candidates. Samples with $f_{max} > 0.75$ and $f_{max} < 0.75$ are enriched in the photon signal and in the meson background, respectively.

as to remove most of the η mesons but few of the photons and π^0s. Candidates with lower $\langle \delta Z \rangle$ were retained, thus providing a sample that consisted of photons, π^0 mesons and a small admixture of η mesons.

The extraction of the photon signal from the mixture of photons and a neutral meson background was done by means of the f_{max} distributions. Fig. 1(b) shows the shape of the f_{max} distribution for the final event sample, after the $\langle \delta Z \rangle$ cut, fitted to the η component determined from the $\langle \delta Z \rangle$ distribution plus freely-varying γ and π^0 contributions. Above an f_{max} value of 0.75, the distribution is dominated by the photons; below this value it consists mainly of meson background. Since the shape of the f_{max} distribution is similar for the η and π^0 contributions, the background subtraction is insensitive to uncertainties in the fitted π^0 to η ratio.

The numbers of candidates with $f_{max} > 0.75$ and $f_{max} < 0.75$ were calculated for the sample of events occurring in each bin of a measured quantity. From these numbers, and the ratios of the corresponding numbers for the f_{max} distributions of the single particle samples, the number of photon events in the given bin was evaluated [5].

6. Cross section calculation and systematic uncertainties

Cross sections are given for the photoproduction process $ep \to \gamma(\text{prompt}) + X$, taking place in the incident γp centre-of-mass energy (W) range 134–285 GeV, i.e. $0.2 < y < 0.9$. The virtuality of the incident photon is restricted to the range $Q^2 \lesssim 1$ GeV^2, with a median value of approximately 10^{-3} GeV^2. The cross sections represent numbers of events within a given bin, divided by the bin width and integrated luminosity. They are given at the hadron level, with an isolation cone defined around the prompt photon as at the detector level. To obtain the hadron-level cross sections, bin-by-bin correction factors were applied to the corresponding detector-level distributions; these factors were calculated using PYTHIA.

The following sources of systematic error were taken into account:

1. *Calorimeter simulation:* the uncertainty of the simulation of the calorimeter response [15] gives rise to an uncertainty on the cross sections of $\pm 7\%$;
2. *Modelling of the shower shape:* uncertainties on the agreement of the simulated f_{max} distributions with the data correspond to a systematic error averaging $\pm 8\%$ on the final cross sections;
3. *Kinematic cuts:* the cuts defining the accepted kinematic range at the detector level were varied by amounts corresponding to the resolution on the variables. Changes of up to 5% in the cross section were observed;
4. $\eta/(\eta + \pi^0)$ *ratio:* the fitted value was typically 25%; variations of this ratio in the range 15–35% led to cross section variations of around $\pm 2\%$;

J. Breitweig, et al. / Physics Letters B 472 (2000) 175–188 185

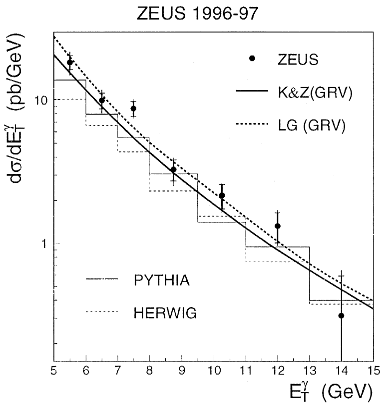

Fig. 2. Differential cross section $d\sigma/dE_T^\gamma$ for prompt photons produced over $-0.7 < \eta^\gamma < 0.9$. The inner (thick) error bars are statistical; the outer include systematic errors added in quadrature. The data points are plotted at the respective bin centres (see Table 1; bin centring corrections are negligible). Predictions are shown from PYTHIA and HERWIG at the hadron level (histograms), and from LG and K&Z (curves). In K&Z, the default 4-flavour NLO $\Lambda_{\overline{MS}}$ value of 320 MeV is used.

5. *Vertex cuts:* narrowing the vertex cuts to $(-25, +15)$ cm from their standard values of $(-50, +40)$ cm gave changes in the cross sections of typically $\pm 4\%$.

In addition, studies were made of the effects of using HERWIG instead of PYTHIA for the correction factors, of varying the E_T distribution applied to the single-particle samples, and of varying the composition of the Monte Carlo simulation in terms of direct, resolved and radiative processes. These gave changes in the cross sections at the 1% level. The 1.6% uncertainty on the integrated luminosity was neglected. The individual contributions were combined in quadrature to give the total systematic error.

7. Theoretical calculations

In presenting cross sections, comparison is made with two types of theoretical calculation, in which the pdf sets taken for both the photon and proton can be varied, although there is little sensitivity to the choice of proton pdf. These are:

(i) PYTHIA and HERWIG calculations evaluated at the final-state hadron level, as outlined in Section 4. Each of these programs comprises a set of LO matrix elements augmented by parton showers in the initial and final states together with hadronisation;

(ii) NLO parton-level calculations of Gordon (LG) [16,17] and of Krawczyk and Zembrzuski (K&Z) [18]. Pointlike and hadronic diagrams at the Born level are included, together with virtual (loop) corrections and terms taking into account three-body final states. The radiative terms are evaluated by means of fragmentation functions obtained from experiment. In both calculations, the isolation criterion was applied at the parton level.

The LG and K&Z calculations differ in several respects [16–19]. The K&Z calculation includes a box-diagram contribution for the process $\gamma g \to \gamma g$ [20], but excludes higher-order corrections to the resolved terms which are present in LG. A value of $\Lambda_{\overline{MS}} = 200$ MeV (5 flavours) is used in LG while in K&Z a value of 320 MeV (4 flavours) is used, so as to reproduce a fixed value of $\alpha_S = 0.118$ at the Z^0 mass. The standard versions of both calculations use a QCD scale of p_T^2. Both calculations use higher-order (HO) versions of the GRV [14] and GS [21] photon pdf sets.

8. Results

Fig. 2 and Table 1 give the inclusive cross-section $d\sigma/dE_T^\gamma$ for the production of isolated prompt photons in the range $-0.7 < \eta^\gamma < 0.9$ for $0.2 < y < 0.9$. All the theoretical models describe the shape of the data well; however the predictions of PYTHIA and especially HERWIG are too low in magnitude. The

Table 1
Differential cross sections for inclusive photoproduction of isolated photons with $-0.7 < \eta^\gamma < 0.9$, averaged over given transverse-energy intervals, for $0.2 < y < 0.9$ ($134 < W < 285$ GeV). The first error is statistical, the second is systematic

E_T	$d\sigma/dE_T^\gamma$ pb GeV^{-1}
5.0 – 6.0	$18.4 \pm 2.1^{+2.6}_{-2.8}$
6.0 – 7.0	$9.9 \pm 1.3^{+1.2}_{-1.3}$
7.0 – 8.0	$8.7 \pm 1.1^{+0.9}_{-0.7}$
8.0 – 9.5	$3.3 \pm 0.6^{+0.4}_{-0.5}$
9.5 – 11.0	$2.2 \pm 0.4^{+0.2}_{-0.3}$
11.0 – 13.0	$1.3 \pm 0.3^{+0.2}_{-0.2}$
13.0 – 15.0	$0.3 \pm 0.3^{+0.2}_{-0.1}$

186 J. Breitweig, et al. / Physics Letters B 472 (2000) 175–188

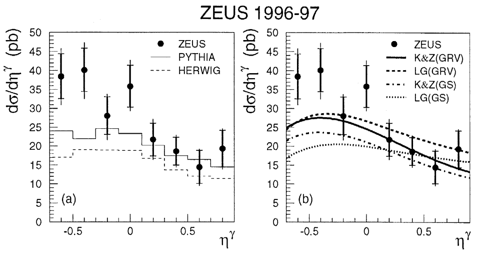

Fig. 3. Differential cross-section $d\sigma/d\eta^{\gamma}$ for isolated prompt photons with $5 < E_T^{\gamma} < 10$ GeV, for $0.2 < y < 0.9$ ($134 < W < 285$ GeV). The inner (thick) error bars are statistical; the outer include systematic errors added in quadrature. Also plotted are (a) PYTHIA and HERWIG predictions using the GRV(LO) photon parton densities; (b) LG and K&Z NLO predictions using GRV(HO) and GS(HO) photon parton densities.

LG and K&Z calculations give better agreement with the data.

Fig. 3 and Table 2 give the inclusive cross-section $d\sigma/d\eta^{\gamma}$ for isolated prompt photons in the range $5 < E_T^{\gamma} < 10$ GeV for $0.2 < y < 0.9$. Using the GRV pdf's in the photon, PYTHIA gives a good description of the data for forward pseudorapidities. The HERWIG distribution, while similar in shape to that of PYTHIA, is lower throughout; this is attributable chiefly to the lower value of the radiative contribution in HERWIG (see Section 4). The LG and K&Z calculations using GRV are similar to each other and to PYTHIA. All the calculations lie below the data in the lower η^{γ} range.

The effects were investigated of varying some of the parameters of the K&Z calculation relative to their standard values (NLO, 4 flavours, $\Lambda_{\overline{MS}} = 320$ MeV, GRV photon pdf). Reducing the number of flavours used in the calculation to three (with $\Lambda_{\overline{MS}} = 365$ MeV) reduced the cross sections by 35–40% across the η^{γ} range, confirming the need to take charm into account. A LO calculation (with $\Lambda_{\overline{MS}} = 120$ MeV and a NLO radiative contribution) was approximately 25% lower than the standard NLO calculation. Variations of the QCD scale between $0.25E_T^2$ and $4E_T^2$ gave cross-section variations of approximately $\pm 3\%$.

Fig. 3(b) illustrates the effects of varying the photon parton densities, comparing the results using GRV with those using GS. The ACFGP parton set [22] gives results (not shown) similar to GRV. All NLO calculations describe the data well for $\eta^{\gamma} > 0.1$, as does PYTHIA, but are low at more negative η^{γ} values, where the curves using the GS parton densities give poorer agreement than those using GRV.

As a check on the above results, the same cross sections were evaluated with the additional requirement that each event should contain a jet (see [5]) with $E_T \geq 5$ GeV in the pseudorapidity range $(-1.5, 1.8)$. Both the measured and theoretical distributions were found to be of a similar shape to those in Fig. 3.

The discrepancy between data and theory at negative η^{γ} is found to be relatively strongest at low values of y. Fig. 4 shows the inclusive cross section $d\sigma/d\eta^{\gamma}$ as in Fig. 3, evaluated for the three y ranges 0.2–0.32, 0.32–0.5 and 0.5–0.9 by selecting the y^{meas} ranges 0.15–0.25, 0.25–0.4 and 0.4–0.7 at

Table 2
Differential cross sections per unit pseudorapidity for inclusive photoproduction of isolated photons with $5 < E_T^{\gamma} < 10$ GeV, averaged over laboratory pseudorapidity intervals of ± 0.1 about the given central values. The γp centre-of-mass energy (W) ranges are in GeV. Results are listed for the full range of fractional incident photon energy y and in three subdivisions. The first error is statistical, the second is systematic

η^{γ}	$d\sigma/d\eta^{\gamma}$ (pb)			
	$0.2 < y < 0.9$ $134 < W < 285$	$0.2 < y < 0.32$ $134 < W < 170$	$0.32 < y < 0.5$ $170 < W < 212$	$0.5 < y < 0.9$ $212 < W < 285$
-0.6	$38.9 \pm 5.9^{+4.3}_{-4.7}$	$10.0 \pm 3.3^{+1.8}_{-2.2}$	$15.2 \pm 3.6^{+2.4}_{-2.5}$	$13.7 \pm 3.2^{+2.3}_{-3.1}$
-0.4	$40.1 \pm 5.7^{+4.3}_{-5.1}$	$17.0 \pm 3.6^{+3.1}_{-1.9}$	$13.8 \pm 3.2^{+2.1}_{-2.7}$	$9.3 \pm 2.8^{+1.5}_{-2.2}$
-0.2	$27.7 \pm 5.0^{+2.8}_{-4.1}$	$11.4 \pm 3.1^{+2.1}_{-2.2}$	$11.7 \pm 2.9^{+1.9}_{-2.0}$	$4.6 \pm 2.1^{+0.7}_{-1.3}$
0.0	$35.1 \pm 5.5^{+4.1}_{-3.6}$	$17.7 \pm 3.5^{+3.1}_{-2.2}$	$9.1 \pm 3.0^{+1.7}_{-1.6}$	$8.3 \pm 2.7^{+1.3}_{-1.9}$
0.2	$21.0 \pm 4.4^{+3.3}_{-3.0}$	$9.9 \pm 2.5^{+2.1}_{-1.8}$	$5.7 \pm 2.4^{+1.2}_{-1.1}$	$5.4 \pm 2.4^{+1.1}_{-1.4}$
0.4	$18.7 \pm 3.7^{+2.1}_{-2.2}$	$7.2 \pm 2.1^{+1.4}_{-0.9}$	$7.9 \pm 2.4^{+1.4}_{-1.6}$	$3.6 \pm 1.7^{+0.6}_{-0.9}$
0.6	$14.4 \pm 4.4^{+2.1}_{-2.3}$	$6.8 \pm 2.7^{+1.4}_{-1.0}$	$5.8 \pm 2.5^{+0.9}_{-1.3}$	$1.8 \pm 2.2^{+0.6}_{-0.7}$
0.8	$19.5 \pm 4.9^{+2.1}_{-2.6}$	$6.8 \pm 2.9^{+1.3}_{-1.3}$	$10.1 \pm 3.4^{+2.3}_{-1.5}$	$2.6 \pm 2.2^{+0.5}_{-0.9}$

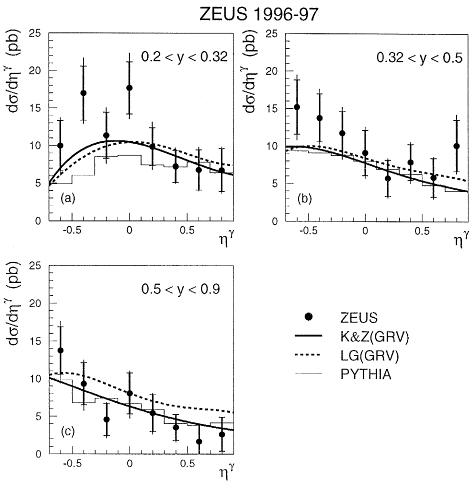

Fig. 4. Differential cross-section $d\sigma / d\eta^\gamma$, for isolated prompt photons with $5 < E_T^\gamma < 10$ GeV, compared with PYTHIA and with LG and K&Z NLO predictions, using GRV photon parton densities as in Fig. 3. The inner (thick) error bars are statistical; the outer include systematic errors added in quadrature. The plots correspond to the W ranges (a) 134–170 GeV, (b) 170–212 GeV, (c) 212–285 GeV.

the detector level. The numerical values are listed in Table 2. In the lowest y range, both theory and data show a peaking at negative η^γ, but it is stronger in the data. The Monte Carlo calculations indicate that the peak occurs at more negative η^γ values as y increases, eventually leaving the measurement acceptance. In the highest y range (Fig. 4(c)), agreement is found between theory and data. The movement of the peak can be qualitatively understood by noting that for fixed values of E_T and x_γ, where x_γ is the fraction of the incident photon energy that contributes to the resolved QCD subprocesses, measurements at increasing y correspond on average to decreasing values of pseudorapidity. By varying the theoretical parameters, the discrepancy was found to correspond in the K&Z calculation to insufficient high x_γ partons in the resolved photon.

9. Summary and conclusions

The photoproduction of isolated prompt photons within the kinematic range $0.2 < y < 0.9$, equivalent to incident γp centre-of-mass energies W of 134–285 GeV, has been measured in the ZEUS detector at HERA, using an integrated luminosity of 38.4 pb^{-1}. Inclusive cross sections for $ep \to \gamma + X$ have been presented as a function of E_T^γ for photons in the pseudorapidity range $-0.7 < \eta^\gamma < 0.9$, and as a function of η^γ for photons with $5 < E_T^\gamma < 10$ GeV. The latter results have been given also for three subdivisions of the y range. All kinematic quantities are quoted in the laboratory frame.

Comparisons have been made with predictions from leading-logarithm parton-shower Monte Carlos (PYTHIA and HERWIG), and from next-to-leading-order parton-level calculations. The models are able to describe the data well for forward (proton direction) photon pseudorapidities, but are low in the rear direction. None of the available variations of the model parameters was found to be capable of removing the discrepancy with the data. The disagreement is strongest in the W interval 134–170 GeV, but not seen within the measurement acceptance for $W > 212$ GeV. This result, together with the disagreements with NLO predictions seen also in recent dijet results at HERA [4], would appear to indicate a need to review the present theoretical modelling of the parton structure of the photon.

Acknowledgements

It a pleasure to thank the DESY directorate and staff for their unfailing support and encouragement. The outstanding efforts of the HERA machine group in providing high luminosity for the 1996–97 running are much appreciated. We are also extremely grateful to L.E. Gordon, M. Krawczyk and A. Zembrzuski for helpful conversations, and for making available to us calculations of the NLO prompt photon cross section and a computer program (K&Z).

References

[1] ZEUS Collab., M. Derrick et al., Phys. Lett. B 322 (1994) 287; B 348 (1995) 665; B 384 (1996) 401.

[2] H1 Collaboration, T. Ahmed et al., Phys. Lett. B 297 (1992) 205; H1 Collaboration, T. Abt et al., Phys. Lett. B 314 (1993) 436; H1 Collaboration, T. Ahmed et al., Nucl. Phys.

B 445 (1995) 195; H1 Collaboration, S. Aid et al., Phys. Lett. B 392 (1997) 234.
[3] ZEUS Collab., J. Breitweg et al., Eur. Phys. J. C 4 (1998) 591.
[4] ZEUS Collab., J. Breitweg et al., Eur. Phys. J. C 1 (1998) 109; DESY 99-057, to appear in Eur. Phys. J.
[5] ZEUS Collab., J. Breitweg et al., Phys. Lett. B 413 (1997) 201.
[6] ZEUS Collab., M. Derrick et al., Phys. Lett. B 297 (1992) 404.
[7] A. Andresen et al., Nucl. Instr. Meth. A 309 (1991) 101; A. Bernstein et al., Nucl. Instr. Meth. A 338 (1993) 23; A. Caldwell et al., Nucl. Instr. Meth. A 321 (1992) 356.
[8] N. Harnew et al., Nucl. Instr. Meth. A 279 (1989) 290; B. Foster et al., Nucl. Phys. B (Proc. Suppl.) 32 (1993) 181; Nucl. Instr. Meth. A 338 (1994) 254.
[9] ZEUS Collab., M. Derrick et al., Z. Phys. C 65 (1995) 379.
[10] R. Brun et al., CERN-DD/EE/84-1, 1987.
[11] H.-U. Bengtsson, T. Sjöstrand, Comp. Phys. Commun. 46 (1987) 43; T. Sjöstrand, CERN-TH.6488/92.
[12] G. Marchesini et al., Comp. Phys. Commun. 67 (1992) 465.
[13] A.D. Martin, R.G. Roberts, W.J. Stirling, Phys. Rev. D 50 (1994) 6734.
[14] M. Glück, E. Reya, A. Vogt, Phys. Rev. D 46 (1992) 1973.
[15] ZEUS Collab., J. Breitweg et al., Eur. Phys. J. C 6 (1999) 67; ZEUS Collab., M. Derrick et al., Z. Phys. C 72 (1996) 399.
[16] L.E. Gordon, Phys. Rev. D 57 (1998) 235; private communication; L.E. Gordon, hep-ph/9706355; A. Buijs, F. Erné (Eds.), Proc. Photon 97, Egmond aan Zee, World Scientific, Singapore, 1998, p. 173.
[17] L.E. Gordon, W. Vogelsang, hep-ph/9606457; G. D'Agostini, A. Nigro (Eds.), Proc. DIS96, Rome, World Scientific, Singapore, 1997, p. 278.
[18] M. Krawczyk, A. Zembrzuski, hep-ph/9810253; A. Buijs, F. Erné (Eds.), Proc. Photon 97, Egmond aan Zee, World Scientific, Singapore, 1998, p. 162; private communication.
[19] M. Klasen, hep-ph/9907366.
[20] B.L. Combridge, Nucl. Phys. B 174 (1980) 243.
[21] L.E. Gordon, J.K. Storrow, Nucl. Phys. B 489 (1997) 405.
[22] P. Aurenche et al., LPTHE preprint 92/13; Z. Phys. C 64 (1994) 621.

References

[1] F. Halzen and A.D. Martin, *Quarks and Leptons*, John Wiley Sins Inc. (1984)

[2] R. P. Feynman, Phys. Rev. Lett. **23**, 1415 (1969)

[3] SLAC–MIT Collab., Bloom, E. D. et al., Phys. Rev. Lett. **23**, 930 (1969);
SLAC–MIT Collab., Breidenbach, M. et al., Phys. Rev. Lett. **23**, 935 (1969)

[4] C. G.Callan and D. Gross, Phys. Rev. Lett. **22**, 156 (1969)

[5] Deden et al., Nucl. Phys. B **85**, 269 (1975)

[6] T. Eichten et al., Phys. Lett. B **46**, 274 (1973)

[7] TASSO Collab., R. Brandelik et al., Phys. Lett. B **86**, 243 (1979)

[8] H1 Collab., I. Abe et al., Nucl. Phys. B **407**, 515 (1993);
ZEUS Collaboration, M. Derrick et al., Phys. Lett. B **316**, 412 (1993)

[9] V. N. Gribov, L. N. Lipatov, Sov. J. Nucl. Phys., **15**, 438 (1972);
L. N. Lipatov, Sov. J. Nucl. Phys., **20**, 96 (1975);
Y. L. Dokshitzer, Sov. Phys. JETP, **46**, 641 (1977);
G. Altarelli, G. Parisi, Nucl. Phys. B **126**, 298 (1977)

[10] C. F. Weizsäcker, Zeits. f. Phys., **88** 612
E. J. Williams, Proc. Roy. Soc. London, **A139** (1933) 163
E. J. Williams, Phys. Rev., **45** (1934) 729

[11] H. Abramowicz et al., Int. J. Mod. Phys. A**8** 1005 (1993)

[12] J. J. Sakurai, Phys. Rev. Lett. **22**, 981 (1969)

[13] L. Gordon and J. Storrow, Z. Phys. C **56**, 307 (1992)

[14] TOPAZ Collaboration, Phys. Lett. B **332**, 477 (1994)

[15] AMY Collaboration, Phys. Lett. B **325**, 248 (1994)

[16] M. Glück, E. Reya and A. Vogt, Phys. Rev. D **46**, 1973 (1992)

[17] A. C. Bawa and W. J. Stirling, J. Phys. G**14**, 1353 (1988);
A. C. Bawa, M. Krawczyk and W. J. Stirling, Z. Phys. C **50**, 293 (1991)

[18] ZEUS Collaboration, J. Breitweg et al., Phys. Lett. B **413**, 201 (1997)

[19] L. E. Gordon and W. Vogelsang, Phys. Rev. D **50**, 1901 (1994);
L. E. Gordon and W. Vogelsang, Phys. Rev. D **52**, 58 (1995)

[20] P. Aurenche et al., Z. Phys. C **56**, 589 (1992)

[21] J. Huston et al., Phys. Rev. D **51**, 6139 (1995)

[22] L. E. Gordon, Phys. Rev. D **57**, 235 (1998)

[23] H1 Collaboration, Proc. *Eur. Phys. Soc. Conference*, Jerusalem (1997)

[24] E629 Collaboration, M. McLaughlin et al., Phys. Rev. Lett. **51**, 971 (1983)

[25] NA14 Collaboration, P. Astbury et al., Phys. Lett. B **152**, 419 (1985)

[26] NA3 Collaboration, J. Badier et al., Z. Phys. C **31**, 341 (1986)

[27] WA70 Collaboration, M. Bonesini et al., Z. Phys. C **37**, 535 (1988);
WA70 Collaboration, M. Bonesini et al., Z. Phys. C **38**, 371 (1988)

[28] NA24 Collaboration, C. D. Marzo et al., Phys. Rev. D **36**, 8 (1987)

[29] UA6 Collaboration, G. Sozzi et al., Phys. Lett. B **317**, 243 (1993);
UA6 Collaboration, G. Ballocchi et al., Phys. Lett. B **436**, 222 (1998)

[30] E706 Collaboration, L. Apananevich et al., Phys. Rev. D **59**, 74007 (1999)

[31] R412 Collaboration, P. Darriulat et al., Nucl. Phys. B **110**, 365 (1979)

[32] R107 Collaboration, E. Amaldi et al., Phys. Lett. B **77**, 240 (1978)

[33] R806 Collaboration, E. Anassontzis et al., Z. Phys. C **13**, 277 (1982)

[34] UA1 Collaboration, C. Albajar et al., Phys. Lett. B **209**, 385 (1988)

[35] UA2 Collaboration, J. Alitti et al., Phys. Lett. B **263**, 544 (1991)

[36] UA2 Collaboration, J. Alitti et al., Phys. Lett. B **288**, 386 (1992)

[37] UA2 Collaboration, J. Alitti et al., Phys. Lett. B **299**, 174 (1993)

[38] CDF Collaboration, F. Abe et al., Phys. Rev. Lett. **68**, 2734 (1992);
CDF Collaboration, F. Abe et al., Phys. Rev. D **48**, 2998 (1993);
CDF Collaboration, F. Abe et al., Phys. Rev. Lett. **73**, 2662 (1994)

[39] DØ Collaboration, S. Abachi et al., Phys. Rev. Lett. **77**, 5011 (1996);
DØ Collaboration, S. Abbott et al., Phys. Rev. Lett. **84**, 2786 (2000)

[40] CDF Collaboration, F. Abe et al., Phys. Rev. Lett. **70**, 2232 (1993);
W. Chen, Ph. D. Thesis, State University of New York, Stony Brook (1997)

[41] ALEPH Collaboration, D. Decamp et al., Phys. Lett. B **264**, 476 (1991);
DELPHI Collaboration, P. Abreu et al., Z. Phys. C **53**, 555 (1992);
L3 Collaboration, O. Adriani et al., Phys. Lett. B **292**, 472 (1992);
OPAL Collaboration, G. Alexander et al., Phys. Lett. B **264**, 219 (1991)

[42] OPAL Collaboration, M Z. Akraway et al., Phys. Lett. B **246**, 285 (1990)

[43] ALEPH Collaboration, D. Buskulic et al., Z. Phys. C **69**, 365 (1996)

[44] OPAL Collaboration, K. Ackerstaff et al., Eur. Phys. J. C **2**, 39 (1998)

[45] H. Hayashi, Proc. *Photon Workshop*, Lund (1998)

[46] L. Apanasevich et al., Phys. Rev. D **59**, 74007 (1999)

[47] M. Glück et al., Phys. Rev. Lett. **73**, 388 (1994);
W. Vogelsang and A. Vogt, Nucl. Phys. B **453**, 334 (1995)

[48] E. Laenen, G. Sterman and W. Vogelsang, `hep-ph/0002078`

[49] C. Oleari, `hep-ph/9912206`, Proc. *1999 UK Phenomenology Workshop*, Durham (1999)

[50] P. Hoyer, M. Maul and A. Metz, `hep-ph/0003257`

[51] S. Catani et al., JHEP **9903**, 025 (1999)

[52] N. Kidonakis and J. F. Owens, Phys. Rev. D **61**, 094004 (2000)

[53] E. Laenen, G. Oderda, and G. Sterman, Phys. Lett. B **438**, 173 (1998)

[54] H. Lai and H. nan Li, Phys. Rev. D **58**, 114020 (1998)

[55] H. nan Li, Phys. Lett. B **454**, 328 (1999)

[56] E. Laenen, G. Sterman and W. Vogelsang, Phys. Rev. Lett. **84**, 4296 (2000)

[57] The ZEUS Detector Status Report, DESY (1993)

[58] A. Andresen et al., Nucl. Instr. Meth. A **309**, 101 (1991);
A. Bernstein et al., Nucl. Instr. Meth. A **338**, 23 (1993);
A. Caldwell et al., Nucl. Instr. Meth. A **321**, 356 (1992)

[59] N. Harnew et al., Nucl. Instr. Meth. A **279**, 290 (1989);
B. Foster et al., Nucl. Phys. B (Proc. Suppl.) **32**, 181 (1993);
B. Foster et al., Nucl. Instr. Meth. A **338**, 254 (1994)

[60] J. Andruszków et al., DESY 92-066 (1992)

[61] W. H. Smith et al., ZEUS Note 89-084 (1989)

[62] ZEUS Collaboration, ZEUS Note 95–133 (1996)

[63] R. Brun et al., CERN DD/EE84–1 (1987)

[64] S. Chekanov and S. Magil, ZEUS Note 00–006 (2000);
Figure 4.8 is provided by S. Chekanov and S. Magil

[65] H.–U. Bengtsson and T. Sjöstrand, Comp. Phys. Comm. **46** 43 (1987);
T. Sjöstrand, Comp. Phys. Comm. 82 74 (1994)

[66] G. Gustafson, B. Andersson and C. Petersen, Z. Phys. C **1**, 105 (1979)

[67] T. Sjöstrand, Comp. Phys. Comm. **39**, 347 (1986)

[68] G. Marchesini, B. R. Webber, G. Abbiendi, I. G. Knowles, M. H. Seymour, L. Stanco, Comp. Phys. Comm. **67**, 465 (1992)

[69] Els de Wolf (editor) et al., ZEUS trigger simulation library

[70] A. Caldwell, ZEUS PHANTOM library

[71] J. Repond, ZEUS PHANTOM library

[72] J.Huth et al., Proc. *Summer Study on High Energy Physics*, Snowmass (1990)

[73] J. M. Butterworth, L. Feld and R. L. Saunders, ZEUS Note 97-057 (1997)

[74] P. Bussey, ZEUS PHANTOM library

[75] M. Seymour, `hep-ph/9707349`

[76] S. Catani et al., Nucl. Phys. B **406**, 187 (1993)

[77] S. D. Ellis and D. E. Soper, Phys. Rev. D **48**, 3160 (1993)

[78] G. Briskin, Ph. D. Thesis, Tel Aviv University (1998)

[79] A. Quadt, ZEUS PHANTOM library

[80] Particle Data Group, D. E. Groom, et al., Eur. Phys. J. C **15**, (2000)

[81] K. Umemori, Ph. D. Thesis, Tokyo University, Tokyo (1999)

[82] ZEUS Collaboration, J. Breitweg et al., Eur. Phys. J. C **6**, 67 (1999);
ZEUS Collaboration, M. Derrick et al., Z. Phys. C **72**, 399 (1996)

[83] L. Gordon and W. Vogelsang, Proc. *DIS '96 Workshop*, Rome, eds. G. D'Agostini and A. Nigro, Rome, 278 (1997) and `hep-ph/9606457`

[84] M. Krawczyk and A. Zembrzuski, private communication and Proc. *Photon '97 Conference*, eds A. Buijs and F. Erné, Egmond aan Zee, 162 (1997); `hep-ph/9810253`

[85] M. Klasen, `hep-ph/9907366`

[86] B. Combridge, Nucl. Phys. B **174**, 243 (1980)

[87] L. Gordon and J. Storrow, Nucl. Phys. B **489**, 405 (1997)

[88] P. Aurenche et al., LPTHE preprint 92/13;
P. Aurenche et al., Z. Phys. C **64**, 621 (1994)

[89] ZEUS Collaboration, J. Breitweg et al., Eur. Phys. J. C **11**, 35 (1999)

[90] P. Bussey, S. W. Lee, K. Umemori, ZEUS Note 99-046 (1999)

[91] S. Kuhlmann, Proc. *DIS '99 Workshop*, eds J. Blumlein and T. Riemann, Zeuthen, 241 (2000)

[92] ZEUS Collaboration, M. Derrick et al., Phys. Lett. B **348**, 665 (1995)

[93] M. Kimber and A. D. Martin, private communication

[94] A. D. Martin, R. G. Roberts and W. J. Stirling, Phys. Rev. D **50**, 6734 (1994)

[95] P. Bussey, S. W. Lee, ZEUS Note 00-026 (2000)

[96] T. Sjöstrand, private communication;
C. Bálazs, J. Huston and I. Puljak, `hep-ph/0002032`;
G. Miu and T. Sjöstrand, Phys. Lett. B **449**, 313 (1999)

[97] ZEUS Collaboration, M. Derrick et al., Phys. Lett. B **354**, 163 (1995)

[98] J. A. Lauber, L. Lönnblad, M. H. Seymour, Proc. *Photon '97 Conference*, eds A. Buijs and F. Erné, Egmond aan Zee, 52 (1997)

[99] OPAL Collaboration, K. Ackerstaff et al., CERN–EP–2000–082 (2000)

[100] H1 Collaboration, S. Aid et al., DESY 00-085 (2000)

[101] U. Baur et al., `hep-ph/0005226`

[102] M. Begel, Ph. D. Thesis, University of Rochester, NY (1998) and private communication. We thanks him for providing information for figure 9.19.

[103] R209 Collaboration, D. Antreasyan et al., Phys. Rev. Lett. **47**, 12 (1981)

[104] ZEUS Collaboration, M. Derrick et al., Phys. Lett. B **293**, 465 (1992)

[105] ZEUS Collaboration, J. Breitweg et al., Phys. Lett. B **472**, 175 (2000)